Focused Ion Beam Technology: Implementation in Manufacturing Platforms and Process Optimisation

A thesis submitted to the University of Wales, Cardiff

for the degree of

Doctor of Philosophy

by

Valentina Lubomirova Velkova

Manufacturing Engineering Centre

School of Engineering

University of Wales, Cardiff

United Kingdom

2011

SUMMARY

Process chains are regarded as viable manufacturing platforms for the production of Micro and Nano Technology (MNT) enabled products. In particular, by combining several manufacturing technologies, each utilised in its optimal process window, they could benefit from the unique advantages of high-profile research technologies such as the focused ion beam (FIB) machining.

The present work concerns the development of process chains and the investigation of pilot cost-effective implementations of the FIB technology in manufacturing platforms for fabrication of serial replication masters. Thus, Chapter 2 contains the background for this research providing overview and critical discussion of the different manufacturing technologies and the specific features and advantages of the FIB technology.

Chapter 3 presents a novel process chain for fabrication of replication masters for serial manufacture. The proposed process chain is validated for serial fabrication of organic electronic devices on flexible substrates. The advantages and limitations of the component technologies in the proposed manufacturing route are discussed and their interdependencies in a process chain for producing both nano- and micro- structures are analysed. In particular, the successful implementation of the FIB technology into high-throughput manufacturing routes is investigated.

Chapter 4 develops further the process chain proposed in Chapter 3 and justifies the utilisation of FIB milling in a cost effective route for serial fabrication of 3D structures and the achievement of function and length scale integration (FLSI) in products. A complex 3D

functional pattern is designed and then used to validate this route for serial manufacture of component that integrates micro and nano scale functional features. The produced replication tool is utilised for the hot embossing of structures incorporating different 2.5D and 3D length-scale features.

To improve the 3D layer-based FIB milling process it is necessary to address the obtainable accuracy in "z" direction. For this reason, in Chapter 5 a methodology for depth estimation in FIB machining is developed and validated. The layer thickness variations are investigated with regard to exposure parameters in layer-based FIB milling of 3D features. The methodology is verified by FIB machining of functional 3D features, which depths/heights fall within predetermined tolerance intervals. The proposed generic methodology represents an important step in broadening the use of this technology for micro and nano structuring.

Chapter 6 investigates the behaviour of several amorphous materials suitable for fabricating serial replication masters by FIB milling. The main focus is on depth estimation in FIB machining as a major factor affecting the process accuracy. The objective was to derive material related constants for estimating the obtainable depth and total machining time relative to Si for a given material. The layer thickness methodology developed in Chapter 5 is applied as a basis for deriving these constants. The results are discussed in regard to the materials' response to ion sputtering. The constants are verified by simulating the FIB milling of complex 3D structures in the investigated materials and then comparing the resulting profiles to those obtained experimentally after FIB milling.

Finally, in Chapter 7 the main findings of this research are identified and the results of each of the investigations are summarized.

ACKNOWLEDGMENTS

DECLARATION

This work has not previously been accepted in substance for any degree and is not concurrently submitted in candidature for any degree.

Signed   *Valentina L Velkova*   (candidate)   Date *21-March-2011*

STATEMENT 1

This thesis is being submitted in partial fulfillment of the requirements for the degree of PhD

Signed   *Valentina L Velkova*   (candidate)   Date *21-March-2011*

STATEMENT 2

This thesis is the result of my own independent work/investigation, except where otherwise stated. Other sources are acknowledged by explicit references.

Signed   *Valentina L Velkova*   (candidate)   Date *21-March-2011*

STATEMENT 3

I hereby give consent for my thesis, if accepted, to be available for photocopying and for inter-library loan, and for the title and summary to be made available to outside organisations.

Signed   *Valentina L Velkova*   (candidate)   Date *21-March-2011*

CONTENTS

LIST OF FIGURES

LIST OF TABLES

NOTATION

AR   Aspect ratio

BARC   Bottom anti-reflective coating

BMG   Bulk metallic glasses

CAD   Computer aided design

CAM   Computer aided manufaturing

CF4   Carbon tetraflouride

CI   Confidence interval

CVD   Chemical vapour deposition

EB   Electron beam

EDM   Electrical discharge machining

EHT   Extra high tension (voltage)

EUV   Extreme ultraviolet

FIB   Focused ion beam

FIBL   Focussed ion beam lithography

FLSI   Function and length scale integration

FWHM   Full width at half-maximum

HAZ   Heat-affected zone

HE   Hot embossing

IB   Ion beam

IC   Integrated circuit

IM   Injection moulding

LCD   Liquid crystal display

LED   Light emitting diode

LEE   Light extraction efficiency

LIGA	Lithography, electroplating, and moulding
LMIS	Liquid metal ion sources
MCP	Multichannel plate
μEDM	Micro electrical discharge machining
μIM	Micro-injection moulding
MEMS	Micro-electromechanical systems
MET	Micro engineering technologies
MNT	Micro and nano technologies
MOEMS	Micro-opto-electromechanical systems
MST	Micro systems technologies
NIL	Nano-imprint Lithography
OTFT	Organic thin film transistors
PET	Polyethylene terephthalate
PMLP	Projection maskless nano-patterning
PMMA	Polymethyl methacrylate
PVD	Physical vapour deposition
R2R	Roll-to-roll/ reel-to-reel
RIE	Reactive ion etching
SEM	Scanning electron microscopy
S-FIL	Step and flash imprint lithography
SIMS	Secondary ion mass spectrometry
STL	Stereolithography
UV-NIL	Ultraviolet nano-imprint lithography
3D	Three dimensional
C_f	Material related constant for depth estimation in FIB milling

C_t Material related constant for time estimation in FIB milling

D_A Area dose, $[\mu As/cm^2]$

D_L Area dose per layer, $[\mu As/cm^2]$

d_t Dwell time, $[ms]$

F_D Dose factor

h Layer thickness $[nm]$

H Total depth/height $[nm]$

I Current, $[A]$

M Atomic mass

MR Milling rate, $[\mu m^3/\mu As]$

MR^r Relative milling rate, $[\mu m^3/\mu As]$

N_A Avogadro's number

N_L Number of layers

R_s Sensitivity coefficient, $[sA/cm^3]$

S Number of sputtered atoms

S_S Area step size $[nm]$

t Time, $[s]$

t_{DWELL} Area dwell time, $[ms]$

Tm Melting temperature, $[^oC]$

$u(x)$ Standard uncertainty, $[nm]$

$u(P)$ Measurement uncertainty, $[nm]$

$u_c(x)$ Combined standard uncertainty, $[nm]$

U Expanded uncertainty, $[nm]$

Y Sputtering yield, $[atoms/incident\ ion]$

ρ Density

μm	Micrometer
η	Number of ions that strike the sample
θ	Angle of incidence, [$^{\text{o}}$]
ν_{eff}	Effective degrees of freedom
ν	Degrees of freedom
V	Volume, [cm^3]

CHAPTER 1

INTRODUCTION

1.1 Motivation

Most of the improved functionality of advanced mobile phones, data storage devices, holograms for data protection, micro fluidic mixers or medical implant stencils nowadays is based on the development and serial manufacturing of Micro and Nano Technology (MNT) enabled products. Such products are indispensable part of our everyday life – from electronic devices and communication technologies to medicine and airspace. The high-throughput mass production of most of the non-electronic micro-components is achieved by the use of serial replication technologies like micro injection moulding, hot embossing, imprinting and their different variations. The continuous market demand for improved products integrating more and more functions into a unit product of constantly decreasing size and weight had raised the requirements towards MNT in terms of process capabilities, production time and cost. Thus, innovative manufacturing solutions to meet the constant demand for better and more sophisticated products are the focus of industry and research community efforts.

Lately the notion of combining several manufacturing technologies, each utilised in its optimal process window, is increasingly attracting the attention of industry and researchers. The implementation of such process chains is especially viable in the field of master making where along with the strict requirements in terms of surface

structuring, surface roughness, aspect ratio etc., tool qualities like robustness, wear resistance and long life time also have to be guaranteed.

However, due to issues posed by compatibility and complementarity of integrated processes, error factors at every stage of these process chains and the diversity of fabrication technologies available the development and cost-effective implementation of such process chains is not a straightforward task. Especially, further research is required with the aim to increase the throughput and robustness of existing and new emerging manufacturing routes.

Meanwhile, the design and implementation of novel process chains as manufacturing platforms for mass production could benefit from the technology advances which are already utilised in laboratories and are also characterised in pilot research applications. Such technologies offer unique advantages but their implementation in 'single-process' fabrication solutions (Dimov *et al.*, 2006) is limited due to their low throughput or high processing times. One such technology is the focused ion beam (FIB). It is regarded as not viable for serial production when utilised on its own due to shortcomings like high machining times, small working areas and high production cost. At the same time, advantages like precise patterning with resolution down to tens of nm, capability to machine virtually any material, process flexibility and ability to structure complex 3D features in both micron and sub-micron and nano dimensional ranges, and ultimately offering capabilities for length-scale integration, could make FIB machining an indispensable part of manufacturing routes aiming at achieving function and length scale integration (FLSI) into a single component and products.

This research is dedicated to the development of such manufacturing routes and in particular to the investigation of pilot cost-effective implementations of the FIB technology in process chains for fabrication of serial replication masters.

1.2 Research Objectives

The overall aim of this research was to investigate the cost-effective implementation of the FIB technology in serial production as a component technology in process chains for manufacturing of replication masters. Since both process chain development and FIB milling are broad research and development areas with many open research issues and different development trends, this work is focused only on some of these important research topics. Especially, some open issues related to the use of the FIB technology for 3D micro and nano structuring are addressed in this research with the objective to create the necessary pre-requisites for its successful and cost-effective integration into master-making process chains. Thus, the following main research topics are the focus of this work:

- development and validation of cost-effective process chains for fabrication of replication tool incorporating the FIB milling as a component technology;
- cost-effective production of complex 3D features of different length scale dimensions onto a single component;
- accurate depth estimation in layer-based FIB milling;
- the machining response of different master-making materials during layer-based FIB milling.

After identifying the factors affecting the FIB milling process and its effective integration with other complementary micro and nano structuring technologies, empirical and analytical methods and tools were applied for the validation of the concepts and manufacturing solutions developed in this research. Further to this, a process simulation was performed employing software tools based on specific ion sputtering models, to verify and support the findings and results related to the FIB milling research. In addition, process monitoring and control as well as alignment techniques were utilised to guarantee the process stability and positional accuracy during both the consecutive application of different component technologies in process chains and the structuring of different length scale features on the same area of a workpiece. Thus, to achieve the overall aims of this research the following objectives were set:

- To develop a cost-effective multiple-process manufacturing platform for production of masters for serial replication containing micron and sub-micron features which implements the FIB machining as a component technology. Also, to assess the error factors at each stage of such chains and their possible impact on the overall effectiveness and to validate the chains for serial replication, e.g. for roll to roll (R2R) hot embossing.

- To validate multiple-process manufacturing platforms, where the advantages of FIB machining for structuring precisely complex 3D features of micron, submicron and nano- dimensions are utilised for producing replication masters incorporating different length scale features. Also, to analyse the resulting structures throughout the different stages of the process chains to the final product and perform an uncertainty analysis.

- To develop a methodology for depth prediction during layer-based FIB milling, as a mean for a depth control, and validate it for the production of complex 3D structures. Special attention should be paid to the factors affecting the process uncertainty and the selection and optimisation of the sets of process parameters used.

- To investigate the response to FIB machining of different materials suitable for producing replication tools, especially amorphous and single crystal ones, and determine the milling rate achievable on them. Thus, to estimate accurately the obtainable depth and total machining time when producing micro and nano structures on such materials.

To achieve the objectives of this research analytical investigation of the FIB milling technology is carried out employing empirical studies as well as process simulation. Results from each experimental run are analysed and the effects of the investigated factors on the process performance and/or the overall effectiveness of the applied sequence of processes are discussed and assessed. Furthermore, recommendations are made on how to optimise process performance thus addressing the research concerns outlined in this section.

1.3 Thesis Organisation

The thesis consists of seven chapters. The main investigations of the research are presented in Chapters 3 to 6, while Chapters 2 and 7 are a literature review and summary of the made contributions to knowledge, respectively.

Chapter 2 provides the background for the research carried out in this thesis. This chapter consists of three main sections. In the first section, the concept and the need for process chains are presented and critically analysed. Also, the implementation of a wide variety of manufacturing processes as component technologies in process chains is described and discussed. The second section provides a review of the FIB technology outlining the specific advantages that this process offers when utilised in its optimal process window. In the third section the concepts investigated in this research are summarised and its specific focus is described.

In Chapter 3 the design and validation of a novel master-making process chain for serial replication of large area electronic devices on flexible substrates is presented. The chapter starts with description of the main concept of the proposed process chain and detailed analysis of the process chain design specific features and component technologies. Then, the experimental set-up for realization of the proposed process chain, including the design of the test device and process conditions for each technology, as well as measuring and inspection of the produced structures at each stage of the process chain is described. Finally, the obtained results after each stage of this process chain and the end product are critically analysed and assessed to validate the proposed manufacturing route. In addition, possible error factors that could affect each of the component technologies as well as the end product are discussed and conclusions are made about their influence on the overall performance of the proposed process chain.

In Chapter 4 develops further the concept proposed in Chapter 3 for fabrication of replication masters with a special focus on achieving 3D function and length scale

integration in a single component. The advantages that the FIB technology offers in regard to high-resolution 3D structuring are discussed as an integral part of the proposed master making process chains. Also, a special attention is paid to the pattern preparation approaches. Then, the multiplication of a given pattern over large areas and the successful transfer of the complex 3D geometries onto replication tools are investigated. Finally, the resulting 3D profiles at different stages of the considered process chain are studied and the factors affecting its overall performance are analysed.

Chapter 5 addresses the FIB machining issues with regards to achievable depth and its estimation. In particular, a methodology for depth estimation in layer-based FIB milling is developed and validated empirically for exposures with particular sets of process parameters for a given material. Experiments are designed and performed with the selected sets of parameters to account for several process factors affecting the FIB milling technology. Then, the obtained results are critically analysed to assess the process uncertainty and define tolerance intervals for any calculated layer depths. Finally, the methodology is validated by FIB machining of complex 3D features.

Chapter 6 investigates the behaviour of several amorphous materials suitable for fabricating serial replication masters by FIB milling. The main focus is on depth estimation in FIB machining as a major factor affecting the process accuracy. Material specific constants are derived for estimating the milling rates, and thus the obtainable depth and total machining time relative to Si for the considered materials. A layer thickness methodology is applied as a basis for deriving these constants. The results are discussed in regard to the materials' specific responses to ion sputtering.

The empirical constants are verified by simulating FIB milling of complex 3D structures in the investigated materials and then comparing the resulting profiles to those obtained experimentally after FIB milling.

In Chapter 7 the generic conclusions of this work are summarised. Based on them the main contributions to knowledge are presented and some possible directions for further investigations are discussed.

CHAPTER 2

LITERATURE REVIEW

In this chapter a review of the capabilities and possible implementations of the FIB technology into cost-effective master-making process chains is presented. It consists of three main sections covering the state-of-the-art of the main topics addressed by this research and also discusses the open research issues associated with them. In the first section the implementation of process chains for the fabrication of products integrating micro and nano-scale features is discussed. Then, the second section provides a review the FIB technology and a discussion on the advantages that it offers with regard to its integration in process chains for achieving length-scale integration in products. Next, a summary of the open research issues and the put forward concepts to address them in this research are presented.

2.1 Process chains in micro- and nano- manufacturing

2.1.1 Concept of process chains

In the last decade, manufacturing industry has witnessed a rapid increase in demand for micro-products and micro-components in many industrial sectors including the electronics, optics, medical, biotechnology and automotive sectors (Alting *et al.,* 2003; Hansen *et al.*, 2006). Examples of applications include medical implants, drug delivery systems, diagnostic devices, connectors, switches, micro-reactors, micro-engines, micro-pumps and printing heads. These microsystem-based products represent key value-adding elements for many companies and, thus, an important

contributor to a sustainable economy (Dimov *et al.*, 2006). As a result of the current trend towards product miniaturisation, there is a demand for advances in micro- and nano-manufacturing technologies and their integration in new manufacturing platforms. In this research, the definitions for micro- and nano-manufacturing are adopted from Madou (Madou, 2002). More specifically, micro-manufacturing refers to the fabrication of products or components where the dimensions of at least one feature are in the micrometre range. Similarly, nano-manufacturing refers to the production of devices where some of the dimensions are in the nanometre range. Usually a combination of technologies, in the form of a process chain, is necessary to achieve a high throughput and cost-effective production of micro-components and devices incorporating micro/nano features and surfaces. As a result, there is a trend to move from designing miniaturised products for specific materials and technologies to designing processes and process chains to satisfy the specific functional and technical requirements of emerging multi-material products. In turn, to develop new enabling process chains and new manufacturing platforms based on them, it is necessary to characterise the "component" technologies and pay special attention to their interfaces and thus to achieve the necessary compatibility and complementarity between them.

The integration of micro- and nano- technologies in new manufacturing platforms also referred to as process chain development, usually targets two very significant objectives (Brousseau *et al.*, 2009):

1. to enable both function integration (incorporation of different functions) and length- scale integration (combination of macro-, micro-, sub-micron and nano- dimensions) in existing and new products, and

2. to provide for the cost-effective manufacture of such products in a wide range of materials.

The importance of meeting these two requirements is discussed in further detail in the following sub-sections.

2.1.2 Function and Length Scale Integration

In recent years the trend towards product miniaturisation, together with the advantages that the integration of multiple functions into a single component could bring, "fuelled" the interest in developing manufacturing solutions for producing features/structures with dimensions ranging from millimetre to nanometre scales onto a single product (Velkova *et al*., 2011). In this study it is referred to as a trend towards and/or respective manufacturing routes for achieving Function and Length Scale Integration (FLSI) in products.

FLSI is a product development approach that offers many advantages such as reduction of production cost and time, as well as products' overall dimensions (Bigot *et al*., 2009). The methods for achieving FLSI can be classified into three main types: assembly, single process machining/structuring and multi-process fabrication of a single component. However, the successful implementation of FLSI arises very specific issues that can be summarized (Bigot *et al*., 2009) in two main streams:

Assembly related issues

Assembly is a key stage in the fabrication of a product, which may require the use of various processes to integrate parts manufactured separately due to different technical reasons, e.g. complexity, capabilities and/or incompatibility of the available manufacturing processes (Hansen *et al*., 2005). The cost and reliability of bonding techniques used when dealing with micro components, as well as the dimensional

accuracy of the parts to be assembled are of particular concern. The assembly related issues can further be subdivided into issues related to (1) macro-meso scale assembly and (2) micro-nano scale assembly.

- **macro-meso scale assembly**

Macro-meso scale assembly is a common problem for many "micro-products", which are often made of macro-meso components containing micro-nano functional features. Thus, the assembly itself might not occur at micro-nano scale but at the macro-meso scale. Standard macro assembly methods such as mechanical fastening, welding and gluing can generally be employed for macro-meso scale tasks. Their implementation even for single-scale dimensions' products poses significant issues related to handling and transportation of components during assembly (Eriksson *et al.,* 2006). In addition, the presence of micro-nano features increases the complexity of the assembly operations that have to be designed carefully to avoid damage or contamination of such intricate structures. Furthermore, the choice of materials for micro-nano structuring is often limited which can lead to incompatibilities between the materials to be bonded. In addition, tighter tolerances may be required in order to perform reliably macro-meso scale assembly operations in order to ensure a proper function interaction between structures with different length scale features.

- **micro-nano scale assembly**

In the case of products having dimensions too small to be manipulated with standard handling systems, new issues arise. In addition to the issue of high precision and positional accuracy requirements for the handling systems, there are different forces acting on components due to scale effects, e.g. electrostatic, Van der Waals and

surface tension forces that become dominant over gravitational forces (Danchev and Kostadinov, 2006). Those phenomena have to be taken into account when applying micro-nano assembly technologies such as bonding. There are many bonding methods such as welding, adhesive, diffusion or soldering (Tsuchiya *et al.*, 1999).

Some micro components can be picked and placed manually by highly skilled operators using high power microscopes and micro-tweezers (Van Brussel *et al*, 2000). With the introduction of virtual reality techniques to aid in preparing and visualising the assembly solutions prior to physical conception, manual operations can be considerably improved. However, one intrinsic drawback of manual operations is the loss of direct hand-eye coordination. Manual assembly remains difficult, time consuming and therefore very expensive (Cecil *et al.*, 2007).

Automatic assembly and handling of micro components are required in high throughput production systems but there are no established generic approaches. To find solutions for specific products, designers can only rely on latest surveys of the micro assembly techniques available and adapt them to the problems at hand (Cecil *et al.*, 2007).

Finally, one of the latest types of micro-assembly technology is called self-assembly. It can be defined as a process by which two or more separate and relatively simple components are oriented to one another to form a functional entity, without interference or external handling (Srinivasan *et al.*, 2002). Self-assembly technologies have the potential to automate the handling and integration of sub-micron components.

Multi-scale machining related issues

For various economical and technical reasons assembly steps should generally be avoided. It is always more cost effective to achieve the required functionality as early as possible in the production lines, thus simplifying any assembly steps if not possible to eliminate them at all. In the attempts to avoid assembly operations, the implementation of a chain of multiple processes working on a single component is becoming a preferred option. However, there are a number of issues to this approach as well, related to the use of (1) a single manufacturing process or (2) a sequence of processes, to produce the functional features cost-effectively (Bigot *et al.,* 2009).

- **single process length scale issues**

In an attempt to minimise the number of processes used in a chain and therefore the overall production time and cost, a single step process can be applied to achieve the necessary FLSI. Such a solution, however, requires significant research and development (R&D) efforts to implement in scale-up manufacture. ''Design for manufacture'' approaches in designing the products are usually needed to account for the specific manufacturing constraints of the selected high-throughput technologies. Also, due to the difference in sizes, various features might require different levels of process control in order to achieve a correct output. Thus, optimising part design and process parameters becomes increasingly challenging. In addition, the machine setup must allow for an accurate positioning of the workpiece in order to achieve the necessary repeatability when producing batches of components.

- **multiple process length scale issues**

It is often the case that a single process is not sufficient to machine a range of functional features with different dimensions in a given material. Therefore, it is necessary to apply consecutively two or more complementary manufacturing technologies in a chain to achieve the necessary FLSI. By opting for process chains, integration issues arise in achieving the necessary dimensional accuracy between functional features produced using multiple machine setups due to handling, alignment and referencing errors. The most common problem when employing several manufacturing technologies in sequence is related to alignment difficulties (Bigot *et al*., 2009). Alignment marks have to be considered at early stages of component design and the use of very accurate vision and measuring equipment would often be necessary to produce micro- and nano- features on a single component.

The concept of process chains is that, when chains of processes are employed the objective is to use each technology integrated in them in its most cost-effective processing window. Another type of integration issue that may arise is associated with the compatibility of the subsequent processes. It involves mainly the aspects related to material properties and resulting surface integrity after machining employing different physical phenomena. Therefore, a process chain for the manufacturing of multi-scale features should be carefully designed and optimised in order to take into account the constraints of each manufacturing technology and the influence that they can have on previously machined features or subsequent processes in a chain.

Although a broad range of technologies can be utilised in micro and nano manufacturing they are viable only in their cost effective processing window in regard

to features' sizes and/or throughput. Therefore, to achieve FLSI in products it is necessary to look for or develop process chains that combine the capabilities of complementary technologies (Bigot *et al*., 2009; Brousseau *et al*., 2009; Allen *et al*., 2008). Such multi-process fabrication paradigm for a single component relies on novel integrations of manufacturing technologies, which operate in their cost-effective processing windows, to design and implement viable manufacturing platforms (Velkova *et al*., 2010; Scholz *et al*., 2009). The aim of such technology integration is to multiply innovatively the capabilities of component technologies, taking into account and minimising the constraints of each manufacturing process and the influence it can have on previously machined features or subsequent process in the chain. In this way the advantages of compatible and at the same time complementary technologies are utilised at their best while reducing the impact of their shortcomings on the overall product realisation.

The masters/inserts for serial replication of micro- and FLSI components are a product of a great market importance (Brecher *et al*., 2007; Piotter *et al*., 2008; Kolew *et al.,* 2010). Thus research and development efforts are concentrated on both their improvement and, at the same time, on reduction of their production time and cost. Therefore, the maturity of process chains applied for their fabrication and the diversity of manufacturing technologies utilised are a significant factor in achieving these objectives.

2.1.3 Technologies utilised for the fabrication of replication tools incorporating different function and length-scale (FLSI) features

The most important requirement for achieving a high throughput production of FLSI

components is the design of viable manufacturing platforms for their cost-effective fabrication. A number of technologies have been utilised for mass production of non-electronic micro-components. CD and DVD data storage devices, various micro fluidic devices, sensors, optical switches, micro lenses and holograms for data protection imprinted on credit cards and bills (Pietarinen *et al.*, 2006; Leech and Lee, 2006) are among the most well known products that incorporate micro- and nano-scale functional structures and at the same time are produced in large series. In spite of the diversity of these application areas, the most viable micro fabrication technologies for their high-throughput manufacture are different implementations of micro injection molding and roll-to-roll (R2R) processes. A key requirement for successful application of these technologies is the availability of precision production master having a long lifetime that can deliver a very high yield (Velkova *et al.*, 2010). Depending on the size and the features of the functional structures to be replicated the masters are usually produced by employing process chains that combine the capabilities of the following technologies:

- Mechanical micromachining

- Laser structuring;

- Micro Electro Discharge Machining (μEDM);

- LIGA (lithography, electroplating, and moulding);

- LIGA-based technologies.

The capabilities of these component technologies in fabrication of moulds are analysed by many researchers and their advantages and disadvantages are well understood (Heckele and Schomburg, 2004). The laser structuring, the conventional mechanical micromachining technologies and μEDM are suitable for machining

features with a resolution down to few microns with relatively good aspect ratios and surface quality (Giboz *et al*., 2007). However, they are not applicable for fabricating structures that incorporate sub-micron and nano- features.

Conversely, LIGA (Hormes *et al*., 2003) and LIGA-based technologies, e.g. X-ray, Extreme UV (EUV), Ion Beam (IB) and Electron Beam (EB) LIGA, are a flexible way for producing structures incorporating micron and sub-micron features with high aspect ratios, good surface roughness and sub-micron tolerances (Alting *et al*., 2003). Most commonly used are the UV and X-ray LIGA while the more recent implementations of this technology, EUV-LIGA, EB-LIGA and IB-LIGA, are considered more efficient but still more complex and expensive (Giboz *et al*., 2007). In terms of master-making, a major advantage of these technologies are their capabilities to produce structures with well defined and smooth sidewalls, an important factor in achieving a reliable replication (Malek and Saile, 2004). At the same time, a major disadvantage of the LIGA process is that it cannot be used for producing masters in conventional tooling materials like steel.

Currently, the process of nickel electroforming proves to be a viable and widely used method for producing replication tools (Leech *et al*., 2004) due to the fact that it provides for a good hardness and wear resistance. The process also allows features of more complex shapes and various sizes to be replicated. Moreover, a very wide range of technologies can be used to fabricate electroforming masters with desired structures, e.g. laser ablation, µEDM, photolithography, EB lithography and focussed ion beam (FIB) machining. However, the use of any particular technology is viable only within a given optimal processing window in regard to achievable resolution,

surface quality and removal/structuring rates. As discussed in the previous section, usually a sequence of processes applied for machining of complex topographies, which incorporate different FLSI features, is the most cost-effective mean for the manufacturing of a final product. While the increase of the process steps leads to an increase in the overall uncertainty and total error associated with any selected manufacturing route, a well-designed process chain can have a significant positive impact on accuracy and cost-effectiveness of the whole master-making process (Dimov *et al*., 2006). Therefore, the process chain design should be paid a special attention in order to achieve the targeted compatibilities of component technologies, and at the same time to minimise the effects of various factors that can influence their overall performance. It is still a challenging task to combine technologies with different cost-effective processing windows, and thus to design viable tool-making process chains for producing components with both micro- and nano-features and/or realising complex 3D shapes.
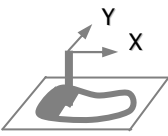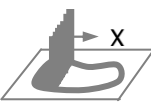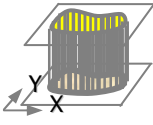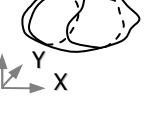
Some attempts have been made to develop such process chains (Leech and Lee, 2007; Bissacco *et al*., 2005) however further research is necessary to address the complex issues that arise in achieving a function and length-scale integration and 3D patterning simultaneously in a given process chain.

2.1.4 Review of micro- and nano- manufacturing technologies

To make feasible proper selection of manufacturing processes and order them in cost-effective master-making process chain, a thorough knowledge of their capabilities and limitations is necessary. Therefore this section presents a brief review of some of the main micro- and nano- manufacturing technologies, considered as viable for

implementation in master-making manufacturing routes (Dimov *et al*., 2006).

A broad range of technologies exists for micro- and nano-manufacturing, and the physical principles implemented in them are very diverse. Several researchers have proposed classification schemes to categorise these technologies. For example, Masuzawa (Masuzawa, 2000) focussed on micromachining processes and classified them according to the implemented machining phenomena. According to other researchers (Madou, 2002) the micro-fabrication techniques can be categorised as traditional or non-traditional methods and lithographic and non-lithographic methods. An alternative classification, suggested by Dimov et al. (Dimov *et al*., 2006) classifies the micro-manufacturing technologies according to their process 'dimension' and material relevance – Figure 2.1. In this classification, the first group of technologies performs material removal and deposition employing "1D processing", e.g. structuring by a milling cutter or a laser beam. The second group includes technologies that utilise multiple 1D processing, e.g. 3D printing. Next, the technologies falling in the group of "2D processes" perform structuring by employing masks, e.g. photolithography. Finally, "3D processing" can be carried out using technologies for surface modification and deposition, e.g. PVD, CVD and electroplating or technologies for volume structuring such as injection moulding and embossing. Studying this classification, it can be concluded that generally, the manufacturing flexibility of the technologies increases from right to left, e.g. less time and effort are required to setup the process, while the production throughput and the process complexity increases from left to right.

Dimension capabilities	1D Processing	Multiple 1D Processing	2D Processing	3D Processing (Surface)	3D Processing (Volume)
Metals	LH, EDM, ECM, Grinding	MF, Grinding	Lap, Pol, MF	Lap, Pol, ECP, EF, EP	EDM, MF
Polymers	3DL	3DP	EBL, IBL, LL, PUL, XL		HUE, NIL, NI, R2RE, IM
Ceramics	3DL, Grinding	3DP	IBL, LL,	Lap, Pol	NIL, NI, R2RE
Any material	EBM, FIB, LA, PM, AWJ, Drilling, Milling, Turning, SLS		Etch, PMLP, SP	PVD, CVD, SC, SA	Casting, MCIM, PIM (1)

Key:

3DL	3D Lithography	Lap	Lapping
3DP	3D Printing	LH	Laser hardening
AWJ	Abrasive water jet	LL	Laser lithography
Casting	Casting	MCIM	Multi-component injection moulding
CVD	Chemical vapour deposition	MF	Metal Forming
DL	Direct LIGA	Milling	Milling
Drilling	Drilling	NI	Nano-imprinting
EBM	Electron beam machining	NIL	Nano-imprint lithography
EBL	Electron beam lithography	PIM	Powder injection moulding
ECM	Electrochemical machining	PUL	Photo / UV lithography
EDM	Electrical discharge machining	PM	Plasma machining
EF	Electroforming	PMLP	Projection mask-less nanopatterning
ECP	Electro-chemical polishing	Pol	Polishing
EP	Electroplating	PVD	Physical vapour deposition
Etch	Etching	R2RE	Reel to reel embossing
FIB	Focused ion beam	SA	Self assembly
Grinding	Grinding	SC	Spin coating
HUE	Hot/UV embossing	SLS	Selective laser sintering
IBL	Ion beam lithography	SP	Screen printing
IM	Injection moulding	Turning	Turning / Diamond turning
LA	Laser ablation	XL	X-ray lithography

Figure 2.1 Map of technologies according to process dimension and material relevance – adapted from (Dimov *et al.*, 2006).

Perhaps the most widespread classification is that of Brinksmeier et al. (Brinksmeier *et al.,* 2001) which is shown in Figure 2.2. In particular, the authors considered two generic technology groups: Micro System Technologies (MST) and Micro Engineering Technologies (MET). MST encompasses the processes for the manufacture of MEMS and micro-opto-electromechanical systems (MOEMS), while MET cover the processes for the production of highly precise mechanical components, moulds and microstructured surfaces.

2.1.4.1 MEMS processes

The manufacturing processes associated with the MEMS/MOEMS and microelectronics fields are based on 2D or planar technologies. This implies the fabrication of components or products on or in initially flat wafers (Alting *et al.*, 2003). Most MEMS technologies use silicon as the substrate material and a sequence of complex chemical processes (Jing *et al.*, 2007; De Grave and Brissaud, 2005). The wafer fabrication processes can be divided into six basic steps: cleaning/oxidation, photolithography, etching, implantation, diffusion, and metrology. The operations may vary widely depending on product configurations or the technology in use (Arisha *et al.*, 2004).

Photolithography is the main technique used to define the shape of the micromachined structures. It involves the processing of wafers in order to build up the layers and patterns of metal and wafer material to produce the required circuitry. During the photolithography process the pattern is transferred from a mask onto photosensitive polymer and finally replicated into the underlying layer. The object of this multi-step
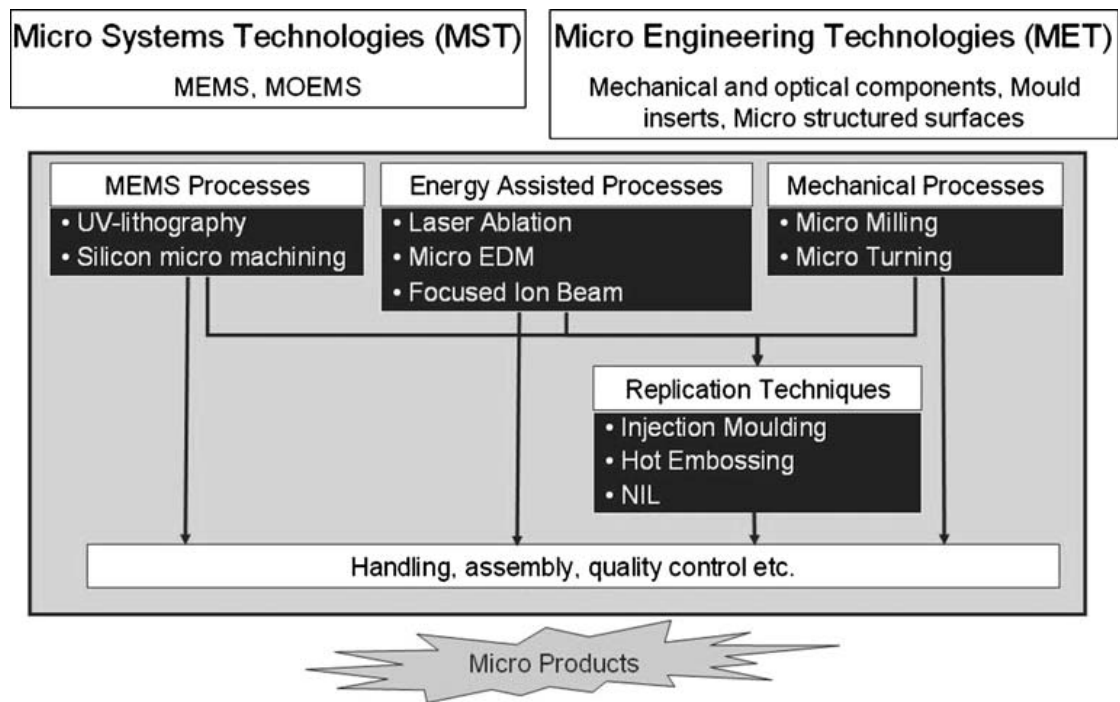
Figure 2.2 Process technologies for micro-manufacturing – adapted from
(Brinksmeier *et al*., 2001).

process is the accurate and precise definition of a three-dimensional pattern on a semiconductor substrate (Arisha *et al*., 2004).

The subsequent chemical or physical processes can be divided into two main categories: thin film deposition (creating functional layers on the silicon substrate) or additive processes and etching processes (removing material). The specific sequence of processes is not given on beforehand, but must be defined by the designer.

The thin film deposition processes can be divided into several main categories: Chemical Vapour Deposition (CVD), Physical Vapour Deposition (PVD), Electrochemical Deposition and Spin-on deposition. The first three are subdivided into: CVD – atmospheric pressure CVD, Low pressure CVD, Plasma enhanced CVD and Vapour phase epitaxy CVD; PVD – Vacuum evaporation, molecular beam epitaxy and sputtering and for Electrochemical Deposition – electroless plating and electroplating (Alting et al., 2003).

The material removal, or etching, can be wet etching where the wafer is immersed in a bath of etchant, which must be agitated to achieve good process control or dry etching which makes use of plasma or vapour under pressure. Wet etching processes are subdivided into isotropic and anisotropic (single crystal) etching, while dry etching could be vapour etching, plasma etching and reactive ion etching.

The various lithography and LIGA processes were discussed in detail in section 2.3.1 of this literature review chapter.

Lithography-based technologies for micro-electromechanical systems (MEMS) are capable to produce micro- and submicrometre-size features. However, these techniques are capital intensive and inevitably require cleanroom environment (Rajurkar *et al*., 2006), and have limitations concerning the range of materials that can be processed and the complexity of the geometry they can produce. Thus, MEMS techniques cannot meet the demand for miniaturised products and components that require 3D and high aspect ratio features, resistance to aggressive environments and enhanced-force micro-actuation.

2.1.4.2 Mechanical processes

This category includes technologies like micro-milling, micro-turning, micro-drilling, ultraprecision micro-milling, micro-grinding and micro-abrasive machining. All of them can be characterised as direct tool-workpiece contact material removal processes. In general, mechanical processes for micromachining have higher material removal rates and are capable of generating 2D and 3D micro features on wide range of materials (Liu *et al*., 2004; Dornfeld *et al*., 2006). Their limitations include their inability to machine hard materials and lack of mass production capabilities (Rajurkar *et al*., 2006). Among those technologies, micro-milling is perhaps the most widely applied one in the field of master making for microinjection moulding and HE.

Micro-milling

Micro-milling is characterised by relatively high removal rates and employs tools that can have a diameter down to 10 µm (Filiz *et al*., 2008). The main application areas of micro-milling include the manufacture of micro-parts for watches, keyhole surgery, housings for microengines, tooling inserts for microinjection moulding and hot

embossing, and housings and packaging solutions for micro-optical and micro-fluidics devices. It has emerged as an effective technique for machining high aspect and/or complex 3D micro-features due to its flexibility, cost-effectiveness, accuracy and the surface finish that can be achieved in a wide range of engineering materials such as aluminium alloys, stainless steel, titanium, brass plastics, ceramics and composites (Filiz *et al*., 2007; Pham *et al*., 2009). However, typical drawbacks of the process are material deformation related issues such as burr formation and significant deviations of the dimensions of the machined features relative to the nominal values, due to tool deflections. Also, as the features' size has to comply with the minimum tool diameter, the minimum size of concave features is limited to 100 µm. Even though there is no such constraint for convex structures they have to withstand the cutting forces without excessive elastic deformation (Bissacco *et al*., 2005).

2.1.4.3 Energy assisted processes

Laser milling/ablation

Laser milling involves applying laser energy to either remove material through ablation in a layer-by-layer fashion or join components (Pham *et al*., 2002). This technology is suitable for machining of a wide range of materials including metals, ceramics, glass, polymers and semiconductors. It is particularly appropriate for hard materials that are difficult to machine by conventional means (Dubey and Yadava, 2008). This important process characteristic is due to the fact that extremely high power can be released within a very short time interval, pulse duration, onto a spot of a few micrometres in diameter (Meijer *et al*., 2002).

Two main ablation regimes according to the laser pulse length used have been distinguished (Petkov *et al*., 2008): ultrashort pulses: femtosecond (fs) and picosecond (ps), and longer pulses: nanosecond (ns) and microsecond (ms). Major advantage of the ultrashort pulse laser ablation is the negligible thermal effect into the substrate and almost no heat-affected zone (HAZ). Due to its nature the ultrashort pulse laser ablation provides for small feature size, smooth finishing surface and flexible structuring (Zheng *et al*., 2006). Conversely, in long pulse laser milling, undesirable effects such as HAZ, recast layers, micro-cracks, shock wave surface damage and debris from ejected materials are observed.

Two different approaches to pulsed laser ablation/milling can be applied: direct writing and mask projection (Gower and Rizvi, 2000). Even though direct writing is a relatively simple technique, the limitations to the complexity of the produced features' geometry and the small area covered are a significant drawback. The mask projection method on the other hand can produce many types of structures and is suitable for batch production. However, the necessity of a mask makes this approach relatively expensive (Alting *et al*., 2003).

Micro Electrical Discharge Machining (µEDM)

Micro electrical discharge machining is a thermal process for contactless material removal of electrically conductive materials (Bissacco *et al.,* 2007). Current µEDM configurations include (Rajurkar *et al.,* 2006): µEDM milling, µEDM sinking (Kunieda *et al*., 2005), µEDM drilling, µEDM grinding (Rees *et al*., 2007) and micro-wire EDM (Rees *et al*., 2008). Those diverse process developments have led to the current wide use of µEDM for the manufacture of micro-structures and tools

employed in mass production of micro- components such as inserts for microinjection moulding and hot embossing. In addition, the almost negligible machining forces, no burr formation and good repeatability of the process have made µEDM the best means for producing micro-features with high aspect ratios (Pham *et al*., 2004). However, there are some specific drawbacks of this technology, such as tool/electrode wear, positioning errors, inspection issues and low removal rates (Kunieda *et al*., 2005; Hansen *et al.*, 2007) that limit its application.

Focussed Ion Beam

FIB patterning is a technology that is used for producing not only complex 3D microstructures but also nano-sized features. FIB can perform milling operations, and in the presence of a precursor gas, it can also be employed for ion beam-induced deposition (Shinji and Yukinori, 1996) or gas-assisted etching (Fu *et al*., 2005). This technology enables direct patterning of almost any material with high accuracy and resolution. In particular, it is possible to achieve structures with lateral dimensions less than 50 nm (Allen *et al.,* 2009).

Many of the advantages, characteristic for the FIB technology, such as flexibility, high resolution and high surface quality, are extremely important for master making (Scholz *et al*., 2009; Youn *et al*., 2006). However, a major disadvantage of this technology is its relatively low removal rates, which makes it expensive and non-feasible to utilise as a stand-alone manufacturing mean. However, to address this issue a multi-ion beam concept was proposed that combines the high resolution capabilities of the FIB technology with the higher throughput advantage of parallel lithography systems. In particular, to satisfy the requirements for high productivity, a projection

maskless nano-patterning (PMLP) system is under development (Platzgummer *et al*., 2008). Furthermore, Dimov et al. (Dimov *et al*., 2006) concluded that some component technologies in process chains are not viable on their own but by integrating them with other complementary technologies can lead to the development of novel process chains. Example of such process is the focussed ion beam structuring. Considering the many advantages this technology has to offer, a major objective of this research is to explore and justify its cost-effective implementation in process chains. More specifically, the main area of interest is the manufacturing platforms for fabrication of tools for serial replication, incorporating different length-scale features. Therefore, the capabilities of FIB technology are discussed in details in a separate section of this chapter.

2.1.4.4 Replication Technologies

Nano-imprint Lithography (NIL)

NIL is a process that can produce nanometre scale patterns. This is achieved by pressing a template on a monomer or polymer imprint resist and subsequently curing the resist by heat or UV light. Although thermal NIL is widely employed for micro- and nano- replication of thermosetting polymers, it is difficult if not impossible to replicate micro- and nano- features in one processing step due to issues related to differences in polymer flow in micro and nano patterns, big thermal shrinkage and variations of residual layer thickness (Lalev *et al*., 2009). UV-NIL and especially the Step and Flash Imprint Lithography (S-FIL) process is considered to be a better option for the simultaneous imprinting of nano and micro patterns as they offer several major advantages (Resnik *et al*., 2005) such as: uniform patterning of large surface areas, due to low imprinting forces and low resist viscosity, absence of

thermal expansion, uniform thickness of the residual layer, capability to imprint micro and nano features simultaneously, imprinting of complex 3D topography and the possibility to use fragile substrates. Therefore it is considered an enabling technology for the fabrication of organic nanoelectronics, MEMS, optical components and semiconductor devices (Austin *et al*., 2005; Guo, 2007).

However, it should be noted that the big disadvantage of this technology is the limited number of resists suitable for the S-FIL process and the constraints regarding the achievable aspect ratio of the imprinted features (Guo, 2007).

Electroforming

Electroforming is a material deposition process for the manufacture of metal parts. An electrolytic bath is used to deposit electroplatable metals onto a conductive patterned surface. In practice, nickel, copper and iron are used for deposition. Once the metal has been deposited to the desired thickness, the electroformed part is separated from the master substrate. Depending on the application, the thickness of the metal layer can vary between a few micrometres to several millimetres (McGeough *et al.*, 2001). Applications of electroforming range from the production of consumer products to the fabrication of specialised aerospace components (McGeough *et al.*, 2001). In recent years, electroforming has gained importance for the production of micro- and nano-scale metallic devices and the creation of precision injection moulds with micro- and nano- scale features. This is due to the ability of the process to replicate complex shapes accurately and with a good surface finish. However, when applying electroforming for fabricating masters it is important that the following properties are achieved (Tang, 2008):

- *Even distribution of the electro deposited material*. This is important in order to minimise the follow up machining after plating. Also, this is very important in fabricating high aspect ratio structures, e.g. filling evenly deep trenches and other features with depth to width ratio from 2 to 5 or even higher, without forming voids inside them.

- *Reduction of internal stresses*. This is necessary in order to minimise the changes in the electroformed masters when they are released from the mandrel.

- *Wear resistance.* As the masters will be used for thermal replication, a hard Ni deposit will extend the life-time of the tool. However, there are trade-offs because increasing the wear resistance through increased hardness can lead to brittleness. In particular, this will be the result of the thermal cycles during replication which can trigger the Ni re-crystallisation and can lead to transportation of any impurities to the grain boundaries.

- *Corrosion resistance*. This is even a more important consideration in electroforming masters with micro and nano structured surfaces. The smallest corrosion attack could be devastating for such structures.

Despite the many advantages those two processes offer, there are a number of limitations to them as well, the main being processing cost/time and restricted range of materials to be used for replication. That is why, rather than used in a "fabrication of a final product" stage, some alternative application of those two replication

31

technologies in process chains should be considered. One way to achieve their cost-effective implementation is to utilise them at earlier stages of the designed manufacturing routes, making them complementary to other replication technologies regarded as more appropriate for serial replication.

Serial Replication Technologies

The concept of master-making process chains discussed in this study is suitable for a number of serial replication technologies for scale-up micro manufacture including micro-injection moulding (μIM), R2R imprinting and hot embossing (HE) together with some of their variations such as compression injection moulding and R2R thermoforming (Heckele and Schomburg, 2004). A common challenge in all of them, especially when micro and nano structures have to be replicated simultaneously, is the reliable and cost-effective fabrication of stamps or inserts. This, together with the necessary optimisation of the respective replication process, determines the overall effectiveness of such manufacturing platforms. The advantages and disadvantages of these high throughput replication processes are discussed below.

μIM and HE appear to be the two most industrially viable processes for fabrication of micro components (Giboz *et al.*, 2007). Due to its specific processing conditions, hot embossing is widely used for replicating structures/features with dimensions in the sub-micron range and high aspect ratios. However, the HE cycles are relatively long, usually 5 to 10 minutes, and therefore this technology is more suitable for small to medium series production and prototyping (Heckele and Schomburg, 2004; Giboz *et al.*, 2007). Conversely, the shorter cycle time in μIM determines its effectiveness for large series production, i.e. of more than 1000 parts (Theilade and Hansen, 2007).

Injection compression moulding can be considered as a hybrid process that combines the capabilities of μIM and HE. Especially, the shrinkage of the polymer during the cooling stage of the process can be minimised during its compression stage, which leads to a better replication accuracy. This technology is widely used for mass production of CDs and DVDs (Heckele and Schomburg, 2004).

R2R imprinting has attracted researchers and industry with its potential for a high throughput manufacture (Chia-Jen *et al*., 2008; Makela *et al*., 2007; Velten *et al*., 2010). The process is capable of replicating micro and nano topography at relatively high speed. Depending on the set-up, thermo and UV curable resist materials can be used. One of the major difficulties associated with this technology is the structuring of the rollers, particularly at nano scale. A variation of this technology is R2R thermoforming. It is used for forming of foils with complex cross-sections as it allows easy demolding but high aspect ratios could hardly be achieved.

2.1.5 Error factors in implementing process chains

By combining the capabilities of complementary technologies for direct micro and nano structuring, novel approaches for function and length scale integration can be implemented and successful process chains for the production of masters for serial replication developed. To implement it effectively in new micro manufacturing platforms the various potential problems or errors at each stage of the process chain should be identified and carefully analysed in order to minimise their effects on the overall uncertainty associated with its practical utilisation. This is very important in order to assess subjectively whether and how they could affect its overall performance

and thus compromise its manufacturing robustness and efficiency in terms of cost and time.

Generally the possible errors in such integrated process chains can be attributed to the following main sources (based on ISO, 1995):

- **Process.** Those include the specifics of the process or processes in a given component technology used in a process chain and encompass the influence of the working parameters and also the material properties of the workpiece. They could affect the total performance of the technology or cause any deviations from the targeted result/product.

- **Equipment.** They are associated with the condition and reliability of the equipment integrated in the process chain, both production and measurement ones, that can affect the system setup at different stages, e.g. calibrations and system monitoring during and after the process execution, as well as measurement uncertainty of any inspection operations. These errors are specific to the equipment selected to implement any given process chain and therefore only generic issues are identified in this research.

- **Human factor.** This is a highly subjective and rather unavoidable source of error based on the experience of the operator and/or the number of operators involved.

- **Environment.** This includes the impact of external, e.g. stochastic factors such as noise, oscillations and vibrations, temperature changes, atmospheric conditions and air purity.

2.2 Advantages and disadvantages of the FIB technology

To discuss the benefits of the implementation of the FIB technology in process chains and FLSI component fabrication, its principle of operation and the physical phenomena associated with the process are discussed in this section.

2.2.1 FIB process characteristics

Initially developed in the 1970s (Krohn and Ringo, 1975; Seliger *et al*., 1979) and undergoing constant improvements ever since, the FIB technology has been utilised as a tool for mask repair, device modification, failure analysis and integrated circuit (IC) debugging. In principle the focused ion beam can operate in two modes: ion beam direct write and ion beam projection. The latter, also known as focussed ion beam lithography (FIBL) utilises a stencil mask and is regarded as an alternative of conventional optical lithography (Kaesmaier and Löschner, 2000). As it still has some major limitations that restrict its field of application, FIBL could hardly be considered as cost-effective for FLSI products' fabrication and is therefore out of the scope of this research.

The FIB direct write mode, also known as FIB milling, can broadly be defined as the process of creating patterns through 'direct impingement of the ion beam on the substrate' (Tseng, 2004). The successful implementation of the FIB milling technology relies on its capability to operate a focused ion beam with a suitable beam

size, shape, current and energy to remove a required amount of material from a pre-defined location in a controllable manner. However, when an energetic ion strikes the surface of a target material, different ion-target interactions, including milling, deposition, implantation, swelling, backscattering and nuclear reaction, can occur. Some of those interactions are not completely separable and could cause unwanted side effects for particular applications. In order to avoid such undesirable effects the nature of the ion-target interactions should be well understood and accounted for when implementing a specific FIB process.

The ion – target interaction

 The basic principle behind the FIB milling is that the kinetic energy of the incident ion and its momentum are transferred to the target through elastic and inelastic interactions (Prenitzer *et al*., 2003). In the case of inelastic interactions (electronic energy loss) part of the ion energy is transferred to the electrons of the target material and ionization takes place. In the elastic interaction (nuclear energy loss) the ion energy is transferred to the atoms of the target. The incident ions interact only with the atoms at the surface or near the surface layer of the target causing a collision cascade on the atoms. If the ion energy (or momentum) is adequate, the collision can transfer sufficient energy to the surface atom to overcome its surface binding energy (3.8 eV for Au and 4.7 eV for Si), and the atom is ejected as a result. This interaction is called sputtering and is the governing effect in FIB milling. The process is presented schematically in Figure 2.3a. Because the interaction depends solely on momentum transfer to remove the atoms, sputtering is a purely physical process.

The number of atoms ejected or removed per incident ion, referred to as sputtering yield, *Y*, is generally utilised to characterise the efficiency of the material removal. The sputtering yield is usually in the range 1-50 atoms/ion and is a function of a number of variables including the ion and target material atoms' masses, the ion energy and angle of incidence, the target temperature and the ion flux. The sputtering yield can be expressed (Smentkowski, 2000) as:

$$Y[atoms / incident\_ion] = S[atoms]/\eta \qquad (2.1)$$

In Equation (2.1), $S[atoms] = V.\rho$ is the number of sputtered atoms and η is the number of ions that strike the sample. *V* and ρ denote the volume of the resulting crater [cm^3] and the density of the sputtered material [$atoms/cm^3$], respectively. η can be expressed in terms of the ion current, *I* [*A*], the sputtering time, *t* [*s*], and the charge on an electron, $1.e^{-1}$, where $1.e^- = 1{,}6.10^{-19}[C] = 1{,}6.10^{-19}[As]$:

$$\eta = I.t / e^- \qquad (2.2)$$

To calculate *Y* for actual FIB milling of a given material and since in reality the quantity of removed material is best described by the crater volume, *V*, Equation (2.1) can be expressed in the form:
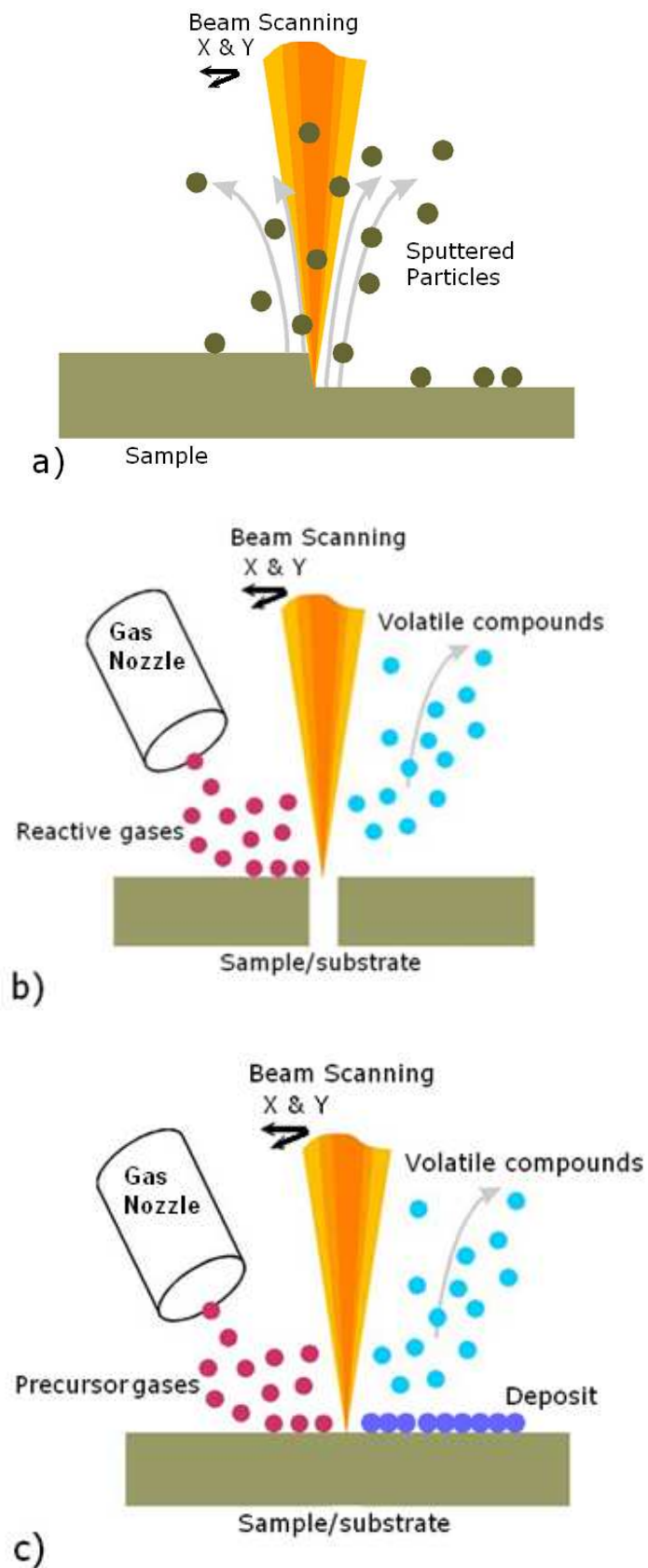
Figure 2.3 Main FIB principles of operation a) ion beam sputtering, b) FIB etching and c) local deposition – adapted from (Gierak, 2009)

$$Y = (V.\rho.e^-)\big/I.t = (V.\rho.1,6.10^{-19})\big/I.t \qquad (2.3)$$

Alternatively, *Y* can be defined based on the number of sputtered grams by multiplying the number of atoms obtained in Equation (2.3) by the atomic mass, *M*, of the sputtered species and dividing it by Avogadro's number, N_A:

$$S[g] = S[atoms].M\big/N_A \qquad (2.4)$$

$$Y[g/incident\_ion] = S[g]/\eta = (V.\rho.M.e^-)\big/(I.t.N_A) =$$
$$= (V.\rho.M.1,6^{-19})\big/(I.t.N_A) \qquad (2.5)$$

Initially, the sputtering yield increases as the ion energy increases, but the yield starts to decrease as the energy exceeds the level beyond which the ions can penetrate deep into the substrate. At this stage of interactions, implantation or doping can take place in which the ions become trapped in the substrate as their energy is expended. Investigations (Tseng, 2004; Gierak, 2009) have revealed that the necessary energy for having a proper sputtering is between10 and 100 keV for most of the ion species used for milling. For ion energies higher than 100 keV, implantation occurs as the ions can easily penetrate into and be trapped in the interior of the substrate, whereas ion energies higher than 1 MeV result in dominant backscattering and nuclear reactions.

During sputtering, certain amount of the ejected atoms or molecules is frequently redeposited back into the sputtered region, particularly with increasing milling depth or when higher aspect ratios are targeted. The redeposition makes it difficult to

control the amount of material removed by sputtering. Theoretically, the essence of FIB milling is to carefully control both the material sputtering and the redeposition, so that a precise amount of material can be removed (Tseng, 2004).

2.2.2 Principle of operation and types and structure of the FIB systems

The need for a better control and real time monitoring of the FIB process has led to the development of FIB machines that combine in one scanning electron microscopy (SEM) and FIB columns. Basically, in such setups the FIB column is integrated on a platform together with a SEM one, and their two optical axes converge at the same point on the sample surface. This 'cross-beam' or 'dual-beam' architecture (Figure 2.4a) was initially developed in the beginning of the 1980s (Sudraud *et al.*, 1988) and allowed *in situ* observation and non-destructive control during the FIB machining (Gierak, 2009). Also, successfully addressing issues like positioning accuracy of the ion beam spot and the associated sample moving and positioning, this configuration has become immediately very popular and is widely used in the microelectronics industry. In fact, nowadays most of the FIB manufacturers offer this type of instruments (Figure 2.4b) (Carl Zeiss, 2011; FEI Company, 2011; Orsay Physics, 2011).

Apart from the SEM integrated column, the typical FIB system normally includes an ion source, ion optics column, a beam deflector and sample-holding or substrate stage (Wang, 1997). A typical two-lens FIB system is shown in Figure 2.5. The ion sources that are currently available include Al, Ar, As, Au, Be, B, Cs, Cu, Ga, Ge, Er, Fe, H, Li, Ni, P, Pb, Pd, Pt, U and Zn. As mentioned earlier, Ar, B and P ions are widely used in microelectronics for implantation of semiconductor materials, whereas the

popular ion species for micro- and nanofabrication are As, Be and Ga (Tseng, 2004). Because of the high melting temperature and the reactivity or volatility associated with the pure metals, many of these ion species are produced from liquid metal alloy sources, also frequently referred to as liquid metal ion sources (LMIS). The LMIS has been used to provide reliable and steady ion beams for a variety of ion species (Bischoff, 2008). The ion beam generated from LMIS is directed through a mass separator and a drift tube. The purpose of the mass separator is to allow only the ions with a fixed mass-charge ratio to pass through (Ward, 1985). Then the drift tube situated under the mass separator eliminates those of the ions which are not directed vertically. The lower lens located below the drift tube helps reduce the beam spot size and improve the focus. Then, the electrostatic beam, following the lower (objective) lens, controls the final ion beam trajectory and the landing spot of the ions on the substrate.

Often a multichannel plate (MCP) is situated above the target. The MCP helps in viewing the substrate/sample by collecting the secondary electron emissions for imaging (Reyntjens and Puers, 2001). The nozzle shown in Figure 2.5 is used for FIB-induced etching and/or chemical vapour deposition. The whole setup is usually placed in a low pressure chamber, where a vacuum of approximately 1×10^{-7} mbar is maintained. This is done in order to increase the ion mean paths and to avoid beam strength reduction due to the interference of particles in the chamber (Melngailis, 1987). Such a system would usually produce ion energies from 50 to 250 keV with the minimum full width at half-maximum (FWHM) beam diameter down to 5-7 nm (Frey *et al.*, 2003). FWHM is defined as the distance between the locations on the intensity profile at which the intensity reaches half of its maximum value. Achieving
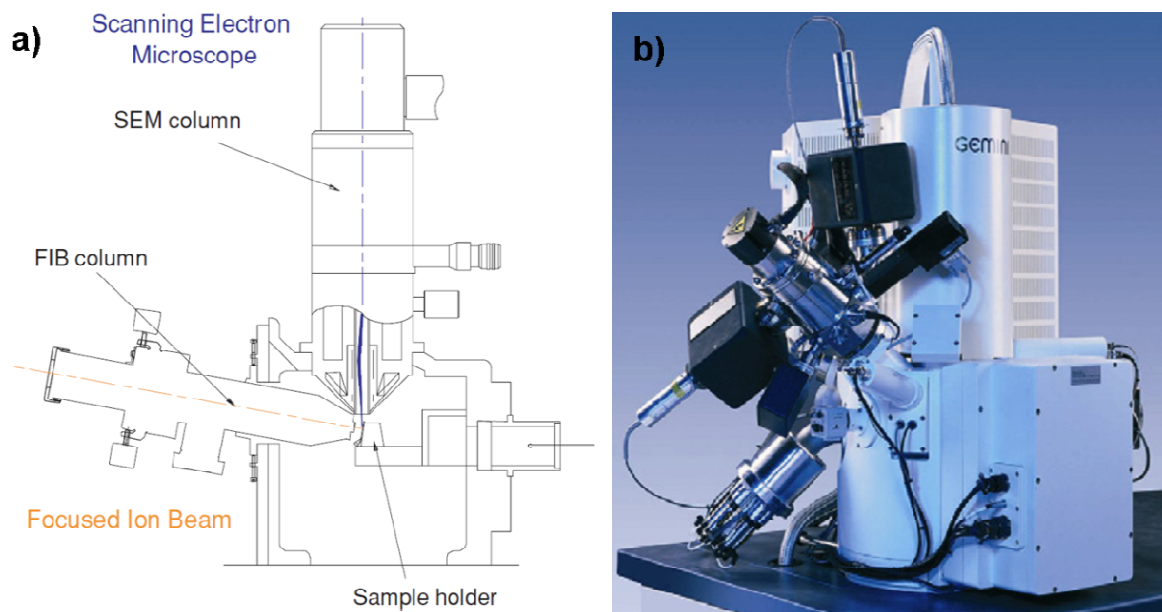
Figure 2.4 Combined FIB/SEM systems: a) schematic presentation of the FIB/SEM device developed by Sudraud (Sudraud et al., 1988), and b) commercially available SEM/FIB system by from Carl Zeiss – adapted from (Gierak, 2009)
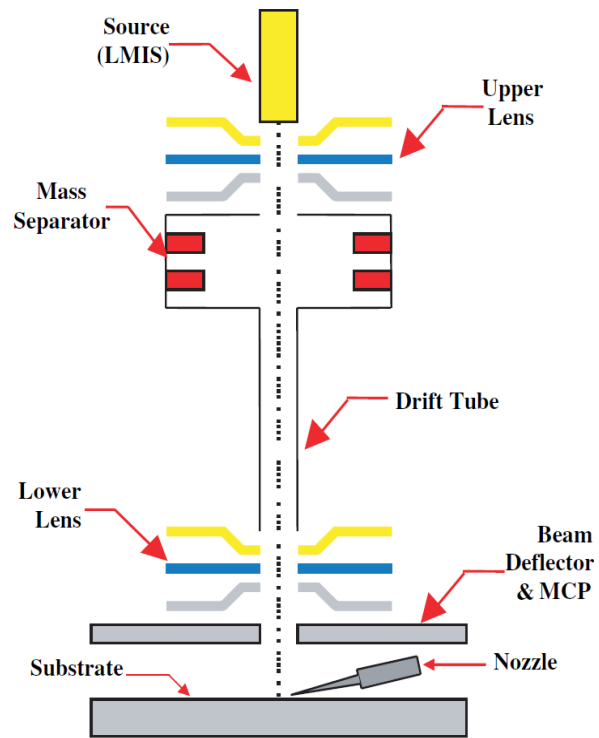
Figure 2.5 Two-lens FIB system configuration – adapted from (Tseng, 2004)

such a range of ion energies allows the system to be used for both sputtering and implantation. FWHM is used to describe the diameter of the focused ion beam, in which the ion intensity is highly non-uniformly distributed; frequently, its intensity is close to a Gaussian profile.

To perform FIB structuring the ion beam is moved in a linear fashion along the sample; the beam displacement usually being referred to as scanning. In the computer-controlled FIB systems, milling is done in a precise pixel-by-pixel movement (Tseng, 2004). The scanning can be performed in two ways: raster scan or serpentine scan, as shown in Figure 2.6. In raster scanning – Figure 2.6a the beam moves in the same direction throughout the whole exposure. Certain disadvantage here is the increase in the overall processing time due to the time required for the beam to return to coordinate and settle before performing the next scan. On the other hand, in the serpentine scan, direction is reversed after each pass – Figure 2.6b.

Besides the ion beam and its intensity, the other important parameters that determine the actual FIB milling process are the dwell time, d_t [ms], and the area step size, S_S, [nm]. The dwell time is defined as the time the ion beam spends on a given spot or pixel, whereas the step size is the distance between the centres of two adjacent pixels – Figure 2.6. To mill a smooth profile with a constant rate of material removal or milling rate, the ion intensity rate (the ion flux) with respect to the scanning direction has to be uniform or unwavering. To achieve this, the pixel spacing must be small enough to allow a proper overlap between adjacent pixels so that a smooth uniform profile can be milled. In addition, to mill a smooth surface between the scan lines, the area step size between adjacent scan lines must be also small enough to allow a proper
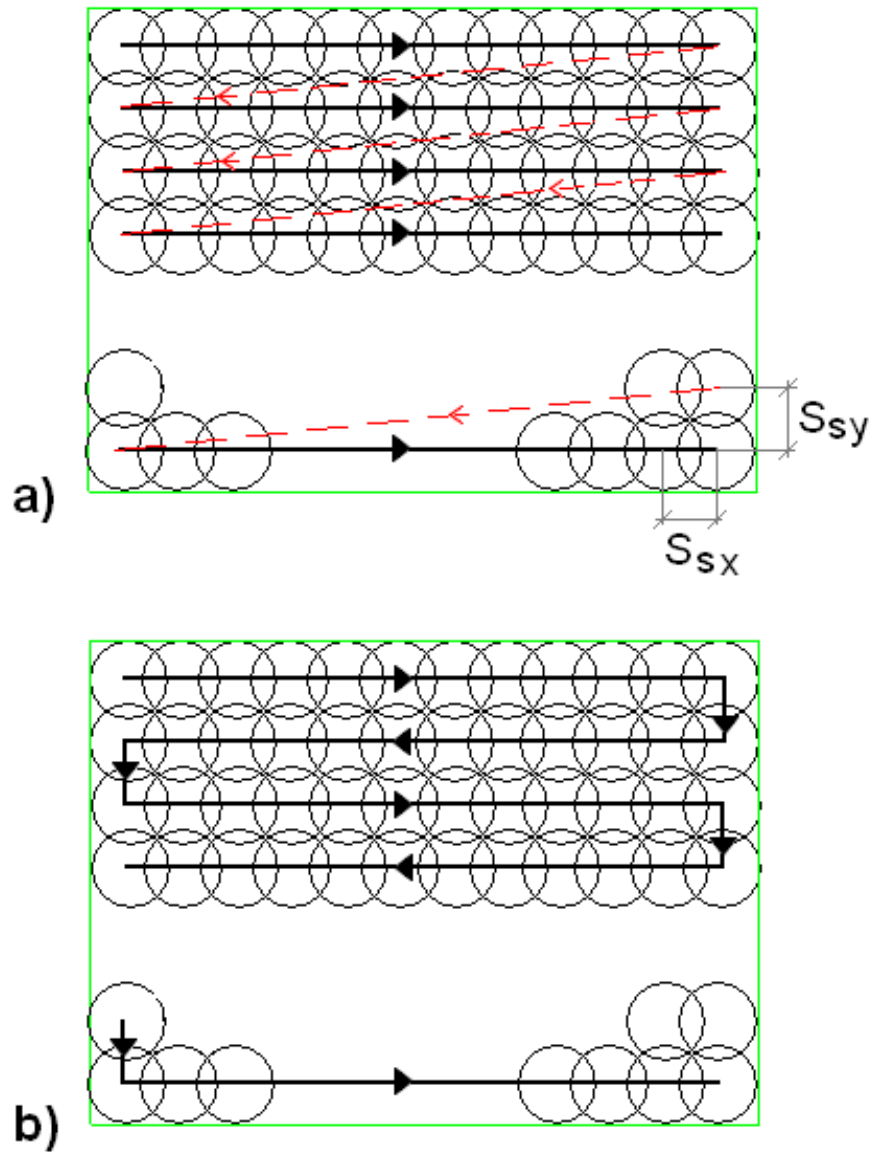
Figure 2.6 FIB milling scanning strategies: a) raster scanning, and b) serpentine scanning.

overlap between adjacent lines. In some cases the parameters are combined in a dose, term that is used to describe the exposure amount (ion dose) over a certain area. In general, the larger the exposure dose, the deeper the milled structure; however, due to the redeposition effects and especially for high aspect ratio (AR), submicron features filling of the milled structure and/or non-flat bottom occurs. Thus, when performing FIB milling with one pass over the targeted area, a structure with V-shaped profile is obtained (Li *et al*, 2003; Tseng, 2004). However, when 2.5D (microchannel) structures have to be produced, there are several requirements that should be satisfied, in particular: (i) flat channel bottom, (ii) nearly vertical sidewalls and (iii) high AR profile. Furthermore, when producing 3D features it is essential that the overall geometry of the target feature is produced accurately and usually within tight tolerances.

That is why usually a number of consecutive passes of the milled area are applied to meet those requirements. In this case, the passes can be regarded as layers stacked along the normal of the sample surface; hence this type of machining is typically referred to as layer-based FIB milling. If the area dose is distributed in a relatively big number of layers the following improvements can be achieved: (i) the re-deposition effects can be minimised, if not entirely eliminated, and thus (ii) accurate, predictable structures with flat bottoms can be obtained. Further development of the layer-based milling approach has enabled the predictable fabrication of 3D features (Lalev *et al*., 2008 Lalev *et al*., 2009; Svintsov *et al.,* 2009).

2.2.3   FIB modes of application

As discussed in the previous section different phenomena can occur at various energy

levels depending on the specific ion-target interactions. This, in turn, makes possible the utilisation of the FIB technology as a versatile mean of structuring. Especially, whereas the FIB milling can be used as a material removal technology, the ion implantation allows for alterations of the material properties of the target. In addition, chemically-enhanced FIB milling techniques such as etching and deposition have found applications in the microelectronics industry.

Ion Implantation

This phenomenon is widely used in the microelectronics industry as a means for doping of semiconductor materials. Through ion implantation the properties of a given material can be modified by inserting selected ions within its atomic lattice. The penetration depth of the ions is usually adjusted in the micrometer range. Commonly used ions are B, As, Ge, P and Si implanted in materials such as silicon and gallium arsenide and the implantation doses vary in the range 10^{11} ions/cm^2 – 10^{16} ions/cm^2. Apart from microelectronics, this technique has been successfully applied for improvement of the surface properties (surface energy and absorption) and reduction of surface corrosion, as well as for improvement of the mechanical properties of materials (i.e. reducing wear and friction) (Gierak, 2009).

Chemical Reactive Ion Etching (RIE)

The chemical reactive ion etching – Figure 2.3b, was initially proposed (Kosugi *et al.*, 1991) as a solution to the effects of the redeposition phenomenon, such as contamination of the surface of the specimen, partial filling of a previously milled structure in case of deep milling and possible occurrence of short circuit between interconnects (Santschi *et al.,* 2006). Chemically assisted FIB milling processes are

based on the local injection in the working chamber of a reactive gas. The surface of the sample adsorbs part of the injected gas that readily reacts with the sputtered atoms of the target in forming volatile compounds. These volatile products do not redeposit since they are evacuated by the pumping system of the chamber. Nowadays, a number of etching processes and recipes are available for improving etching selectivity between given materials, decrease of redeposition and substantial improvement of the achievable aspect ratios (width/depth) of the milled features (Gierak, 2009). Certain drawbacks of this method are the contamination effects on the sample surface and the limitations in ultimate resolution due to scattering effects of the incoming ions in the adsorbed gas layers (Hon *et al.,* 2008).

FIB Deposition

Figure 2.3c shows the principle of FIB local deposition. This technique is based on a mechanism of energy transfer between the secondary electrons generated by the collision of the focused ion beam with the substrate/sample surface. This energy transfer is due to locally 'cracking' gas molecules injected and absorbed on the target surface. The non-volatile compounds of this reaction, which are generally selected for their metallic or insulating properties, form a solid deposit adhering to the sample surface. The materials usually used for deposition are platinum (Pt) and/or tungsten (W) (Hon *et al.,* 2008). A major advantage of the FIB technology due to the deposition technique is that, since it can easily be combined with direct milling, it enables the use of the same tool for creating structures by both material removal (milling) and material add-up (depositing) with relatively good three-dimensional *in situ* process control (Jeon and Melngailis, 2006).

The doping, RIE and deposition (which can be considered complementary to the FIB milling in terms of micro-nano-manufacturing) find many applications in the silicon-based manufacturing. Therefore, the FIB capabilities and limitations are relatively well studied. In regard to the cost-effective implementation of the FIB technology into manufacturing platforms for fabrication of replication masters those techniques appear to be somewhat secondary, or complementary, to the FIB milling. Therefore, this research is focussed on exploring/investigating the challenges and capabilities of the direct FIB milling.

FIB Milling – Characterisation and Functions

The nature of the FIB milling allows for the fabrication of high-resolution, complex sub-micron 2.5D and 3D features through controlled material removal. As already mentioned, the sputtering and redeposition are two governing phenomena that cause material removal. In fact, in order to achieve the targeted shape, especially in FIB machining of 3D features, it is of crucial importance that the effects of redeposition be taken into account. Besides the sputtering yield/rate and the redeposition, the homogeneity of the FIB milling process is strongly affected by the properties of the target material (crystal, polycrystalline, amorphous, doped etc.) as well as by the angle of incidence of the ion beam.

2.2.4 Angle of incidence

The angle of incidence, usually denoted as θ [$^\circ$] has a direct and very substantial influence on the sputtering yield. As shown in Figure 2.7 a θ is defined as the angle between the direction of the ion beam and the surface normal. When the incidence energy of the ions is high enough, approximately above 1 keV (Kim *et al.*, 2007 a),

the relationship between Y and θ can be expressed by the cosine rule, and is proportional to $1/cos\ \theta$ (Svintsov *et al.*, 2009). This angular dependence is observed for a wide range of angles θ, as well as for lots of materials, ions species and their energies (Andersen and Berish, 1981). Figure 2.7b shows the sputtering yield as a function of θ, obtained for silicon sample sputtered with Ga^+ ions accelerated at 20 and 30 keV. As shown in Figure 2.7b increasing the incidence angle increases the sputtering yield until it reaches its maximum near 80°; then it decreases very rapidly to zero as the incident angle approaches 90°. As mentioned earlier, the amount of sputtering is dominated by surface collision cascades. As the angle of collision between the ions and target atoms increases from normal incidence, the possibility of the target atoms escaping from the surface during the collision cascades increases and eventually this leads to an increased sputter yield. After reaching a maximum, the sputter yield decreases again as the ion approaches glancing incidence because of the increase in reflected ions and the fact that more and more collision cascades terminate at the surface before they are fully developed.

This θ - Y relationship has also been verified by numerous simulations performed by various research groups (Frey *et al.*, 2003; Lehrer *et al.*, 2001).
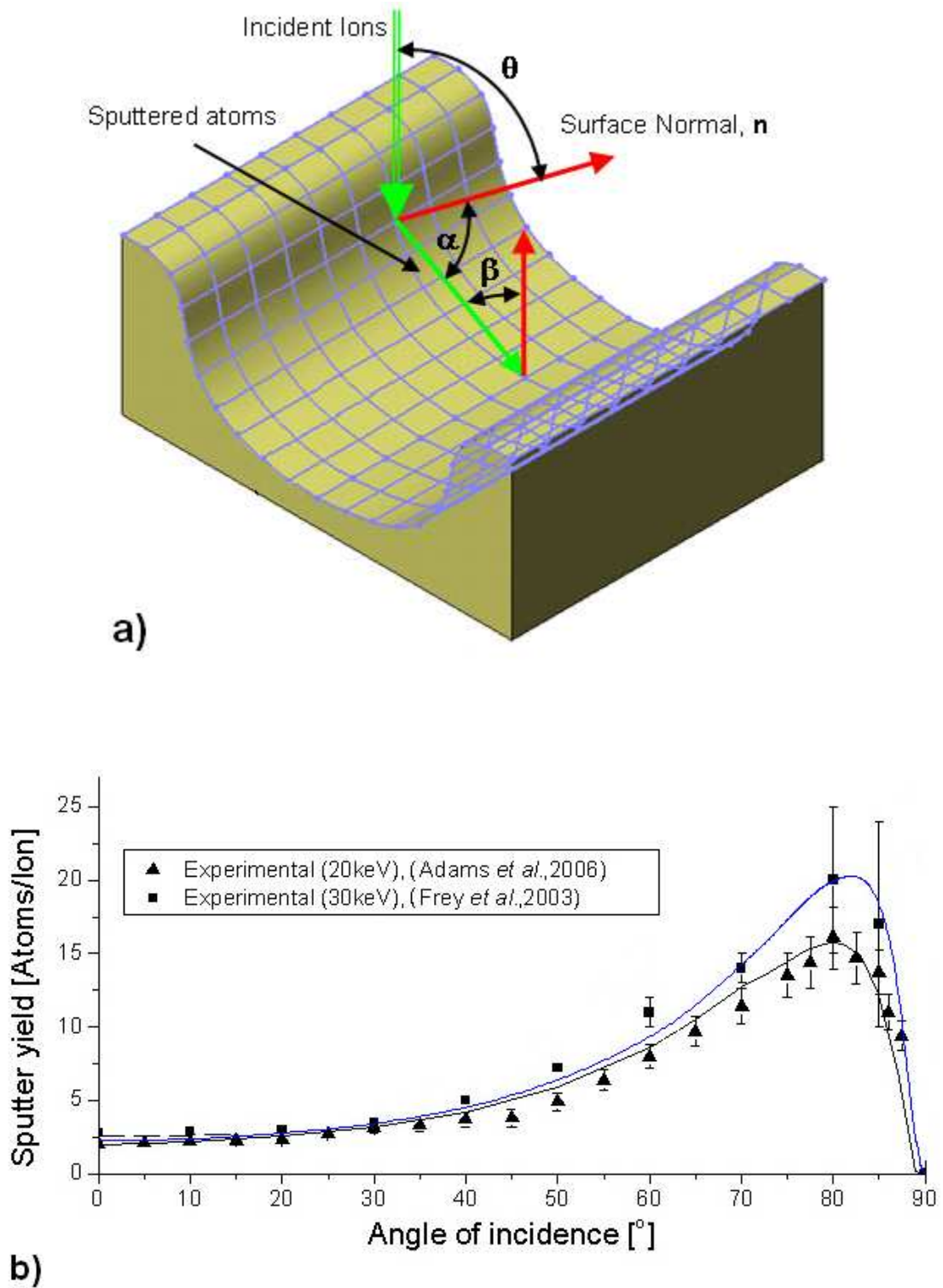
Figure 2.7 FIB milling characteristics: a) angle of incidence of ion beam, θ, and b) sputtering yield to angle of incidence relationship – adapted from (Kim *et al*., 2007 a). α and β in a) represent the emission angle of sputtered atoms and incident angle of redeposited atoms, respectively.

2.2.5 FIB processing of different materials

Due to the nature of the FIB milling process the FIB technology allow the machining of virtually all kinds of materials ranging from metals to polymers. The machining behaviour of the different materials, however, might yield very different results for unique FIB milling conditions (Prenitzer *et al*., 2003). This behaviour also referred as milling rate is directly related to the sputtering yield, *Y*. The relationship is discussed in further details in Chapter 6. The response of the materials to ion sputtering depends mainly on their material structure - crystalline, polycrystalline, amorphous etc.

More particularly the polycrystalline materials exhibit significant grain anisotropy leading to non-uniform ion etching and re-deposition of the materials. This phenomenon is not observed in mono-crystalline materials such as silicon and alumina which are utilised for electron and ion patterning.

Unlike the polycrystalline materials the amorphous structures (silica, amorphous metallic glasses, and bulk metallic glasses - BMG) are very suitable for charged particles milling because of their isotropic structure. Furthermore their properties are identical, irrespective of their macro-orientation towards the particle beam.

For metallic glasses with high metalloid concentration the electronic transport would be dominated by s-like nearly free electrons, resulting in dramatic changes of transportation properties of these alloys compared to their crystalline counterparts (Ivkov *et al*., 1989; Li *et al*., 2007). Thus, in amorphous metals, the energy dissipation during the ion exposure is minimised, leading to an increase of the sputtering yield. Furthermore, a higher surface integrity of the produced micro and nano-structures can

be obtained in the non-crystalline materials because no crystalline defects, such as dislocation pile-ups, point defect agglomerates and grain boundaries are present to facilitate the formation of micro-cracks and pores.

In addition to that, if the dose level of the ions is not high enough, amorphization may occur in the bombarded area of a crystalline substrate and can induce swelling on the substrate surface. In amorphization, the incident ions in most cases are buried in the target material and may also displace atoms in their lattice so that the displaced atoms redeposit on the nearby surface. Since most of the FIB roughly resembles a Gaussian ion distribution, the intensity at the tail of the beam is much smaller than that at the centre region and it is not strong enough to sputter materials but is sufficient to cause amorphization that induces substrate swelling. Normally, the intensity to cause swelling is two to three orders of magnitude lower than the optimized sputtering intensity and the swelling disappears if the intensity increases, as reported by several research groups (Stanishevsky, 1999; Frey *et al.,* 2003; Lugstein *et al,* 2003). During channel milling, the FIB always has a tail region that possesses the right dose to cause maximum swelling.

Also, the ion irradiation generates electric charges that might cause drifts of the ion beam or damage to the feature being milled or the overall device structure. Thus non-conductive materials are usually coated with a nanometer-thick layer of conductive material, most often Cr, Au (AuPd) or Cu (Tseng *et al.,* 2005;Prenitzer *et al.*, 2003), prior to FIB machining.

2.2.6 Simulation of ion sputtering and FIB milling

As discussed earlier process specifics like incident angle dependency, re-deposition and backscattering are inseparable part of the FIB milling process and have a significant influence on the FIB machining outcome. Thus they should always be taken into consideration when designing a FIB milling procedure. That, however, is not a straightforward task and attempts have been made to predict the FIB milling outcome by simulating the process.

A software package, TRIM (TRansport of Ions in Matter), has been widely used for predicting the sputtering yield for many different ions at a wide range of energies. TRIM is a comprehensive Monte Carlo program, which calculates the stopping ranges of ions into matters by applying a quantum mechanics in describing analytically ion–atom collisions (Biersack and Haggmark, 1980). The calculations are made efficiently by the use of statistical algorithms, which allow the collision results to be averaged over the intervening gaps. Especially, with the use of TRIM the distribution of ions and the kinetic phenomena associated with the ion's energy losses can be studied, including target damage, phonon production, ionization and ion reflection, implantation and sputtering.

While TRIM has proved to be very efficient for simulating of the purely physical sputtering other software tools are necessary to model the milling process when producing complex and/or 3D features. Especially, such simulation software should take into account the effects of FIB milling specifics like angle-dependent sputtering, re-deposition and backscattering with regard to the dimensions of the target structure. Kim et al. (Kim *et al.*, 2007 a) proposed such tools, in particular AMADEUS 2D

(Kim *et al.*, 2007 b) and AMADEUS 3D simulators. Especially, the AMADEUS 3D software could be used to simulate the resulting surface topography after FIB machining that takes into account the angle-dependent sputtering yield and the effects of redeposition. The development of tools with 3D simulation capabilities were also reported by other researchers in the field (Katardjiev *et al.*, 1994; Vasile *et al.*, 1999).

The IonShaper® (Platzgummer *et al.*, 2006) simulator considers both the angle of incidence dependant sputtering and the redeposition but when utilised for 3D feature simulations showed substantial discrepancies between the profiles predicted by the software and the actual ones (Rommel *et al.*, 2010). Also, a major drawback of this software is that 3D simulations can only be performed for axisymmetric features. Svintsov et al. (Svintsov *et al.*, 2009) proposed another simulation model and by applying it an improvement of the simulation accuracy was reported. This model was implemented in the IonRevSim software (Zaitsev *et al.*, 2009) that was specially developed for FIB and multi-ion beam (Dietzel *et al.*, 2006) applications and takes into account the angular-dependency of the sputtering rate. The software simulates the sputtering process during FIB machining based on the isotropic local etching model (Svintsov *et al.*, 2009; Zaitsev *et al.*, 2009). This model allows for the 3D ion sputtering process to be simulated by varying some external parameters, such as sputtering sensitivity (sputtering rate), number and shape of layers, area step size and beam diameter. In addition to its simulation capabilities, the IonRevSim software provides a data preparation solution that serves as a tool for estimating/calculating the FIB processing parameters that should be applied to produce a given structure.

2.2.7　FIB milling of complex 3D features

Process specifics like beam spot sizes in the nanometer range and being a direct-write (maskless and resistless) technology determine the flexibility and high resolution patterning capability of the FIB technology. Those capabilities enable the utilisation of FIB milling for the reliable realisation of precise complex and/or 3D features. However, due to the redeposition effects and the incidence angle dependant sputtering, the FIB milling is feasible for producing structures with AR not much higher than 1 (Kim *et al*., 2007 a). Despite this, the capabilities in regard to achievable shapes, low surface roughness and the wide range of materials that can be machined, make FIB milling highly efficient for the fabrication of complex patterns. The structuring of 3D shapes, however, requires some specific "data preparation" steps before the actual milling can be performed.

2.2.8　Data preparation for 3D FIB structuring

Two main data preparation approaches can be applied for FIB milling of 3D patterns: the use of bitmap data files employing the built-in software of the FIB systems or GDSII data files where the FIB milling process is externally controlled by conventional lithography software (Lalev *et al*., 2008).

In the first case each bitmap data file represents a cross-section of the 3D structure, i.e. it can be regarded as one slice from a stack of slices defining a given 3D shape. Therefore, a sequence of such cross-sections or a stack of bitmap files are necessary to produce a 3D feature/structure. As they are processed one by one with the built-in FIB software while the probe current and milling time for every single file has to be specified manually, this is a very slow and impractical approach. In addition, the

precise alignment of the layers cannot be guaranteed and also errors in the layers' exposure order are possible. Thus, this approach can compromise the accuracy of the targeted 3D structure.

In contrast, the second approach allows for creating and exposing of the whole 3D model as a single file. Standard CAD packages are used to create the 3D models of the targeted structures and then they are exported into neutral data files using stereolithography (STL) format. This file format is used due to its acceptance as an industry standard data exchange format for layer-based manufacturing and its simplicity. However, the STL files cannot be applied for FIB milling directly, and therefore they have to be converted into the GDSII stream file format. It can be utilised to mill 3D features directly, while the FIB is externally controlled by lithography software. The GDSII files can be utilised to realise two different FIB machining modes, in particular layer-based and quasi-stationary modes presented schematically in Figure 2.8.

In the first mode the 3D geometry is defined as a stack of layers ordered along the vertical axis of the feature or structure (Figure 2.8 a). Each layer represents a cross-section of the 3D model at a given height along its z-axis. The number of layers determines the accuracy of the feature/structure that will be produced. In general, a bigger number of layers will result in a better resolution and profile accuracy. However, there might be some constraints regarding the number of layers that can be used to represent a given 3D model due to some limitations of the lithography software. All the layers are machined in a strict bottom-to-top sequence.
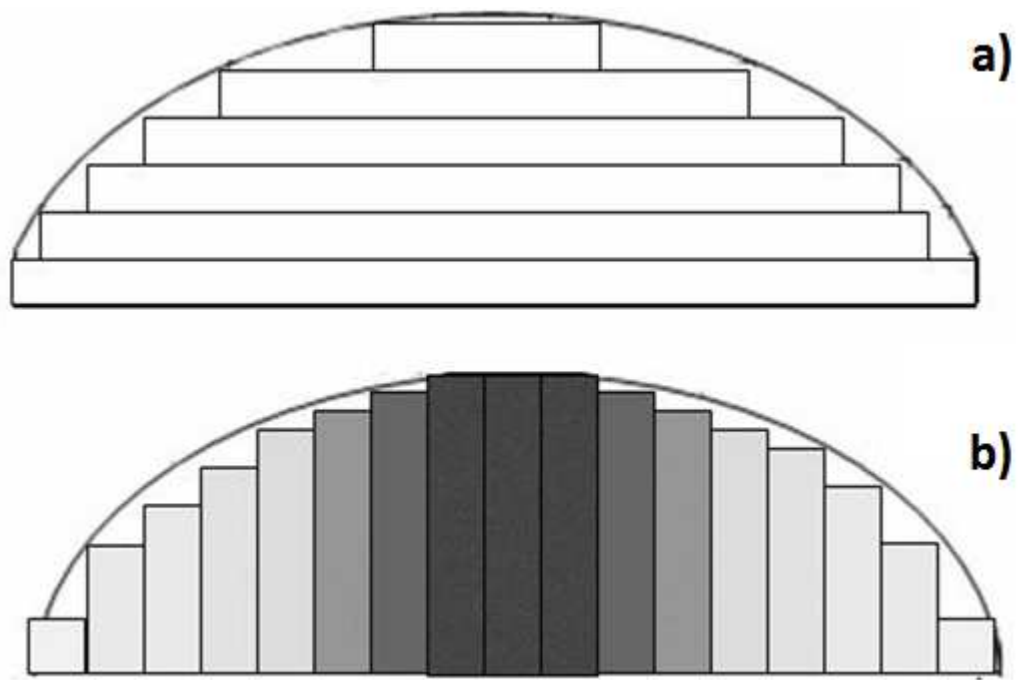
Figure 2.8 FIB machining modes: a) layer-based and b) quasi-stationary.

In the second mode the overall exposure dose for a given 3D structure is divided into a number of smaller doses. Each of them is assigned to an exposure pixel of the model. The dose at each pixel is determined by the targeted structure depth at any respective point. This could roughly be viewed as a vertical slicing of the model, as shown in Figure 2.8b.

To facilitate the file generation and also to minimise the number of translations between software formats new software for data preparation and generation, IonRevSim, was developed specially for FIB machining (Svintsov *et al*., 2009). One of its advantages is that, when utilised in its layer-based mode, there is no upper limit to the number of layers that can be used to define a structure and the maximum number is determined by the minimum layer thickness. Furthermore, when the GDSII file is transferred to the lithography software all the pre-defined layers are embedded into one 'zero' layer and therefore the 'maximum 64 layers' restriction posed by the software can be eliminated.

Even though there are simulation tools available to estimate the sputtering rate and the resulting layer depth after FIB machining it is not a trivial task to set up the processing parameters so that the actual structure's depth matches the targeted one (Velkova *et al*., 2011b).

2.2.9 Overview on the FIB milling capabilities

Since the early developments (Seliger *et al*., 1979) the FIB technology has been improving continuously in terms of processing capabilities and achievable resolution of the patterned structures, especially in lateral dimensions. The FIB technology

developments were aimed at achieving sub-micron structuring, and nowadays all new FIB systems' configurations are targeting nanometre-size patterning (Gierak, 2009).

Indeed, many research teams have reported patterning of 2.5D structures like channels (Prenitzer *et al.*, 2003; Hopman *et al.*, 2007;), gratings (Wang *et al.*, 2007; Li et al., 2010; Vick *et al.*, 2010) and holes (Kapsa *et al*, 2004; Hopman *et al.*, 2007) of micron, submicron and nanometer dimensions with relatively low surface roughness (Urbanek *et al.,* 2010). Furthermore, by implementing layer-based milling combined with specific data preparation techniques, several researchers (Lalev *et al.*, 2009; Svintsov *et al.,* 2009) reported the fabrication of 3D structures in fused silica (SiO_2) with features of approximately 1.5 µm in lateral dimensions. Furthermore, using solely FIB Scholz et al., (2009) reported the production of micro lenses in silicon and then the machining of nano lenses on their concave surfaces with high shape and positional accuracy. However, as it was mentioned in the previous section, the correct estimation of the resulting overall feature depth obtainable in FIB milling is still a major issue.

A big challenge to the successful implementation of the FIB milling process in economically viable practical applications like master-making process chains is the high processing time dictated by the low material removal rates of the process. To overcome this limitation FIB milling could be used for structuring in the submicron/nano dimensional range on top of micro-features produced by employing other technologies. Alternatively, FIB could be applied to structure small arrays of submicron/nano features, which can then be replicated over a larger area. However, to be able to benefit fully from the advantages that the FIB milling technology offers, further investigations and development efforts are necessary to address successfully

its limitations.

2.3 Summary

In the first section of this chapter the concept of process chains is presented and the advantages and disadvantages of their implementation for the production of components incorporating features with millimetre, micrometer and nanometer dimensions, such as tools for serial replication, are discussed. Then, the most widely used production technologies in micro- and nano- manufacturing are reviewed and their possible applications in cost-effective manufacturing routes are discussed with regard to their advantages and limitations.

The second section reviews various aspects associated with the use of the FIB technology. To justify its cost-effective implementation in process chains for serial manufacture its principle of operation, working modes and applications were analysed. The advantages and limitations of the FIB technology in performing 2.5D and 3D patterning are discussed in details and the opened research issues that restrict its broader use are identified.

In this Literature Review Chapter the following issues were identified for investigation:

- A number of factors like process compatibility, complementarity, and alignment issues should be taken into account for the successful implementation of a process chain. Further investigation of those factors on master - manufacturing routes as well as the verification of an actual process chain for high throughput production is necessary.

- The influence of constraints like the low material removal rate on the overall

cost-effectiveness of the process chain should be examined, especially when the production of 3D features with tight tolerances is required. Also its compatibility with other technologies for micro and submicron structuring, preceding or following it immediately, should be studied further.

- A major issue in FIB milling is that the feature's milled depth cannot be predicted accurately. That is particularly problematic when 3D patterning is concerned. Therefore a thorough investigation of the process parameters and their impact on the milled depth is carried out in this research.

- The FIB technology can be used to structure virtually all kinds of materials, with the amorphous materials exhibiting better response to ion sputtering than crystalline ones. Properties like high hardness, fracture toughness and fatigue strength make the amorphous alloys very appropriate for fabrication of masters for serial replication. Thus their FIB machinability needs to be studied with emphasis on the vertical direction i.e. milled depth.

CHAPTER 3

DESIGN AND VALIDATION OF A NOVEL MASTER-MAKING PROCESS CHAIN FOR ORGANIC AND LARGE AREA ELECTRONICS ON FLEXIBLE SUBSTRATES

3.1 Introduction

In this chapter a novel combination of complementary technologies is proposed to fabricate masters for serial replication. It explores the notion that the use of any particular technology is viable only within a given optimal processing window, and therefore a sequence of processes should be applied for producing cost-effectively complex structures, e.g. incorporating different FLSI features. The proposed process chain utilises the electroforming technology for producing nickel replication tools with relatively high hardness and wear resistance. Also, this technology allows features of more complex shapes and various scales to be replicated, which in turn makes possible the use of a wide range of technologies for structuring and fabrication of the electroforming masters.

Three main objectives were set when designing and implementing this process chain, in particular:

1. to develop a manufacturing platform for serial fabrication of organic electronic devices, especially to validate it for R2R serial imprinting of large area organic electronic devices;

2. to investigate whether the FIB technology could be used cost-effectively for serial production;

3. to explore the capabilities of the FIB milling process for achieving FLSI into a single product.

3.2 Process Chain Design

The proposed process chain for fabricating Ni shims that can be used as masters for serial replication is presented in Figure 3.1. It employs the FIB technology to machine precisely very complex nano and micro 2.5D and 3D structures (Scholz *et al*., 2009). However, this technology can be applied for patterning accurately and cost-effectively only relatively small areas, e.g. up to 100x100 µm without stitching, due to its low material removal rates. Thus, it is not suitable for structuring bigger surfaces. Hence, to make the best use of this process, it should be applied only for patterning of relatively small areas, e.g. the machining of sub-micron and nano-structures on nanoimprint lithography (NIL) templates (Li *et al*., 2007 a). Micro structuring, which usually is required for patterning larger areas of the masters/templates, can be performed more efficiently by employing other technologies such as photolithography or laser ablation. Therefore, by structuring a template in two stages, first by performing micro and then high resolution sub-micron and nano patterning, the fabrication time can be reduced drastically and thus the cost effectiveness of such master-making process chain can be improved significantly. Then, by employing Step and Flash Imprint Lithography (S-FIL) (Resnick *et al.*, 2005) it is possible to use such templates to pattern 4" or 8" wafers, which can be used as masters for the subsequent electroforming process. Finally, Ni shims fabricated in this way can be integrated onto R2R rollers, and thus, used for imprinting of UV- and thermally curable polymers.
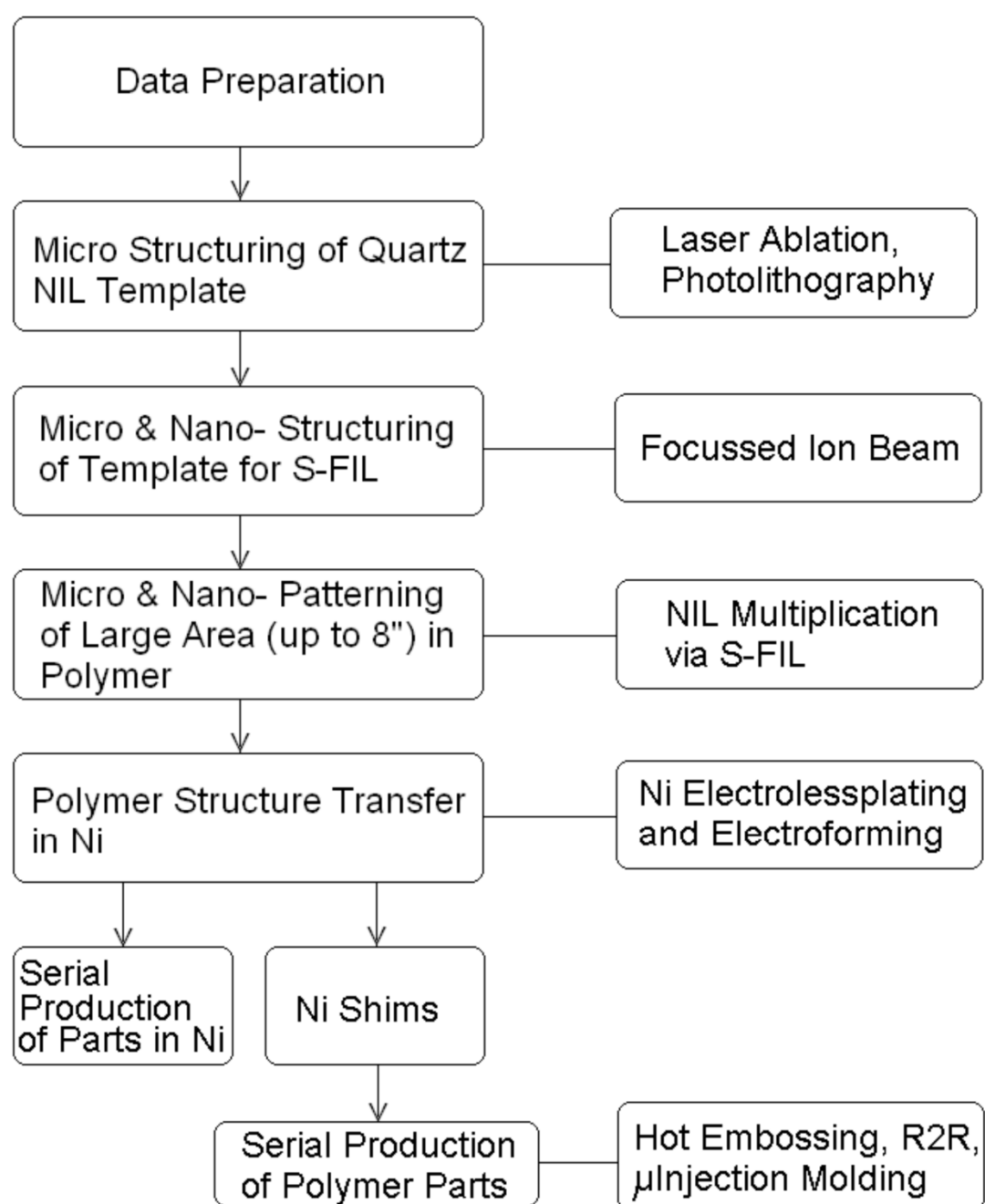
Figure 3.1 The stages of the proposed master-making process chain

A more detailed description of the different "component" technologies and steps that are integrated in the proposed process chain is provided in the following sub-sections.

3.2.1 Data preparation

This initial stage of the process chain involves the CAD design of the desired structures and the follow-up data preparation for their machining. For relatively simple features like 2.5D channels bitmap data can be designed externally and uploaded into most of the FIB systems, or can be created directly using their build-in pattern generators. A more sophisticated approach requires the use of a lithography software and hardware like Elphy Quantum (Raith GmbH) or Nanomaker where various 2D shapes can be easily designed, multiplied, and if necessary the respective exposure doses specified. However, the generation of complex 3D shapes like diffractive optical elements, necessitates a different approach. It was proposed to realise such 3D structures by designing their features in any 3D CAD package and then, by following a sequence of translational operations, the 3D geometry to be converted into a stack of layers ordered along the vertical axis of the model (Lalev *et al*., 2008). After such a 'slicing' step, the model is exported into a GDSII stream file format and each GDSII layer represents a set of exposure pixels defining a cross-section, a slice, of the model at a given point along its vertical axis.

3.2.2 Template structuring

The next stage of the process chain involves fabrication of the template necessary for UV-NIL. The patterning of the template mesa is performed in two stages: micro-structuring and nano structuring, respectively. The material used for the UV-NIL templates is fused silica as it has to fulfil several very important requirements, in

particular, the workpiece must have a good transparency in the UV region, it should be amorphous, since the lack of polycrystalline structure is a pre-requisite for patterning surfaces with very low roughness by dry etching and/or FIB machining, and must have a good wear resistance.

Micro structuring

This stage involves mainly the usage of two technologies: photolithography and laser machining, which are cost-effective for micro structuring relatively large areas (up to tens of cm^2) of the template with a good dimensional accuracy and surface roughness. Especially, F2 laser ablation can be used for direct structuring or in projection mode for machining the mesa of fused silica templates without triggering any material crystallisation (Lalev *et al*, 2009). The later is an important issue since any phase transformations would have affected the machining results of any subsequent nano-structuring steps employing FIB. In case of photolithography, after exposure, a follow-up step is required to transfer the pattern to the mesa by dry etching. It is worth pointing out that there are certain drawbacks associated with such a micro-structuring step. In particular, if photolithography is employed, the resolution is limited to 1 micrometer (Maalouf *et al*., 2009), a mask is required, the 3D patterning capabilities are limited and a subsequent dry etching is necessary. F2 laser ablation is an attractive alternative solution due to its direct structuring capability, however it should be noted that this machining route is significantly more expensive than the photolithography one and the achievable resolution is around 5 micrometers. The structuring times of both technologies are within the minute range.

Sub-micron and nano structuring

The next stage in the process chain is FIB machining of sub-micron and nano features over the pre-existing micro topography.

The FIB milling process offers many advantages, e.g. flexibility, high resolution and high surface quality that are extremely important for master making (Scholz *et al*., 2009; Youn *et al.*, 2006). However, a major disadvantage of this technology is its relatively low removal rates. To address this issue a multi-ion beam concept was proposed that combines the high resolution capabilities of the FIB technology with the higher throughput advantage of parallel lithography systems. In particular, to satisfy the requirements for high productivity, a projection maskless nano-patterning (PMLP) system is under development (Platzgummer *et al.*, 2008). Its working prototype, which incorporates 48,000 beams working in parallel, demonstrated a significant increase of the removal rates and improved resolution compared to conventional single focused ion beam systems.

Another important issue when structuring processes are integrated in process chains is the alignment of new features to any pre-existing features/topography on the wafer or workpiece. In the proposed chain this alignment could be realized either by manually positioning the sample stage while inspecting the sample in SEM or FIB imaging mode, or automatically, by using "feature recognition" option available in some FIB systems to find alignment marks machined in the previous processing steps.

Finally, an ion beam sputtering simulation software can also be employed to reduce some negative effects such as re-deposition of sputtered material and over-etching (Svintsov *et al*., 2009). Its utilisation as a data pre-processing step before FIB milling

makes possible the optimisation of the process parameters and even model modifications in order to counteract the material re-deposition.

3.2.3 UV-NIL imprinting

The multiplication of the features, structured on the fused silica templates, onto a wafer is carried out through UV-NIL. As discussed in the previous chapter the UV-NIL and especially the S-FIL process offer several major advantages, compared to the thermal NIL, that make it the better option for the simultaneous imprinting of nano and micro patterns (Resnick *et al.*, 2005). In particular, the process capability to pattern uniformly large surface areas and imprint micro and nano-features simultaneously, as well as the absence of thermal expansion and the possibility to imprint even complex 3D topographies were considered crucial for the cost-effective implementation of this process chain. Therefore, the S-FIL technology was selected for the proposed master making manufacturing platform.

3.2.4 Electroforming

This stage is necessary in order to fabricate replicas in Ni of the S-FIL imprinted wafers and then to utilise them as masters for serial replication. The electroforming process allows very precise replicas of wafers with nano- and micro-topography to be produced (Tang, 2008). Furthermore, it is a relatively fast and inexpensive way for fabricating robust tools, Ni-shims, which can be used as hot embossing stamps, skins for R2R rollers and injection moulding inserts for serial production of polymer components (Leech and Lee, 2006).

Finally, it should be noted that the proposed master making process chain can also be

implemented for serial production of components in Ni resembling the direct LIGA process (McGeough *et al.*, 2001). Since the latter is not within the scope of this research it will not be discussed further.

3.2.5 Serial replication

The proposed master-making process chain can be used for a number of serial replication technologies for scale-up micro manufacture including micro-injection moulding (µIM), R2R imprinting and hot embossing (HE) together with some of their variations such as compression injection moulding and R2R thermoforming (Heckele and Schomburg, 2004).

To make the best use of their specific features, such as high-throughput manufacture, replication of different length-scale structures at relatively high speed and the wide range of materials that can be processed, R2R imprinting was selected as a serial replication process to validate the proposed process chain in this research.

3.3 Experimental Set-up

3.3.1 Test device

To test the proposed master-making process chain a single device organic thin film transistors (OTFT) was selected. With commonly used low-cost industrial patterning and printing technologies for producing such devices, the maximum operation frequencies that can be expected from organic logic gates are in the 10 kHz range due to the limited resolution of these techniques; the minimum achievable channel length is in the range of 10 µm. By applying the new process chain it will be possible to reduce the critical dimensions of OTFT towards the submicron channel length regime,
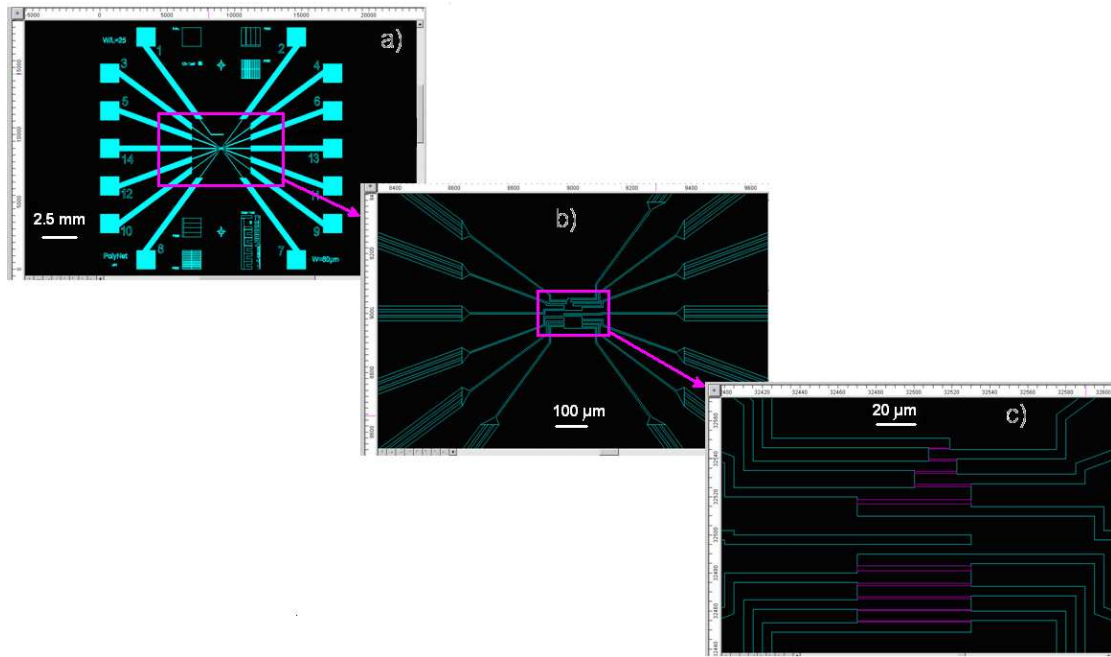
Figure 3.2 The OTFT design a) overall view, b) magnified central area, and c) the interconnecting trenches to be structured by FIB.

and thus to achieve switching frequencies in the MHz region. Apart from achieving this downscaling, the minimisation of the parasitic capacitance is another contributing factor in reducing the switching time. To validate this, together with the capabilities of the proposed process chain, the OTFT design presented in Figure 3.2 was used. Figure 3.2a shows the photomask design. The test device comprises of different layouts of pads, connectors-width-to-distance tests, areas for channels to be machined by FIB (Figure 3.2c) and various test-structures parallel and perpendicular to the R2R imprint direction.

The main functional structure of the device consists of multiple micro-channels as shown in Figure 3.2b that are interconnected through micro- and sub-micron trenches. Also, this design is a good example of a proper implementation of the FLSI concept (Bigot *et al.*, 2009) as it incorporates both micro- and sub-micron dimensional features on a millimeter-scale area. A magnified image of the center of the OTFT design is shown in Figure 3.2c. As it can be seen on the sketch, the interconnecting channels vary in size. The minimum trench width is 450 nm, followed by 600 nm, 900 nm, 1.2 µm, 2.4 µm and 5 µm. Their length is determined by the distance between the big micro channels and is in the range from 11.25 to 60 µm. The targeted depth of the whole structure is 450 nm.

3.3.2 NIL template fabrication

A fused silica template with a mesa, with dimensions 25x25 mm and height of 30 µm was manufactured by grinding, prior to the micro structuring stage. Then, the micro channel structures, including the 5µm interconnecting trenches in the template, were produced by photolithography. Microposit S1813 photoresist was spun on the mesa at

4000 rpm giving a film thickness of ~1.8 µm after baking at 97 ℃ for 2 min. The template was then placed in the Karl Suss mask aligner for exposure. The resist was exposed using a UV light (365 nm wavelength) for 6 sec. A developer solution with a ratio of 6:1 DI water to Microposit developer 2401 was used. The developing time was 45 sec. The template was then rinsed in DI water and then dried with N_2 gas. Following the photolithography step, dry etching was used to transfer the pattern into the fused silica. To carry out this operation an Oxford Instrument PlasmaPlus 80 reactive ion etching (RIE) system was used. The resist acted as a dry etching mask with a selectivity of 3:1 to the fused silica. A mixture of 80 % carbon tetraflouride (CF4) and 20% oxygen (O_2) was used as an etching gas. The template was etched for 20 min at 40 mTorr pressure applying 100 W RF power.

The sub-micron and some of the micro channels on the active area of a UV-NIL template were machined by FIB milling on a Carl-Zeiss XB 1540 FIB/SEM cross-beam system. The build-in pattern generator was used to design the channels. To avoid charging, the template was coated with 20nm Cr film. The submicron and micron trenches up to 2.4 µm were machined on the template by applying probe currents ranging from 50 to 200 pA. Their alignment to pre-existing structures on the template mesa was performed manually by utilising the imaging capabilities of the FIB system. Figure 3.3a shows part of the central area of the OTFT with the FIB-structured interconnecting trenches.

3.3.3 NIL and electroforming

An UV-NIL system, Imprio 55, was employed to multiply the template topography on a 4" wafer employing the S-FIL process. The imprinting was performed on a double-
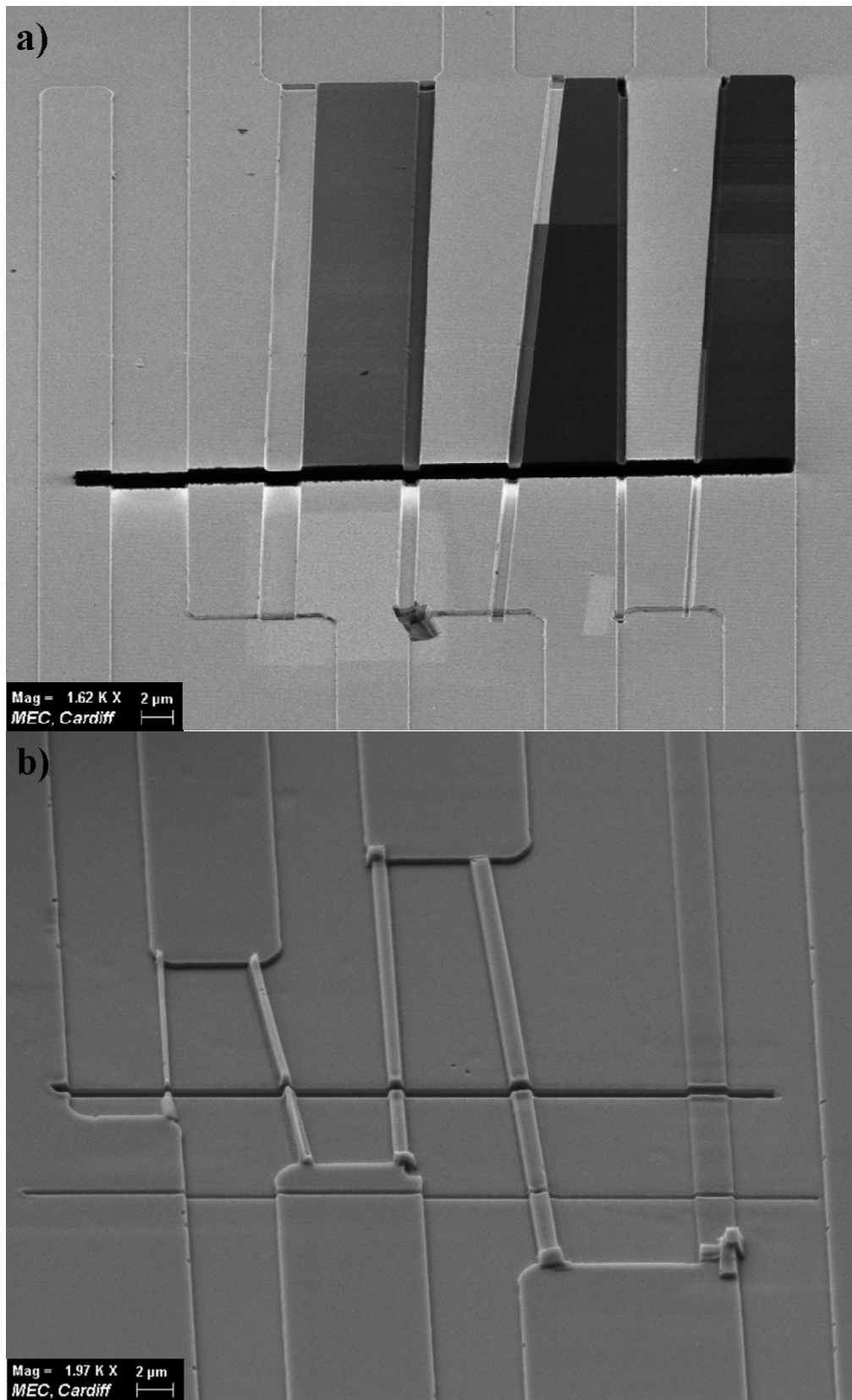
Figure 3.3 Central area of the OTFT with the interconnecting trenches on a) the FIB-

structured template and b) the NIL imprint of the template

sided polished silicon wafer spin-coated with a 60nm thick layer of DUV30J, which served as a planarization layer and a bottom anti-reflective coating (BARC). After stripping the Cr coating the wafer and the template were mounted into the NIL system. Utilising a drop-on-demand build-in dispensing system, an array of pico-litre sized drops of a low viscosity monomer, Monomat^{TM}, was spread over the imprinting field before the template was lowered onto the drops. When the surface tension of the liquid is broken, capillary action draws the fluid into the template features and thus spreading the resist across the template active area. Then, the fused silica template was exposed to 355nm UV light in order to cross-link the monomer and solidify it. Finally, the template is withdrawn, leaving an exact replica of the structured template on the wafer surface. To multiply the template topography the process is repeated to imprint an array of fields. Part of the central area of the OTFT on one of the NIL imprints is shown in Figure 3.3b.

For the 4" (round) Ni shim fabrication a commercial electroforming system, Digital Matrix SA/1m, was utilised. The parameters used to carry out the electro chemical deposition were as follows: electrolyte: Nickel Sulfamate, bath temperature: 50^oC, head rotation speed: 30 rpm, pH 3.96, current density: 0.1/0.5 A/dm^2, waveform: Spiked down/Ramp down, cycle time: 10 ms. The obtained shim had a thickness of 100 µm. The central area of transistor on the shim is presented in Figure 3.4a

3.3.4 R2R hot embossing

The VTT's Pico pilot production facility, shown in Figure 3.5a, was used to test the shim produced applying the proposed process chain. The machine consists of two gravure printing units for thin film deposition and a hot embossing unit. The
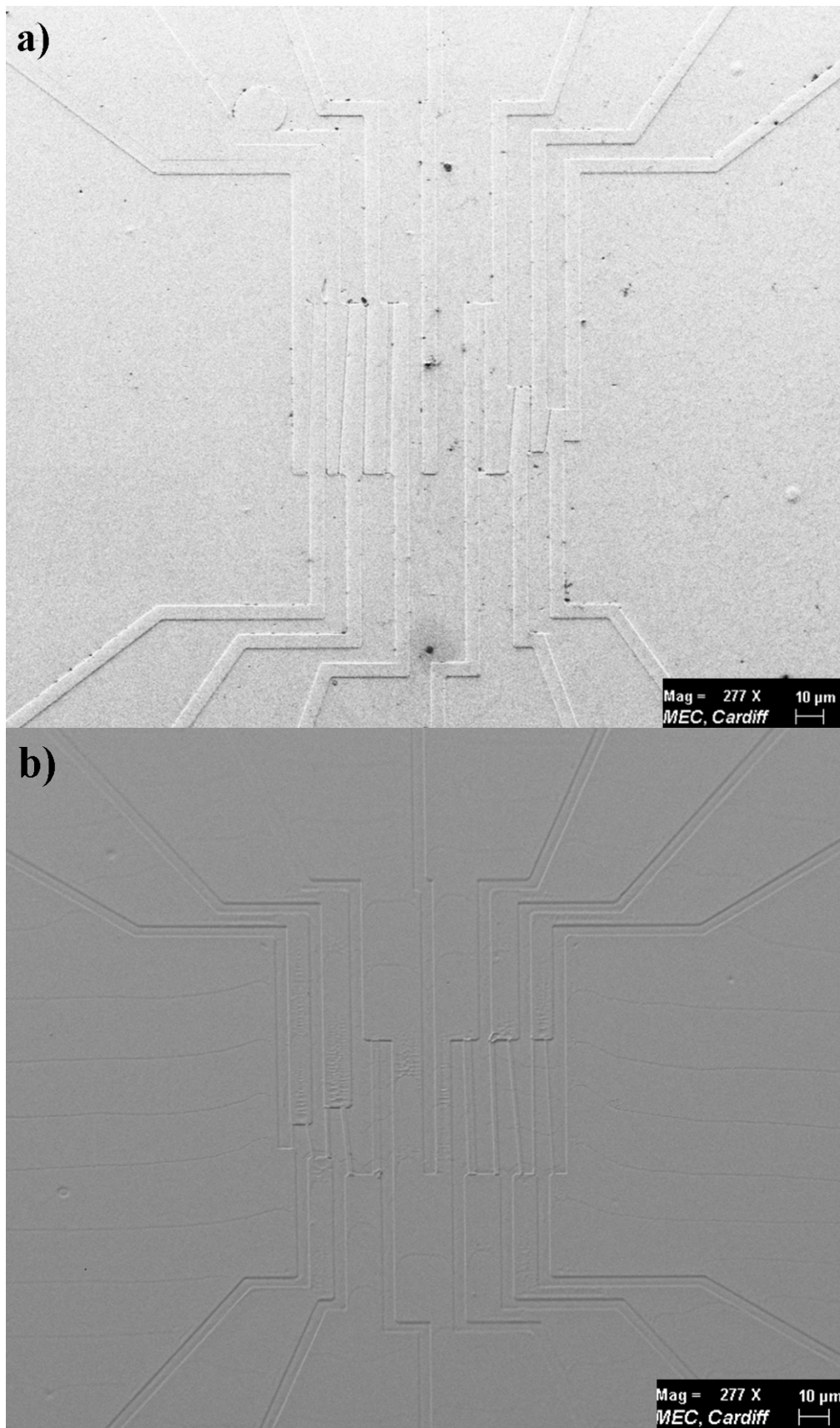
Figure 3.4 Central area of the OTFT after a) electroforming of the NIL imprint, and b)

R2R imprinting of the shim

prefabricated shim was laser welded to a sleeve which was then mounted on the R2R hot embossing machine. The sleeve with the shim is shown in the Figure 3.5b.

For R2R tests, mr-I 7030E resist was deposited using forward gravure printing on top of PET Melinex ST504 substrate. The printing cylinder parameters were: mesh 64 lines/cm, depth of cell 44 µm and transfer volume 13 ml/m^2. Printing speeds of 2, 4, 6 and 8 m/min were used during the resist deposition and then dried with hot air, which temperature was 120 °C. Based on a carried out visual inspection the best printing speed for consistent deposition of high quality films was determined to be 4 m/min. The layer thickness of the resist was measured using a Wyco optical profilometer and it was 300 nm.

After the resist deposition, R2R hot embossing was performed. The embossing speed was 10 m/min, and the applied pressure was 4 bar at a temperature of 120 °C. Figures 3.5c and 3.5d show the hot embossing roll used in the carried out tests and a zoom-in image of the replicated structure, respectively. Figure 3.4b shows the R2R imprint of the transistor's central area seen on the Ni shim in Figure 3.4a.

3.3.5 Inspection

SEM images of the features were taken using Carl-Zeiss XB 1540 at each stage of the process chain and then analysed with the build-in SmartSEM software. 50 pA FIB probe current was used for making cross-sectional cuts of the inspected structures (Figure 3.6). To minimize the measurement error all images were taken at 3 kV EHT and the same SEM aperture. After a calibration with a reference sample, the measurement error of the instrument in XY direction was assessed to be in the range
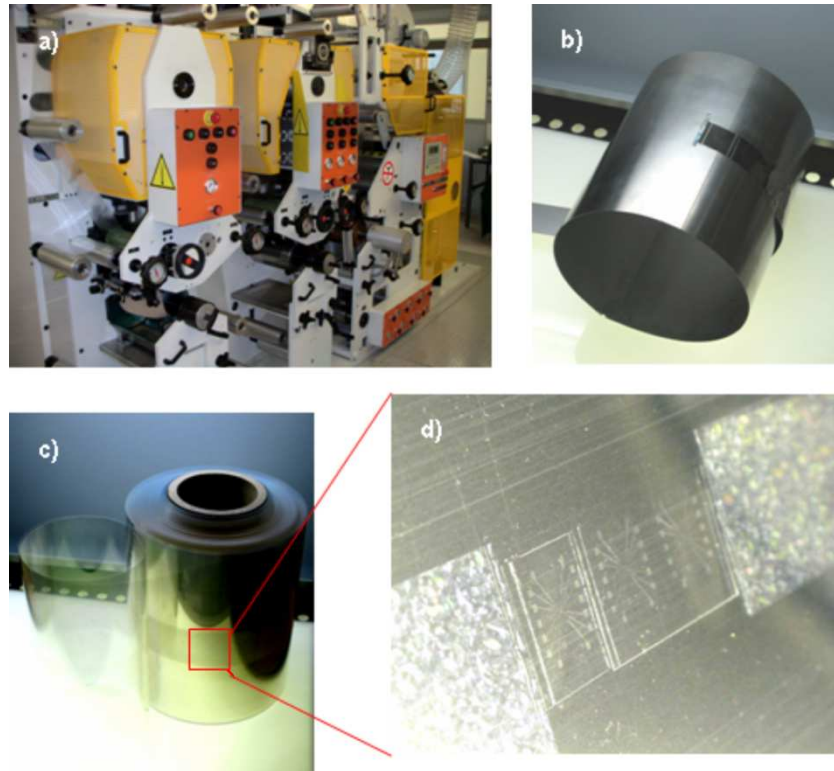
Figure 3.5 R2R replication process a) VTT's Pico R2R hot embossing installation, b) a roller with an integrated Ni shim, c) an imprinted PET roll and d) a zoom-in of the imprinted PET roll

of 1 to 3 %. All the samples were measured at 36 degree tilt in order to be able to image the vertical walls of the structures. In addition, the "tilt compensation" option of the SmartSEM software was utilised in order to measure accurately the features' height. Cross-sectional SEM images of the 450 nm channel on the quartz template, S-FIL imprinted wafers, the Ni shim and the R2R replica are presented in Figure 3.6.

3.4 Discussion

3.4.1 Analysis of the results

The experimental results obtained after each step of the proposed process chain are discussed in this section. As the OTFT channels had tapered sided walls, the measurements of their width were taken at the bottom, top and in the middle of each structure. The full width at half maximum (FWHM) value of the channels was used to compare the results after each step of the proposed process chain. Table 3.1 shows the measured FWHM values of the channels.

The difference between the width of the channels of the template and the NIL imprint, in percentage, is shown in Figure 3.7. It is not difficult to see that there is a tendency the difference to decrease with the increase of the channel width. This can be explained with the fact that with the increase of the width the aspect ratio of the features decreases due to the constant depth of the channels. In particular, it is more difficult to machine high aspect ratio channels and any deviations during the template structuring affect the follow-up replication processes. In addition, it should be taken into account that the relative measurement error, in percentage of the nominal width, increases with the decrease of the nominal dimensions of the channels. The average difference for all channels is around 5.6 %, which is more than have been expected.
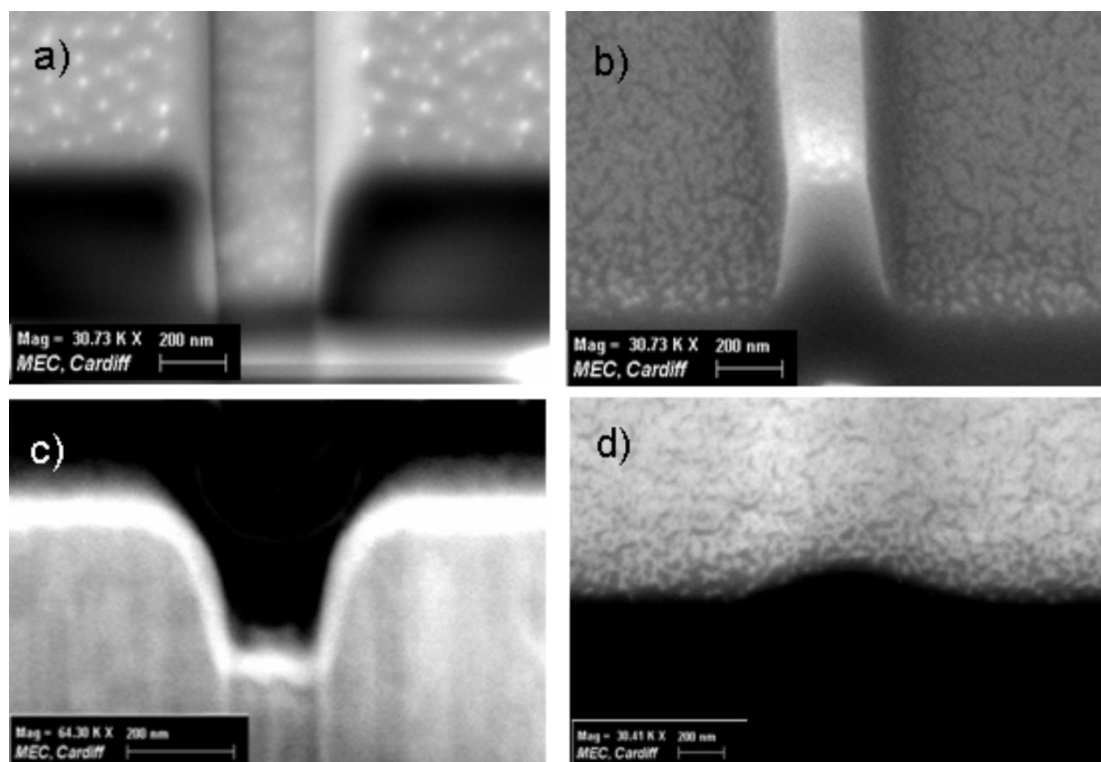
Figure 3.6 SEM images showing a cross-sectional cut of a 450 nm channel on a) the fused silica template, b) the NIL imprinted replica of the template, c) the Ni shim fabricated from the NIL imprinted master and d) the R2R replica of the shim

Table 3.1 FWHM values of the channels measured at each stage of the process chain

Target width [nm] / Chain's stage	450	600	900	1200	2400	5000
Template	379.3	481.5	812.1	989	2232	4995
NIL imprint	343.6	457.5	743.8	920.3	2126	4800
Ni shim	348.4	477.2	750	912	2141	4846
R2R imprint	664	753.4	1181	1331	2802	5406

This result could be explained with the resist shrinkage after the UV curing, which was expected to be approximately up to 3% for Monomat^{TM} (Resnick *et al.*, 2005), the measurement errors and the used exposure parameters, in particular curing time, that were not optimised.

Also, Figure 3.7 shows the difference in percentage between the channels' widths of the imprints and the Ni shim produced with them. As expected the tendency of the features with bigger lateral dimensions and low aspect ratios to replicate better was observed again. With an average deviation of 1.5 %, the Ni shim appears to be an excellent replica of the NIL imprints.

The changes of the FWHM values for all channels after each processing step are shown in Figures 3.8a and 3.8b. In spite of the fact that there is a relatively big difference between the size of the channels on the R2R replica and the template it is clear that the plotted lines are relatively parallel, since the difference of the respective FWHM values for all channels is almost constant, approximately 300 and 500 nm for the sub-micron and micron channels, respectively. This shows a high level of consistency in replicating the fused silica and NIL masters, and also indicates very good process compatibility between the component technologies in the process chain, especially for the targeted length scale range.

The big deviation in the FWHM values of the R2R replica channels and those of the Ni shim can be explained with the use of embossing parameters that were not optimised, especially the embossing temperature. In addition, the phenomenon known as polymer relaxation is expected to contribute to this (Kong *et al.*, 2006; Harsono *et*
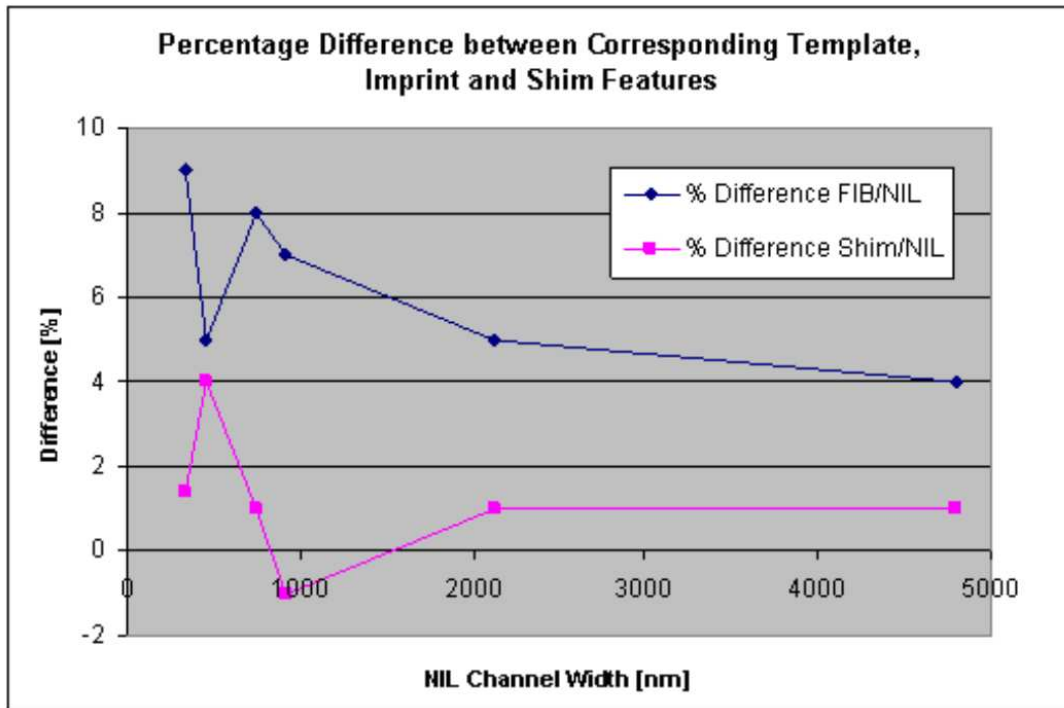
Figure 3.7 The percentage difference in imprint features' dimensions with regard to the template and the Ni shim
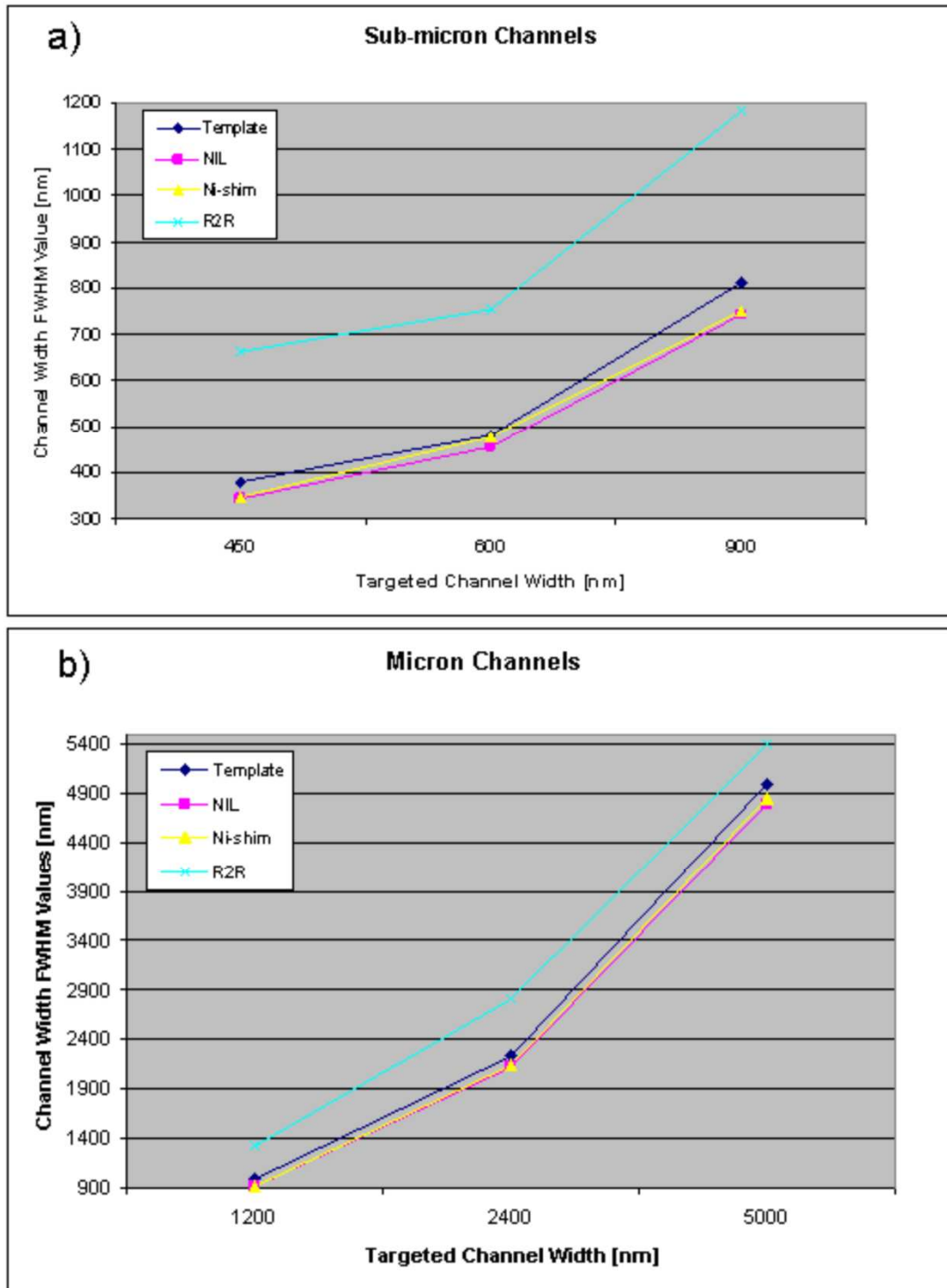
Figure 3.8 FWHM of the channels' width, a) the sub-micron channels b) the micron channels

al., 2006). However, it is important to state that this deviation can be minimised by modifying the device models or by introducing measures to "freeze" the polymer immediately after the thermal imprinting step. Since the main objective of this research is to design and validate a process chain for a reliable fabrication of serial replication tools incorporating the capabilities of the FIB technology, the optimisation of the R2R process parameters is not discussed in this study.

The significant difference between the channels' aspect ratios on the Ni shim and on the R2R replica – Figure 3.9 can be explained again with the effects of the polymer relaxation after the replication step and the insufficient embossing temperature. It can also be seen from Figure 3.9 that these effects on the replica are strongly pronounced for the features with higher aspect ratios. In addition, Figure 3.10 shows that the difference in percentage between the widths of the channels on the shim and on the R2R replica, and their respective heights are almost the same, with only a 4% average. This can be attributed to the fact that after de-moulding, the molecular chains tend to regain their original shape, and thus to keep constant the volume of the structures. Thus, the channel height decreases in order to compensate for any expansions in the XY plane.

3.4.2 Error factors

When different technologies are integrated into process chains the possible causes of faults or errors at each stage of these chains should be taken into account, and the total error at the end should be analysed carefully. Thus, a sound judgement of whether and how such errors could affect the outcome could be made as well as an assessment of the overall performance of a given process chain in terms of cost and production time.
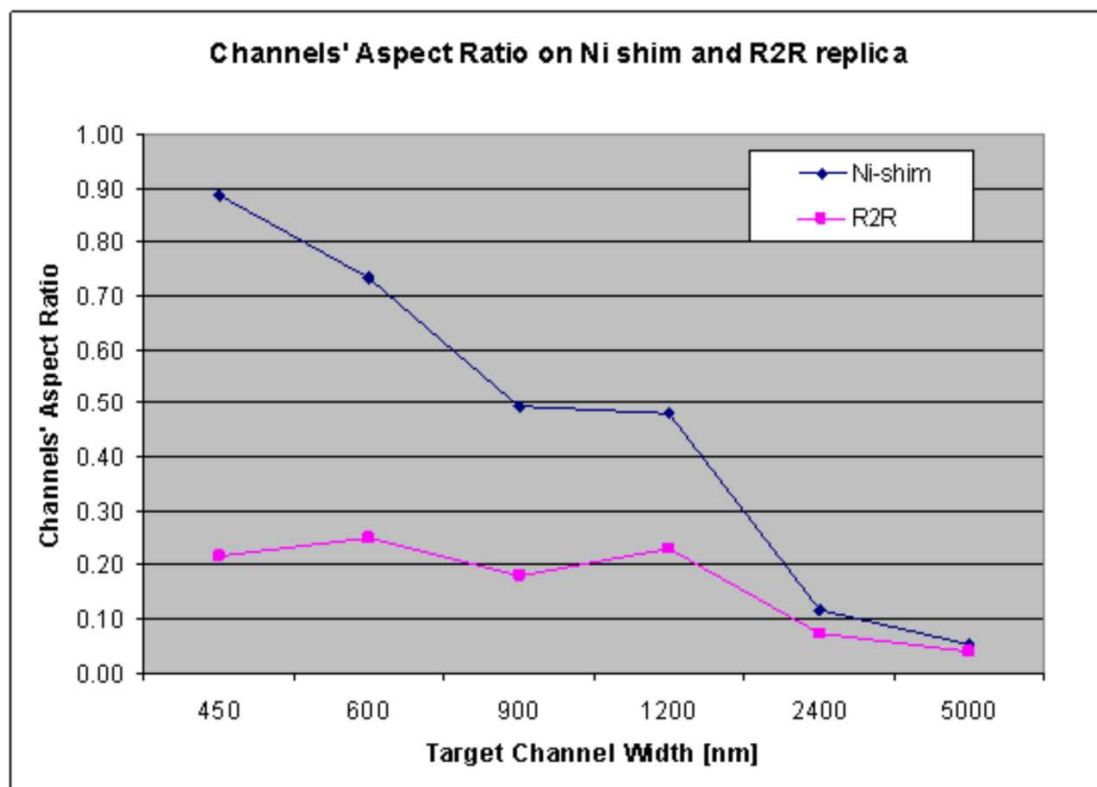
Figure 3.9 Channels aspect ratio for the Ni shim and the R2R replica
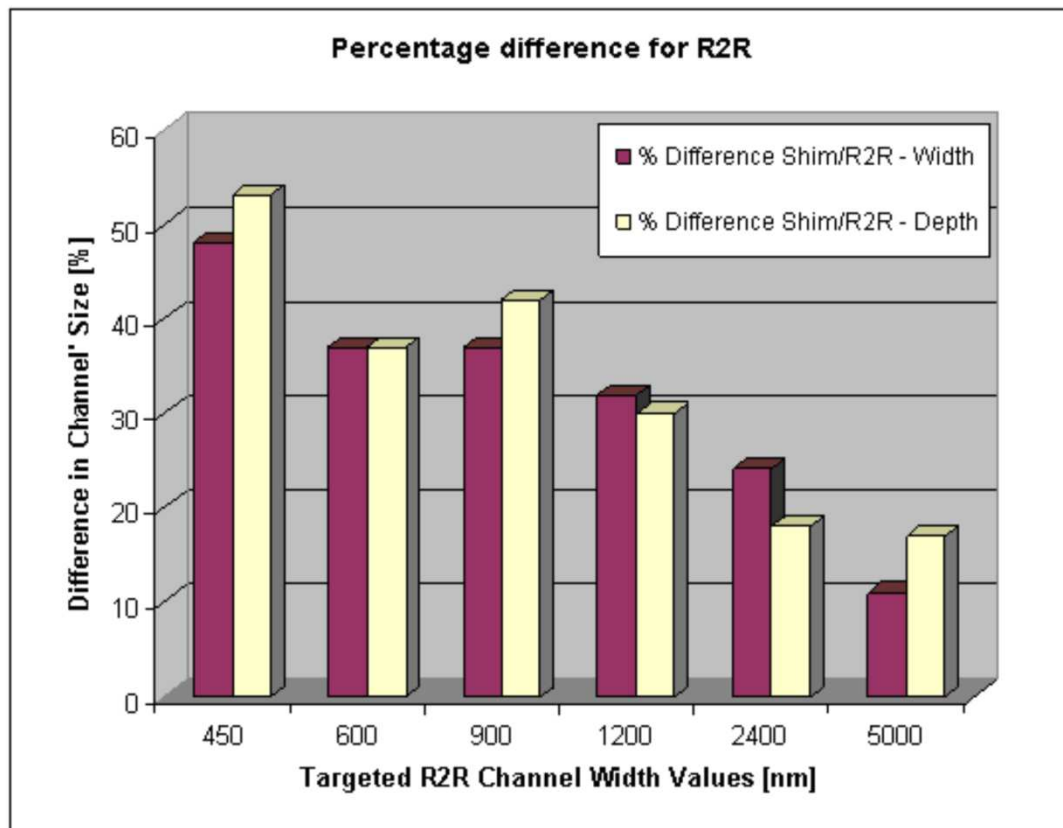
Figure 3.10 The percentage difference between R2R and Ni shim features in vertical

and horizontal directions

As discussed earlier in Section 2.1.5 generally the possible sources of error for every process can be associated with: the process, equipment, human factor and environment. Following this classification the possible error factors for each of the processes in the proposed process chain are summarised in Table 3.2. With the presumption that the human factor can have an effect on every process it is not considered separately for each stage.

It should also be noted that apart from the stated technology-associated error factors, the measurement errors could have a major influence on the outcome and thus affect the whole effectiveness of the process chain. Therefore, the measurement uncertainty should always be accounted for. The procedure for determination of the uncertainty of the used measurement instruments, in this case SEM, is described in details in Appendix A. The uncertainty, U, of the FWHM values of the channels, was calculated following an established procedure (Kirkup and Frenkel, 2006): $U = k.u_c(x)$, where k

is a 95% confidence interval (CI) coverage factor, and $u_c(x) = \sqrt{\sum_{i=1}^{n} \left(\frac{\partial f}{\partial x_i} \right)^2 u^2(x_i)}$ is

the combined standard uncertainty, which includes the measurement uncertainty $u(P)$ and x denotes the FWHM value. In this research $u(P)$ was calculated as 3% of the measurand. Even though the calculations of the SEM uncertainty prove that the instrument was very well calibrated and quite accurate at the time (with measurement error of less than 1% for all tested magnifications – Appendix A), the expected error of the measuring instrument is in the range 1-3% (private correspondence with Carl Zeiss). Thus, as a conservative judgement, a value of 3% was used when calculating the measurement uncertainty $u(P)$. Table 3.3 shows the FWHM values of the channels and the associated uncertainties, FWHM $\pm U$, for all stages of the process chain,

Table 3.2 Possible error factors at each stage of the process chain

Error Factor / Chain Processes	Process	Equipment	Environment
Data Preparation	1. Use of translators or any other programmes as intermediate steps during the data preparation 2. The choice of algorithms and/ or approaches	1. Software capabilities and limitations 2. Generation and use of different file formats and their input into the system	N/A
Photolithography	1. Resist properties with regard to exposure: • sensitivity, • thickness, • resolution 2. Developer solution 3. Dry etching	1. Positioning errors due to manual alignment	N/A
Laser Ablation	1. CAM tolerance 2. Substrate uniformity	1. Laser source 2. Optics 3. Galvo scanner 4. Stage positioning	Temperature
FIB	1. Data preparation 2. Beam shift 3. Surface charging 4. Material machining response	1. Stage accuracy 2. Beam condition • probe current • beam focus, stigma and wobble	Noise Vibrations Magnetic field

S-FIL	1. Template accuracy 2. Residual layer thickness	1. Template and wafer levelling 2. Stage accuracy 3. Overlay alignment accuracy 4. System levelling	Temperature Vibrations
Electroforming	1. Current density 2. Temperature 3. Applied waveforms and frequencies	1. Master resistance to the electrolyte 2. Master cleaning before electroforming	N/A

Table 3.3 FWHM values of the channels and their uncertainties for 95% CI

Target Width	Template		NIL imprint		Ni shim		R2R imprint	
	FWHM	U [nm]	FWHM	U [nm]	FWHM	U [nm]	FWHM	U [nm]
450	379.3	23	343.6	30	348.4	22	664	40
600	481.5	34	457.6	40	477.2	29	753.4	44
900	812.1	50	743.8	45	750	45	1181	73
1200	989	74	920.3	60	912	54	1331	120
2400	2232	146	2126	125	2141	126	2802	165
5000	4995	296	4800	284	4846	295	5406	361

whereas a more detailed data on the carried out calculations is provided in Appendix B.

Even though it is difficult to estimate the influence of different factors at the various steps of the proposed process chain on its overall performance, the following ones are considered to have the highest impact: the measurement uncertainty including the system calibration and the human factor, the optimisation of the processing conditions of different component technologies, and material properties, especially the materials' response to UV exposure and thermal curing.

3.5 Summary and conclusions

In this chapter a cost effective process chain for fabrication of Ni shims incorporating different length scale features was proposed and validated for R2R imprinting of organic electronic devices. In the study, the capabilities of photolithography as a micro structuring technology were combined with those of FIB milling to fabricate templates incorporating sub-micron and nano features on top of pre-existing micro structures. S-FIL process was employed for consistent multiplication of such templates on 4" wafers in order to replicate reliably different length scale features in one step. The transfer of such polymer replicas into Ni shims was also successfully implemented resulting in relatively negligible deviations from the targeted dimensions.

The results of the research carried out in this chapter can be summarised as follows:

1. The deviations of less than 5% in the targeted dimensions of the respective 2.5D features at the different steps of the process chain indicate good process compatibility of the selected manufacturing technologies for the particular length scale range.

2. Even though it is hard to estimate the effects of error factors at each stage of the process chain and their possible influence on its overall performance, the careful selection of compatible and at the same time complementary technologies can minimise the overall uncertainty.

3. A successful implementation of the FIB technology as a mean for high precision structuring at sub-micrometer and nano-scale level in a master-making process chain for serial production was demonstrated.

4. The proposed fabrication route for fabrication of Ni shims incorporating a wide range of micro and nano features can be used for high-throughput fabrication of organic electronic devices on flexible substrates employing serial replication technologies like R2R imprinting.

CHAPTER 4

PROCESS CHAIN FOR SERIAL MANUFACTURE OF 3D MICRO- AND NANO-SCALE STRUCTURES

4.1 Introduction

In this chapter the capabilities of process chains as effective manufacturing platforms for high-throughput fabrication are explored further in regard to the production of FLSI products incorporating complex three-dimensional features. In addition, the advantages the FIB technology offers in terms of 3D structuring at micro- and nano-level and its compatibility with the other component technologies are investigated.

In this research, by adapting the process chain for fabricating replication masters, discussed and validated in Chapter 3, Ni shims containing 3D micro and nano (submicron) structures were produced and then employed for serial replication through hot embossing. In addition to validating this process chain as a potential solution for serial production of components containing complex 3D structures, the research presented in this chapter aims at proving that the designed manufacturing route is cost-effective for a large range of 'interchangeable' technologies, so long as they are implemented in their optimal process windows.

4.2 Process chain design considerations

When there are specific requirements in terms of producing complex 3D patterns of micron and submicron scales in the end product, several issues related to the choice of geometry and pattern generation should be accounted for during the design stage of the manufacturing route. The following sub-sections discuss these issues in detail.

4.2.1 Selection of 3D functional structures

In many application areas like optics, optoelectronics and biomedical industry, the realisation of complex multiple 3D structures at micro and nano scales is a crucial issue that poses further constraints in designing and implementing successful FLSI manufacturing solutions. Such applications usually require structures like lenses and pyramids, having micron and/or nanometre dimensions, to be produced as large arrays rather than as single features i.e. structured surfaces containing numerous 3D features (Lee *et al.*, 2006; Paivanranta *et al.*, 2008; Yan *et al.*, 2009). Usually, there are strict technical requirements in regard to such arrays of 3D features, e.g. geometrical accuracy, aspect ratio (AR), positional and alignment accuracy and field stitching, which make the design and implementation of cost effective solutions for their manufacture even more difficult. A major issue in manufacturing 3D structures at different scales in order to achieve FLSI arises from the high uncertainties associated with the achievable dimensional accuracy of the resulting profiles, especially in vertical direction (Lalev *et al.,* 2008). Therefore, it is important to study the various factors affecting the process chains for 3D structuring starting from their designs and then going through their implementation stages.

Arrays of pyramids are commonly utilised as functional features in various application areas. The micro pyramids, as structures incorporated into larger-scale products find important applications in the field of electronics, e.g. light emitting diodes and liquid crystal displays (LCDs) (Chen and Chien, 2006) and optical systems (Coquillat *et al.*, 2008). They can also be utilised in micro-fluidic devices where pyramid structures located on the bottom of a 200 μm channel could facilitate and speed up liquids' mixing or act as traps for microbeads (Toepke and Kenis, 2005).

Other application areas are micro-optical devices and MOEMS where arrays of pyramids are used to manipulate light in order certain improvements in the devices' properties to be achieved. That is due to their geometry that allows multiple refraction and reflection of light, having the pyramids' sides act like mirrors. Therefore it is important that the sides have very good surface roughness in the range from 3 to 5 nm (rms) (Trupke *et al.*, 2006; Lin *et al.*, 1998).

Arrays of micro pyramids are also used to increase the light extraction efficiency (LEE) of light emitting diodes (LEDs) (Lee *et al.*, 2007) as well as to enhance the brightness of LCDs (Lee *et al.*, 2006; Lin *et al.*, 2000). Especially, the pyramids in these applications are employed to manipulate light emitted at them in three different modes: direct and indirect recycle and effective refraction. For example, if placed on the top of polymer films, pyramids' sides refract and reflect light so that it propagates through several of them. As a result redirecting and redistribution of light occurs thus increasing its intensity in the viewing angles ±35º.

4.2.2 Pattern generation

The patterning flexibility and sub-50 nm resolution that the Focused Ion Beam technology offers for 3D structuring are utilised in this study. As discussed in detail in Chapter 2, two main data preparation approaches are usually applied for FIB milling of 3D patterns: the use of 1) bitmap data files by software built-in in the FIB systems or 2) GDSII data files with the FIB milling process being externally controlled by conventional lithography software (Lalev *et al.*, 2008). While they both are layer-based milling approaches in their essence, the GDSII data files allow for a more flexible and faster structuring. Furthermore, due to the fact that all layers are exposed

as a single file thus eliminating the possibility of errors due to misalignment or mixed exposure order of the layers, features with better resolution and profile accuracy are usually obtained. Thus, since the aim of the structuring stage of a process chain is to successfully produce arrays of high resolution 3D features, GDSII data files were used for FIB milling in this research.

4.2.3 Process chain

The process chain for fabricating replication tools validated in the previous chapter is modified to fabricate Ni shims incorporating different 2.5D and 3D length-scale features. Usually for producing a structure or pattern with required dimensional accuracy, surface roughness, production time etc. several technologies can be considered suitable, when applied in their optimal process windows. In order to show that a wide range of such 'interchangeable' technologies can be cost-effectively implemented as component processes at various stages of the manufacturing route, several modifications were made to the process chain studied in Chapter 3, as shown in Figure 4.1.

The initial concept of the process chain is maintained i.e. micron-sized area of accurately structured high-resolution features is replicated on 4'' wafers through UV-NIL process, and then the structures imprinted on the wafers are transferred onto Ni shims to be used as masters for serial replication. However, during the structuring stage and the micro structuring stage, in particular, the capabilities of laser direct writing are employed to produce 2.5D micron-sized features. The laser technology was preferred to photolithography as the structure design selected for this research had much smaller overall dimensions than the OTFT in Chapter 3. This eliminated the
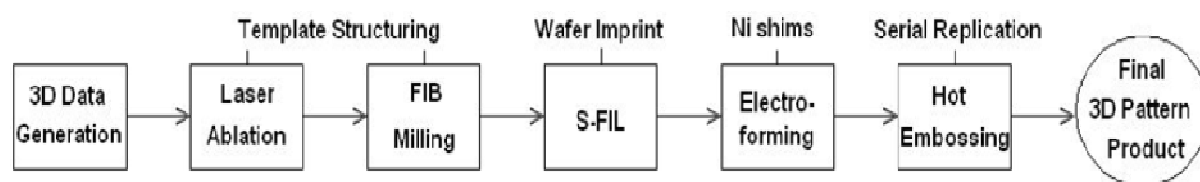
Figure 4.1 Technology steps of the selected process chain

need of designing and producing an expensive mask and thus reduced the time needed to complete the structuring step of the proposed process chain. Since the FIB machining is the most suitable technology for producing accurately sub-micron and nano-scale structures of complex 3D geometries on a small area, it was applied at the nano-structuring stage of the proposed process chain.

To validate the applicability of the fabricated masters for different serial replication technologies, the produced Ni shims were utilised to produce small series of parts through hot embossing (HE).

4.3 Experimental set-up

4.3.1 Template design

The design developed to validate the process chain for serial production of complex features of different length-scale dimensions is depicted in Figure 4.2. The structure that was replicated consisted of 6 x 12 arrays of holes with diameters of approximately 20 μm, depth of 1 μm and around 10 μm spacing between them, and in each of them arrays of 3D features was fabricated. The 3D geometry selected for patterning was a negative pyramid with a square base of 2.2 x 2.2μm and height of 0.5 μm. 0.2 μm was added at each side of the pyramids' base of 2 x 2 μm to compensate for some potential errors during the FIB milling of the individual pyramids, like overlapping or sudden beam drifts. The pyramids were produced in a 4x4 arrays, as shown in Figure 4.3 a.

a)

150

150
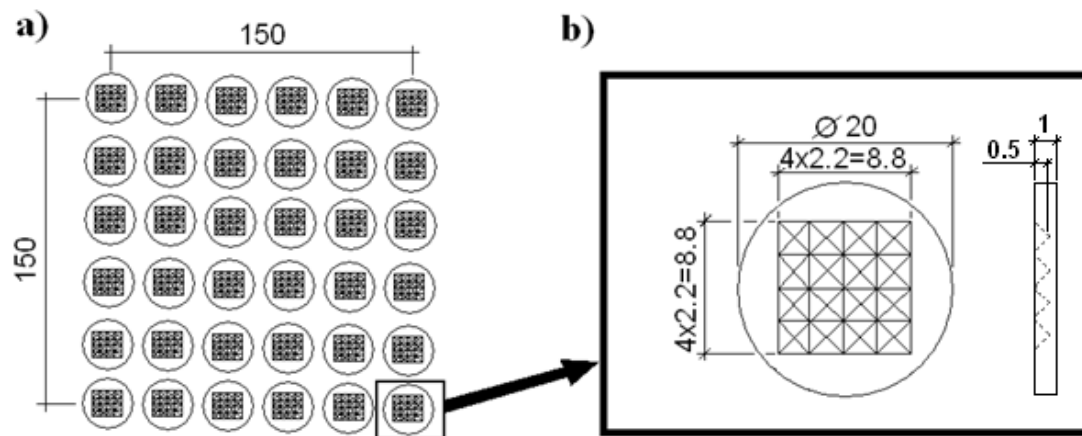
All dimensions are in microns

b)

Ø 20
4x2.2=8.8

4x2.2=8.8

1
0.5

Figure 4.2 Design of the selected test structures
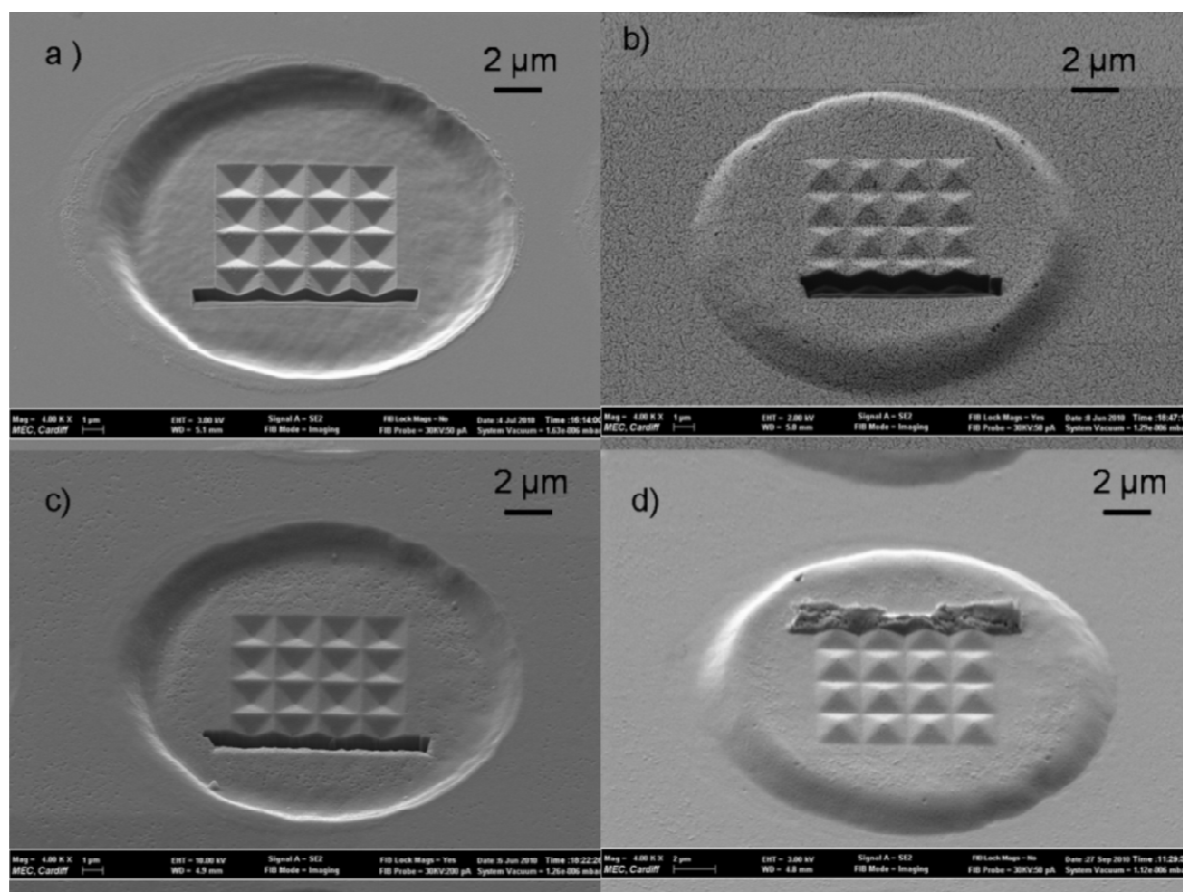
Figure 4.3 Cross-sectional profiles of the 3D structures on: a) the fused silica
template, b) the NIL imprinted replica of the template, c) the shim fabricated from the
NIL imprint and d) the HE replica of the shim

4.3.2 NIL template fabrication

The array of micro holes were machined employing a LPF220 excimer laser system with the following characteristics: pulse duration 26 ns, wavelength 157 nm, pulse energy 40 mJ, frequency 2 kHz, fluence 1.35 J/cm2 and demagnification optics 25X. Then, a Carl-Zeiss XB 1540 FIB/SEM system was used to produce the 3D patterns. The file containing the geometry data of a 2.2 x 2.2 x 0.5 μm negative pyramid was directly utilised by a conventional lithography software and hardware to complete the FIB milling operation. Raith lithography hardware and Elphy Quantum software were employed to control the FIB structuring externally.

An analytical model of the pyramid was used to generate the GDSII file employing the IonRevSim software (Svintsov et al., 2009). As the software provides for both layer-by-layer and area dose assignment modes, a layer-based approach was specified with 100 layers for better profile accuracy and higher resolution. This model was transferred to Elphy Quantum software where the single negative pyramid geometry was multiplied into a 4x4 array of unique pyramids. That pattern was exposed with an area dose, defined by setting up of the associated processing parameters like dwell time, dose factor and area step size. A 100 pA probe current was utilised.

The alignment of the pyramids in regard to the existing micro holes was carried out by manually positioning the sample stage while inspecting the sample in SEM or FIB imaging modes. However, an automatic alignment can also be realised by employing the 'feature recognition' option available on the system but it will require alignment marks to be introduced on the template.

4.3.3 NIL and electroforming

After structuring the template at two different scales with the F2 laser and the FIB system, an UV-NIL system, Imprio 55, was employed to multiply the template topography on a 4'' wafer with the S-FIL process (Resnick et al., 2005). The UV curable resist used to produce imprints on the wafers was MonomatTM (Lalev et al., 2009).

Next, the S-FIL imprinted wafers were used to transfer the structures on a Ni shim by electroforming (Tang, 2008). To assure uniform conductivity a 20 nm gold coating was applied. To fabricate the Ni shims a commercial electroforming system, Digital Matrix SA/1m, was employed. The process settings used to carry out the electro-chemical deposition were: electrolyte Nickel Sulfamate, bath temperature 50^oC, head rotation speed 30 rpm, pH 3.98, baume 37.8, current density 0.5A, waveform Spike down/Ramp down, cycle time 10 ms. The shims were grown to a thickness of 100 µm.

4.3.4 Hot embossing

Finally, the Ni shim was validated as a stamp for hot embossing (HE) on the HEX03Jenoptik Mikrotechnik system. The HE process was performed with the following process settings: force 25 kN, holding time 60 s, temperature during embossing 140^oC, cooling down/demolding temperature 85^oC. HE was used to replicate the Ni shim on a small batch of a 5 µm thick PMMA sheets.

4.3.5 Inspection

SEM images (Carl-Zeiss XB 1540) of the micropyramids' arrays were taken at each

stage of the process chain. The cross-sectional profiles of the micropyramids were analyzed with the built-in SmartSEM software. The cross-sectional cuts were performed with 50 pA probe current. To minimize the measurement error all images were taken at the same magnification (11kX), 10kV EHT and the same aperture. All features on the sample were measured at a 36° tilt allowing observation of the vertical walls of the 3D structures. The tilt compensation option of the SmartSEM software enables measurement of the 'true' value of the vertical dimensions. After calibration with a reference sample, the measurement error of the instrument in XY direction was assessed to be in the range 1 to 3 %. SEM images of the design, taken after each process stage, at a 'tilt' correction angle of 36°, are shown in Figure 4.3.

4.4 Discussion

An analysis of the resulting 3D structures at each stage of the process chain was carried out in two steps: (1) analysis of the lateral dimensions in the XY plane followed by (2) a detailed investigation of the resulting depths/heights of the structures along the z-axis. The resulting pyramids' shape indications on the template, the imprint, the shim and the HE replica shown in Figure 4.3 were analysed and the obtained measurements are presented graphically in Figure 4.4. Eight arrays of pyramids were measured and each measurement was repeated 9 times.

It is well known that the FIB technology produces extremely accurate features in terms of lateral dimensions (Lalev et al., 2008). However, their depths/heights, especially when milling 3D patterns, depend highly on the selected exposure dose, which in turn is specified through the combined adjustments of several FIB processing parameters, such as dwell time, beam current and number of layers
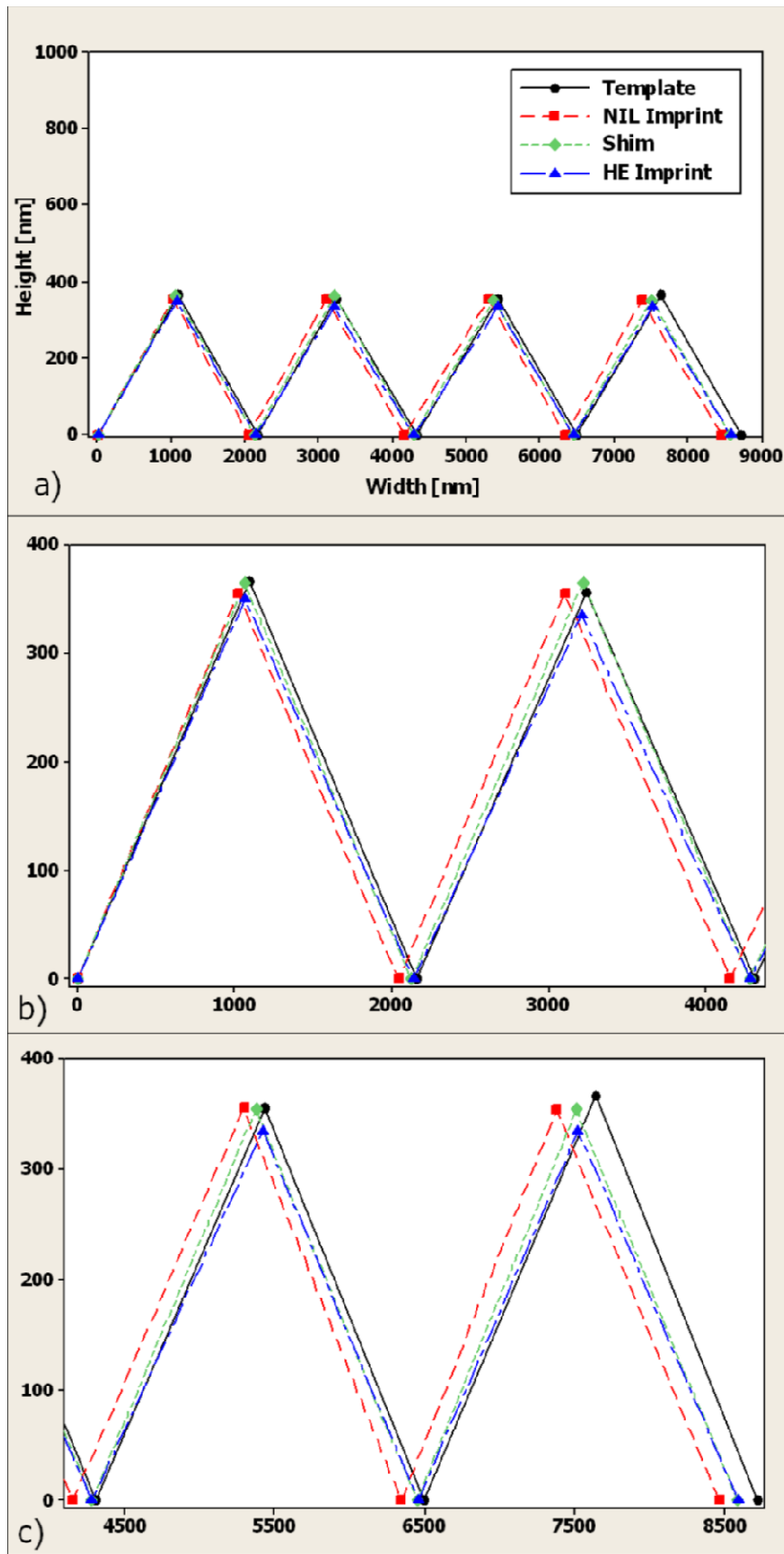
Figure 4.4 Pyramid shape indication at each stage of the process chain (a), and their magnified views for b) the first and the second, and c) the third and fourth pyramids in the row.

(Velkova et al., 2011 b). In addition, factors like measurement errors and process uncertainty could contribute further to the obtained results along the Z axis.

Table 4.1 presents the measured heights and widths of the pyramids, along with their calculated tolerance ranges. The consecutive pyramids in the row are denoted as P1, P2, P3 and P4, respectively. The tolerance range for each value in the table represents the expanded uncertainty, U, which was determined, following an established procedure (Kirkup and Frenkel, 2006), out of 9 repeated measurements and includes the uncertainty of the measuring instrument $u(P)$. To account for the worst-case scenario the measurement uncertainty $u(P)$ of the SEM was considered to be 3% of the measurands' average value. The tolerance ranges for the target nominal values were calculated to be 130 nm, or: $2.2 \pm 0.130 \, \mu m$.

4.4.1 Analysis of lateral dimensions in the XY plane

The inspection of the template shows that the sides of the produced pyramids deviate on the average only 1.4 % from the specified 2.2 μm width. Even for the first two pyramids in the row, which exhibited the maximum deviation of 2%, those values were within the calculated tolerance range of the target width of 2200 nm, and could therefore be attributed to the measurement error of the instrument.

The difference between the width of the pyramids on the template and the NIL imprints, in percentage, is shown in Figure 4.5a. The average difference is 2.9% and it is within the expected range. However, it can be seen that while the middle pyramids, the second and third, in the array appear to be more accurate imprints with just 1.9% and 0% deviation, respectively, the first and the forth pyramids deviate more, 5.3%

Table 4.1 Pyramids' dimensions at each stage of the process chain

	P1		P2		P3		P4	
	Width [nm]	Depth [nm]	Width [nm]	Depth [nm]	Width [nm]	Depth [nm]	Width [nm]	Depth [nm]
FIB	2156±127	366.1±22	2156±127	356±21	2187±129	356±21	2217±130	366.1±22
NIL	2042±120	355.3±21	2115±124	355.3±21	2188±129	355,3±21	2115±124	354.2±21
Shim	2125±125	364.6±22	2156±127	364.6±22	2167±127	354.2±21	2136±126	354.2±21
HE	2142±126	350±21	2142±126	335±20	2172±128	335±20	2132±125	335±20

and 4.6%, respectively. These deviations from the template profile could be explained with the resist shrinkage after the UV curing, which was expected to be up to 3% for Monomat^{TM} (Resnick *et al.*, 2005), measurement errors, and the used exposure parameters, in particular curing time, that were not optimised.

The difference between the template and NIL imprint profiles is not so significant but some slight shifts to the left of both the bases and the tips of the pyramids are observed, which become most evident in the forth pyramid in the row. However, the sides of the pyramids on the imprint appear to be parallel to their corresponding ones on the template indicating that there is a uniform offset in the pyramids' shift and therefore the overall symmetry of the 3D structure is maintained. Possible reasons for the pyramids' tips and edges to appear shifting gradually might be that the bottom left edge of the first left pyramid was always used as a reference to measure the individual features in the arrays, and also because the measurements were carried out always from left to right and not randomly. Furthermore, it can be seen from Table 4.1 that the values for each of the pyramids on the NIL imprint are within the tolerance intervals calculated for them. Therefore, this shift could be attributed to a measurement error that adds up as follows:

$$\varepsilon = \sum \left(P_i^{TEMPLATE} - P_i^{IMPRINT} \right) =$$
$$= (2156 - 2042) + (2156 - 2115) + (2187 - 2188) + (2217 - 2115) = 256nm$$

The accumulated total error of 256 nm is significant and indicates that the 'in-chain' measurement strategy applied is not the most suitable one. Therefore, by applying another measurement strategy, such as measuring the relative distances between the
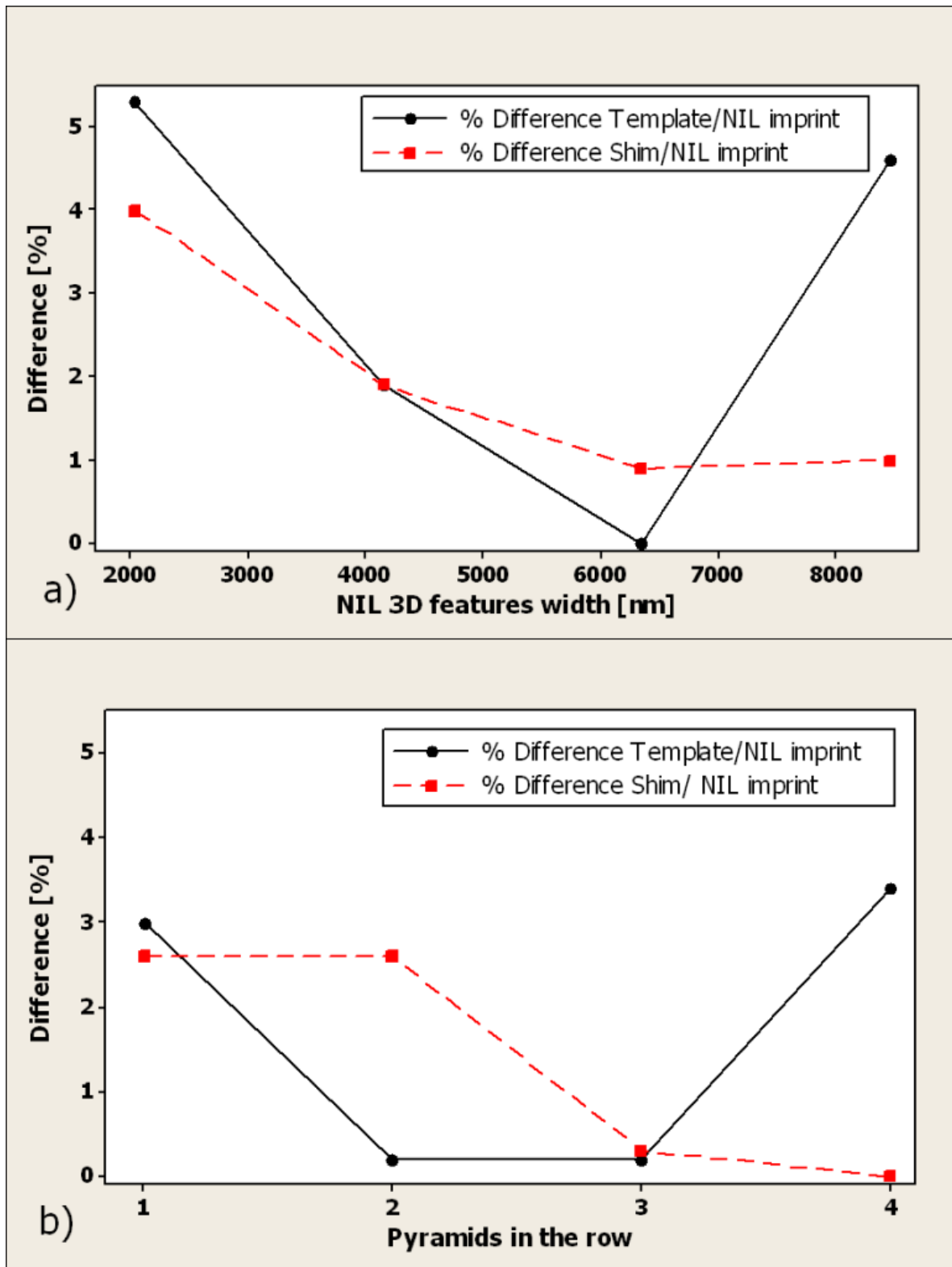
Figure 4.5 Percentage difference between the corresponding template, imprint and shim features' dimensions a) in the XY plane, and b) along the z-axis

pyramids' tips, this increasing offset could be eliminated.

Figure 4.5a also shows the percentage difference between the pyramids' dimensions on the NIL imprint and those on the shim. The difference for the first pyramid in the row seems significant, approximately 4%. However, this difference is much smaller when the shim is compared to the template: approximately 1.4%. Thus, it can be concluded that the two deviations are in opposite directions and they compensate each other to some extent.

On the shim again some slight, even negligible, offset to the left was observed for the last two pyramids in the row. Since this offset is uniform such a shift is most likely due to a systematic error during the measurements. At the same time, the HE imprints of the shim appear to be a very accurate replica of the shim with less than 1% deviation in the XY plane. Again some systematic error is also present here though it is not so evident, being in the range of 4-8 nm.

4.4.2 Analysis of the resulting 3D profiles

The carried out analysis of the SEM images in Figure 4.4 shows that the heights of the pyramids on the FIB structured template are under 0.4 µm instead of the 0.5 µm specified in the data file. In addition to the factors mentioned in Section 2.2 that affect the resulting accuracy in the z direction there are some others issues. In particular, the FIB built-in software contains a module for calculating the machining parameters needed for achieving a targeted depth. It utilises coefficients related to the material properties, such as milling rates and milling frequencies. However, the default values of those coefficients, integrated in the FIB system, are only for machining of silicon

(Si). Since the NIL process requires UV transparent templates, the material utilised to produce the template is fused silica (SiO_2), which is somewhat harder to machine than Si. Hence, the resulting features' depths tend to be less than expected. This issue could be addressed by a systematic study of the FIB machinability of SiO_2, followed by a respective optimisation of the exposure parameters. Such a study is reported in the next chapters of this research.

Figure 4.5b shows the difference, in percentage, between the heights of the pyramids on the template and its NIL imprints. With an average deviation of 1.7 % the S-FIL process proves to be very accurate in replicating complex 3D features with dimensions in the nanometre range. Again, as it was the case for the XY plane, the first and forth pyramids in the array (355.3nm and 354.2 nm, respectively) differ in height significantly more than the central ones, which appear to be almost identical with only 0.2% difference each. In addition, a comparison of the two graphs in Figures 4.5a and 4.5b reveal that the NIL imprints and the Ni shim exhibit the same behaviour in terms of pattern replication in both XY plane and along the Z axis. Also, with an average deviation of only 1.4% along the Z axis and 1.9 % in the XY plane, the Ni shim is a very accurate replica of the NIL imprint. Furthermore, as it can be seen in Figure 4.4, the cross-sectional profiles of the 3D structures on the Ni shim and the template almost overlap, which indicates a high level of consistency in replicating the NIL fused silica template on the wafer employing the S-FIL process. This can also be seen by examining the SEM images of the NIL template and the Ni shim in Figures 4.3a and 4.3c.

The difference in the respective features' heights on the shim and its HE imprint are
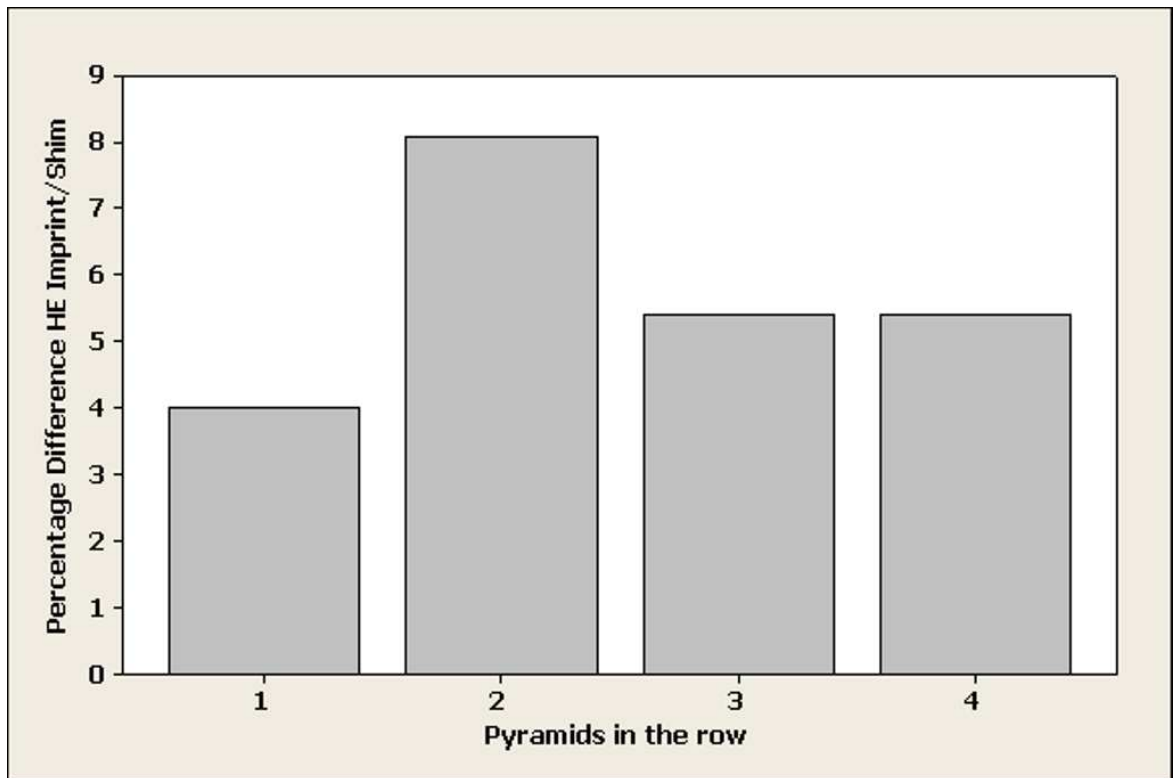
Figure 4.6 Percentage differences between HE replica and Ni shim in vertical direction

given in Figure 4.6. As it can be judged from the results, the use of the Ni shim as a tool for 3D thermal replication is well justified as the deviation of the functional features on the end component is only within 5.7 % on the average in the vertical direction. Even though these results are well within the technical requirements for producing such functional structures further improvements can be achieved by optimising the embossing parameters, especially the embossing temperature.

An analysis of the profiles of the corresponding pyramids on the template, the NIL imprint, the Ni shim and HE replica in Figure 4.4, clearly reveals that they are parallel to each other, indicating that:

- the pyramids' tips were milled exactly on the line of symmetry between the horizontal edges of the pyramids, i.e. the targeted 3D geometry was accurately produced by FIB milling, and
- the tips remained in the centre of the respective pyramids throughout all machining and replication steps of the process chain without compromising the structure's functional requirements.

The results demonstrate the capability of FIB milling in combination with UV imprinting and electroforming to produce replication tools incorporating complex 3D features and patterns. The process chain explores their optimum process windows, the high resolution of FIB direct structuring with both the high throughput and accuracy of the two replication technologies, to achieve cost-effectively FLSI within a single component.

Even though it is difficult to estimate the effects of different factors at the different stages of the process chain on its overall performance, the following ones are regarded as having the highest impact: the optimisation of the processing conditions of different component technologies, the material properties, in particular the materials' response to UV and thermal processing, the pattern generation strategy for 3D features implemented and the measurement uncertainty.

4.5 Summary and conclusions

A cost effective route for 3D structures' fabrication and for achieving FLSI in products was proposed and validated in this chapter. It integrates innovatively compatible and at the same time complementary structuring and replication technologies, operating at their considered optimum processing windows, to fabricate Ni shims incorporating different 2.5D and 3D length scale features. A complex 3D functional pattern was designed and generated as an executable data file by means of specially developed software. Utilising the unique patterning capabilities of the FIB technology a UV template was structured and then replicated on a larger area employing the S-FIL process. The resulting NIL imprints were utilised to produce a Ni shim for serial replication. As a final step in the proposed fabrication route the Ni shim was utilised as a master for hot embossing of an array of micro pyramids. This complex 3D functional structure was successfully and cost-effectively replicated. Thus, the proposed process chain can be considered a viable manufacturing route for achieving FLSI in existing and new emerging products, especially for producing components incorporating 2.5D and 3D features at micro and nano scale. In particular, based on the analysis of the results at each stage of the process chain, the following conclusions can be made:

1. The FIB milling technology with its capabilities for high resolution and accurate structuring of complex 3D features can be considered a viable component technology in process chains for achieving FLSI into a single component.

2. The implementation of this technology in master making process chains is well justified in applying its direct write capabilities to complement other structuring and replication processes.

3. The investigated manufacturing route is characterised with high flexibility that enables the cost-effective integration of technologies with complementary capabilities to produce tools for different high throughput replication processes.

4. The measurement error could lead to a significant impact on the results in the different stages of the process chain so it should always be accounted for and measurement strategies must carefully be considered and applied.

CHAPTER 5

METHODOLOGY FOR DEPTH PREDICTION IN LAYER-BASED FIB MILLING OF 3D FEATURES

5.1 Introduction

The realisation of complex 3D structures in micro and especially nano-scale manufacturing is of a major importance. Functional features like lenses and pyramids find applications in the field of electronics (Lee *et al.*, 2008), optical systems (Coquillat *et al.*, 2008; Paivanranta *et al.,* 2008) and micro-fluidic devices (Toepke and Kenis, 2005; Seo and Lee, 2004).

3D functional features that satisfy specific technical requirements related to lateral dimensions' accuracy, symmetry and cross-sectional profiles, can be obtained employing Focused Ion Beam (FIB) technology (Svintsov *et al.*, 2009). This technology offers many advantages with regard to achievable feature resolution, flexibility, good surface quality and capability to machine a wide range of materials (Svinsov *et al.,* 2009; Fu, 2001; Velkova *et al.*, 2010).

By employing a layer-based FIB machining it is possible to produce very precise complex 3D features (Svintsov *et al.*, 2009; Lalev *et al.*, 2008). In particular, 3D models of given functional features can be created in any CAD package and then, following a sequence of data processing and transfer operations, the 3D geometry is converted into a stack of layers, 2D cross-sections, ordered along one of the main axes

of the model. Then, after such a 'slicing' step, the model is transferred into the GDSII stream file format (Lalev *et al.*, 2008). Each GDSII layer represents a 2D cross-section of a feature at a given point along the slicing direction, usually the "z" axis. The number of layers used to define a given 3D structure can vary from several to few thousand. However, the selected number of layers is an important process parameter that affects directly the resolution of the produced structures, and also determines the error associated with the approximation of a given 3D geometry as a stack of 2D layers. Though the layer-based method is a reliable means for producing the desired 2D profile in the x-y plane, its accuracy in "z" direction is strongly dependant on the selected FIB processing parameters.

To improve the accuracy of the 3D layer-based FIB milling process it is necessary to identify processing windows and design machining strategies for achieving a better height/depth control. The aim of this research is to develop a reliable methodology for depth estimation in FIB machining. This is achieved through an investigation of the layer thickness variations with regard to exposure parameters in layer-based FIB milling of 3D features. An uncertainty assessment is also conducted to verify the process accuracy in z-direction.

5.2 Research methodology

To achieve the objective of this research it is necessary:

1) to investigate the interdependence between FIB process parameters and layer thickness deviations for a given material and geometry as well as their effects

on the resulting structures, especially their 'total' thickness/height, H, as illustrated in Figure 5.1a, according to:

$$H = \sum_{i=1}^{N_L} h_i \qquad (5.01)$$

where: N_L is the number of layers and h_i is the thickness of the i layer;

2) to identify processing windows with acceptable tolerance intervals in regard to layer thickness variations, U, in particular to assess the process uncertainty in achieving the targeted nominal value of h_i, and ultimately H of a given 3D feature, as illustrated in Figure 5.1 b;

3) to verify that it is possible i) to estimate accurately the height, H, of 3D features produced by layer-based FIB milling, and ii) to determine whether H is within a pre-determined tolerance interval for a given processing window.

These three main aspects that constitute the proposed research methodology are discussed in more details in the sub-sections below.

5.2.1 Effects of FIB process parameters on the layer thickness and the total feature thickness

When layer-based milling is applied, the relationship between the FIB process parameters can be expressed as:

$$D_A = \frac{I * t_{DWELL}}{S_S{}^2}; \left[\mu As/cm^2\right] \qquad (5.1)$$

where D_A is the area dose, I – beam current [pA], S_S – area step size [nm] and t_{DWELL} – area dwell time [ms]. t_{DWELL} is calculated using the expression

118

a)

Number of layers = 10

10.a

1.a

b)

Z

Expected Depth

U

0

X

U - Tolerance Interval
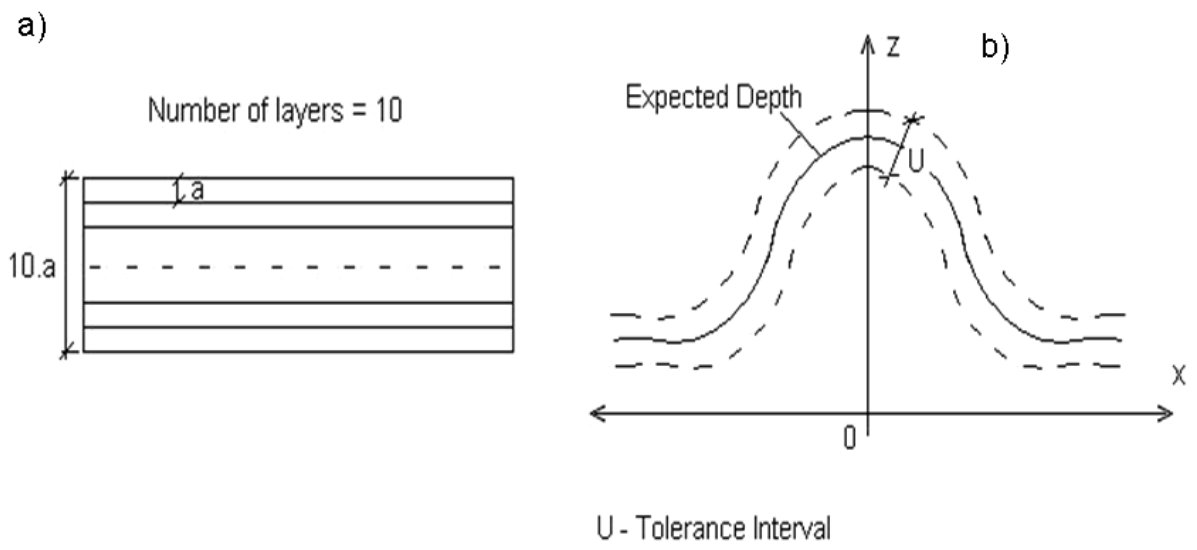
Figure 5.1 (a) layer-based FIB milling strategy and (b) thickness/height variation range

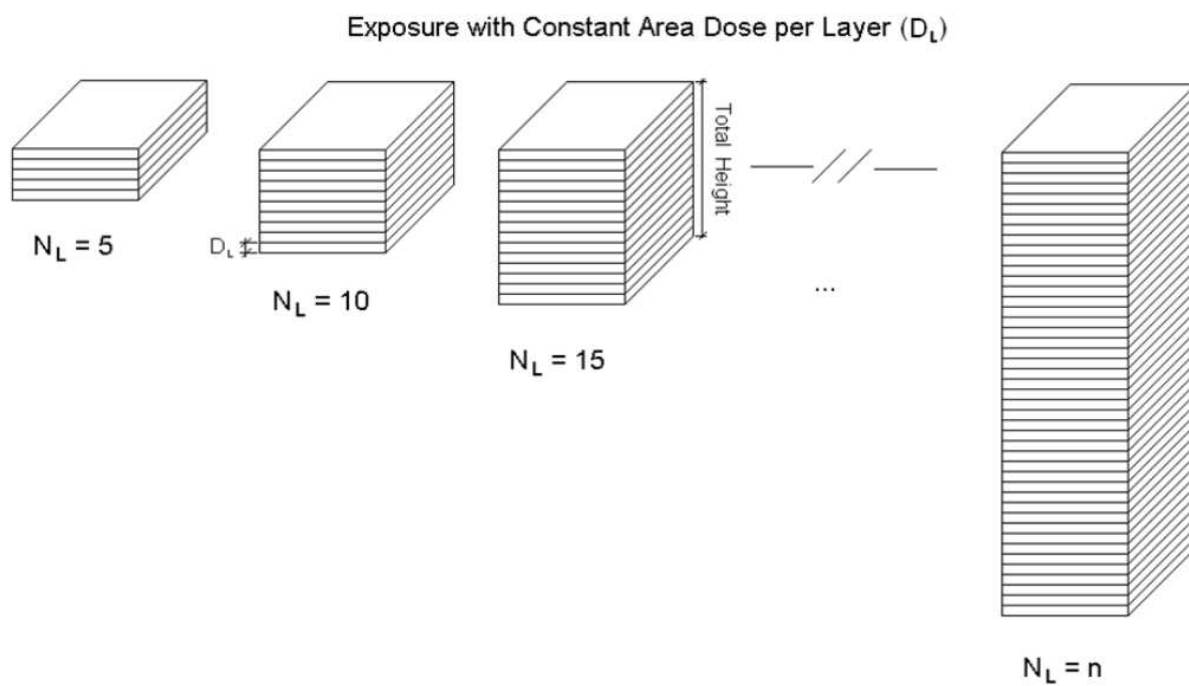Exposure with Constant Area Dose per Layer (D$_L$)

Figure 5.2 Constant D_L exposure approach to layer thickness determination

$$t_{DWELL} = d_t * F_d * N_L \qquad\qquad (5.2)$$

where d_t is the dwell time and F_d is the dose factor, usually $F_d = 1$.

If N_L is set to 1, the area dose expression gives the exposure dose per layer (D_L), and

hence the total dose is distributed uniformly through all layers:

$$D_L = \frac{I * d_t * F_d}{S_S^{\,2}}; \left[\mu As / cm^2\right] \qquad\qquad (5.3)$$

Assuming that all layers have the same thickness h for a given exposure setting, the

total height/depth H of a feature will be the sum of the thicknesses of all constituent

layers used to create it:

$$H = \sum_{i=1}^{N_L} h_i = N_L * h \qquad\qquad (5.4)$$

However, this statement is valid only if the effect of material re-deposition is not

taken into account or is considered to be negligible. As during FIB processing the re-

deposition is unavoidable, it can be expected that the relationship between H and N_L

will not be linear. Therefore, it is necessary to study the interdependence between the

exposure dose and h and thus to determine whether h can be considered constant for a

given material and for the selected dose. This can be investigated by conducting

experiments where features are exposed with the same D_L but different N_L is used to

produce them as illustrated in Figure 5.2. Preliminary tests indicate that the functional

dependence between H and N_L is as shown in Figure 5.3. Thus, by conducting a series

of experiments with N_L from the liner part of the graph, for different beam currents at

the same D_L, h of individual layers can be calculated through interpolation, and then compared.

Based on the outcome of such an experimental study, the effects of the re-deposition phenomenon on the resulting feature height can be studied. Especially, it is possible to investigate how H of a given structure would be affected by keeping D_A constant while changing N_L as shown in Figure 5.4.

5.2.2 Process uncertainty

To verify the value of h obtained for a given layer and determine the tolerance range within which h falls, i.e. the acceptable deviation of h from a given nominal value, the process uncertainty has to be studied.

The layer thickness, h_i, resulting at given process settings can be determined as the gradient in a regression fit of the linear part of the H to N_L relationship (Figure 5.3). An existing methodology for calculating uncertainty in a regression fit gradient can be utilised to determine the uncertainty associated with h_i (Kirkup, 1994). Also, as all H measurements are taken at the same SEM magnification it can be assumed that the standard uncertainty in height measurements is constant. Hence, the formula for calculating the combined standard uncertainty is:

$$u_c = \sqrt{\sum \left(\frac{\partial f}{\partial x_i} \right)^2 u^2(x_i)} \tag{5.5}$$

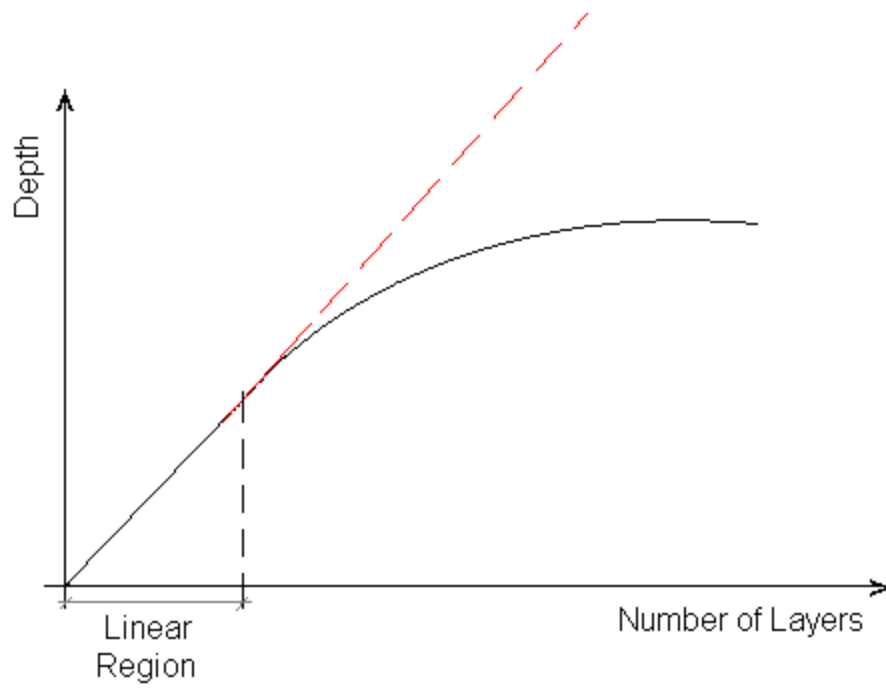where x_i is h_i in the context of this research, and thus the equation can be represented

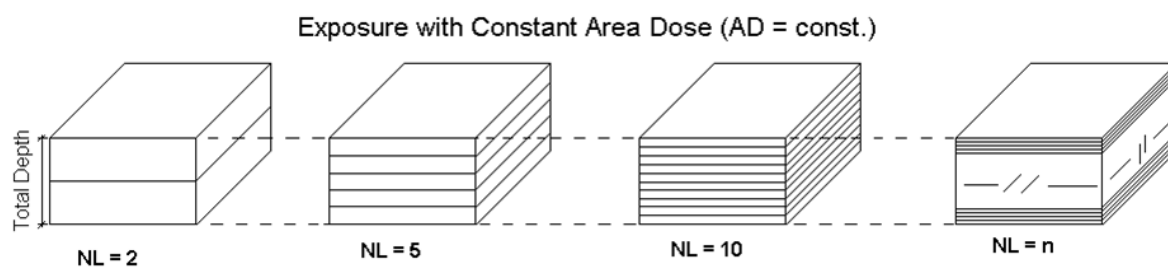Figure 5.3 The generic relationship between H and N_L

Figure 5.4 Determination of re-deposition effects at a constant area dose distributed in different N_L

as:

$$u_c(h) = \frac{u(H).n^{\frac{1}{2}}}{\left[n\sum N_{Li}^2 - (\sum N_{Li})^2\right]^{\frac{1}{2}}} ,$$ (5.6)

where N_{Li} represents the different values of N_L utilised in the experiments, n is the number of observed values, and

$$u(H) = \left[\frac{1}{n-2}\left(\sum (H_i - h_i N_L)^2\right)\right]^{\frac{1}{2}}$$ (5.7)

where H_i is the total thickness for the *i-th* N_L value.

Taking the obtained h_i values from the regression fits for each D_L, the thickness value, h, for a given dose (D_L) can be obtained as the mean value:

$$\bar{h} = \frac{\sum\limits_{i=1}^{n} h_i}{n} , [nm]$$ (5.8)

The uncertainty associated with the calculated h is the so-called expanded uncertainty, U, or the value of h can be expressed as:

$$h = \bar{h} \pm U , [nm]$$ (5.9)

The expanded uncertainty can be determined for a given confidence interval (CI) as follows:

$$U = k.u_c(h), [nm] ,$$ (5.10)

where: k is a coverage factor at certain confidence level for given degrees of freedom

125

ν_{eff}, usually for CI of 95%. Then, the effective degrees of freedom can be determined employing the Welch-Satterthwaite formula (Kirkup and Frenkel, 2006):

$$\nu_{eff} = \frac{u_c^4(h)}{\sum\limits_{i=1}^{n} \frac{c_i^4 u^4(h_i)}{\nu_i}} \tag{5.11}$$

where c_i is a sensitivity coefficient, $\nu_i = n-1$ for Type A uncertainty or $\nu_i = \frac{1}{2}\left(\frac{u(u)}{u}\right)^{-2}$ for Type B uncertainty, with $\frac{u(u)}{u}$ defined as proportional uncertainty in the Type B-evaluated uncertainty, u, and

$$u_c(h) = \sqrt{\sum\limits_{i=1}^{n}\left(\frac{\partial f}{\partial x_i}\right)^2 u^2(h_i)} \tag{5.12}$$

is the combined standard uncertainty, which includes the standard uncertainty of $\bar{h}$:

$$u(\bar{h}) = \sqrt{\frac{\sum\limits_{i=1}^{n}\left(h_i - \bar{h}\right)^2}{n(n-1)}} \tag{5.13}$$

and the measurement uncertainty $u(P)$, or

$$u_c^2(h) = u^2(\bar{h}) + u^2(P) \tag{5.14}$$

where $u(P)$ is taken as 3% of the measurand.

5.2.3 Verification procedure

To verify the proposed methodology for feature depth estimation, FIB milling of 3D test structures can be performed by varying D_L. The two different approaches for generation of 3D models discussed in Section 5.1 were applied. In the first case (Lalev *et al.*, 2008), the model was sliced in 61 layers, the maximum allowed by the Elphy Quantum lithography software while in the second one (Svintsov *et al.*, 2009) the number of layers was chosen to be 100.

5.3 Experimental set-up

A Carl-Zeiss XB 1540 FIB/SEM cross-beam system was employed to carry out the work required according to Section 5.2, especially to conduct the necessary layer-based FIB milling and then characterisation of the produced test features. Raith lithography hardware and software (Elphy Quantum) were utilised to control the FIB patterning externally.

To inspect the features' depth, FIB cross-sectional cuts with 50pA beam current were made and the depth profile was analyzed with the integrated SEM and its SmartSEM software. The vertical walls of all samples were imaged at 36 degree tilt and also to obtain correct measurements, the "tilt compensation" option of the SmartSEM software was applied. To minimise the measurement error all measurements were taken at the same magnification, and 10 kV electron beam energy. All experiments were carried out on a single crystal Si <100> wafer.

5.3.1 Interdependence between layer thickness and exposure dose

Two test features, rectangular trenches, referred to as F1 and F2 hereafter, with

dimensions 1 x 2 x 0.5 μm and 1 x 2 x 0.25 μm, respectively, were designed to investigate the resulting layer thickness after FIB milling. By utilising the approach described in (Lalev *et al.*, 2008) the CAD models were 'sliced' into stacks of layers. In particular, data files with different N_L were created, starting with N_L=5 and increasing to N_L=60 with an increment of 5. Each file was then used to expose a silicon workpiece with the same D_L under the same processing conditions. To keep D_L the same when exposing with different beam currents, d_t was adjusted according to Equation 5.1. Since the experiments were performed with three beam currents, namely 50 pA, 200 pA and 2 nA, d_t was set to 0.1 ms, 0.025 ms and 0.0025 ms, respectively. With F_d of 1 and S_S of 10 nm, D_L becomes:

$$D_L = \frac{50.10^{-6} * 0.1 * 10^{-3} * 1}{10^2 * \left(10^{-7}\right)^2} = 5 * 10^3 \, \mu As / cm^2$$

5.3.2 Interdependence between total thickness and number of layers

To be able to estimate the depth of a given structure, it is necessary to study the change in its total thickness as N_L increases. Therefore series of experiments were conducted adopting the exposure strategy in Figure 5.2. Several different D_L were selected, aiming at determining interdependences between H and N_L and drawing conclusions about the accuracy of the layer-based FIB milling process. To have some consistency with the previous experiments and assure the comparability of the results, the first area dose per layer, $D_L 1$, was selected to be the same as in Section 5.3.1 i.e. $5x10^3$ μAs/cm². With regard to exposure time/production efficiency the other doses were set to 50 % and 20 % of this D_L as follows:

$$D_L1 = 5x10^3 \, \mu As/cm^2,$$
$$D_L2 = 2.5x10^3 \, \mu As/cm^2,$$
$$D_L3 = 1x10^3 \, \mu As/cm^2$$

The same three different FIB beam currents, 50 pA, 200 pA and 2 nA, were applied in this experimental run, with d_t being adjusted again to keep the area dose per layer constant. Similar to the set of experiments, described in Section 5.3.1, F_d was 1 and S_S - 10 nm. The first exposure in these experiments was performed with N_L varying from 2 to 100, applying increment of 2 for layers 2 to 40 and increment of 5 for layers 45 to 100.

To carry out a proper statistical analysis of the obtained results, each experiment was repeated three times under the same working conditions. However, to reduce the number of experimental runs required, the number of layers was increased with a step of 10 layers for the second and third runs.

5.3.3. FIB milling of 3D features

To prove that layer-based FIB milling can be applied for producing complex 3D structures, a square concave pyramid with a 2 x 2 μm base and convex one with the same dimensions but placed in a 4 x 4 μm trench were selected as models for conducting this investigation. Models of the two test 3D features are depicted in Figure 5.5 a and b. The data file of the concave pyramid was created by applying the CAD-CAM approach (Lalev *et al*., 2008) while the convex one was generated using the IonRevSim software (Svintsov *et al.*, 2009). Beam current of 50pA was used to mill all features, except for the deepest convex pyramid, which was produced with 200 pA. To maintain the desired D_L, d_t was set to 0.02 ms, 0.05 ms and 0.1 ms for I=50 pA, respectively and 0.025 ms for I=200 pA.
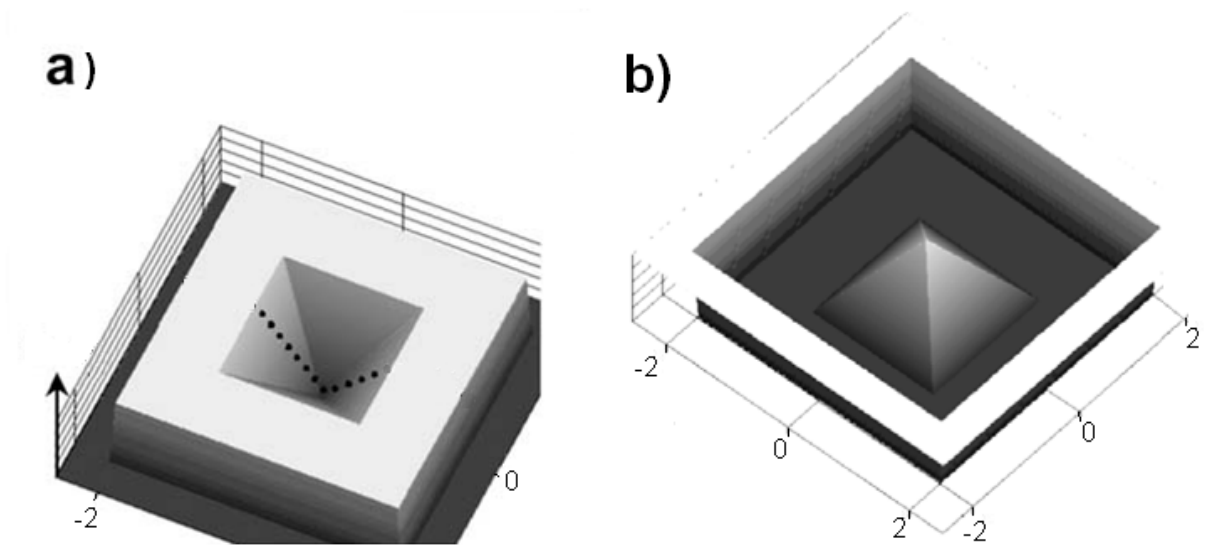
Figure 5.5 Models of the 3D test features' design: a) concave 2x2 μm square pyramid

and b) convex 2x2 μm square pyramid placed into a 4x4 μm trench

5.4 Results and discussions

5.4.1 Interdependence between layer thickness and exposure dose

The cross-sections of the milled structures, as shown in Figure 5.6, were analysed to determine the features' depths. Figure 5.7 shows a plot of the obtained depths as a function of N_L for the three beam currents selected in this study. It can be seen that H of the structures increases linearly with the increase of N_L. The slight deviations from linearity could be attributed to the human factor in conducting the measurements. If linear dependence between N_L and H is defined as $H = a + bN_L$, and $a = 0$ as H is 0 for N_L equal to 0 while b is h, the equation becomes:

$$H = N_L * h . \tag{5.15}$$

After applying a regression fit, the h values corresponding to each of the experimental settings were calculated. Also, the mean h for each I and the whole set of experiments were calculated for CI of 95% as shown in Figure 5.8.

The h values for each I and their respective uncertainties are provided in Table 5.1. The mean h for the three currents, 50 pA, 200 pA and 2 nA, is approximately 17 nm. The mean h obtained at I of 200 pA differs from the other two with approximately 6%. This could be attributed to measurement uncertainty and also some machine related factors such as the calibration accuracy and beam focussing. However, the data analysis performed at CI of 95% shows very good repeatability when the same D_A is applied at different I.

Also, experiments were conducted to investigate the re-deposition effects on the layer

Table 5.1 $\bar{h}$ of test features milled with different I.

Test Feature	50 pA	200 pA	2 nA
F1	17.7 (± 0.9) nm	16.2 (±0.5) nm	18.3 (±1.5) nm
F2	17.6 (± 1.0) nm	16.0 (±0.5) nm	17.6 (±1.6) nm

thickness. First, D_A for two selected feature depths of 500nm and 250 nm was determined. The targeted depth of 500 nm was achieved after milling of 30 layers, i.e. $H = N_L * h = 30 * 17 = 510 nm$, while 250 nm at 15 layers, $H = N_L * h = 15 * 17 = 255 nm$, as shown in Figure 5.9 a) and b), respectively. D_A is then:

$$D_A^{500} = D_L * N_L = 5 * 10^3 * 30 = 150 * 10^3 \left[\mu As / cm^2 \right]$$

$$D_A^{250} = D_L * N_L = 5 * 10^3 * 15 = 75 * 10^3 \left[\mu As / cm^2 \right]$$

As D_A is of a particular interest in these experiments and N_L is predefined, the only parameter that can be adjusted to compensate for any changes in N_L is d_t. Its value was adjusted for the different exposures so that D_A remained constant at all times. Figure 5.10 shows h for the test feature as a function of N_L for each of the selected three beam currents. The solid line represents the targeted h, the ideal case when the re-deposition effect is not taken into account. As it was expected, when D_A was not distributed into a sufficient N_L the resulting h is less than the targeted one. By increasing N_L the actual h is getting closer to the targeted one and eventually, above certain N_L, the two coincide. The results obtained for both features but especially for F2 in Figure 5.10 a) and b) show clearly that the re-deposition effect is stronger at lower I. This is due to the increase of d_t, applied to maintain D_A the same. The analysis of the re-deposition patterns at different I shows that it is possible to optimise the FIB milling parameters so that, for a given D_A, the effects of the re-deposition to be minimised by selecting a higher I, which will also lead to a shorter machining time. However, for both test features it was observed that the re-deposition could be considered negligible above a certain N_L for all I. It can also be seen in Figure 5.10
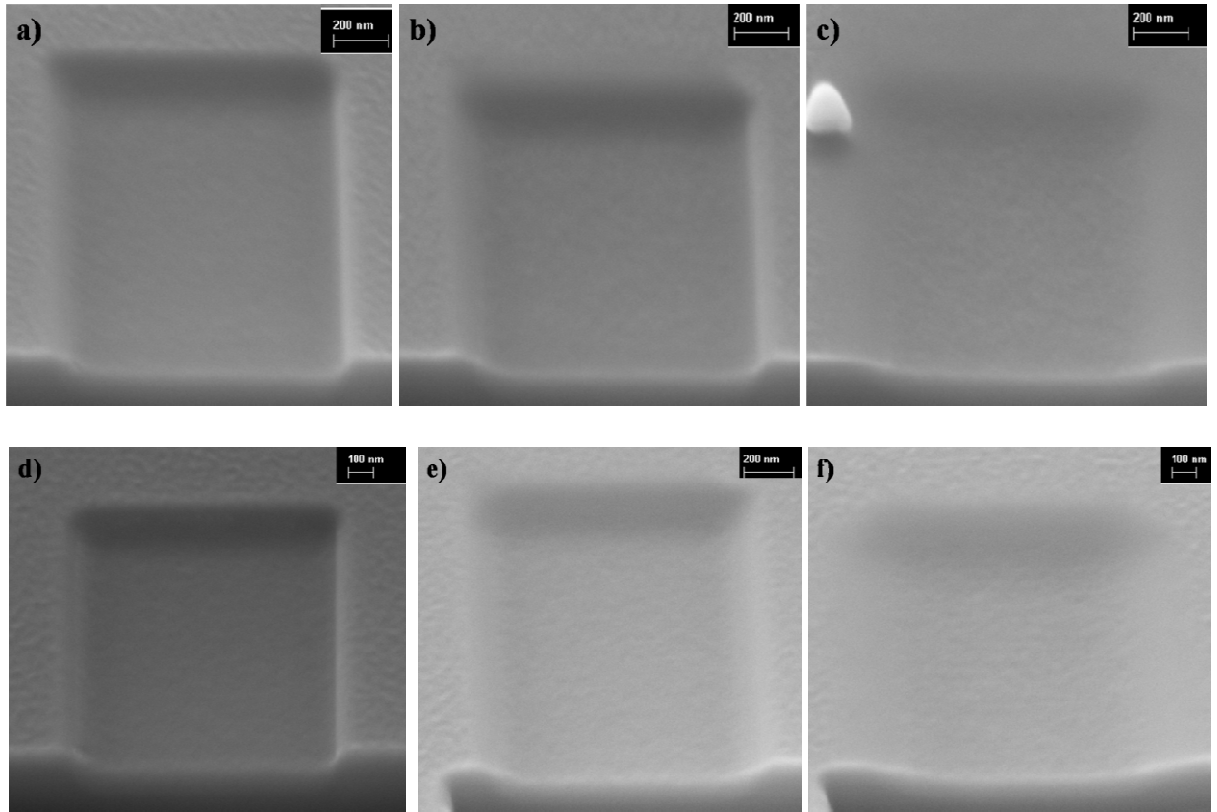
Figure 5.6 Cross-sectional profiles of test structures F1 and F2 milled with 50 pA – a) and d), 200pA – b) and e), and 2nA – c) and f), and N_L =5, respectively.
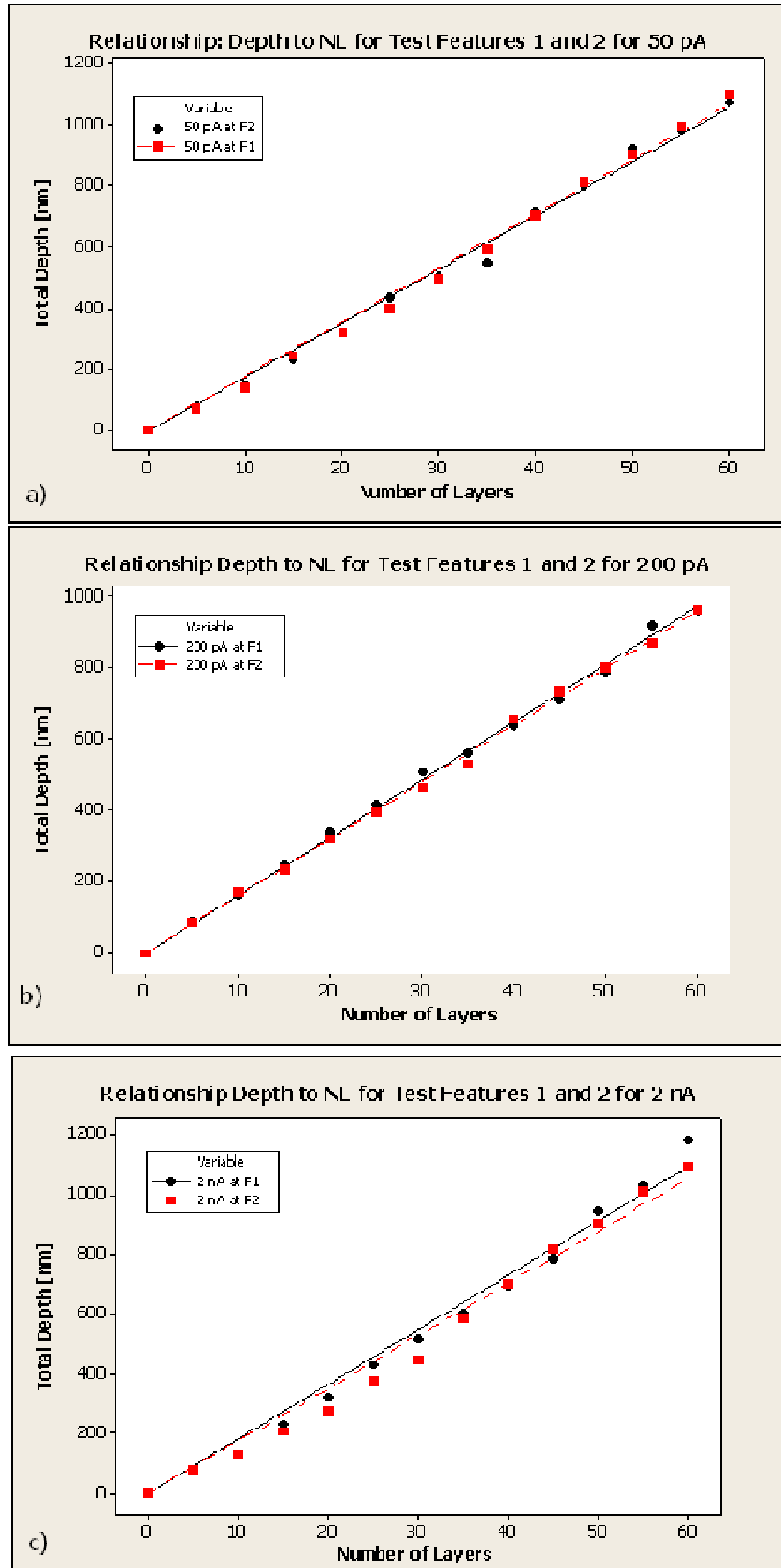
Figure 5.7 Relationship between H and N_L for test features 1 and 2 and a current of a) 50 pA, b) 200 pA, and c) 2 nA.

that for any given D_A there is always a value of h, i.e. critical layer thickness, below which the re-deposition can be considered negligible. For the Si samples used to conduct this empirical study the critical layer thickness is approximately 33 nm at D_A of $150*10^3$ µAs/cm^2 and around 19 nm at D_A of $75*10^3$ µAs/cm^2.

5.4.2 Interdependence between total thickness and number of layers

The results from the experiments discussed in 5.4.1 show that there is a tight margin between the calculated layer thickness and the h value at which the re-deposition cannot be considered negligible anymore. Therefore, a more detailed investigation is necessary in order to determine more precisely the value of h for a given D_L. Figures 5.11 and 5.12 depict the cross-sectional profiles of the trenches milled with different N_L and I, and the interdependence between H and N_L, for the three different D_L at the three currents utilised in this research, respectively. After performing regression fits the resulting h for each D_L were obtained using Equation 5.15 and their mean values were calculated for 95 % CI, based on the results from three runs carried out for each D_L. Figure 5.13 represents the $\bar{h}$ values obtained with I of 50 pA, 200 pA and 2 nA together with the total mean value of h for all currents at each D_L. The results from the experiments confirm that h is almost the same for the three different currents at each of the three investigated D_L. Also, the results suggest that h is proportional to the applied D_L, which could be used in selecting D_L for producing structures with a given depth.

5.4.3 Process uncertainty

The uncertainty in achieving a given h is calculated following the statistical approach outlined in Section 5.2.2. For the three different D_Ls, $\bar{h}$ and the uncertainties
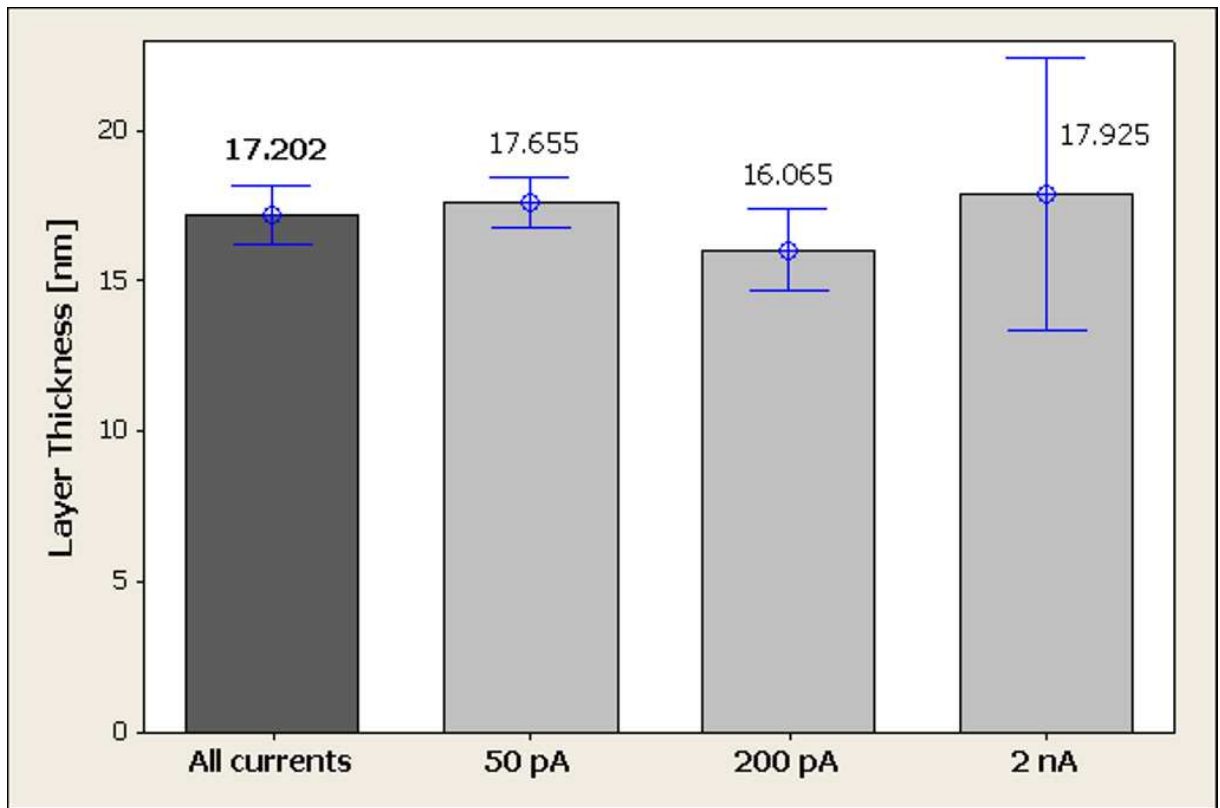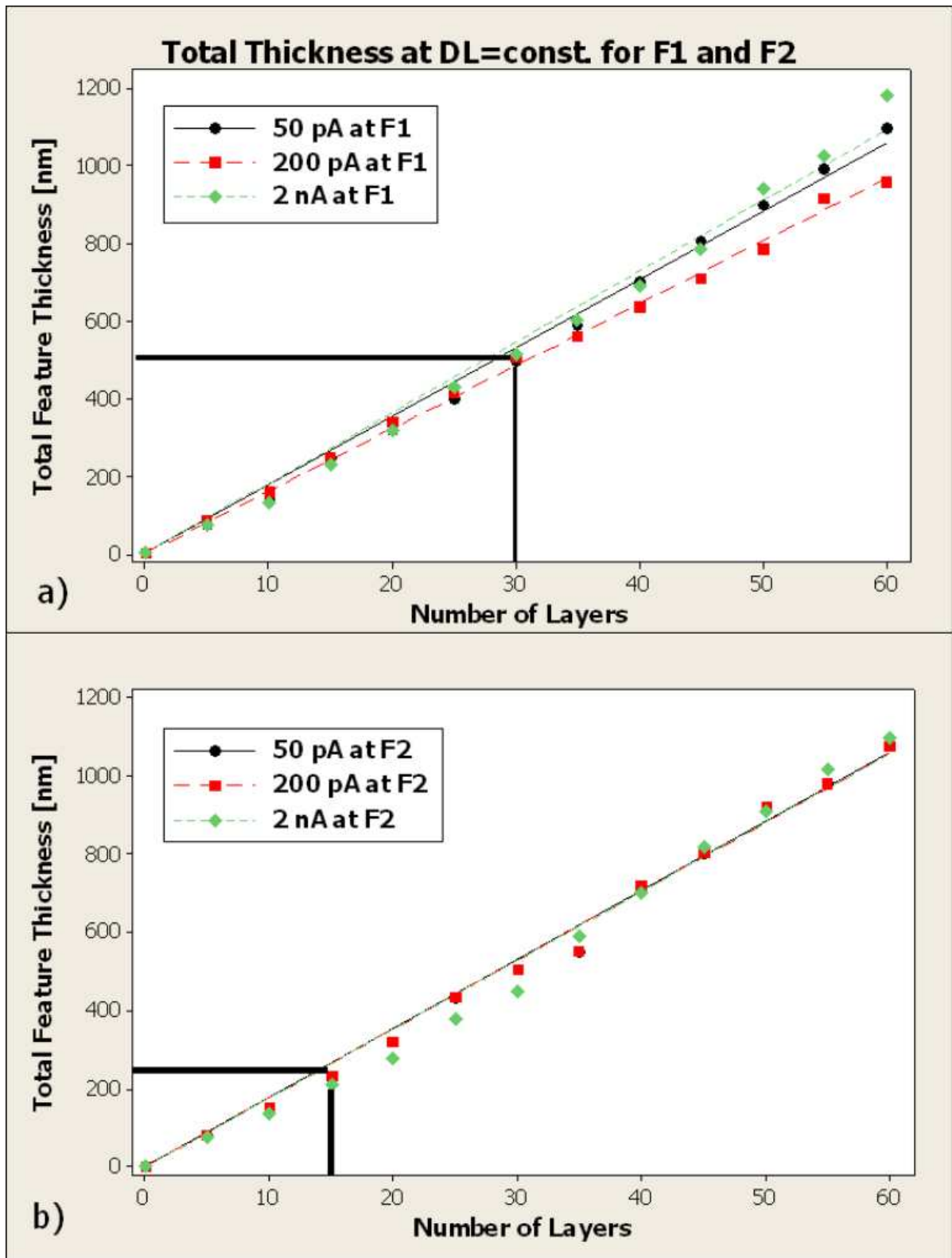
136

Figure 5.8 Mean *h* for CI of 95%

Figure 5.9 H at constant D_A for the three different currents a) test feature 1, and b) test

feature 2

$u(\bar{h}), u(P)$ and $u_c(h)$ were obtained as follows:

D_L 1: $\bar{h} = 15.6nm$, $u(\bar{h}) = 0.17nm$, $u(P) = 0.47nm$ and $u_c(h) = 0.5nm$

D_L 2: $\bar{h} = 7.9nm$, $u(\bar{h}) = 0.11nm$, $u(P) = 0.24nm$ and $u_c(h) = 0.26nm$

D_L 3: $\bar{h} = 3nm$, $u(\bar{h}) = 0.09nm$, $u(P) = 0.09nm$ and $u_c(h) = 0.13nm$

It should be noted that n is 9, as the experiments for the three doses were performed three times for the three different probe currents. The effective degrees of freedom, their respective coverage factors k at CI of 95% and the expanded uncertainties U for these three doses were calculated:

D_L 1: $\nu_{eff} \sim 620 \Leftrightarrow k = 1.98$ and $U = k.u_c(h) = 1.98x0.5 \approx 1nm$

D_L 2: $\nu_{eff} \sim 200 \Leftrightarrow k = 1.98$ and $U = k.u_c(h) = 1.98x0.26 \approx 0.5nm$

D_L 3: $\nu_{eff} \sim 35 \Rightarrow 30 \Leftrightarrow k = 2.04$ and $U = k.u_c(h) = 2.04x0.13 \approx 0.3nm$

Since $h = \bar{h} \pm U$, the values of h for the three doses are:

$$h_{D_L 1} = 15.6 \pm 1.0nm$$

$$h_{D_L 2} = 7.9 \pm 0.5nm$$

$$h_{D_L 3} = 3.0 \pm 0.3nm$$

Respectively, the uncertainty of h based on the first two sets of experiments, performed to investigate the interdependence between h and exposure dose for test features F1 and F2, is obtained as:
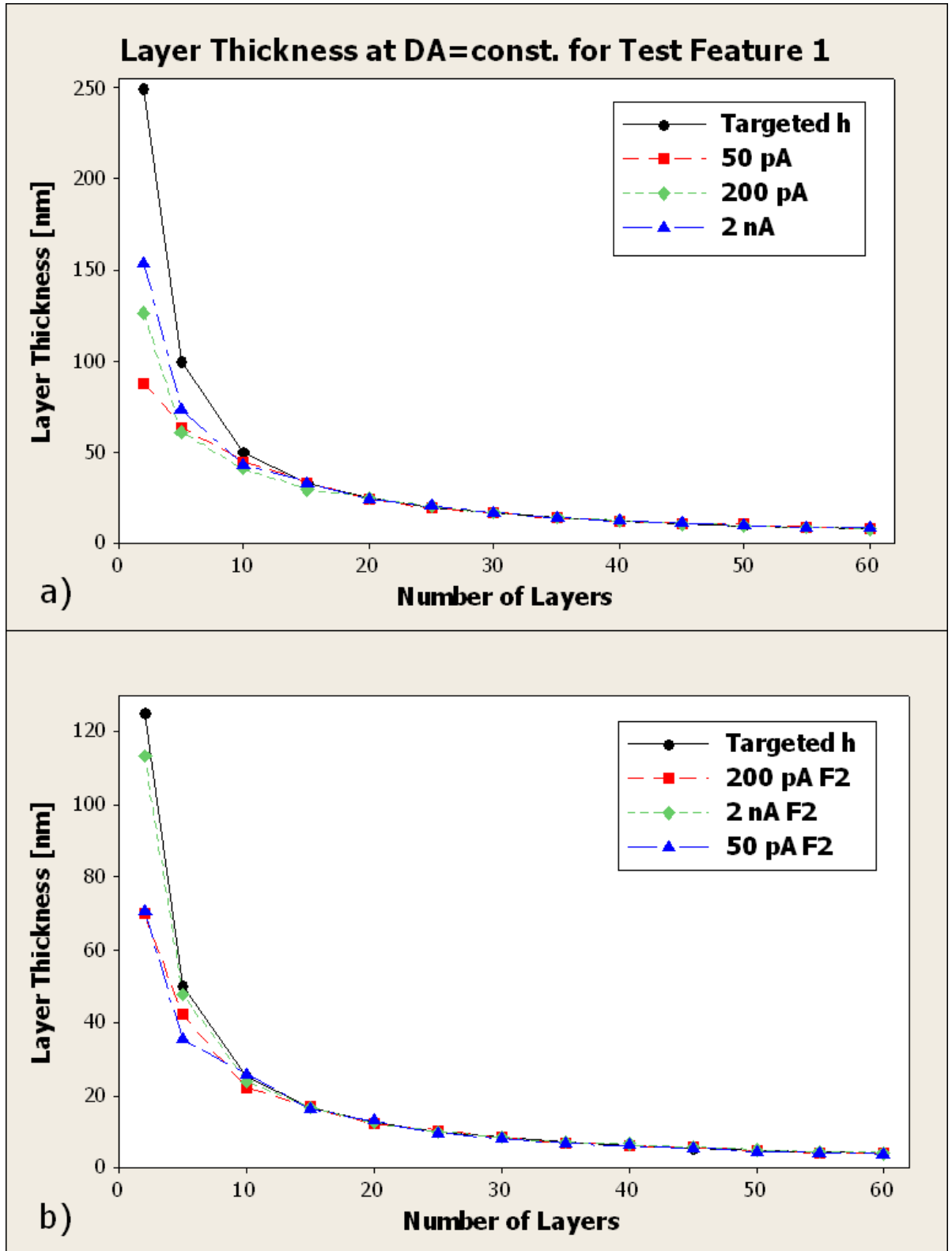
Figure 5.10 Layer thickness as a function of N_L for exposures with constant D_A of a) test feature F1, b) test feature F2, respectively.
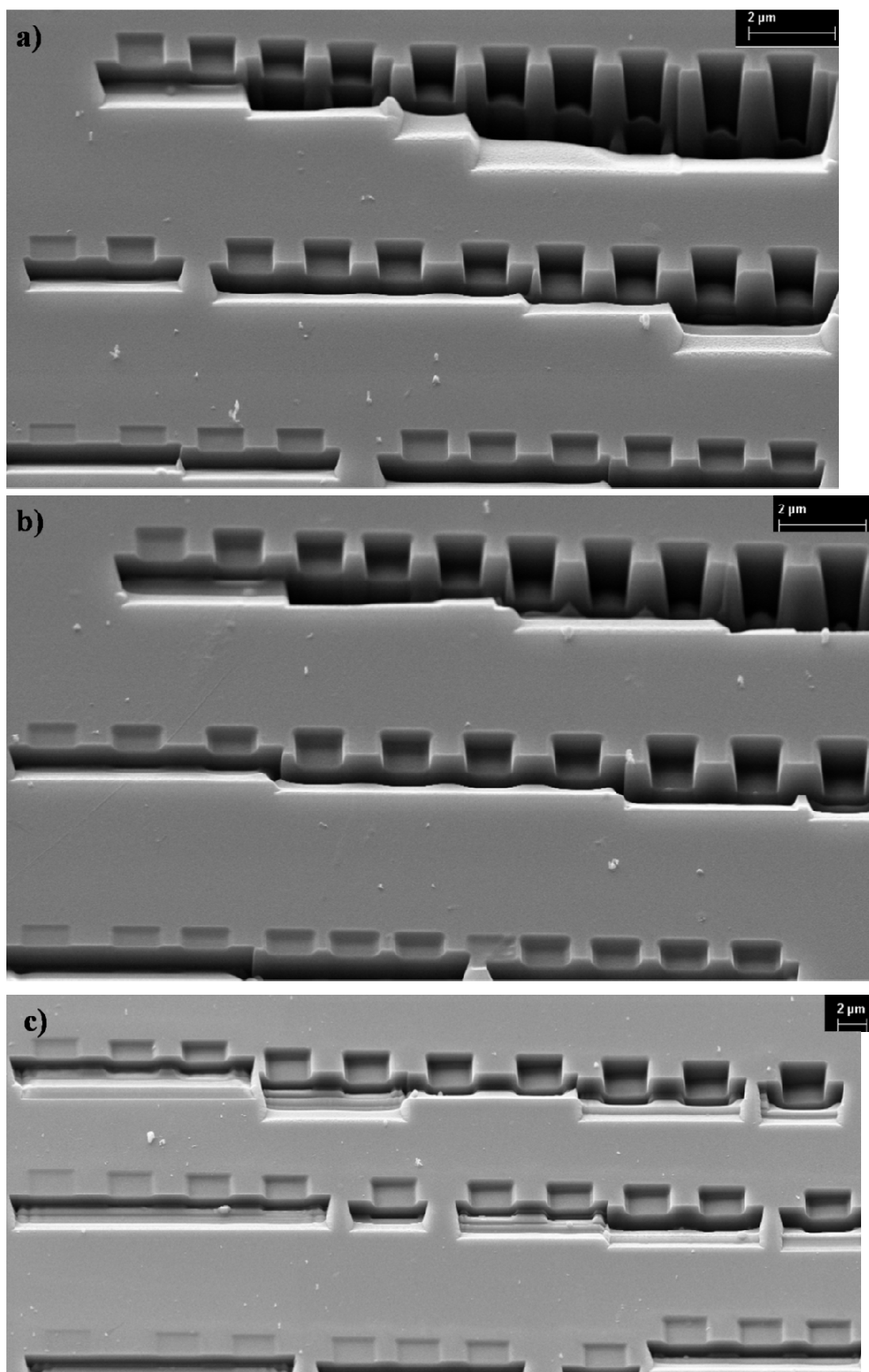
Figure 5.11 Cross-sectional profiles of test trenches milled with a) 50 pA, b) 200 pA

and c) 2 nA

$$U = k.u_c(h) = 2.02x0.64 \approx 1.29nm$$

where $n = 6$ as the experiments were performed for two doses at three different I and $v_{\bar{x}} = n - 1 = 6 - 1 = 5$. Then, $\bar{h}$, the standard uncertainty of $\bar{h}$, measurement uncertainty and the combined standard uncertainty were calculated: $\bar{h} = 17.2nm$, $u(\bar{h}) = 0.375nm$, $u(P) = 0.52nm$ and $u_c(h) = 0.64nm$, yielding $v_{eff} \sim 42 \Rightarrow 40 \Leftrightarrow k = 2.02$. Based on Equation 5.8 and using a rounded value of $\bar{h}$, $h = 17 \pm 1.3nm$.

For the experiments conducted at the three doses both h and its uncertainty are lower in magnitude because the bigger sample size allows us to determine more precisely both $\bar{h}$ and their tolerance intervals.

5.4.4 FIB milling of 3D features

Having determined the uncertainty associated with h for each dose, it is important to validate the results. Especially, it is necessary to verify that the deviation from the targeted total depth of the 61-layers' and 100-layers' pyramids is in the range of $\pm 61*U$ and $\pm 100*U$ [nm], respectively. Figure 5.14 and Figure 5.15 show the cross sectional profiles of the milled 3D structures. The calculated H of the features and the expected deviations of H, together with the measured actual H are provided below. Also, the deviation of the actual from the estimated value of H in percentage is calculated.
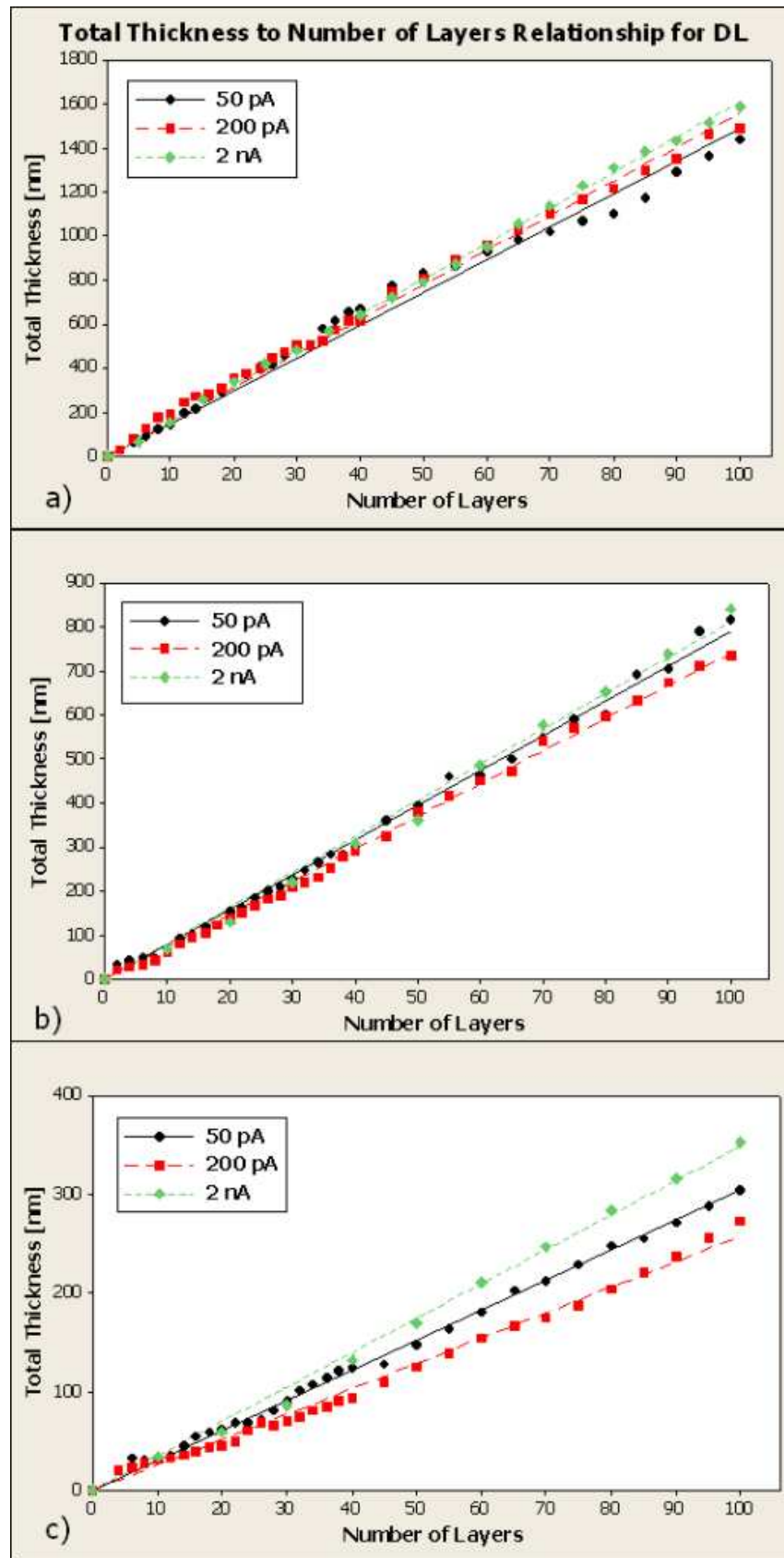
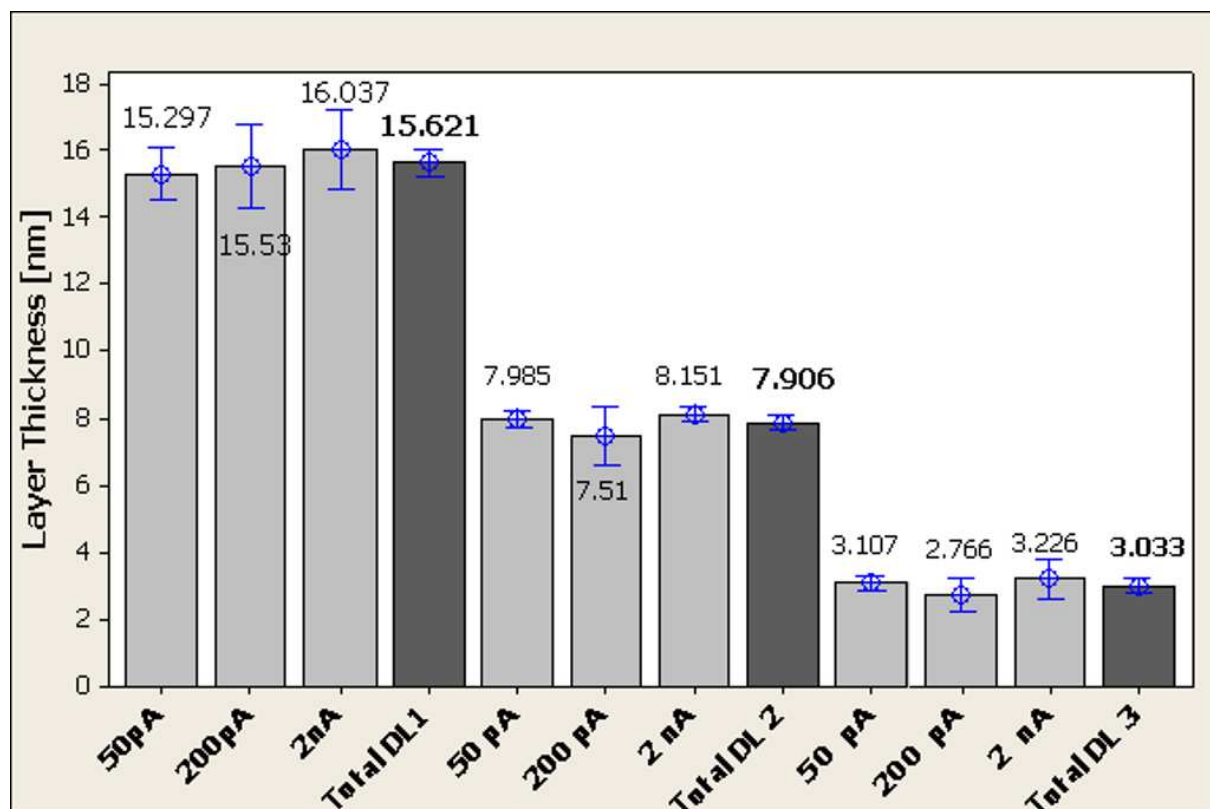Figure 5.12 Interdependence between H and N_L for the three different I at a) D_L 1, b) D_L 2, and D_L 3.

Figure 5.13 Mean layer thickness for 95% CI for $D_L 1$, $D_L 2$ and $D_L 3$.

Concave pyramids

D_L 3 (Figure 5.14a): calculated H-183 ± 18.3nm; actual H-178.7nm; deviation - 2.4%.

D_L 2 (Figure 5.14b): calculated H-481.9 ± 30.5nm; actual H-472.1nm; deviation - 2%.

D_L 1 (Figure 5.14 c): calculated H -951.6 ± 61nm; actual H-902.9nm; deviation - 5%.

Convex pyramids

D_L 3 (Figure 5.15 a): calculated H-300 ± 30nm; actual H - 307.8nm; deviation - 2.6 %

D_L 2 (Figure 5.15 b): calculated H-790 ± 50 nm; actual H - 766.5 nm; deviation - 3 %.

D_L 1 (Figure 5.15 c): calculated H-1560 ± 100nm; actual H-1489nm; deviation-4.6 %.

It can be seen that the actual H of all features are within the estimated range and their deviations are within 2 to 5%. As can be expected the deeper structures, i.e. the structures with bigger h and also those milled with higher doses, tend to deviate more from the estimated values. However, an increase of N_L leads to a better resolution.

In addition, the analysis of the produced 3D features revealed that even though two different approaches were utilised to generate the data for the layer-based FIB machining, the features' actual H was well within the estimated variations from the nominal values, and also the features exhibited similar patterns in terms of deviation from the targeted H. This demonstrates the viability of the layer-based FIB milling methods and also that it is possible to assess accurately the uncertainty associated with the process.

5.4.5 Generic methodology for depth estimation in layer-based FIB milling

Based on the conducted empirical study, the following generic methodology is proposed for optimising the layer-based FIB milling technology when processing different materials, especially to be able to estimate accurately the layer thickness and
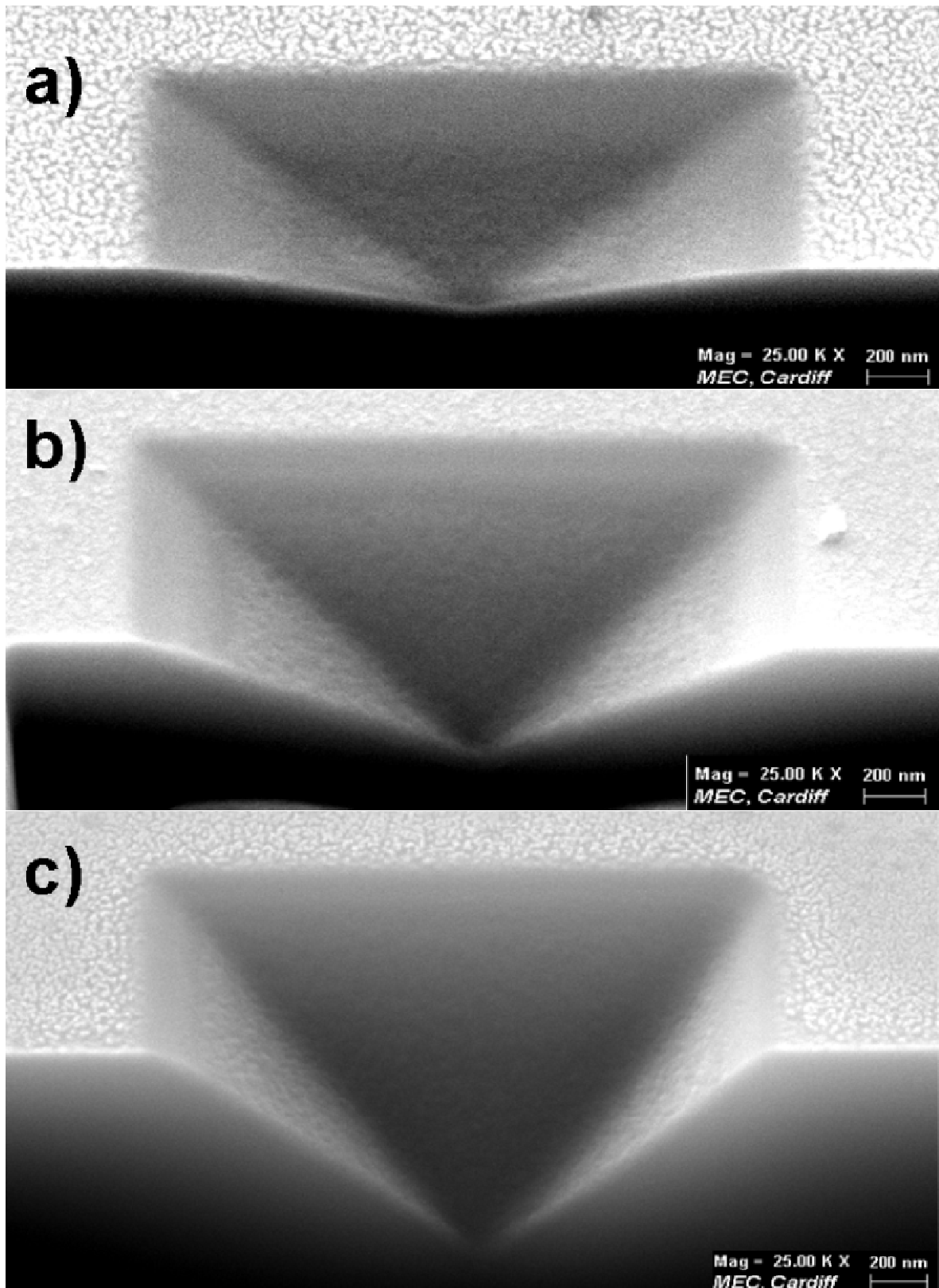
Figure 5.14 Concave square pyramids with 2x2 μm base produced by FIB milling of

61 layers with a) D_L 3, b) D_L 2 and c) D_L 1.

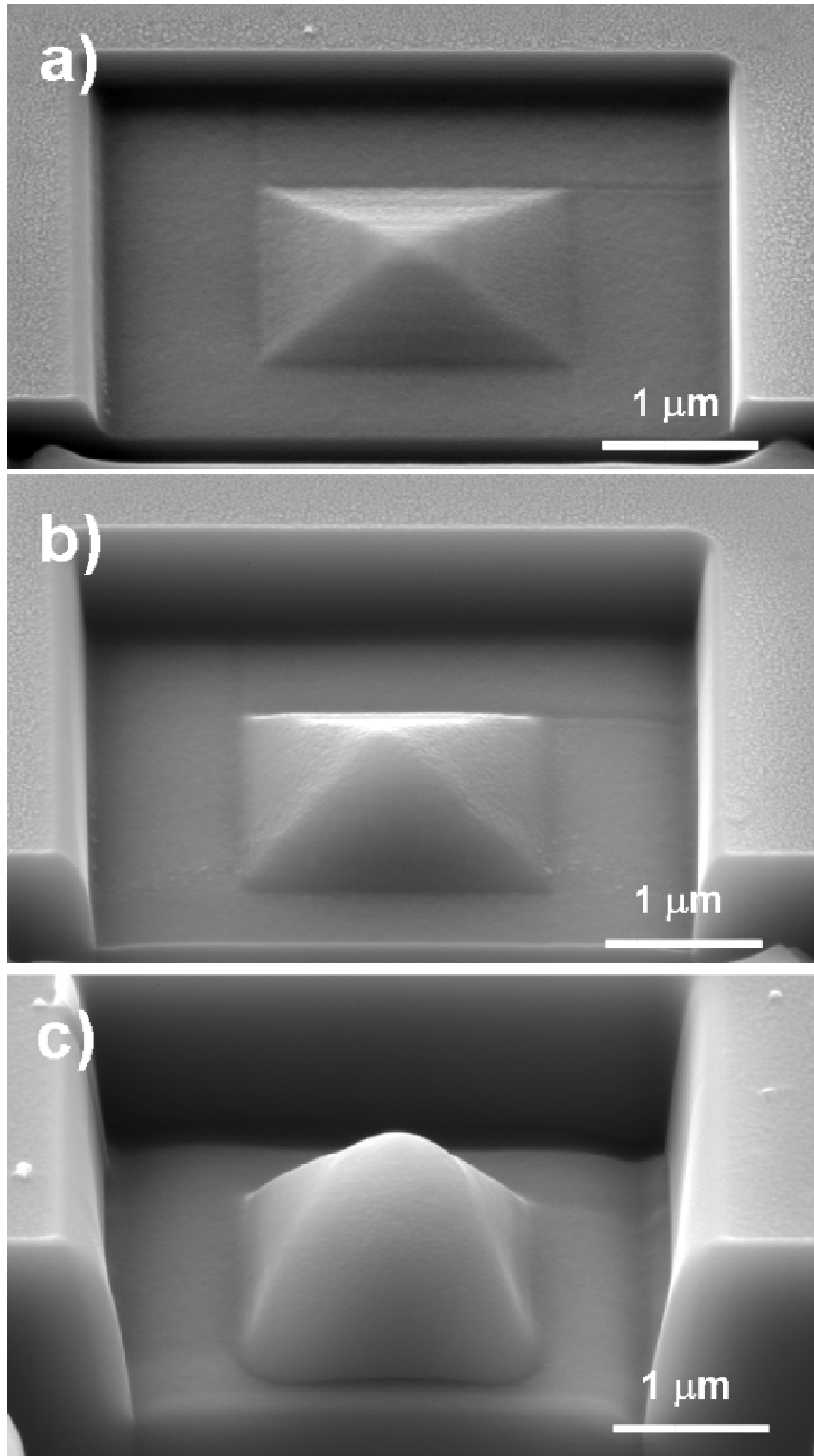Figure 5.15 Convex square pyramids with 2x2 μm base in 4x4 μm trenches, produced by FIB milling of 100 layers with a) D_L 3 with $H = 307.8$ nm; b) D_L 2 with $H = 766.5$ nm and c) D_L 1 with $H = 1489$ nm.

height/depth of complex 3D structures:

1. The (individual) layer thickness for simple 2.5D geometry is established as a function of the selected FIB process parameters. The layer thickness is determined as the gradient in a regression fit for the linear part of a total thickness / number of layers plot.

2. The tolerance intervals related to the thickness of a single layer and a stack of layers are calculated and assessed employing the approach described in Section 5.2.2.

3. Milling of test 3D features applying the selected process parameters is used to verify the calculated thickness values and selected doses.

Such a generic approach can be applied as a simple and systematic way for designing the process, especially finding its optimum processing windows, i.e. number of layers and area doses, when producing complex 3D structures by layer-based FIB milling.

5.5 Summary and conclusions

To improve the 3D layer-based FIB milling process it is necessary to identify the best processing windows and design appropriate machining strategies in order to achieve the targeted accuracy, particularly in "z" direction (i.e. height/depth). For that reason, in this chapter of the thesis a methodology for depth estimation in FIB machining was developed and validated. The layer thickness variations were investigated with regard to exposure parameters in layer-based FIB milling of 3D features. The methodology was verified by FIB machining of functional 3D features, which depths/heights fall within predetermined tolerance intervals. The results demonstrate the viability of this approach. In particular, the validation study showed that depths/heights deviations of

complex 3D structures were well within the estimated values. Several main conclusions are drawn based on the carried out research, in particular:

1. The layer thickness, h, and its tolerance interval are proportional to the D_L applied. The total depth/height, H, increases linearly when the number of layers, N_L, increases to a certain point where re-deposition can no longer be considered negligible. The effects of re-deposition are stronger for D_A exposures with lower I and higher dwell time. However, they can be minimized by exposing given area dose with higher number of layers.

2. The achieved Hs when milling 3D features were within the estimated range and their deviations were only 2 to 5%. Also, the deeper structures, i.e. the structures with bigger h and as well as those milled with higher doses, deviated more from the estimated values. The FIB machining of 3D features, carried out to validate the methodology, supported again the observation that milling with higher number of layers should be used to produce features with a better resolution.

3. The proposed generic methodology can be applied as a simple and systematic way for finding optimum processing windows, i.e. number of layers and area exposure doses, when producing complex 3D structures by layer-based FIB milling. It represents an important step in broadening the use of this technology for micro and nano structuring.

CHAPTER 6

FIB MILLING OF DIFFERENT AMORPHOUS AND SINGLE-CRYSTAL MATERIALS

6.1 Introduction

In the master making process chains that use FIB milling as a component technology, the structuring with FIB is usually carried out on Si wafers (Velkova *et al.*, 2010; Scholz *et al.*, 2009). As the fracture toughness and fatigue strength of Si is not sufficient to utilise it directly for producing replication masters, the patterns of the wafers have to be transferred into another material that is more appropriate for high throughput serial manufacture. To realise such pattern transfers several other processing technologies have to be employed, which adds up more steps in the process chains and thus increases the cost and uncertainties associated with the end products. This undesirable increase of manufacturing complexity can be avoided by performing direct FIB structuring of the masters. However, to create the necessary prerequisites for such direct FIB machining, it is essential to investigate the material response of various tooling materials to ion beam sputtering in order to be able to produce accurately the targeted 3D structures.

The machining response of materials is very important for the successful integration of micro and nano structuring technologies like FIB milling, laser ablation and photolithography (Velkova *et al.*, 2010; Dimov *et al.*, 2006; Velkova *et al.*, 2011 a)

150

into cost-effective master making process chains. Therefore, the search for and implementation of a wider range of materials proves to be increasingly viable (Stanishevsky, 2001). Especially, the use and processing of amorphous alloys have attracted considerable interest due to their superior properties for a number of applications (Inoue, 2000; Zhang *et al.*, 2006). Properties like high hardness, fracture toughness and fatigue strength make those materials appropriate for manufacturing of micro-electro-mechanical systems (MEMS) and micro-sensor systems (X. Wang *et al.*, 2007). Additionally, due to their homogeneous microstructure, lacking lattice defects and grain boundary (Kawasegi *et al.*, 2006), they are considered promising tooling materials for micro and nano- structuring and replication. Therefore, it is of a major importance that their non-crystalline microstructure is maintained during machining, especially when producing components incorporating micro and nano features (Quintana *et al.*, 2009; Minev *et al.*, 2010). Studies on FIB milling of amorphous and polycrystalline Ni-alloys showed that a higher surface integrity could be achieved in the amorphous material under identical processing conditions (Li *et al.*, 2007). Thus, the FIB technology can be used as a means for structuring amorphous alloys at sub-micrometer and nano- scales. However, to apply this technology successfully it is necessary to investigate the process-material interactions in order to be able to produce structures accurately at these scales, especially in the vertical direction. In this context, the research in this chapter develops further the methodology for depth estimation in FIB milling presented in Chapter 5, and implements it to minimise uncertainty in structuring different amorphous materials.

The main objective of the research reported in this chapter is to obtain 'material milling' coefficients for several commercially available amorphous and single crystal

materials that would relate their machining response, machinability, to a benchmark material. This would facilitate not only the estimation of a feature's total depth obtained for a certain material with a given set of process parameters, but also, and most importantly, the production time necessary for obtaining the targeted depth in the selected material. Those coefficients are to be derived with regard to silicon as a benchmark material. The fact that Si <100> is the most commonly used material in microelectronics, and is therefore usually given as a default material in the databases of parameters calculation modules of the FIB, EB and other lithography machines, justifies its selection as a benchmark in this research.

6.2 Theoretical background

6.2.1 Milling rates

The material properties of the workpiece are a key factor affecting the machining results and process predictability in FIB milling. The primary parameter affecting the depth of the machined structures and their accuracy in the direction normal to the machined surface is the sputtering rate/yield of the exposed material (Catalano *et al.*, 2006; Tseng, 2004; Kim *et al.*, 2007 a). However, even if its exact value is known the milled depth usually differs from the estimated one due to effects such as ion implantation and re-deposition of sputtered material. Also, it is important to note that the modules for milling depth calculations of commercially available FIB pattern generators use Si as a default material. However, their databases can include the milling rates for other materials, provided that they are known.

In general, the milling rates account for the sputtering rate and the effects mentioned above, therefore being very difficult to derive accurately. To avoid complex

calculations and minimise the errors in specifying the applicable milling rates for other materials, especially alloys, those milling rates can be expressed in terms of another one already stored in the FIB database, i.e. as a percentage of the Si milling rate. This would provide a much simpler and at the same time very effective depth estimation approach for FIB milling of different materials. This can be realised by relating the milling rates of other materials to that of Si through the use of a material specific constant, C_f, as follows:

$$MR_M^r = C_f * MR_{Si} \tag{6.1}$$

where MR^r_M is the milling rate of a given material and MR_{Si} is the milling rate of Si. The layer-based methodology that was developed in Chapter 5 for estimating the total depth, H, of FIB milled structures will be used to find empirically C_f for the materials considered in this research.

6.2.2 Materials' constants

The relationship between the total depth, H, and the individual layer thickness, h, for any material, M, can be expressed as:

$$H_M = h_M * N_L, \tag{6.2}$$

where N_L is the number of layers, H_M and h_M are the total depth and layer thickness for the given material (Lalev *et al.*, 2008), respectively. For Si the equation becomes:

$$H_{Si} = h_{Si} * N_L \tag{6.2.1}$$

In order to express H_M relative to Si, and taking into account that N_L is the same for all materials in this study, equation (6.1) can be expressed as follows:

$$H_M = \frac{h_M}{h_{Si}} H_{Si} \qquad (6.3)$$

Differentiating equation (6.3) over time, t, would provide the relative milling speed (relative milling rate) for a given material M:

$$\frac{\partial H_M}{\partial t} = \frac{h_M}{h_{Si}} * \frac{\partial H_{Si}}{\partial t} \qquad (6.4)$$

Since the milling rates, usually expressed in [$\mu m^3/\mu As$], are inversely proportional to the time [s] it can be stated that the time necessary to mill a given depth H into a material M will be h_{Si}/h_M times the time needed to achieve the same depth in Si. Therefore, the introduction of a material constant $C_f = h_M/h_{Si}$ for other materials in relation to Si would facilitate the accurate depth calculation for these materials. Also, the inverse value of this constant $C_t = 1/C_f = h_{Si}/h_M$ would allow for the estimation of the total milling time.

However, it is important to stress that this approach can be applied only under the assumption that the linear part of the functional dependence between H and N_L is considered, where the effects of the material re-deposition phenomenon are regarded as negligible (Velkova *et al.*, 2011 b).

6.2.3 Simulation and modelling

To verify the constants obtained for the investigated materials a series of simulations were carried out. Simulation software specially developed for FIB (Svintsov *et al.*, 2009) and multi-ion beam (Zaitsev *et al.*, 2009) applications, IonRevSim, was employed to account for some FIB milling specific effects such as the angular-dependency of the sputtering rate. The software models the FIB sputtering process as an isotropic local etching (Svintsov *et al.*, 2009; Zaitsev *et al.*, 2009). This modelling approach allows a variety of FIB milling parameters such as sputtering sensitivity (sputtering rate), number and shape of strata (layers), exposure step size, dwell time and beam diameter to be taken into account when simulating the 3D ion sputtering process.

6.2.4 Materials' response to FIB milling

As discussed in Chapter 2, in FIB processing the structural state of the material is of high importance. For example, polycrystalline materials exhibit significant grain anisotropy leading to non-uniform ion etching and material re-deposition. At the same time this phenomenon is not observed in mono-crystalline materials such as Si and alumina which are utilised for electron and ion patterning.

Unlike crystalline materials the amorphous ones, e.g. bulk metallic glasses (BMG), do not have a long-range atomic ordering. That is the reason for their identical machining response, irrespective of the incidence direction of the particle beam.

For metallic glasses with high metalloid concentration the electronic transport is dominated by s-like nearly free electrons, resulting in dramatic changes of

transportation properties of these alloys compared to their crystalline counterparts (Li *et al.*, 2007; Ivkov *et al.*, 1989). Thus, in amorphous metals, the energy dissipation during the ion exposure is minimised, leading to an increase in the sputtering yield. Furthermore, a higher surface integrity of the machined micro and nano-structures can be achieved in the non-crystalline materials because of the absence of any crystalline defects.

6.3 Experimental set up

A Carl-Zeiss XB 1540 FIB/SEM cross-beam system was employed to carry out the FIB milling experiments with Ga^+ ions, and then to characterise the produced test structures. Raith lithography hardware and software, Elphy Quantum, were utilised to control the FIB patterning externally. To inspect the depth of the machined features, FIB cross-sectional cuts with 50 pA beam current were made and the depth was measured with the integrated SEM and its SmartSEM software. The vertical walls of all samples were imaged at 36 degree tilt and also, to obtain correct measurements, the "tilt compensation" option of the SmartSEM software was utilised. After a calibration with a reference sample applying the Carl-Zeiss standard procedure, the measurement error of the instrument in XY direction was calculated to be in the range 1 to 3 %. Six commercially available amorphous materials were investigated: Cobalt (Co) – $Co_{70}(SiB)_{23}Mn_5(MoFe)_2$, in as received amorphous state and after explosive treatment (Co*), Iron (Fe) – $Fe_{81}B_{13.5}Si_{3.5}C_2$, Nickel (Ni) – $Ni_{78}B_{14}Si_8$, Titanium BMG - $Ti_{42}Zr_{24}Co_{16}Ni_{15}Be_4$, Quartz (fused silica - SiO_2), and also single-crystals Si <100> and Alumina Al_2O_3. Except for the Ti alloy that was obtained from Liquidmetal[R] Technologies USA, the rest were commercially available materials supplied by Goodfellow Ltd. The composition, designation, structural state and some relevant

properties of these materials are summarised in Table 6.1.

6.3.1 Layer thickness

A square pocket with a 3x3 μm base was used as a test structure to determine the layer thickness of the selected materials. Following the layer depth estimation methodology, FIB milling was carried out by applying a constant area dose per layer (D_L) while increasing the number of layers (N_L). To minimise the effects of stochastic factors in calculating the h values three different D_Ls were used, namely:

$$D_L 1 = 2*10^3 \, \mu As / cm^2$$
$$D_L 2 = 4*10^3 \, \mu As / cm^2$$
$$D_L 3 = 6*10^3 \, \mu As / cm^2$$

The number of layers utilised in the consecutive exposures was as follows: N_L = 20, 40, 60, 80, 100, 120 and 150 while the area step size and the dose factor parameters were kept constant at 10 nm and 1, respectively. 2nA beam current was used during the FIB milling and the dwell time was adjusted to 0.001 ms for $D_L 1$, 0.002 ms for $D_L 2$ and 0.003ms for $D_L 3$, respectively, to account for the different D_Ls during the experiment. To analyse statistically the obtained results, the exposures were repeated three times for each material under the same working conditions.

The verification of the calculated h that is necessary according to the applied methodology, requires complex 3D features to be machined and their measured height/depth, H, to be compared to the estimated ones, $H_{est} = h * N_L \pm U$, where U is the tolerance interval. To conduct this experimental verification, a convex square

Table 6.1 Composition and properties of the investigated materials (Callister, 2003)

Material	Short designation	Structure	Mismatch between the atoms (molecules) of a given material and Ga	Tm, [°C]
Al_2O_3	Al_2O_3	single crystal	1.46	2072
$Fe_{81}B_{13.5}Si_{3.5}C_2$	Fe	amorphous	0.80	1538
$Co_{70}(SiB)_{23}Mn_5(MoFe)_2$	Co[*]	amorphous explosive treatment	0.84	1495
$Ti_{42}Zr_{24}Co_{16}Ni_{15}Be_4$	Ti	amorphous	0.68	1668
$Co_{70}(SiB)_{23}Mn_5(MoFe)_2$	Co	amorphous	0.84	1495
$Ni_{78}B_{14}Si_8$	Ni	amorphous	0.84	1455
Quartz (SiO_2)	SiO_2	amorphous	0.86	1650
Si <100>	Si	single crystal	0.40	1410

[a]: Mismatch between the atoms (molecules) is calculated by dividing Atomic (molecular) mass of the target material, e.g. Co Alloy, by the Ga (ion beam material) atom mass; Tm – melting temperature.

pyramid with a 2x2 µm base placed in a 4x4µm square pocket (Figure 6.1) was milled in each material, applying the three different D_Ls. The data file necessary to machine these pyramids was generated employing the IonRevSim software (Zaitsev *et al.*, 2009) and implemented applying N_L=100 and area step size of 10nm. The currents used in these trials were 50 pA and 200 pA with dwell times adjusted accordingly to maintain the desired D_L.

6.3.2 Materials' constants

To verify the obtained material constants for the considered materials series of simulation studies were performed employing the design and simulation modules of the IonRevSim software (Svintsov *et al.*, 2009; Zaitsev *et al.*, 2009). The 3D structure that was used to conduct these studies was defined utilising the IonRevSim design module. Then, the exposure data as a set of layers were transferred into GDSII format for a direct use as an input to the Elphy Quantum software. The layers were automatically ordered for machining the targeted 3D test structure.

The simulations were performed using the following processing conditions: stratification mode, bottom-top exposure approach (Svintsov *et al.*, 2009), beam current 2 nA and 200 pA, dwell time 0.001 ms and 0.01 ms, area step size 10 nm, number of strata =100, i.e. an exposure of 100 layers with D_L1. The sensitivity coefficients, R_s, used for the different materials are: 2400 [sA/cm^3] for SiO$_2$, 2000 [sA/cm^3] for Si, 1650 [sA/cm^3] for cobalt, 1470 [sA/cm^3] for iron, 1820 [sA/cm^3] for Ni, 1680 [sA/cm^3] for Ti alloy and 500 [sA/cm^3] for Al$_2$O$_3$ (Svintsov *et al.*, 2009).

After conducting these simulation studies, the 3D structures were fabricated in each
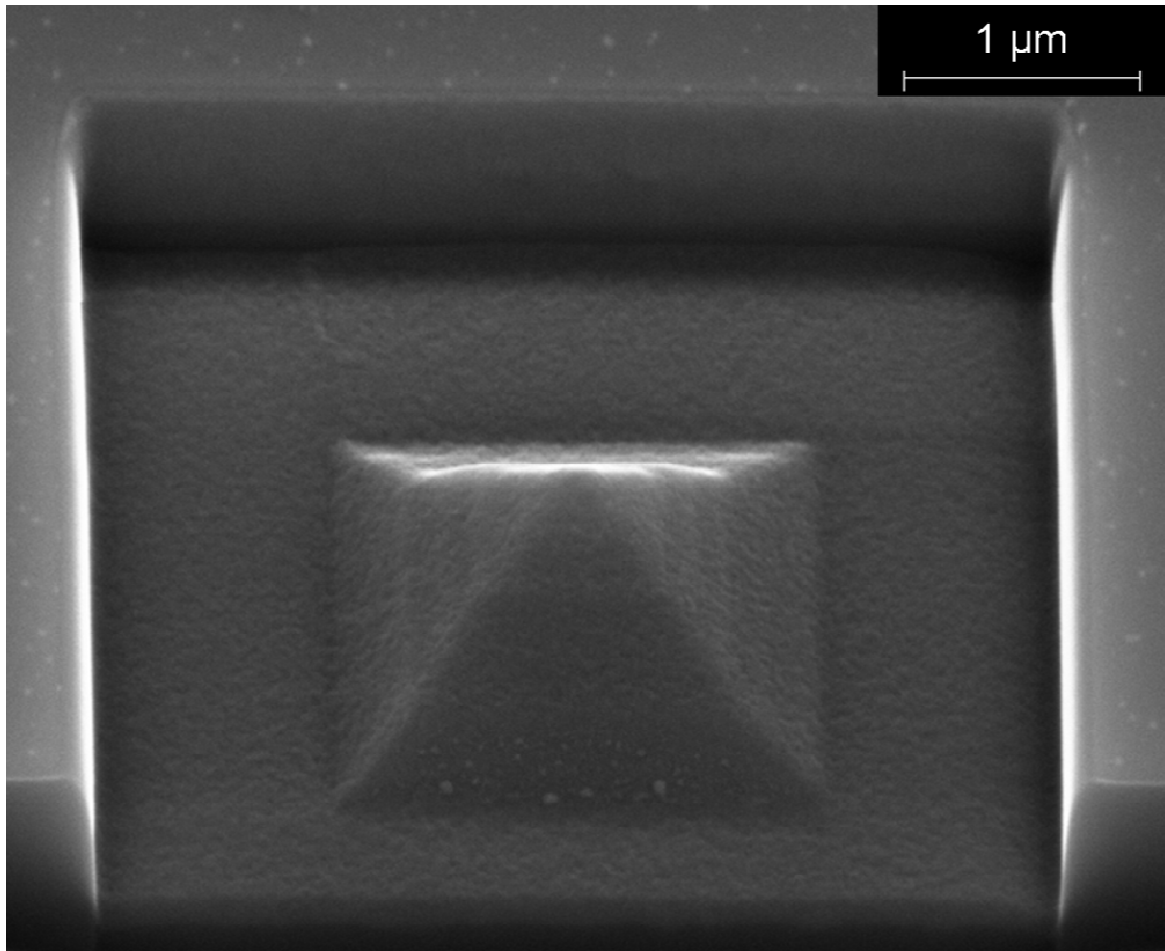
Figure 6.1 Convex square pyramid in a 4x4 µm trench milled in Si.

material by FIB milling and the depth and lateral dimensions of the produced features were compared with the simulation results. Due to the specific application of the 3D test structure as an axon and/or mixer in micro-fluidics, a double-wound spiral with 6x6 µm dimensions as shown in Figure 6.3 a was selected to verify the results. The exposure settings applied in the experiments were: beam currents: 2nA and 200 pA, dwell time: 0.001ms and 0.01 ms, respectively; area step size: 10 nm and N_L=100.

6.4 Results and discussion

6.4.1 Layer thickness

The layer thicknesses, h, obtained for the investigated materials are presented in Table 6.2. The detailed results and respective images from applying the methodology for layer thickness estimation are presented in Appendix C. Again, as it was the case for Si in Chapter 5, the h values and their respective tolerance intervals were proportional to the applied D_L for the eight materials used in this study. Also, as can be seen in both Table 6.2 and Figure 6.2, the h values for the different materials are quite similar, excluding Alumina, which suggests that their responses to FIB milling are similar, too. Therefore, with respect to FIB machining, these materials can be regarded as easily interchangeable, and the most appropriate for a given application can be selected. Thus, any of these materials can be utilised for producing replication masters by FIB patterning without causing any significant increase in the processing time or requiring re-adjustments of the milling parameters. Therefore the overall cost-effectiveness of any designed master/insert manufacturing route can be improved through the implementation of the most suitable material and according machining parameters' optimisation. The layer thickness, h, of all seven materials was less than h_{Si}, justifying again the choice of Si as a reference material for calculating the material

constants.

6.4.2 Materials' constants

The constants, C_f and C_t were derived for each of the eight materials based on the results obtained at the three different D_L utilised in this study. Thus, the C_f value is the average of the obtained results for each D_L, as shown in Table 6.3. It can be seen that, for most of the materials, C_f is identical for all D_L applied, indicating process stability and viability of the applied methodology.

As discussed in Section 6.2.2 the constant C_t can be used to estimate the total milling time for obtaining the targeted depth in a given material with respect to the time necessary to achieve the same depth in Si. Provided that the FIB milling is carried out under the same exposure conditions, this relationship can be expressed as follows:

$$ExposureTime_{material} = C_t * ExposureTime_{Si} \qquad (6.5)$$

It can be seen in Table 6.3 that the exposures would take between 5% and 36% more time for the investigated materials, excluding Alumina. In case of Alumina, to machine a structure with the same H as in Si it would take up to four times longer. The other material that requires a noticeably more machining time is iron, with a 36% increase of the exposure time. Therefore, its selection for direct FIB structuring has to be justified by weighting carefully any application specific advantages that the use of iron could provide. The obtained C_t values support again the possibility to interchange materials discussed in Section 6.4.1, which will allow for a greater

Table 6.2 Layer thickness, h, obtained for the studied materials

D_L [μAs/cm^2] / Material	h, [nm]		
	$D_L 1 = 2 \times 10^3$	$D_L 2 = 4 \times 10^3$	$D_L 3 = 6 \times 10^3$
Silicon (Si)	5.9 ±0.4	12.2 ±1.0	18.1 ±1.8
Alumina (Al$_2$O$_3$)	1.5 ±0.1	3.0 ±0.2	4.5 ±0.3
Cobalt (Co)	5.1 ±0.3	10.2 ±0.6	15.3 ±1.0
Cobalt (Co*)	4.8 ±0.4	9.7 ±0.7	14.5 ±1.2
Iron (Fe)	4.2 ±0.3	9.0 ±0.6	13.7 ±0.8
Nickel (Ni)	5.2 ±0.5	10.6 ±0.7	16.0 ±1.1
Quartz (SiO$_2$)	5.7 ±0.3	11.4 ±0.7	17.3 ±1.0
Ti Alloy	4.8±0.4	10.1 ±0.6	15.2±0.9

Table 6.3 C_f and C_t of the studied master-making materials

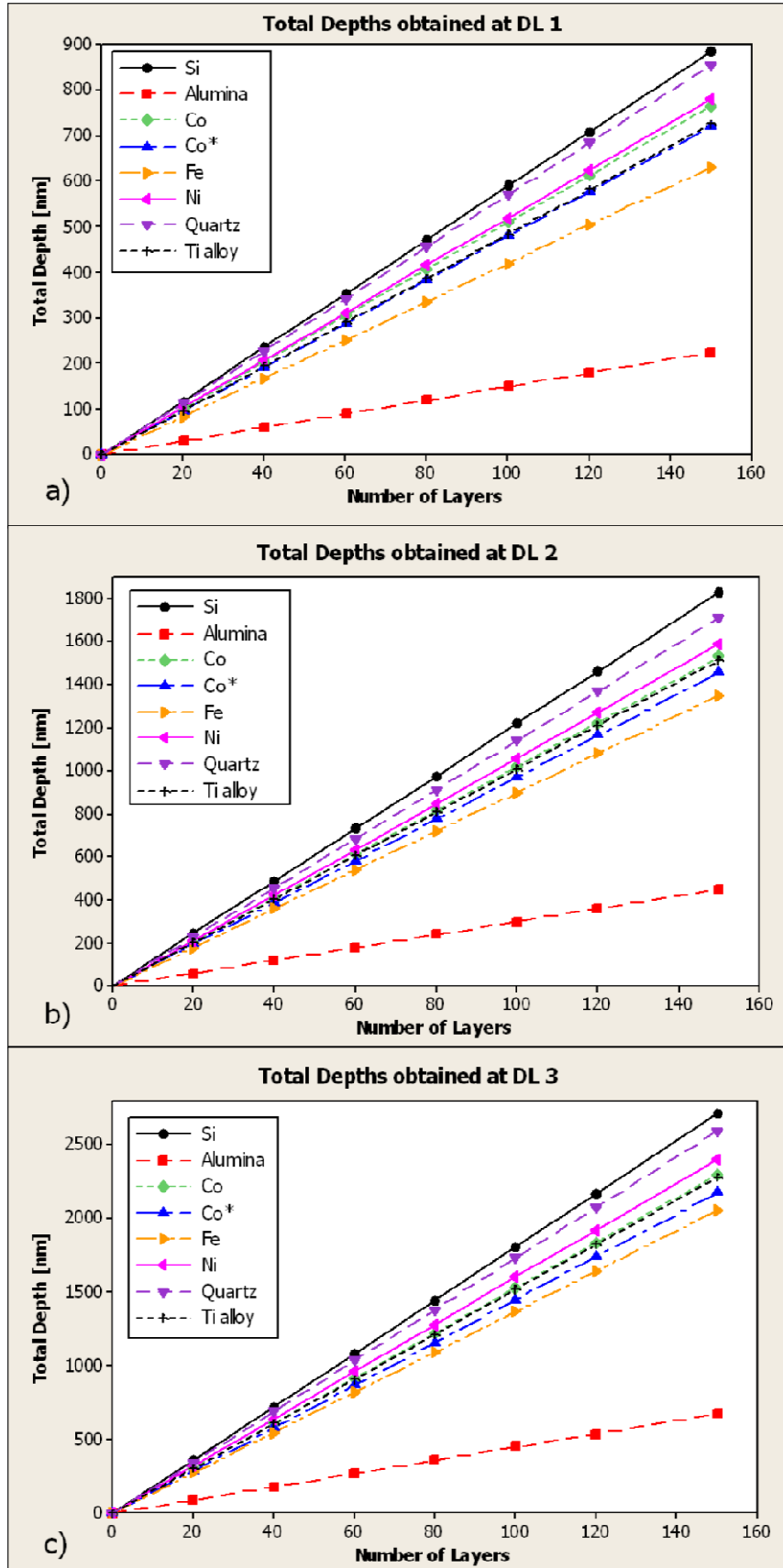|	Al_2O_3	Fe Alloy	Co* Alloy	Ti Alloy	Co Alloy	Ni Alloy	SiO_2	Si (benchmark material)
C_f at DL 1	0.254	0.712	0.814	0.814	0.864	0.881	0.966	1
C_f at DL 2	0.246	0.738	0.795	0.828	0.836	0.869	0.934	1
C_f at DL 3	0.249	0.757	0.801	0.840	0.845	0.884	0.956	1
C_f final	**0.250**	**0.735**	**0.803**	**0.827**	**0.849**	**0.878**	**0.952**	**1**
$C_t = 1/c_f$	**4**	**1.36**	**1.25**	**1.21**	**1.18**	**1.14**	**1.05**	**1**
	Single crystal	**Amorphous**						**Single crystal**

Figure 6.2 Total depth obtained when machining 3x3 µm square pockets with different N_L and D_L for the studied materials: a) D_L 1, b) D_L 2, and c) D_L 3

flexibility when designing application specific process chains. The material with a very similar machinability to Si is quartz with only 5% increase in exposure time. This is especially important for integrating FIB milling in various process chains for fabricating templates for UV Nanoimprint Lithography (NIL). Quartz is utilised in UV-NIL for template fabrication due to its transparency and over 90% transmission of wavelengths in the range from 180 to 600 nm (Lalev *et al.*, 2009). Nickel also shows a relatively good machinability, with a 17% increase in processing time. Thin foils of amorphous Ni can be used directly for FIB structuring and then utilised as inserts for hot embossing (HE). This can provide a very efficient alternative to the time-consuming and expensive approach of producing Ni inserts through electroforming of FIB patterned Si. Both C_f and C_t values obtained for the two types of Cobalt justify their potential usage for producing masters by direct FIB structuring. Ti alloy is also a very suitable material for producing replication masters due to its high wear and thermal resistance and good response to direct FIB structuring, evident from the obtained values for C_f and C_t.

6.4.3 Comparison

As the layer thickness, h, and the corresponding C_f (Tables 6.2 and 6.3) are similar for some of the investigated materials, only images of the simulated and the actual features produced in Si, Co, Al_2O_3 and Fe are presented in Figure 6.3. However, the simulations for the rest of the studied materials can be found in Appendix C and the results obtained for all the investigated materials are included in the following discussion. Table 6.4 summarises the values of the depths, H, obtained from the simulations and FIB milling with 2 nA and 200pA, as well as the percentage difference between the simulated and the achieved H for each material.

Figures 6.3a and 6.3b represent the results from the simulation and the actual FIB milling with 2 nA of a spiral in Si. As it can be expected based on the results reported previously (Lalev *et al.*, 2008; Svintsov *et al.*, 2009) the lateral dimensions of the simulated and milled features are almost identical, less than 2% difference in the targeted 6x6 µm size, as can be seen in Figures 6.3 to 6.6. Even though the calculated *H* of the spiral is approximately 600nm, and is very close to the milled one of 604.8 nm for 2 nA current the edges of the feature are not defined so well as in the simulation results. This can be explained with the relatively big beam diameter when using 2nA beam current, approximately 150 nm, and also due to possible disturbances during exposure that can cause slight beam shifts or defocusing. Furthermore, the same "blurring" of the spiral's edges is observed for the rest of the milled materials as can be seen in Figure 6.4 c-d, Figure 6.5 a-b and Figure 6.6 a-b for Co, Fe and Al_2O_3, respectively. In contrast, FIB milling with a much smaller beam spot will result in a higher feature resolution with much better edge definition as confirmed by both simulation and milling results for 200 pA, or 40 nm beam diameter, depicted on Figure 6.3 c-d, Figure 6.4 a-b and Figures 6.5 c-d and 6.6 c-d. Also, the quality of the milled feature is higher as seen from the percentage difference values in Table 6.4, which are around 2% for most of the investigated materials but not exceeding 4%. However, it should be noted that exposures with the same D_L but with smaller beam diameters, i.e. lower probe currents, lead to a corresponding substantial increase in exposure time as a trade-off. In the direction normal to the machined surface again the simulation and experimental results for *H* show approximately 3% difference for Co for both currents, 493.2 nm, 524.7 nm and 510 nm for measured and estimated *H*, respectively; 4.1% for 200 pA and 4.5% for 2 nA for Fe, indicating it is relatively hard to machine, and relatively low percentages for quartz and nickel, which appear to

167

Table 6.4 Simulated and actual H for the studied materials and their percentage difference

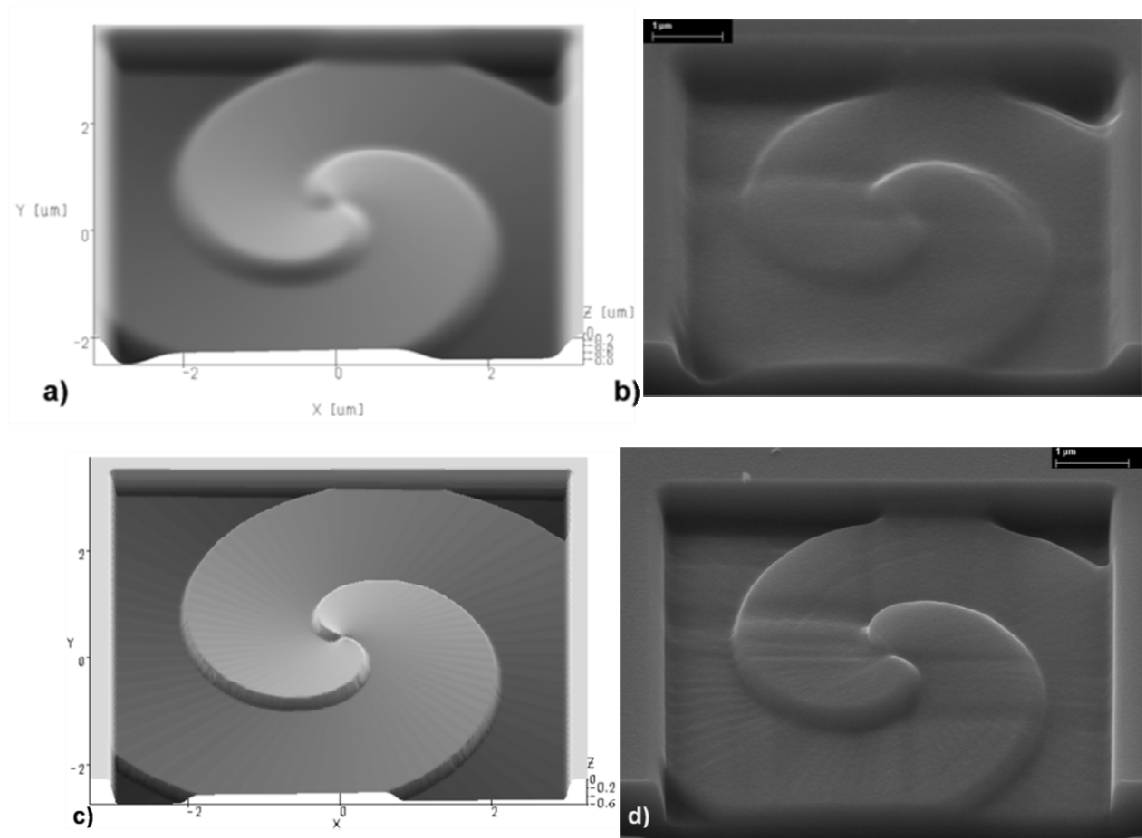| Material	$H^{\text{simulation}}$ [nm]	$H^{200\ \text{pA}}$ [nm]	Difference [%]	$H^{2\ \text{nA}}$ [nm]	Difference [%]
Silicon (Si)	600	612.7	2	604.8	0.8
Alumina (Al$_2$O$_3$)	150	152.8	1.9	143.2	4.5
Cobalt (Co)	510	524.7	2.9	493.2	3.3
Iron (Fe)	420	437.4	4.1	401	4.5
Nickel (Ni)	520	525.2	1	497.4	4.3
Quartz (SiO$_2$)	560	554.3	1	549.2	1.9
Ti Alloy	480	487	1.5	458.1	4.6

Figure 6.3 IonRevSim simulation (left column, a, c) and exposure results (right

column, b, d) for a double-wound spiral in Si for 2nA and 200 pA, respectively

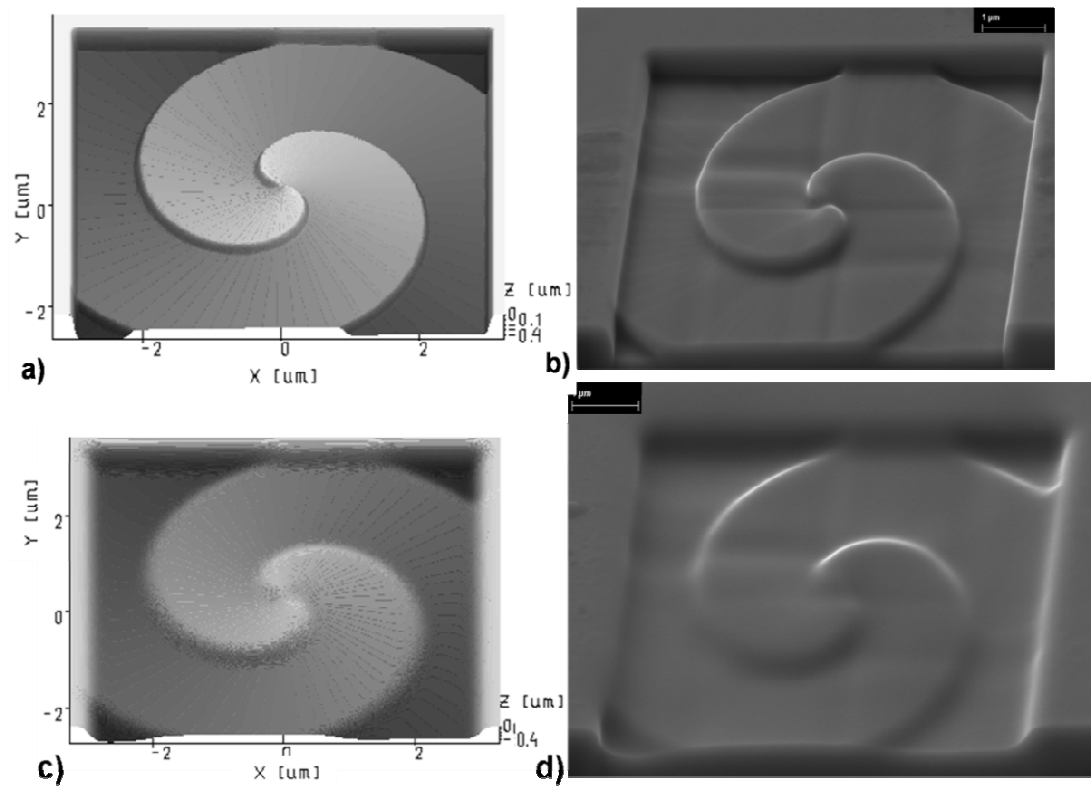Figure 6.4 IonRevSim simulation (left column, a, c) and exposure results (right column, b, d) for a double-wound spiral in Co for 200 pA and 2nA, respectively
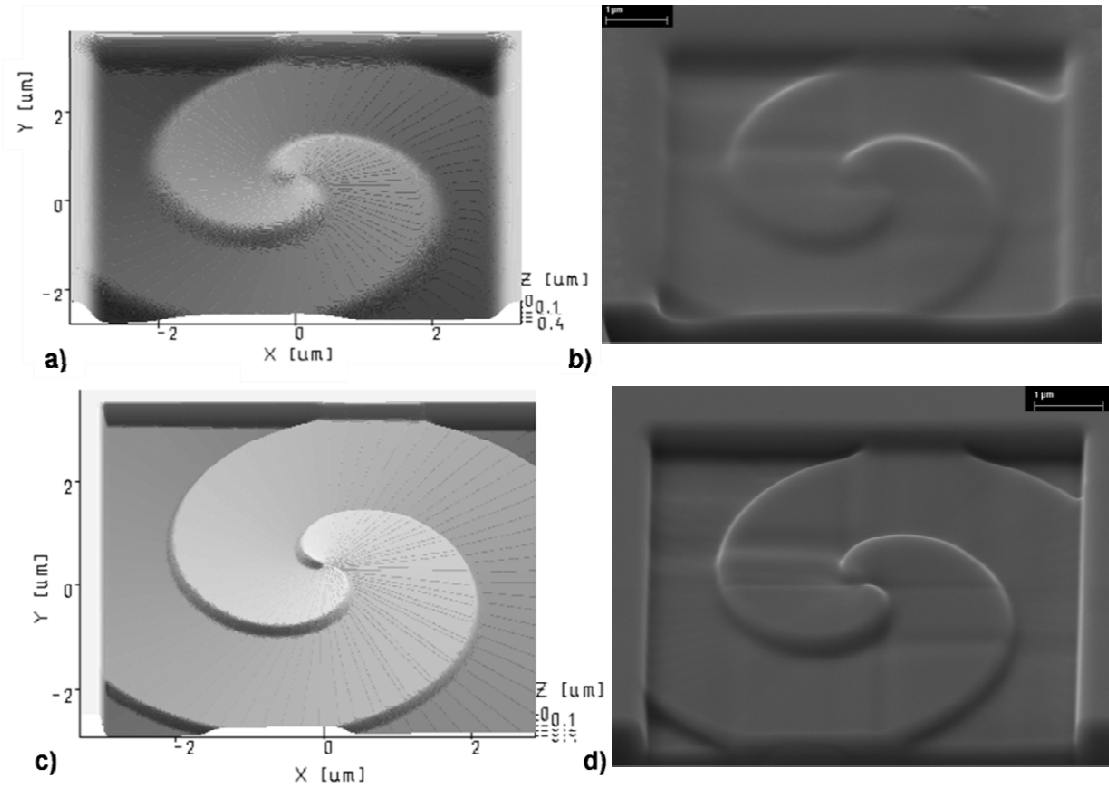
Figure 6.5 IonRevSim simulation (left column, a, c) and exposure results (right column, b, d) for a double-wound spiral in Fe for 2 nA a) and b), and 200 pA c) and d).
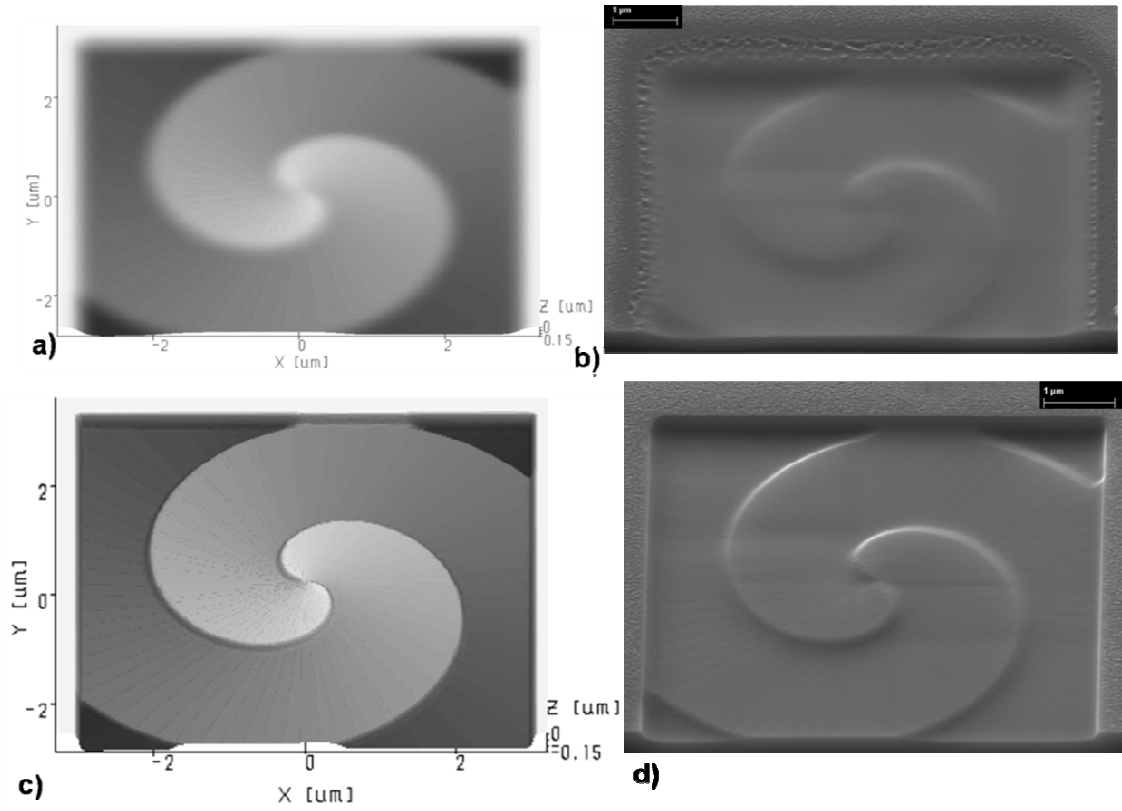
Figure 6.6 IonRevSim simulation (left column, a, c) and exposure results (right column, b, d) for a double-wound spiral in Al_2O_3 for 2 nA and 200 pA, respectively.

have good FIB machining response. It can be seen from Table 6.4 that the alloys, namely Al_2O_3 and $Ti_{42}Zr_{24}Co_{16}Ni_{15}Be_4$, are among the materials exhibiting the highest percentage difference between simulated and actual results. That could be attributed to the fact that, even though a sophisticated software package was utilised for the simulations, it is not a trivial task to calculate precisely the parameters to simulate accurately the interaction between ion beams and complex alloys' targets.

It can be concluded that the simulation results obtained for ion beam sputtering of the investigated amorphous materials are very close to those calculated applying the layer thickness methodology in regard to the resulting feature depth.

The IonRevSim (Svintsov *et al.*, 2009) utilises quite different process variables to simulate the FIB milling process, in particular implementing a sensitivity coefficient, R_S, rather than milling rate to account for the material properties and the machinability of a given material. So it can be regarded as another independent method for assessing the resulting depth in FIB milling. Thus, it can be considered that the depth assessments based on the simulation results and the ones calculated using C_f are of entirely independent origins. The actual exposure outcomes confirm both the values obtained for C_f and the simulations' results. This implies that the derivation method applied in this study is reliable and the obtained material constants can be used to estimate the resulting features' profiles for the considered materials.

6.4.4 Material response

As stated above the milling rates are primarily determined by the sputtering rate (yield) of the material. The sputtering rates are investigated for many PVD/CVD and

charged particle processes (Wilson *et al.*, 1997; Kilner *et al.*, 2004) that involve bombardment with primary ion beams, e.g. O^+, O^-, Cs^+, Ar^+, Xe^+, Ga^+ in Secondary Ion Mass Spectrometry (SIMS), of target materials such as metals, insulators and semiconductors in single crystal, polycrystalline or amorphous states. The main factors that determine the sputtering yield are:

- ***Mass mismatch between sputtering ions and atoms (molecules) of the targeted material.*** This factor has a significant effect on the obtained experimental results because of the significant mass mismatch of Ti, Fe, Co and Ni – based amorphous metals, in the range from 0.68 to 0.86, and single crystal alumina and Si, 1.46 and 0.4, respectively, in regards to Ga (Table 6.1). This mismatch affects the milling speed of the investigated materials (Table 6.3).

- ***The type of the bond in the sputtered material.*** Strong bonds may cause lower sputtering rates. In our case more representative interpretation of this factor could be obtained if the melting temperature (*Tm*) of the materials is used to judge about the bond strength (Table 6.1 and Figure 6.7). The energy of the incident ions is more readily absorbed in covalent bonded materials, and thus less is transferred to the surface, resulting in a reduced atom ejection, sputtering. Therefore in our experiments C_f and respectively the relative milling rates of the covalent bonded single crystal Al_2O_3 is significantly lower compared to the amorphous materials. The amorphous materials exhibit similar sputtering rate behaviour although variations of more than 20 % between the more 'robust' (Ti, Fe) and more 'easily sputtered' (Si, Ni)

amorphous alloys are evident. These differences are statistically significant taking into account that the uncertainties of the milling depth measurements do not exceed 6 to 8%. Therefore, C_f obtained by applying the described methodology must be taken into account when designing and implementing any ion beam milling strategy.

The amorphous $Co_{70}(SiB)_{23}Mn_5(MoFe)_2$ alloy was studied in two forms: as received amorphous state (Co); and after explosive welding (Co*) onto stainless steel substrate to form a laminated composite substrate (Minev *et al.*, 2008). The thereby fabricated laminate substrate could be described as having hard, wear resistant and anti-corrosive surface soft and ductile base, and thus has the necessary mechanical properties for producing masters for thermal replication processes. The sputtering experiments showed small differences of the milling yield between Co and Co*, within 6%, which is comparable to the measurement error. This is an evidence that no significant structural changes were triggered during the explosive treatment of the alloy.

Amorphous silica and single crystal silicon materials have similar relative milling rates with only 5% difference between them, which is again comparable to the measurement error. This confirms the results obtained by other researchers that sputtering rates of Si, amorphous Si, SiO_2, and Si_3N_4 are approximately the same (Wilson *et al.*, 1997). Also, this is another confirmation that the bond energy has a predominant influence on the materials' sputtering behaviour and not the molecular weight when comparing chemical compounds with covalent bonding.
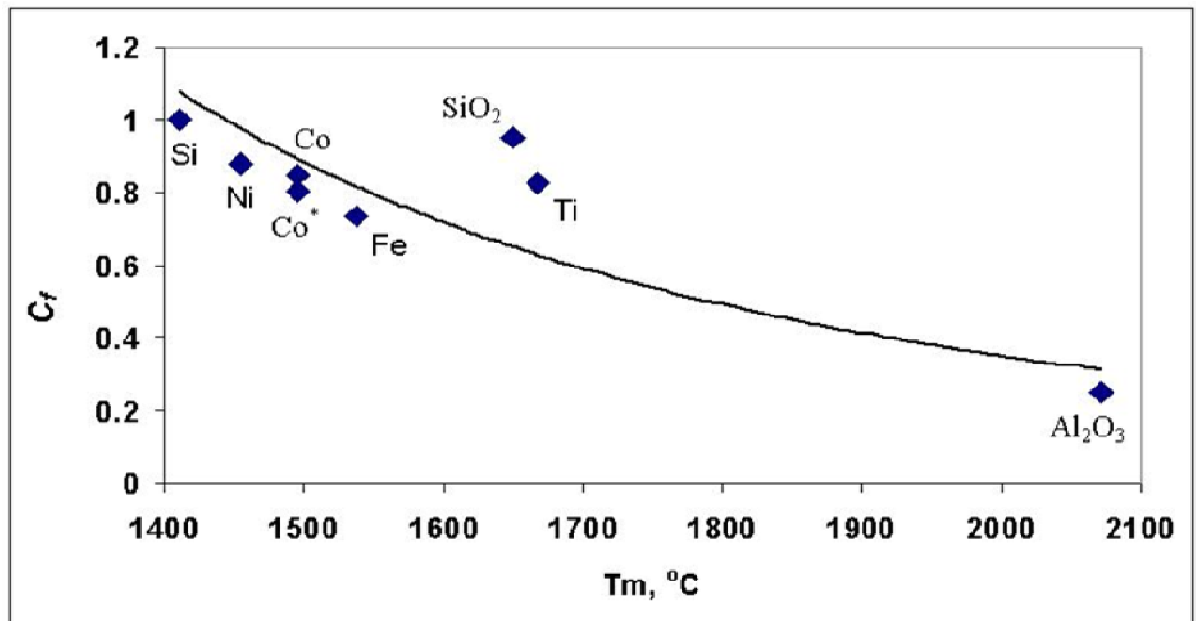
175

Figure 6.7 The dependence between C_f and Tm.

6.5 Summary and conclusions

The investigation carried out in this chapter concerns the behaviour of several amorphous materials suitable for fabrication of serial replication masters during FIB milling. Since depth estimation is a major issue in FIB machining it is the main focus of this research. The objective was to derive material coefficients for each material allowing for the estimation of the milling rate i.e. obtainable depth and total machining time for a given material with regard to Si as a benchmark. The layer thickness methodology was applied as a basis for the coefficients' derivation. The obtained results were discussed with regard to the material aspects of ion sputtering. Then, the coefficients were verified by simulating the FIB machining of a complex 3D feature in the targeted materials and then by comparing the simulation results with the structures obtained after actual FIB exposures. Specially developed software that takes into account the specific phenomena occurring during FIB sputtering in different milieus was employed to perform these simulations.

Based on the investigations reported in this chapter the following conclusion can be drawn:

1. The layer thickness, h, and its calculated tolerance interval are proportional to the applied dose per layer, D_L, for all of the studied materials. Also, the layer thicknesses for the different materials are similar, excluding Al_2O_3, indicating high possibility for material interchange.

2. Calculations of the total milling times for the investigated materials, made by utilising C_t, revealed 5% to 36% increase compared to Si, supporting again

177

the concept of material interchange aiming at employing the most suitable material for a specific application.

3. The material related constants C_f and C_t were verified by simulation studies of FIB milling with 200 pA and 2 nA beam current. The difference between the simulated and milled feature heights, *H*, was much less than 5% for the investigated materials. It was also shown that FIB milling with smaller currents results in higher-resolution features with better edge definition but increases the machining time substantially.

4. The main factors that determine the sputtering yield and thus the FIB machining response of the materials studied in this chapter are (i) the mass mismatch between sputtering ions and atoms of the targeted material, which affects the milling speed and (ii) the type of bond in the sputtered material, and more specifically, the bond energy, which has a predominant influence on the material's sputtering behaviour.

CHAPTER 7

CONTRIBUTIONS, CONCLUSIONS AND FUTURE WORK

7.1 Contributions

The overall aim of this research was to investigate the cost-effective implementation of the FIB technology in master-making process chains for serial replication. To accomplish this task the following research concerns were investigated:

- development and validation of cost-effective process chains for fabrication of replication tool incorporating FIB milling as a component technology;

- cost-effective production of complex 3D features of different length scales onto a single component;

- accurate depth estimation in layer-based FIB milling;

- the machining response of different master-making materials during layer-based FIB milling.

The main research findings and contributions to the existing knowledge in micro and nano manufacturing technologies are presented below.

7.1.1 Process chain for fabrication of replication masters

A novel process chain for fabrication of replication masters was developed and validated for serial fabrication of organic electronic (OTFT) devices. The proposed master-making route relies on using different technologies for micro structuring and

sub-micron and nano patterning that are applied to the fabrication of Ni shims incorporating different length scale features. The inspections carried out after each component technology of this process chain led to the following conclusions.

High aspect ratio features were more difficult to structure. Any deviations during the template structuring stages affect the follow-up replication process and therefore measures should be taken to account for them in advance. This was further confirmed during the replication stage where it was observed that features with bigger lateral dimensions and low aspect ratios replicated better.

The analysis carried out at each stage of the process chain revealed a maximum of 5.6% difference on average between the features' dimensions at the structuring and S-FIL replication stages, and 1.5% difference between corresponding features on the NIL imprint and the Ni shim, which indicated very good process compatibility between the component technologies in the process chain, especially for the targeted length scale range. Finally, the fabricated replication tool was implemented successfully as a master for R2R hot embossing, where a batch of OTFT devices on flexible substrates was produced.

7.1.2 Realisation of 3D structuring and FLSI into a single component

The process chain developed in Chapter 3 was modified to demonstrate the capability of FIB milling in combination with UV imprinting and electroforming to produce replication tools incorporating complex 3D features and patterns of different length scales. The produced tool was validated as a stamp for hot embossing. The main findings made during this investigation are presented below.

The selection of appropriate data generation techniques is of crucial importance for the accurate production of high resolution 3D features. Therefore, the pattern data preparation approach offering most advantages with regard to generation of complex 3D geometries to serve a specific purpose must be utilised. In this research, the layer-based approach, in which the target geometry is defined as a stack of layers ordered along the vertical axis of the structure and all contained into a single data file was found to yield the best outcome for complex 3D features.

The thorough analysis of the obtained results after the implementation of each component technology in this process chain showed an average difference in corresponding features' lateral dimensions of less than 3%, thus justifying the technologies selection in regard to process compatibility. Furthermore, the difference between the structures on the Ni shim and those on the HE replicas was within 1% indicating the high level of complementarity and excellent quality of the process chain's end product. This conclusion is also confirmed by the results obtained from the depth analysis where the average deviation was only within 1.4%.

Analysis of the profiles of the corresponding pyramids on the template, the NIL imprint, the Ni shim and HE replica clearly revealed that they were parallel to each other, indicating that (i) the targeted 3D geometry was accurately produced by FIB milling, and (ii) the tips remained in the centre of the respective pyramids throughout all machining and replication steps of the process chain without compromising the structures' functional requirements.

The following factors that are inherent to the various steps of the process chain were

considered to have the highest influence on its overall performance: the measurement uncertainty including the system calibration and the measurement strategy, the process parameters' optimisation for the different component technologies, the 3D pattern generation strategies and the material properties.

7.1.3 Depth estimation in layer-based FIB milling

To address the issues related to the achievable dimensions in direction normal to the machined surface during FIB milling, a methodology for total feature depth estimation was developed and validated. It relates the total depth to the layer depth obtainable with specified sets of exposure parameters. The findings in this study are summarised below.

The layer thickness can be considered the same for a given area dose per layer for a given material, regardless of the beam current magnitude. The results suggest that the layer thickness is proportional to the applied dose per layer, which could be used in selecting processing windows for producing structures with a given depth. However, it should be noted that there is a critical layer thickness for any given area dose, above which the re-deposition cannot be considered negligible anymore.

The total height/depth of layer-based FIB milled features can be calculated as a product of the layer thickness for a given dose and the number of layers selected to produce them. However, this is only valid for the linear part of the total thickness / number of layers interdependence.

It is possible to estimate accurately the tolerance/uncertainty intervals of machined features' heights. Especially, in the conducted experiments the heights of all FIB milled features were within the calculated tolerance ranges and their deviations were within 2 to 5%. It was observed that an increase of layer thickness and higher doses tend to lead to higher deviations from the targeted values.

7.1.4 Layer-based FIB milling of different amorphous materials

The machining response to FIB milling of several amorphous materials suitable for replication masters was investigated in order to relate their behaviour to that of a benchmark material, such as silicon. The methodology for estimating the ion beam milled depths of different materials relative to Si described in Chapter 6 is an effective and convenient approach for assessing and improving FIB machining strategies and process accuracy in the direction normal to the substrate surface when milling 3D structures. More specifically by applying this methodology for estimating the milling rate of other materials relative to single crystal Si by employing the material specific constant, C_f, it is possible to produce structures with an accuracy within 6 to 8% of their nominal dimensions in the direction normal to the substrate surface. The latter was confirmed by the simulation studies carried out with a specially developed ion sputtering simulation software.

The total time needed to mill a desired feature in a given material can be compared to the time necessary to produce the same structure in Si and thus calculated by utilising the inverse constant of C_f - C_t. The obtained C_t values will facilitate the possible interchange of master materials, which will allow for a greater flexibility when designing application specific process chains.

The sputtering yield of the amorphous materials investigated in this research, SiO_2, Fe, Co, Ni, and Ti based alloys, were experimentally found to be only 14 to 35% lower than those achievable for a single crystal Si and amorphous SiO_2. In addition, the milling rates of these amorphous materials were significantly higher, with factor of 3, compared to that achieved for the single crystal alumina (Al_2O_3). This can be explained with the covalent bonding of Al_2O_3 that results in a reduced atom ejection, sputtering, by the incident ions.

7.2 Conclusions

Based on the research carried out the following generic conclusions can be made:

- The utilisation of process chains as a means for fabrication of replication masters allows the cost-effective combination of the capabilities and advantages of a number of manufacturing technologies. When each of the implemented processes is utilised in its optimal processing window and the technologies are selected so as to guarantee optimal process compatibility and complementarity, the influence of the error factors on the overall process chain performance can be minimised. The unique patterning capabilities of the FIB technology can be cost-effectively utilised for sub-micron and nano structuring in such process chains. The high processing times can be minimised by multiplying the resulting topography over a larger area, e.g. using UV-NIL S-FIL technology, and then transferring it to a suitable tooling material employing electroforming.

- Process chains can be successfully applied for producing components

incorporating complex 2.5D and 3D structures of different length-scales. The implementation of FIB milling as a component technology of process chains guaranteed the precise fabrication of 3D features and showed the technology's important role for the successful achieving of FLSI into a single component/product. Analysis of the complex features' profile revealed that the feature geometry was accurately transferred through the stages of the process chains to the end product and also that a careful selection of inspection strategies in order to minimise measurement uncertainty is required. Furthermore, the successful implementation of the modified process chain proved that the diversity of available technologies allows for flexibility and innovative design solutions when developing process chains for specific applications.

- By investigating in details the relationship between layer depth, total feature depth and area dose in layer-based FIB milling as well as FIB sputtering effects like material re-deposition it was possible to develop a methodology for depth estimation. It allows for accurately calculating the total depth of the feature and a tolerance interval defining its acceptable variations. Validation of the methodology through FIB milling of complex 3D features revealed that it can be reliably applied to different strategies for 3D geometry data generation and wide range of number of layers.

- The obtainable total depth and the total milling time for layer-based FIB machining of a given structure in a selected amorphous material can be estimated by linking the milling rate/sputtering yield of the used material to

that achievable in a benchmark material, e.g. Si. That is accomplished by deriving material related constants C_f and C_t that characterise the material response to FIB milling. By using C_f and C_t the overall cost-effectiveness of any designed master/insert manufacturing route can be improved by utilising the most suitable material and optimised machining parameters.

7.3 Future Work

Alignment issues are of high importance for the successful realisation of process chains combining the capabilities of different component technologies. Thus, the introduction of a system that creates alignment marks as data files that can be utilised by all the consecutive processes could bring significant improvements. If during the design of a process chain the compatibility of the used data format with the software systems applied to control the various component technologies could be assured this can have a significant impact on the cost-effectiveness of the process chain. Also, the use of a common data format at all processing stages would facilitate achieving not only the necessary alignment of structures machined with different technologies but also the necessary level of integration in any process chain.

The uncertainty issues of process chains can be addressed by developing and implementing systematic procedures for preliminary detailed analysis of error factors. This should include risk assessment of the possibility of fault occurrence at each stage of the process chain as well as its influence on the follow-up technologies and the overall quality and cost of end product.

The methodology for layer depth estimation developed in Chapter 5 of this research is based on empirical studies of the linear part of the interdependency between the total feature depth and the number of layers (H-N_L) applied. While it is very accurate for predicting the total feature depth in cases when re-deposition can be considered negligible, a modified version to account for this phenomenon would be a major improvement in planning and performing of layer-based FIB milling. Therefore, a detailed investigation of dependences outside the H-N_L linear range could enable the development of models/strategies that can be used to compensate for re-deposited atoms. Hybrid models, combining layer-based and "dose distribution" or gray tone FIB milling can be possible solution to correcting the non-linearity but would require further investigations.

The material related constants C_f and C_t were derived empirically and even though they were validated through simulation studies performed with a tool utilising entirely different process variables to simulate FIB sputtering, the methodology could benefit from further analytical studies. An in-depth theoretical analysis describing all physical phenomena of the FIB milling and the 'ion-target' interactions, including process specifics like re-deposition of atoms and angle-dependent sputtering, through mathematical models could (i) facilitate the determination of material related constants for other application specific materials, and (ii) eliminate the influence of intrinsic uncertainty factors such as momentary condition of the LMIS and the FIB system, beam defocusing, shift or intensity fluctuations, vibrations and magnetic fields.

APPENDIX A

Determination of the uncertainty for the measuring instrument – Carl-Zeiss XB 1540 Scanning Electron Microscope (SEM)

The applied procedure as well as the equations used for the uncertainty calculations was performed following an established methodology (Kirkup and Frenkel, 2006). The equations used are listed below:

Determination of standard uncertainty in the mean $u(\bar{x})$:

$$u(\bar{x}) = \frac{s}{\sqrt{n}} \qquad\qquad (A.1)$$

$$s = \sqrt{\frac{\sum_{i=1}^{n}(x_i - \bar{x})^2}{n-1}} \qquad\qquad (A.2)$$

Combining standard uncertainties:

$$u^2(y) = \sum_{i=1}^{n}\left(\frac{\partial y}{\partial x_i}\right)^2 u^2(x_i) \qquad\qquad (A.3)$$

Expanded uncertainty U(y)

$$U(y) = k.u(y), \qquad\qquad (A.4)$$

where *k* is a coverage factor determined at a level of confidence (i.e. 95 %) for a given number of degrees of freedom *v:*

$$V_{eff} = \frac{u^4(y)}{\displaystyle\sum_{i=1}^{n} \frac{c_i^4 u^4(x_i)}{v_i}} \,, \tag{A.5}$$

and $\qquad V = n - 1 \tag{A.6}$

A calibration sample with silicon calibration gratings was used in determining the measurement uncertainty of the SEM. It had the following specifications: silicon calibration gratings of the TGX01 series, comprising of a chessboard-like array of square pillars with active area: 2x2 mm; step height 170 ± 4 nm; pitch 3 µm; accuracy of pitch ± 5 nm and side of square of approximately 1.15 µm. The calibration specimen was specifically chosen as it enables obtaining of measurements in two orthogonal directions, which is highly recommended when dealing with SEM calibration and measurement uncertainty (Leach, 2010). Repeated measurements of the pitch at randomly chosen place on the calibration sample were performed. Twenty measurements were taken at each of the three most often utilised magnifications: 3600X, 16 000X (16kX) and 35 kX (22 kX in vertical direction uncertainty calculations). The uncertainty calculations provided below reveal that the measurement uncertainty of the instrument tends to decrease with the increase of the magnification. Therefore, for conducting measurements with the SEM, the highest possible magnifications, achievable for the given dimensional range/scale, are usually selected.

The best estimate of the pitch is presented by the equation:

$$P = X + Z, \tag{A.7}$$

Where X is the mean value obtained through repeated measurements:

$$X = \frac{\sum\limits_{i=1}^{n} x_i}{n} \qquad (A.8)$$

Z is the best estimate of the correction which accounts for the effects of systematic error like calibration error or resolution error etc.

Standard uncertainty in X

It's based on Type A evaluation of uncertainty:

$$u(X) = \frac{s}{\sqrt{n}} \qquad (A.9)$$

The number of degrees of freedom is $v_x = n - 1 = 20 - 1 = 19$

Determination of Z and standard uncertainty in Z

Since it's not known whether the error has positive or negative sign the best estimate of the correction is $Z=0$. It's not based on a statistical analysis, and is therefore Type B evaluation of uncertainty. As already mentioned this is a correction due to error. As the only calibration information available is the pitch accuracy $\delta = 5$nm the standard uncertainty in Z becomes:

$$u(Z) = \frac{\delta}{\sqrt{2v}}, where\, v = n - a, \qquad (A.10)$$

Where a is the number of values calculated based on this sample. In this case $a=0$, since no statistical analysis was performed, so $v = n = 20$.

$$u(Z) = \frac{5x10^{-3}}{\sqrt{2x20}} = 0.00079 = 0.79x10^{-3}\, \mu m$$

As $u(Z)$ is negligibly small the number of degrees of freedom $v_z \rightarrow \infty$.

- **Uncertainty for 3.6 kX**

For magnification of 3.6 kX:

$X = 2.981$ μm

$s = 0.04675$ μm

$u(X) = 0.0105$ μm

Combined uncertainty for 3.6 kX magnification:

$$u^2(P) = u^2(X) + u^2(Z) = 110.25 x10^{-6} + 0.62 x10^{-6} = 110.87 x10^{-6} \, \mu m$$

$u(P) = 10.53 x10^{-3}$ μm

$$V_{eff} = \frac{u^4(P)}{\dfrac{u^4(x)}{V_x} + \dfrac{u^4(z)}{V_z}}, \text{ since } v_z \rightarrow \infty, \text{ the } u(z) \text{ part becomes zero and cancels, so}$$

$v_{eff} = (10.53x10^{-3})^4/[(10.5 \times 10^{-3})^4/19] = 19.22 \sim 19$

$K_{(95\%, 19)} = 2.09$

Expanded uncertainty:

$U(P) = u(P). k = 10.53x10^{-3}x2.09 = 22.01x10^{-3}$ μm

$U(P) = \pm$ **22 nm**

Pitch $= 3 \pm 0.022$ μm

- **Uncertainty for 16 kX**

$X = 2.979$ μm

$s = 0.02565$ μm

$u(X) = 0.0057$ μm

Combined uncertainty for 16 kX magnification

$$u^2(P) = u^2(X) + u^2(Z) = 32.49 x10^{-6} + 0.62 x10^{-6} = 33.11 x10^{-6} \, \mu m$$

$u(P) = 5.75 x10^{-3}$ μm

$v_{eff} = (5.75 x10^{-3})^4 / [(5.7 \times 10^{-3})^4 / 19] = 19.67 \sim 20$

$k_{(95\%, 20)} = 2.09$

Expanded uncertainty:

$U(P) = u(P). \, k = 5.75 x10^{-3} x 2.09 = 12.02 x10^{-3}$ μm

$U(P) = \pm 12$ nm

Pitch $= 3 \pm 0.012$ μm

- **Uncertainty for 35 kX**

$X = 2.991$ μm

$s = 0.01854$ μm

$u(X) = 0.0041$ μm

Combined uncertainty for 35 kX magnification

$$u^2(P) = u^2(X) + u^2(Z) = 16.81x10^{-6} + 0.62x10^{-6} = 17.43x10^{-6} \mu m$$

$u(P) = 4.17x10^{-3} \mu m$

$_{veff} = (4.17x10^{-3})^4/[(4.1 \times 10^{-3})^4/19] = 20.33 \sim 20$

$k_{(95\%, 20)} = 2.09$

Expanded uncertainty:

$U(P) = u(P)x\ k = 4.17x10^{-3}x2.09 = 8.7x10^{-3} \mu m$

$U(P) = \pm\ 9$ nm

Pitch $= 3 \pm 0.009 \mu m$

Determination of the uncertainty in vertical direction

Due to the specific features of the SEM software principle of operation the measurement along the vertical axis is the product of the value measured along the Y-axis in the XY plane and the correction coefficient equal to $1/\cos\zeta$ ($\zeta = 36^o$). That gives the true vertical value provided the 36 degrees' tilt correction option is on. As $\cos\zeta$ is constant, the measurement uncertainty in vertical direction would be equal to the measurement uncertainty along Y axis of the XY plane.

With the same sample taken for determination of the uncertainty along z-axis i.e. depth measurement, and 20 repeated measurements of the pitch along Y axis, *u(Z)* remains:

$$u(Z) = \frac{5x10^{-3}}{\sqrt{2x20}} = 0.00079 = 0.79x10^{-3} \, \mu m$$

- **For magnification of 3.6 kX**

$X = 2.998$ μm

$s = 0.03045$ μm

$u(X) = 0.0068$ μm

Combined uncertainty for 3.6 kX magnification

$$u^2(P) = u^2(X) + u^2(Z) = 46.24x10^{-6} + 0.62x10^{-6} = 46.86x10^{-6} \, \mu m$$

$u(P) = 6.84x10^{-3}$ μm

$$\nu_{eff} = \frac{u^4(P)}{\dfrac{u^4(x)}{\nu_x} + \dfrac{u^4(z)}{\nu_z}}, \text{ since } \nu_z \rightarrow \infty, \text{ the } u(z) \text{ part becomes zero and cancels, so}$$

$\nu_{eff} = (6.84x10^{-3})^4/[(6.8 \text{ x } 10^{-3})^4/19] = 19.11 \sim 19$

$k_{(95\%, \, 19)} = 2.09$

Expanded uncertainty:

$U(P) = u(P). \, k = 6.84x10^{-3}x2.09 = 14.30x10^{-3}$ μm

$U(P) = \pm 14$ nm

Pitch $= 3 \pm 0.014$ μm

- **Uncertainty for 16 kX**

$X = 3.006$ μm

$s = 0.01611$ μm

$u(X) = 0.0036$ μm

Combined uncertainty for 16 kX magnification

$$u^2(P) = u^2(X) + u^2(Z) = 12.96x10^{-6} + 0.62x10^{-6} = 13.58x10^{-6} \; \mu m$$

$u(P) = 3.68x10^{-3}$ μm

$v_{eff} = (3.68x10^{-3})^4/[(3.6 \text{ x } 10^{-3})^4/19] = 19.42 \sim 19$

$k_{(95\%, \, 19)} = 2.09$

Expanded uncertainty:

$U(P)=$ u(P)x k $= 3.68x10^{-3}$x2.09 $= 7.69x10^{-3}$ μm

$U(P) = \pm 8$ nm

Pitch $= 3 \pm 0.008$ μm

- **For magnification of 22 kX:**

$X = 2.994$ μm

$s = 0.01469$ μm

$u(X) = 0.0033$ μm

Combined uncertainty for 22 kX magnification

$$u^2(P) = u^2(X) + u^2(Z) = 10.89x10^{-6} + 0.62x10^{-6} = 11.51x10^{-6} \, \mu m$$

$u(P) = 3.39x10^{-3} \, \mu m$

$$\nu_{eff} = \frac{u^4(P)}{\dfrac{u^4(x)}{\nu_x} + \dfrac{u^4(z)}{\nu_z}}$$, since $v_z \rightarrow \infty$, the *u(z)* part becomes zero and cancels, so

$v_{eff} = (3.39x10^{-3})^4 / [(3.3 \text{ x } 10^{-3})^4 / 19] = 19.52 \sim 20$

$k_{(95\%, 20)} = 2.09$

Expanded uncertainty:

$U(P) = u(P)x \, k = 3.39x10^{-3}x2.09 = 7.085x10^{-3} \, \mu m$

$U(P) = \pm \, 7 \, nm$

Pitch $= 3 \pm 0.007 \, \mu m$

APPENDIX B

FWHM measurements of the OTFT channels and calculated uncertainty

Table B.1 FWHM measurements of the channels at every stage of the process chain

Target Value [nm]	FWHM on the Template [nm]						
450	379.3	379.3	384.4	361.8	384.4	381.3	384.4
600	481.5	488.6	473	481.5	456.6	532.5	456.6
900	812.1	815.4	815.4	848.3	812.1	791	790.1
1200	989	1032	912	1032	1059	987	912
2400	2232	2197	2322	2118	2361	2197	2197
5000	4995	4995	5103	4995	4943	4991	4943
	FWHM on the NIL imprint [nm]						
450	343.6	323.6	401.6	323.6	345.6	343.6	323.6
600	457.6	535.5	456.6	456.6	427.7	441.7	427.7
900	743.8	743.8	768.8	731.2	743.8	731.2	743.8
1200	920.3	978.8	861.5	920.3	920.3	920.3	920.3
2400	2126	2150	2118	2126	2118	2118	2126
5000	4800	4800	4850	4756	4800	4750	4844
	FWHM on the Ni shim [nm]						
450	348.4	357.3	334.2	336.1	348.4	357.3	357.3
600	477.2	467.1	467.1	477.2	477.2	477.2	497.7
900	750	739.8	739.8	780.7	750	739.8	750
1200	912	910.5	910.5	917.9	910.5	910.5	912
2400	2141	2126	2126	2156	2141	2156	2141
5000	4846	4846	4738	5052	4748	4846	4846
	FWHM on the R2R imprint [nm]						
450	664	689	664	664	657.3	645.7	664
600	753.4	756.8	753.4	756.8	749.9	753.4	749.9
900	1181	1131	1181	1181	1181	1231	1181
1200	1331	1575	1252	1331	1245	1331	1252
2400	2802	2799	2802	2784	2802	2841	2784
5000	5406	5135	5677	5406	5406	5135	5677

Table B.2 Uncertainty analysis and calculation for FWHM values at all the stages of the process chain

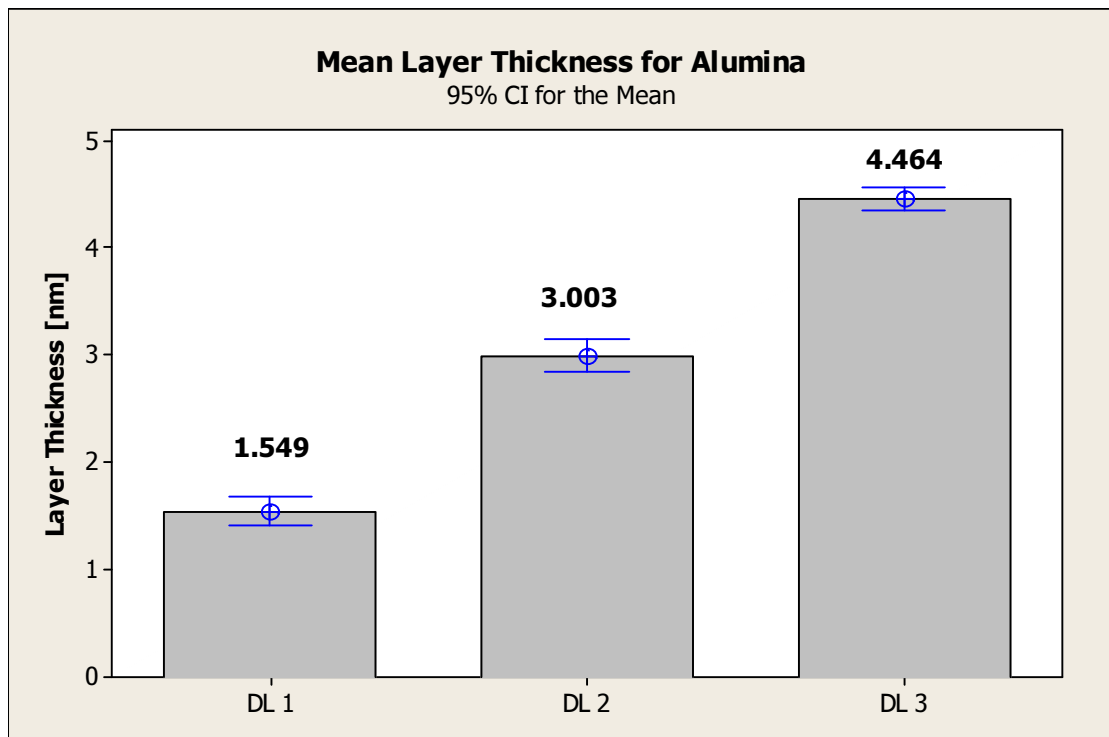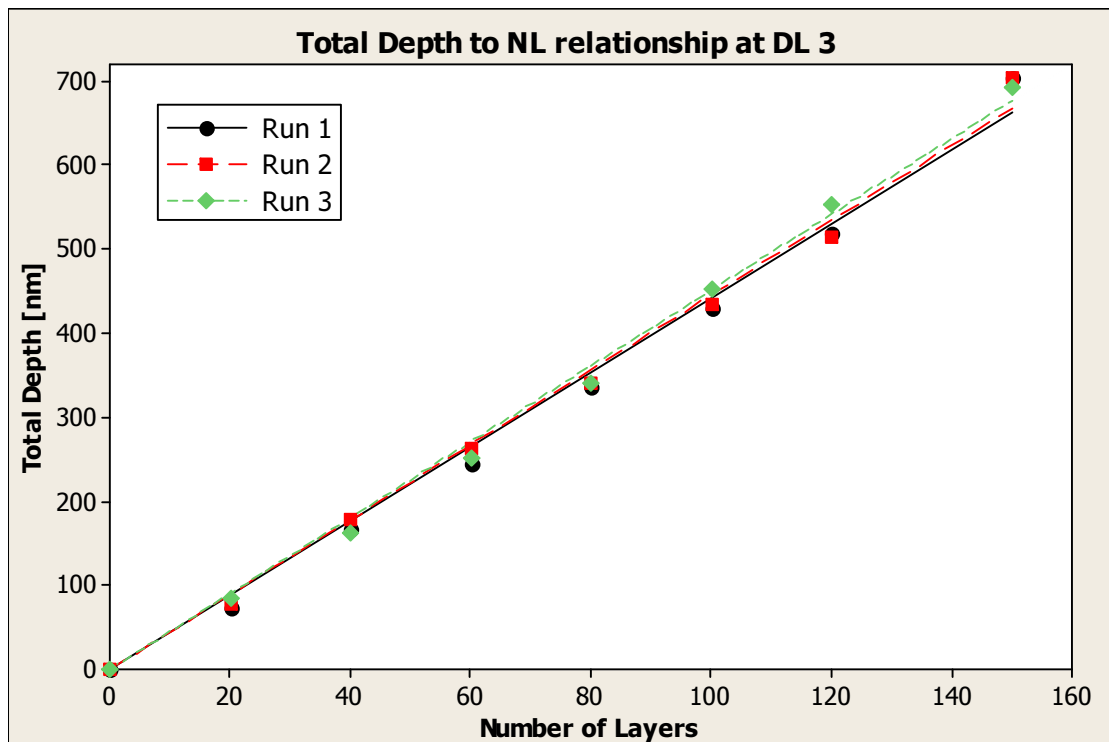| x [nm]	$u(x)$ [nm]	$u(\bar{x})$ [nm]	$u(P)$ [nm]	$u_c(x)$ [nm]	V_{eff}	k	$U = k.u_c(x)$ [nm]
Template							
379.3	8.04	3.04	11.38	11.78	infinite	1.96	23.1
481.5	25.70	9.71	14.45	17.41	~100	1.98	34.5
812.1	19.41	7.34	24.36	25.44	infinite	1.96	49.9
989	58.40	22.07	29.67	36.98	~ 50	2.01	74.3
2232	83.08	31.40	66.96	73.96	~100	1.98	146.4
4995	53.37	20.17	149.85	151.20	infinite	1.96	296.4
NIL imprint							
343.6	27.59	10.43	10.31	14.66	~ 30	2.04	29.9
457.6	36.77	13.90	13.73	19.53	~ 30	2.04	39.9
743.8	12.53	4.74	22.31	22.81	infinite	1.96	44.7
920.3	33.86	12.80	27.61	30.43	~100	1.98	60.3
2126	11.31	4.28	63.78	63.92	infinite	1.96	125.3
4800	38.45	14.53	144.00	144.73	infinite	1.96	283.7
Ni shim							
348.4	9.92	3.75	10.45	11.11	~100	1.98	22.0
477.2	10.20	3.86	14.32	14.83	infinite	1.96	29.1
750	14.46	5.47	22.50	23.15	infinite	1.96	45.4
912	2.70	1.02	27.36	27.38	infinite	1.96	53.7
2141	12.25	4.63	64.23	64.40	infinite	1.96	126.2
4846	103.04	38.95	145.38	150.51	infinite	1.96	295.0
R2R imprint							
664	12.94	4.89	19.92	20.51	~100	1.98	40.6
753.4	2.82	1.06	22.60	22.63	infinite	1.96	44.3
1181	28.87	10.91	35.43	37.07	~100	1.98	73.4
1331	115.05	43.48	39.93	59.04	~ 30	2.04	120.4
2802	19.05	7.20	84.06	84.37	infinite	1.96	165.4
5406	221.27	83.63	162.18	182.47	~100	1.98	361.3

Note: x denotes the average of the FWHM measurements

APPENDIX C

Data and detailed calculations for the materials investigated in Chapter 6

Data for Alumina (Al$_2$O$_3$)

Establishing of the total depth and individual layer thickness, h, as a function of the selected FIB process parameters

Total Depth to NL relationship at DL 3
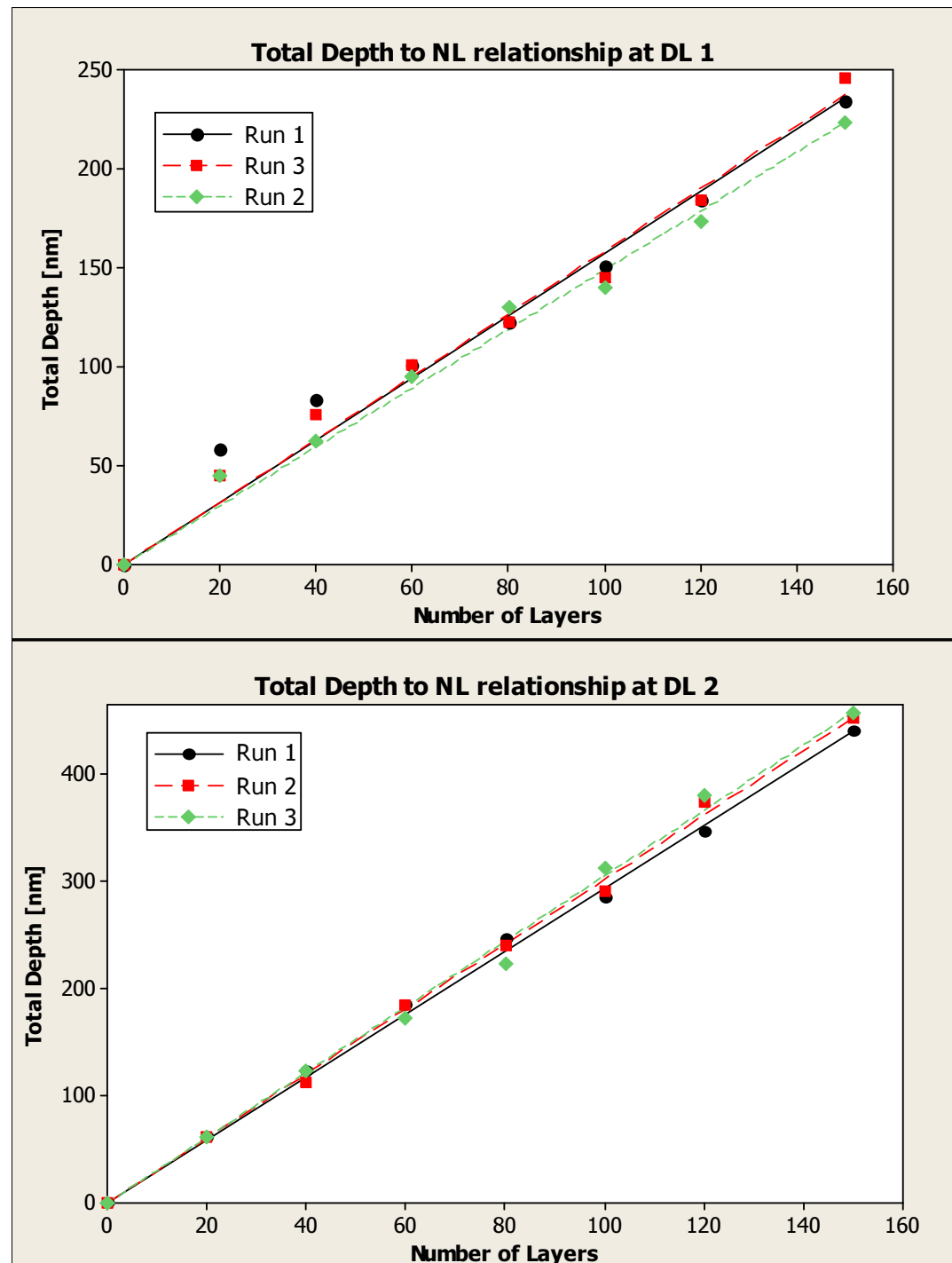
Mean Layer Thickness for Alumina
95% CI for the Mean

Layer thickness, *h*, obtained for Alumina

D_L [µAs/cm^2]	D_L 1 = $2x10^3$	D_L 2 = $4x10^3$	D_L 3 = $6x10^3$
h [nm]	1.5 ±*0.1*	3.0 ±*0.2*	4.5 ±*0.3*

Uncertainty analysis and calculation for the three area doses per layer (D_L)

D_L [µAs/cm^2]	$\bar{h}$, [nm]	$u(\bar{h})$, [nm]	$u(P)$, [nm]	$u_c(h)$, [nm]	V_{eff}	k	$U = k.u_c(h)$, [nm]
D_L 1	1.549	0.03	0.05	0.06	25	2.06	0.12
D_L 2	3.003	0.03	0.09	0.10	~100	1.98	0.19
D_L 3	4.464	0.03	0.13	0.14	~100	1.98	0.27

FIB milling of 3D features- 100 layers convex 2x2 um base pyramids

D_L 1 (Fig. C.1 a): calculated *H* - 150 ± 10 nm; actual *H* – 146.9 nm; deviation - 2%.

D_L 2 (Fig. C.1 b): calculated *H* - 300 ± 20 nm; actual *H* – 317.3 nm; deviation – 5.8%.

D_L 3 (Fig. C.1 c): calculated *H* - 450 ± 30 nm; actual *H* – 464.2 nm; deviation - 3%.
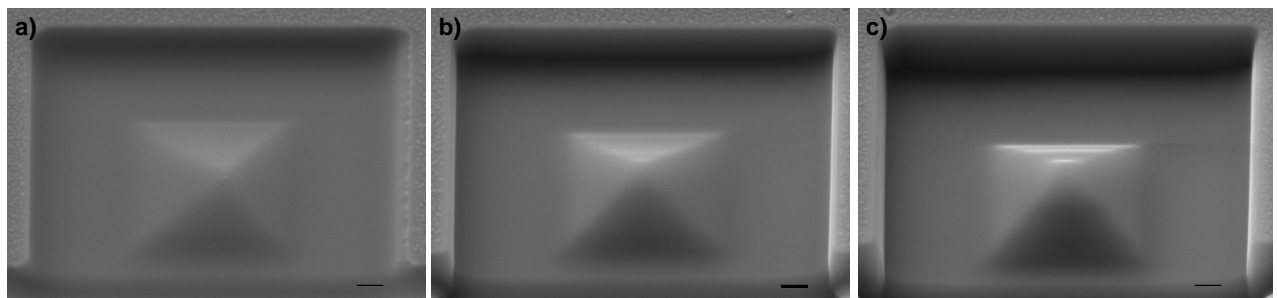
Figure C.1 Convex pyramid with 2x2 µm base in a 4x4 µm trench, produced by FIB milling of 100 layers with a) D_L 1, b) D_L 2 and c) D_L 3. The scale bar denotes 200 nm.

Data for Cobalt ($Co_{80.61}Si_{8.37}Mn_{5.03}C_{2.73}Mo_{1.91}Fe_{1.35}$)

Establishing of the total depth and individual layer thickness, h, as a function of

the selected FIB process parameters

Total Depth to NL relationship at DL 3
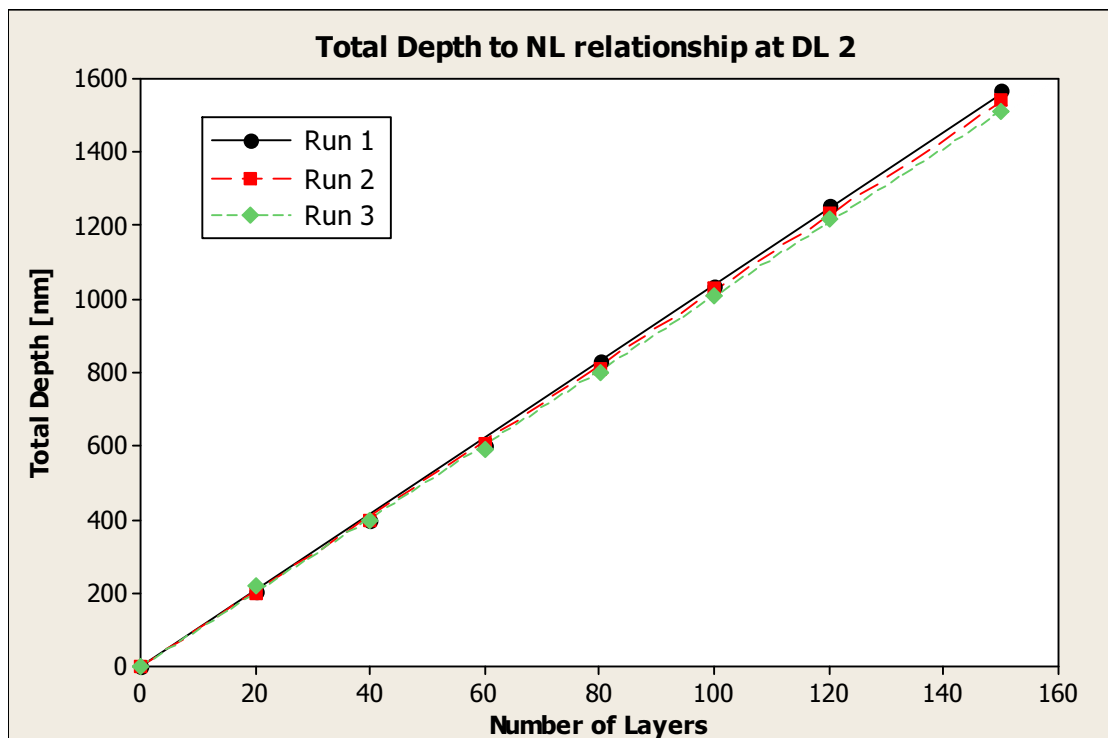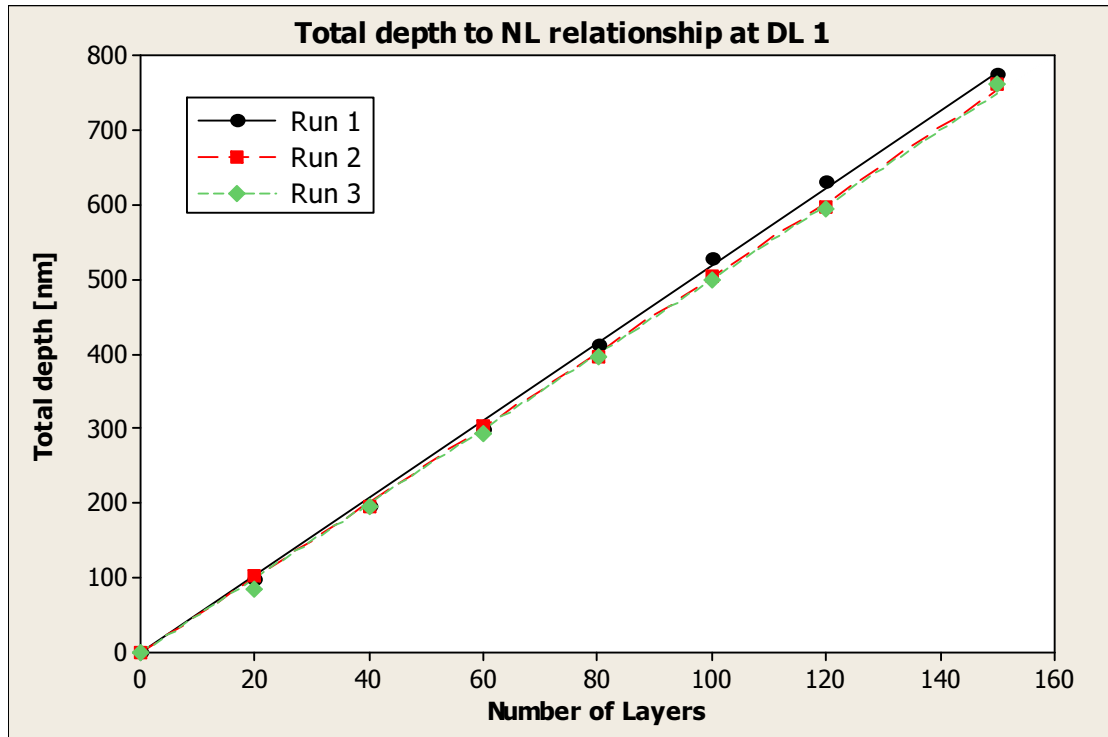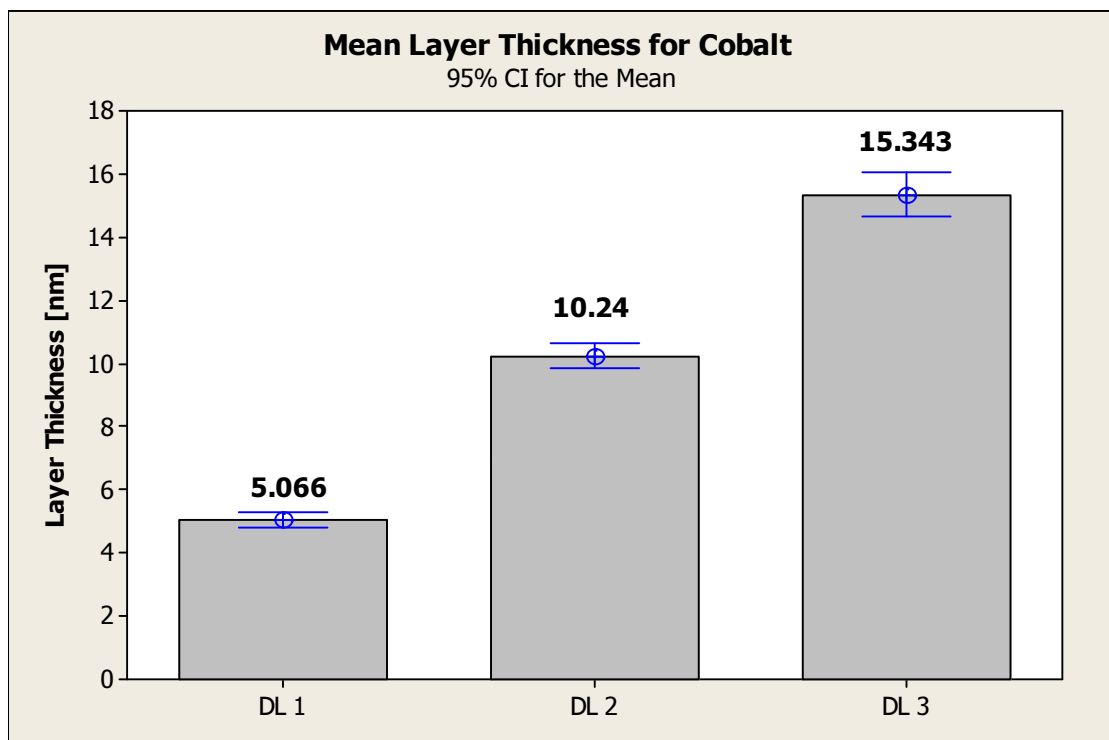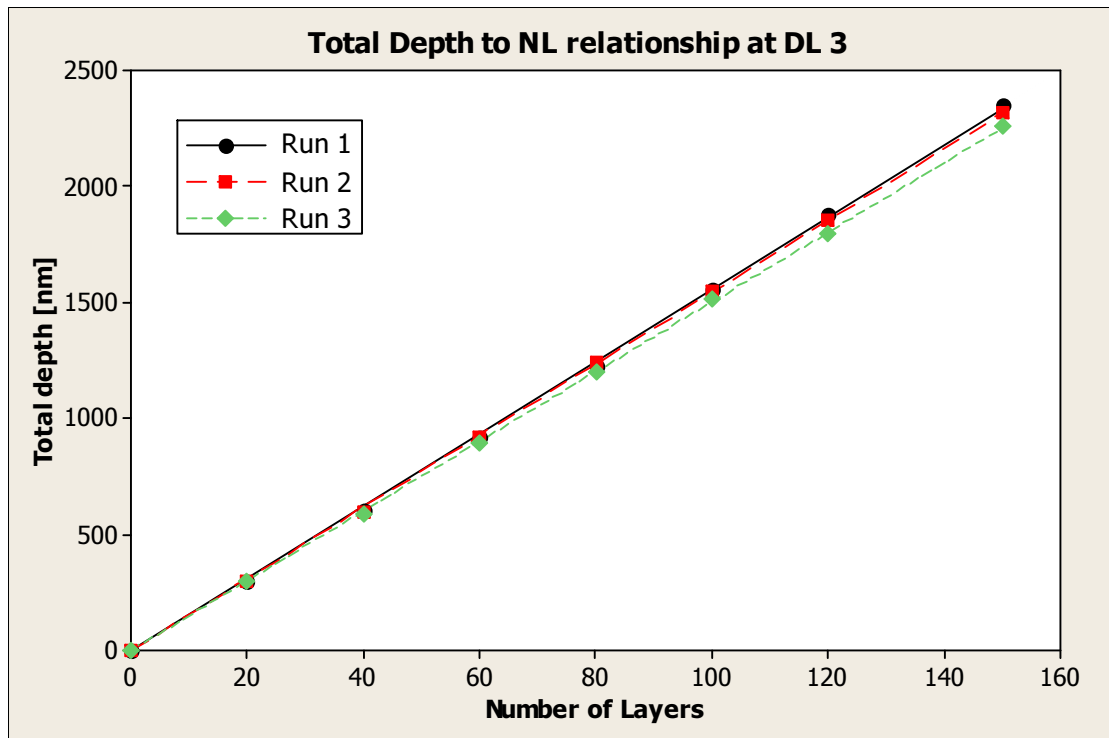
Mean Layer Thickness for Cobalt
95% CI for the Mean

Layer thickness, *h*, obtained for Cobalt

D_L [µAs/cm^2]	D_L 1 = 2x10^3	D_L 2 = 4x10^3	D_L 3 = 6x10^3
h [nm]	5.1 ±0.3	10.2 ±0.6	15.3 ±1.0

Uncertainty analysis and calculation for the three area doses per layer (D_L)

D_L [µAs/cm^2]	$\bar{h}$, [nm]	$u(\bar{h})$, [nm]	$u(P)$, [nm]	$u_c(h)$, [nm]	V_{eff}	k	$U = k.u_c(h)$, [nm]
D_L 1	5.066	0.06	0.15	0.16	~100	1.98	0.32
D_L 2	10.240	0.09	0.31	0.32	~100	1.98	0.64
D_L 3	15.343	0.17	0.46	0.49	~100	1.98	0.97

FIB milling of 3D features – 100 layers convex pyramid

D_L 1 (Fig. C.2 a): calculated *H* - 510 ± 30 nm; actual *H* – 519.2 nm; deviation – 1.8%.

D_L 2 (Fig. C.2b): calculated *H* - 1020 ± 60 nm; actual *H* – 1063 nm; deviation – 4.2%.

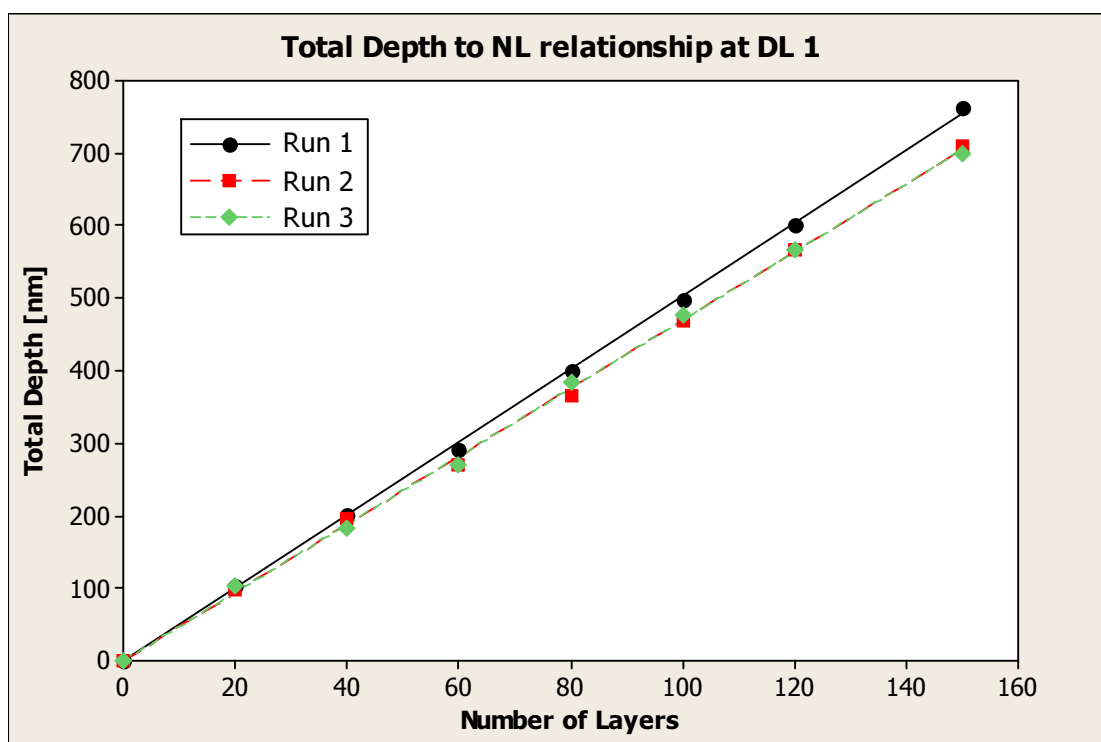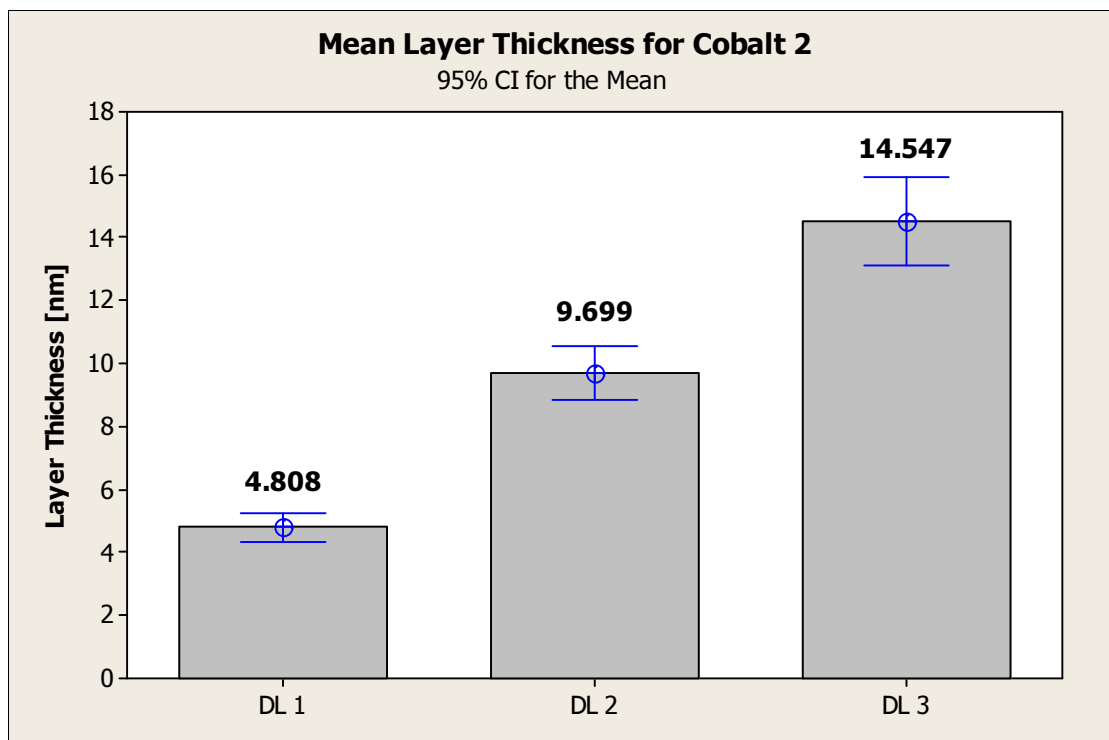**D_L 3** (Fig. C.2 c): calculated *H* - 1530 ± 100 nm; actual *H* – 1606 nm; deviation - 5%.
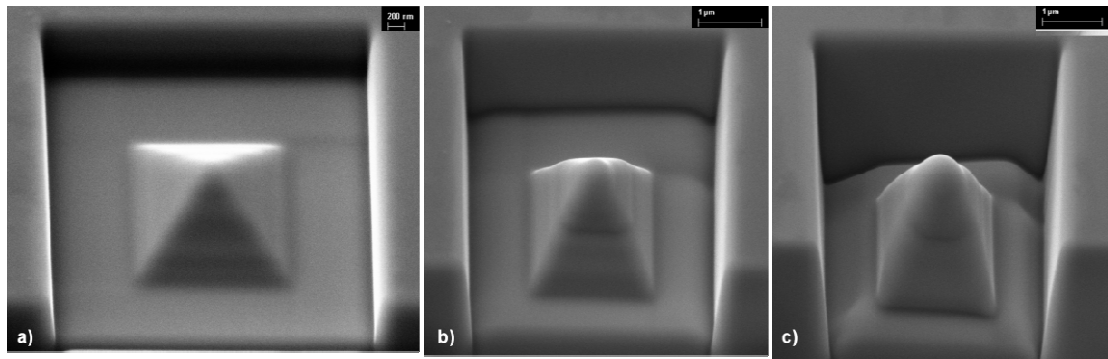
Figure C.2 Convex pyramid with 2x2 µm base in a 4x4 µm trench, produced by FIB milling of 100 layers with a) D_L 1, b) D_L 2 and c) D_L 3.

Data for Cobalt* ($Co_{81.29}Si_{8.26}Mn_{4.95}C_{2.17}Mo_{2.10}Fe_{1.24}$)

Establishing of the total depth and individual layer thickness, h, as a function of the selected FIB process parameters

Total Depth to NL relationship at DL 3
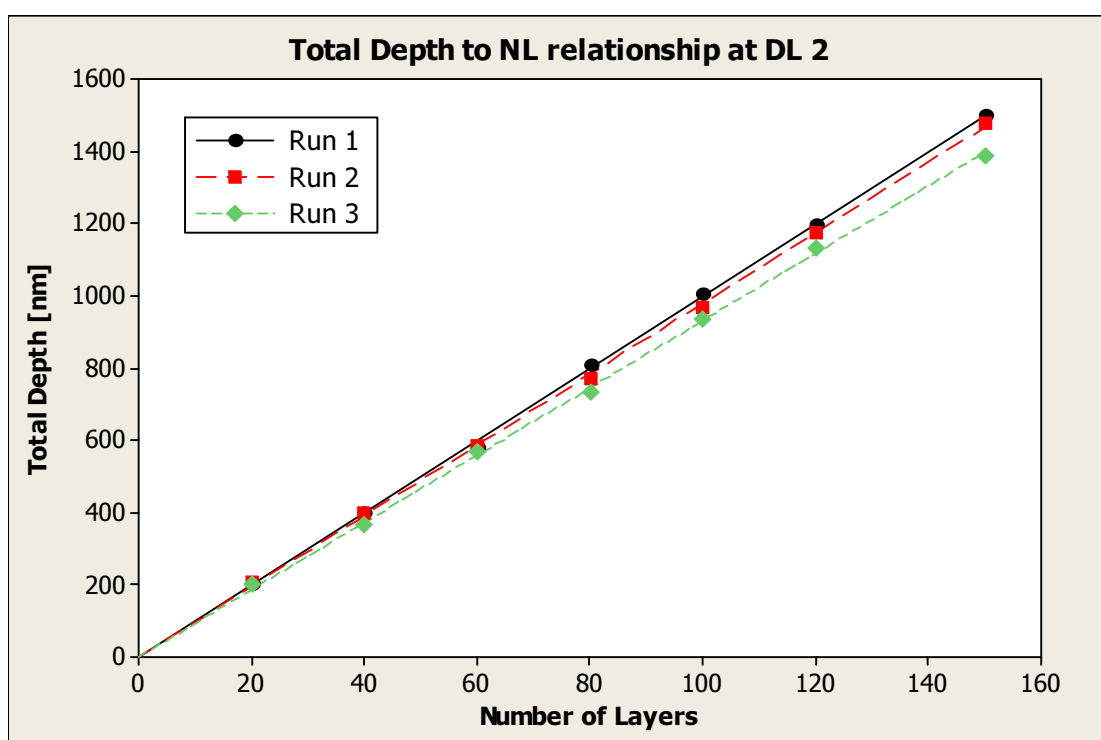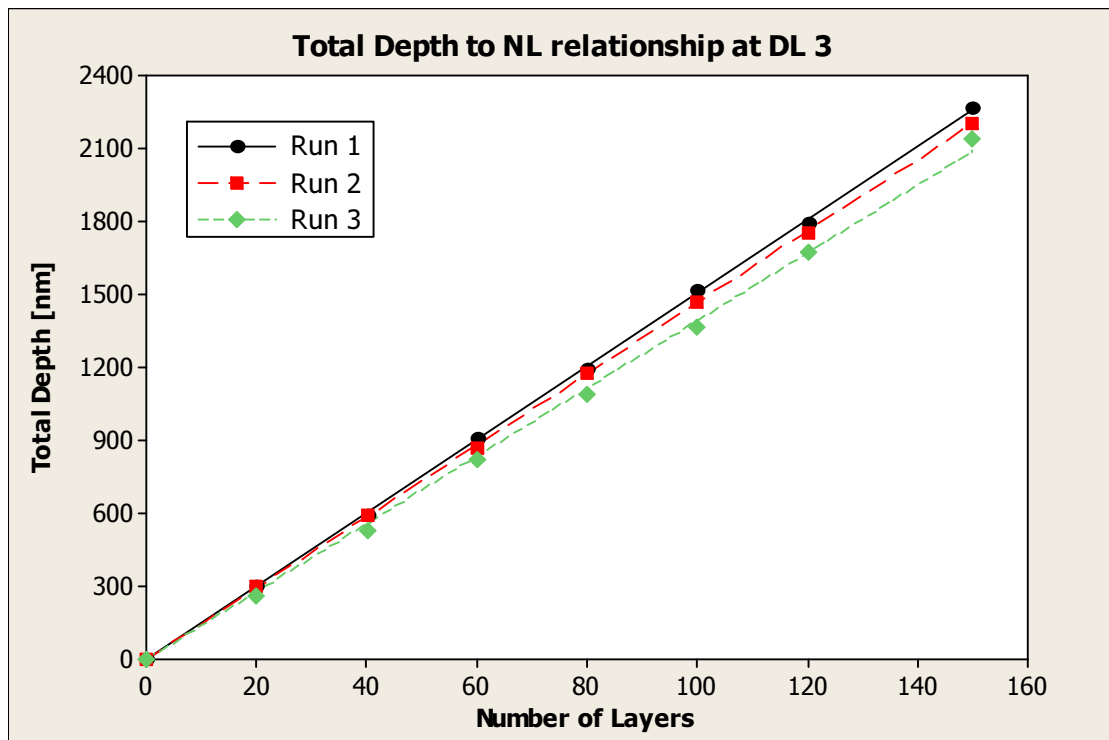
Mean Layer Thickness for Cobalt 2
95% CI for the Mean

Layer thickness, *h*, obtained for Cobalt*

D_L [μAs/cm^2]	$D_L 1 = 2x10^3$	$D_L 2 = 4x10^3$	$D_L 3 = 6x10^3$
h [nm]	4.8 ±0.4	9.7 ±0.7	14.5 ±1.2

Uncertainty analysis and calculation for the three area doses per layer (D_L)

D_L [μAs/cm^2]	$\bar{h}$, [nm]	$u(\bar{h})$, [nm]	$u(P)$, [nm]	$u_c(h)$, [nm]	V_{eff}	k	$U = k.u_c(h)$, [nm]
$D_L 1$	4.808	0.11	0.14	0.18	15	2.13	0.39
$D_L 2$	9.699	0.20	0.29	0.35	20	2.09	0.74
$D_L 3$	14.547	0.33	0.44	0.54	16	2.12	1.16

FIB milling of 3D features – 100 layers convex pyramid

D_L 1 (Fig. C.3 a): calculated *H* - 480 ± 40 nm; actual *H* – 464.2 nm; deviation – 3.3%.

D_L 2 (Fig. C.3 b): calculated *H* - 970 ± 70 nm; actual *H* – 952 nm; deviation – 1.9%.

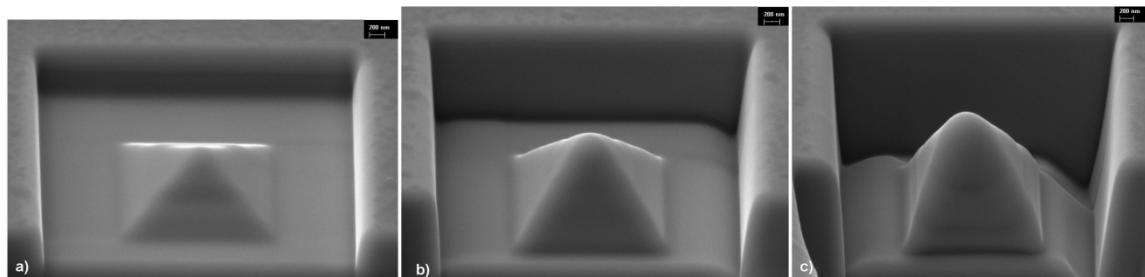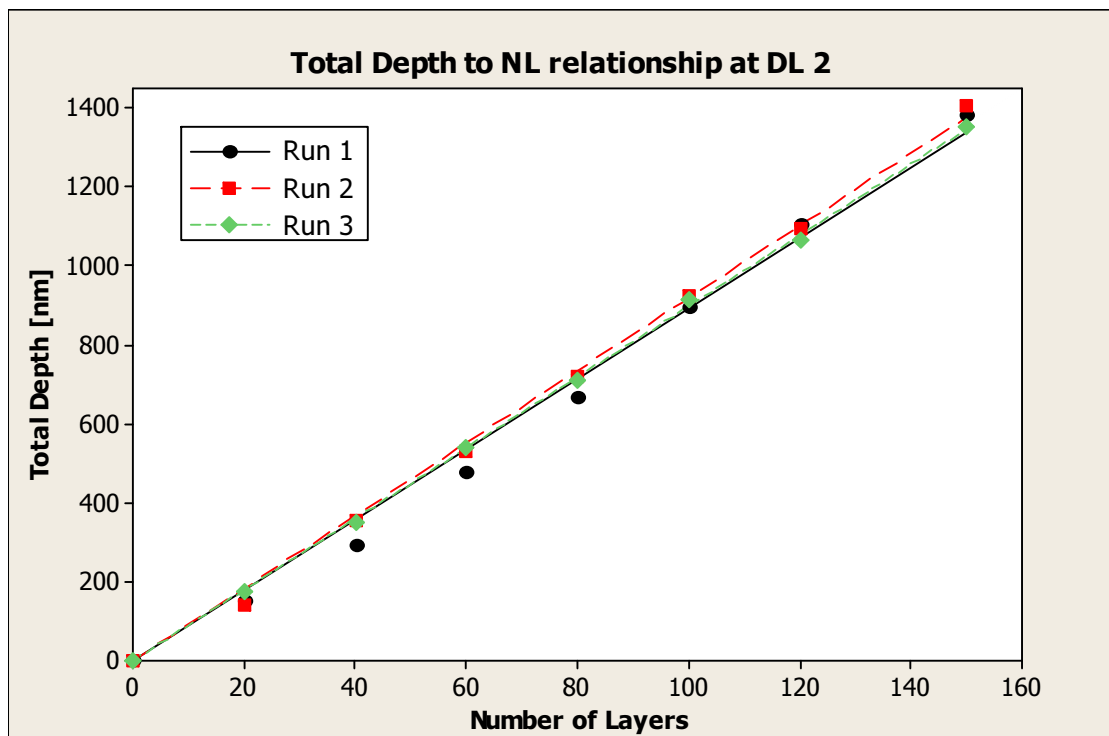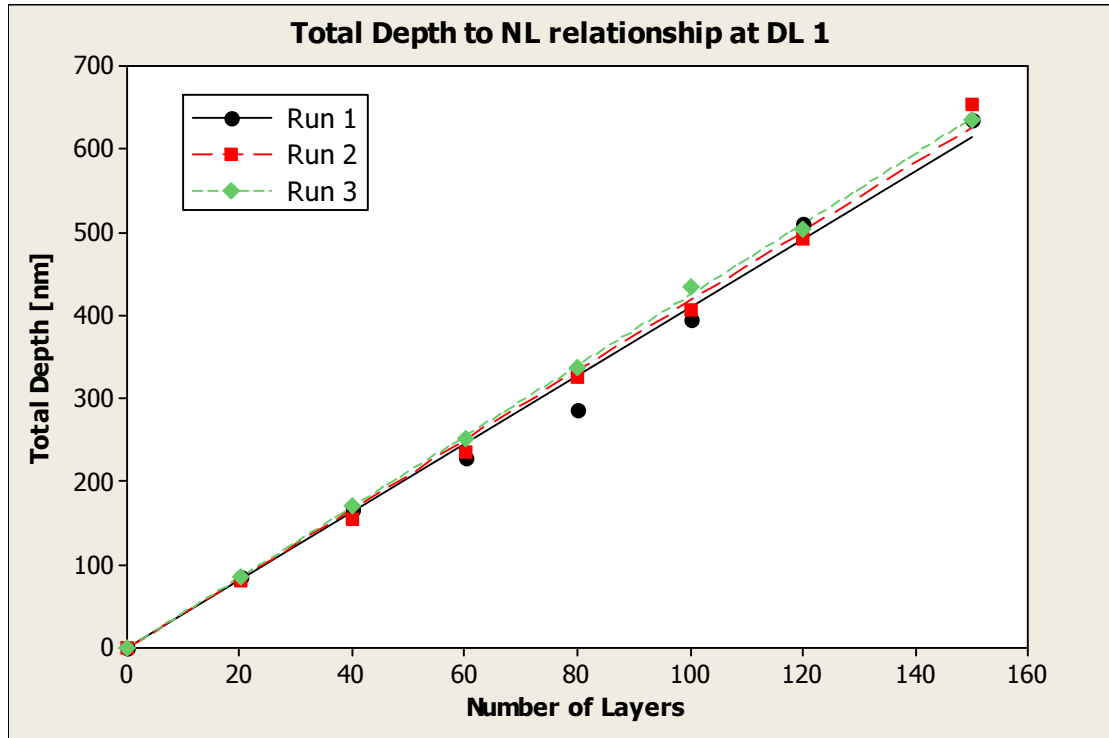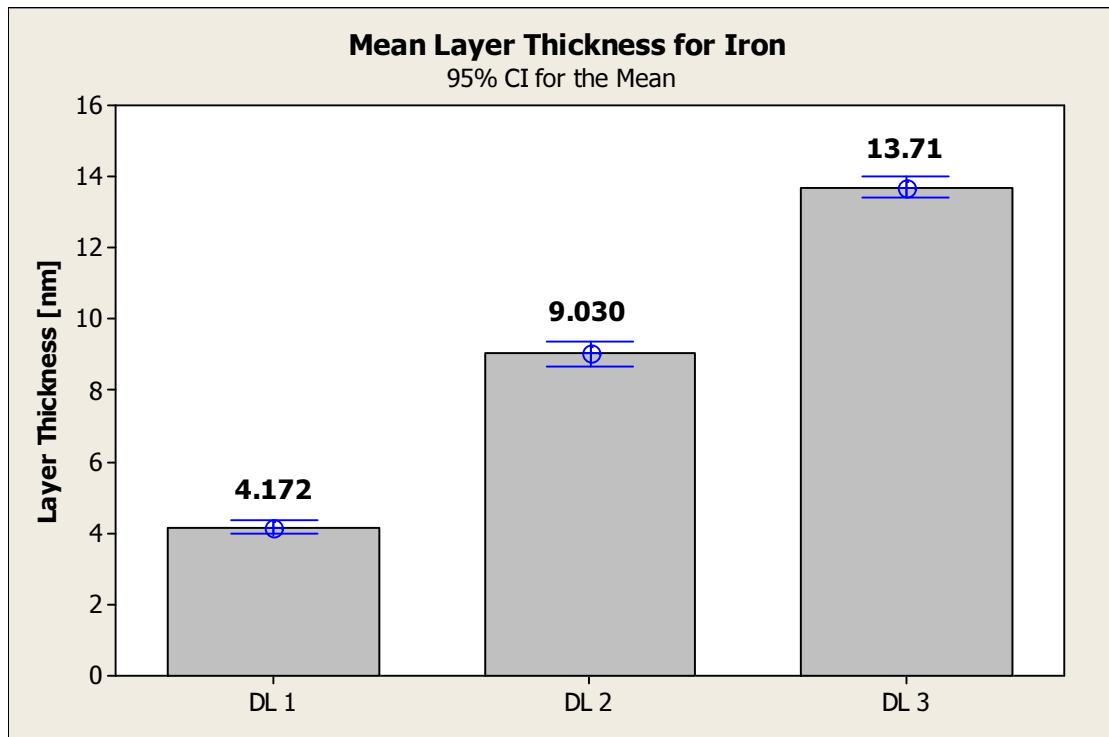**D_L 3** (Fig. C.3c): calculated *H*- 1450 ± 120 nm; actual *H*– 1530 nm; deviation– 5.5%.

Figure C.3 Convex pyramid with 2x2 μm base in a 4x4 μm trench, produced by FIB milling of 100 layers with a) D_L 1, b) D_L 2 and c) D_L 3.

Data for Iron (Fe$_{81}$B$_{13.5}$Si$_{3.5}$C$_2$)

Establishing of the total depth and individual layer thickness, h, as a function of

the selected FIB process parameters

Total Depth to NL relationship at DL 3
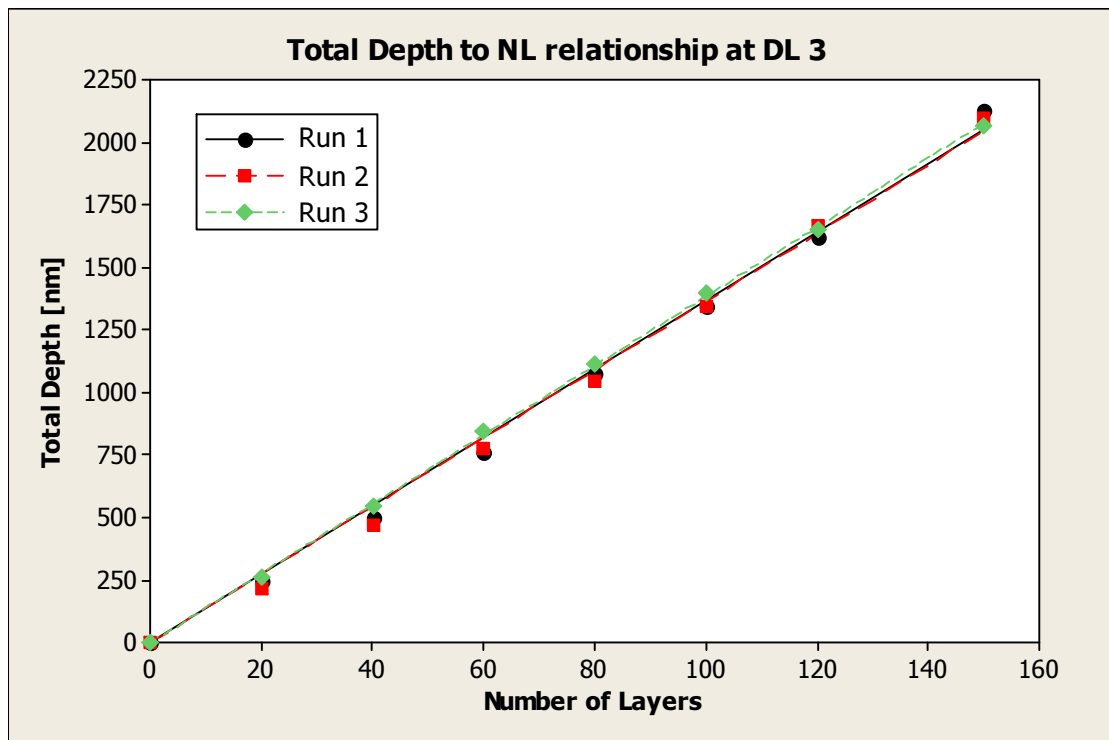
Mean Layer Thickness for Iron
95% CI for the Mean

Layer thickness, *h*, obtained for Iron

D_L [μAs/cm^2]	D_L 1 = 2x10^3	D_L 2 = 4x10^3	D_L 3 = 6x10^3
h [nm]	4.2 ±0.3	9.0 ±0.6	13.7 ±0.8

Uncertainty analysis and calculation for the three area doses per layer (D_L)

D_L [μAs/cm^2]	$\bar{h}$, [nm]	$u(\bar{h})$, [nm]	$u(P)$, [nm]	$u_c(h)$, [nm]	ν_{eff}	k	$U = k.u_c(h)$, [nm]
D_L 1	4.172	0.04	0.13	0.13	~100	1.98	0.26
D_L 2	9.030	0.08	0.27	0.28	~100	1.98	0.56
D_L 3	13.710	0.07	0.41	0.42	infinite	1.96	0.82

FIB milling of 3D features – 100 layers convex pyramid

D_L 1 (Fig. C.4 a): calculated *H* - 420 ± 30 nm; actual *H* – 426.7 nm; deviation – 1.6%.

D_L 2 (Fig. C.4 b): calculated *H* - 900 ± 60 nm; actual *H* – 931.6 nm; deviation – 3.5%.

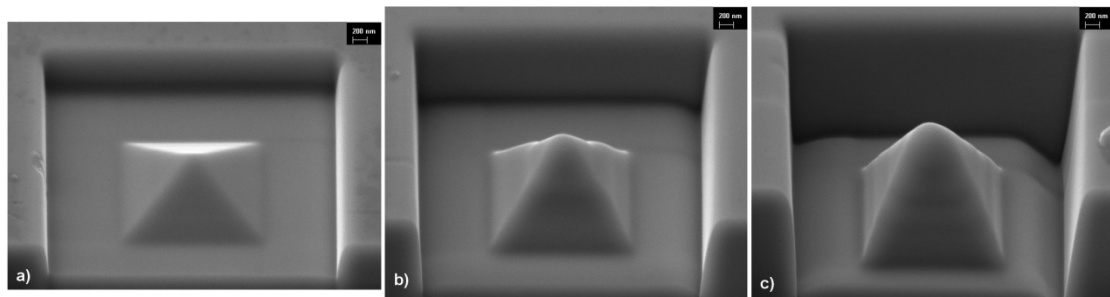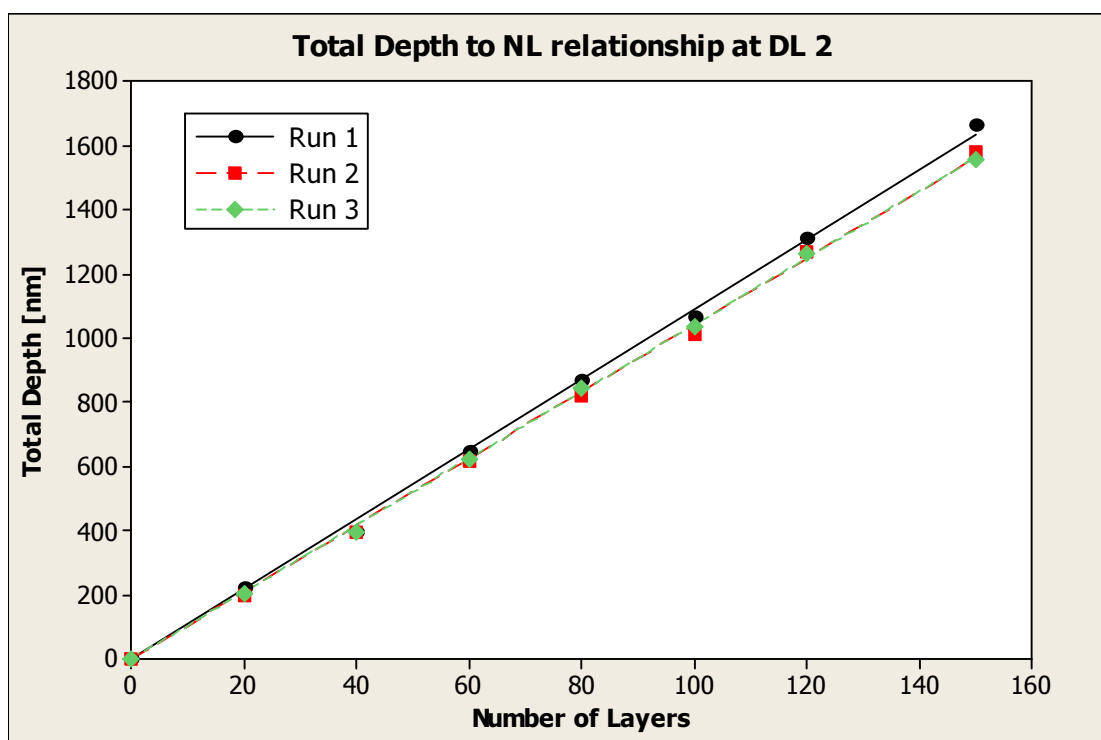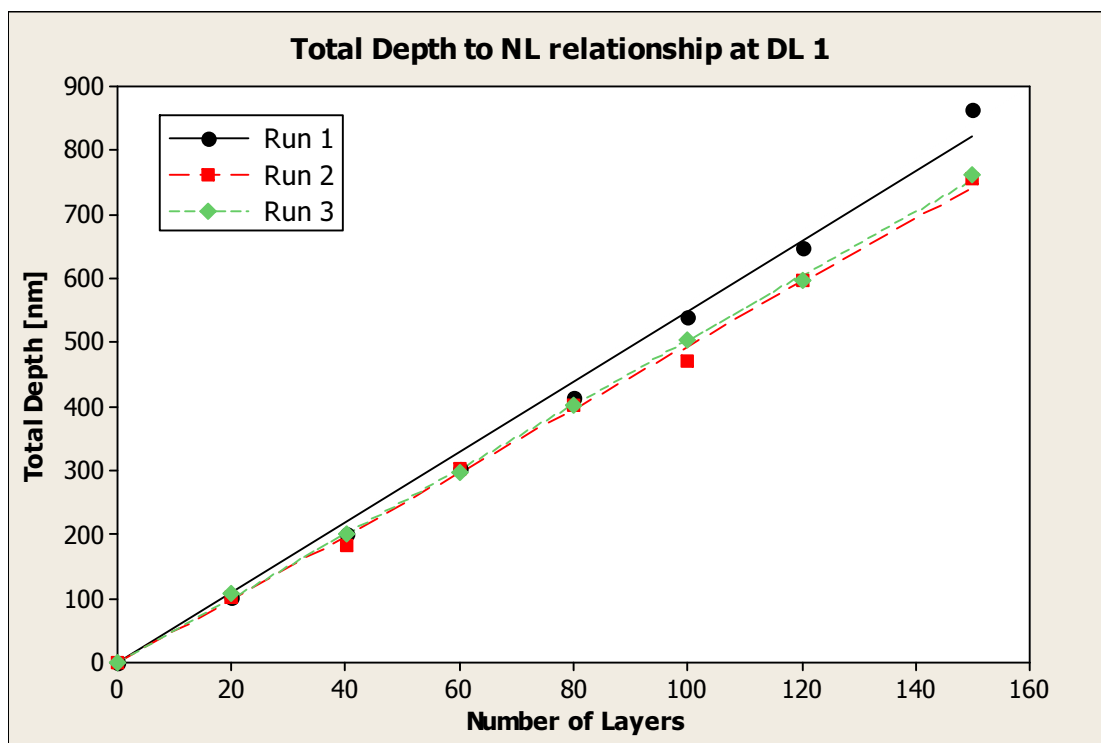**D_L 3** (Fig.C.4c): calculated *H* - 1370 ± 80 nm; actual *H* – 1358 nm; deviation – 0.9%.

Figure C.4 Convex pyramid with 2x2 μm base in a 4x4 μm trench, produced by FIB milling of 100 layers with a) D_L 1, b) D_L 2 and c) D_L 3

Data for Nickel (Ni$_{92.58}$Si$_{5.15}$Fe$_{0.29}$C$_{1.98}$)

Establishing of the total depth and individual layer thickness, h, as a function of

the selected FIB process parameters

Total Depth to NL relationship at DL 1

Total Depth to NL relationship at DL 2

Total Depth to NL relationship at DL 3
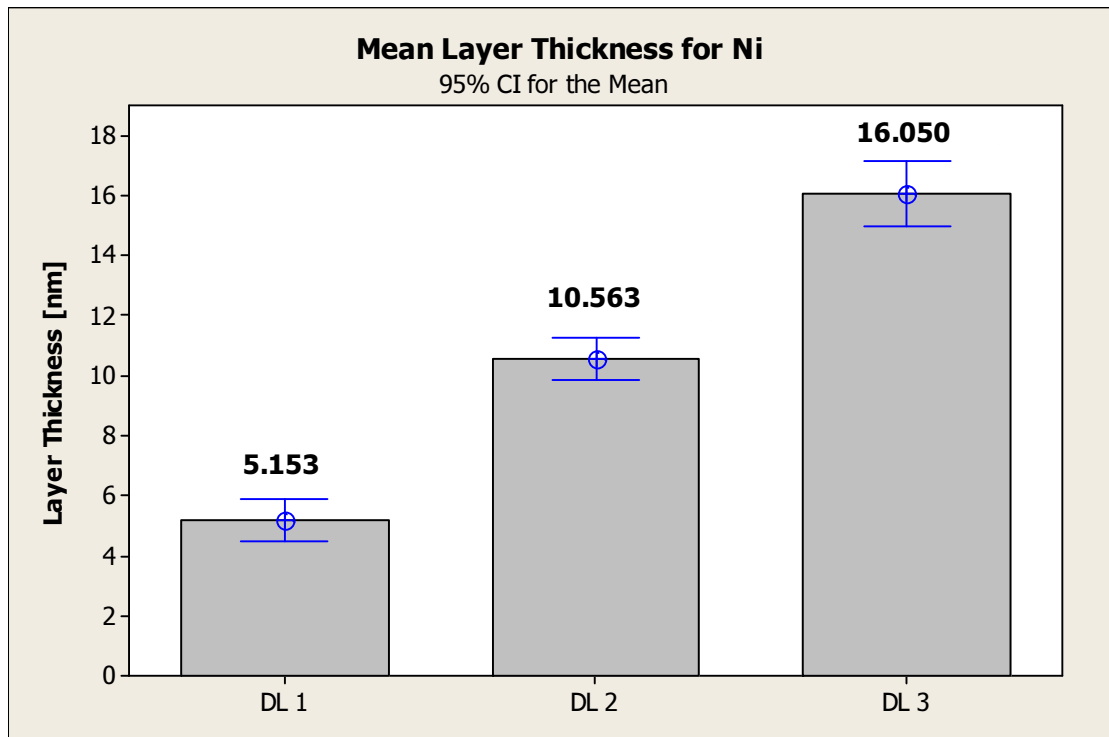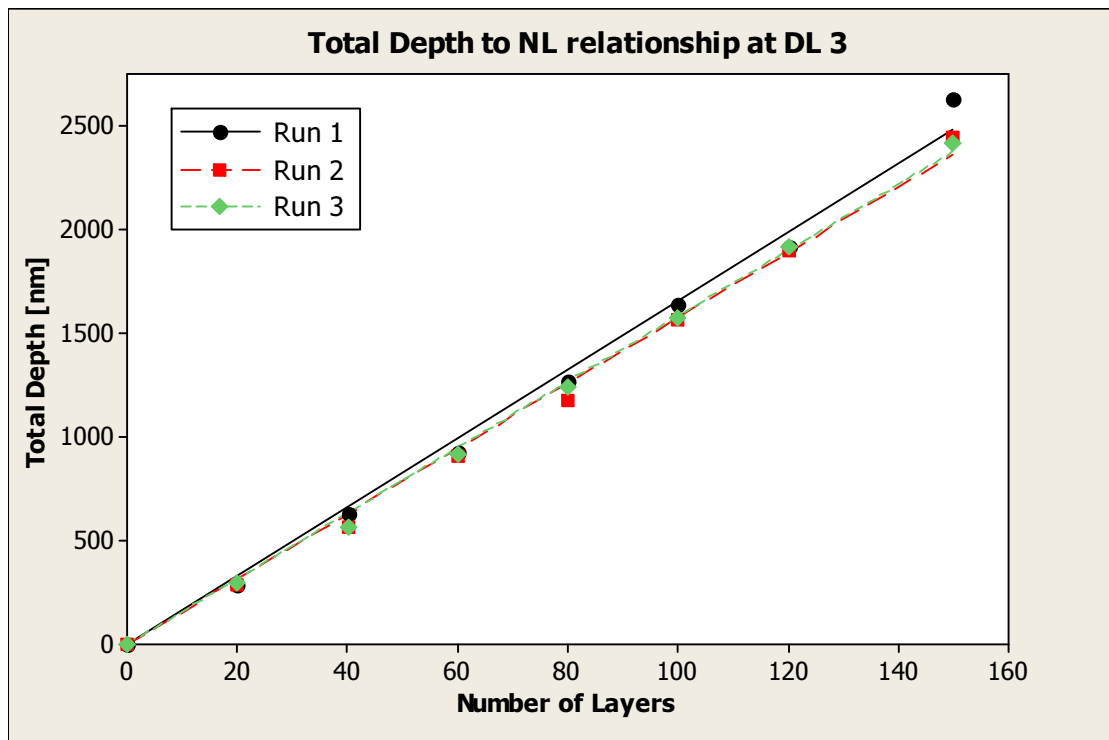
Mean Layer Thickness for Ni
95% CI for the Mean

Layer thickness, *h*, obtained for Nickel

D_L [µAs/cm^2]	D_L 1 = 2x10^3	D_L 2 = 4x10^3	D_L 3 = 6x10^3
h [nm]	5.2 ±0.5	10.6 ±0.7	16.0 ±1.1

Uncertainty analysis and calculation for the three area doses per layer (D_L)

D_L [µAs/cm^2]	$\bar{h}$, [nm]	$u(\bar{h})$, [nm]	$u(P)$, [nm]	$u_c(h)$, [nm]	ν_{eff}	k	$U = k.u_c(h)$, [nm]
D_L 1	5.153	0.16	0.15	0.23	7	2.36	0.53
D_L 2	10.563	0.16	0.32	0.36	40	2.02	0.72
D_L 3	16.050	0.26	0.48	0.55	40	2.02	1.10

FIB milling of 3D features – 100 layers convex pyramid

D_L 1 (Fig. C.5 a): calculated *H* - 520 ± 50 nm; actual *H* – 511.2 nm; deviation – 1.7%.

D_L 2 (Fig. C.5b): calculated *H* - 1060 ± 70 nm; actual *H* – 1022 nm; deviation – 3.6%.

D_L 3 (Fig. C.5c): calculated *H*- 1600 ± 110 nm; actual – 1606 nm; deviation– 0.4%.
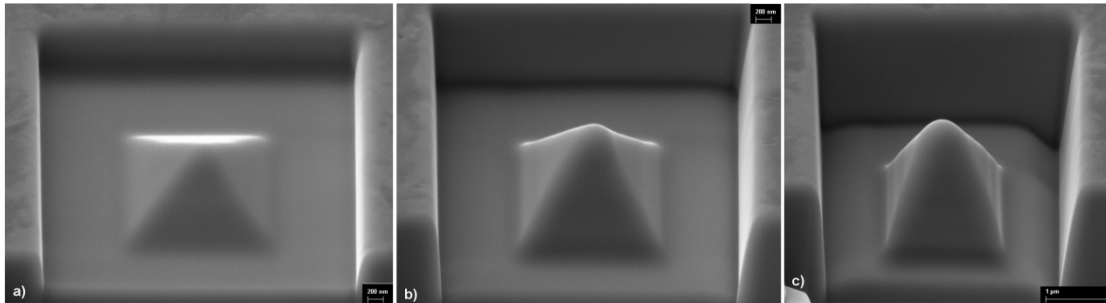
Figure C.5 Convex pyramid with 2x2 µm base in a 4x4 µm trench, produced by FIB milling of 100 layers with a) D_L 1, b) D_L 2 and c) D_L 3

Data for Quartz (SiO$_2$)

Establishing of the total depth and individual layer thickness, h, as a function of the selected FIB process parameters

Total Depth to NL relationship at DL 3
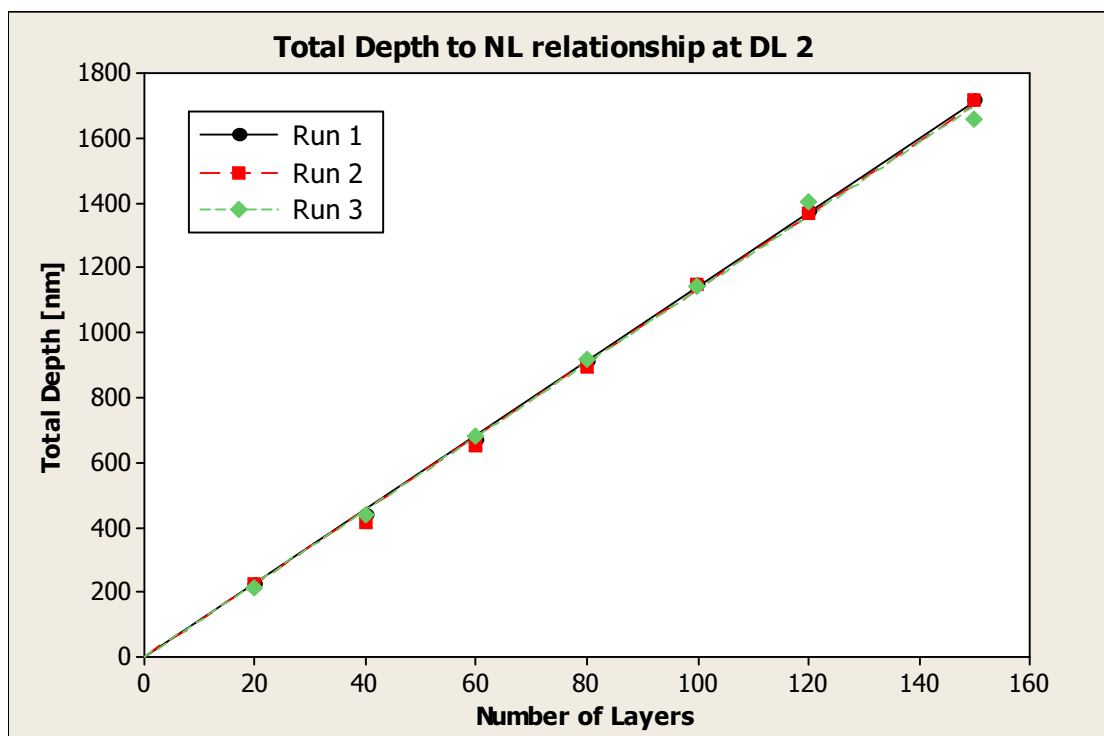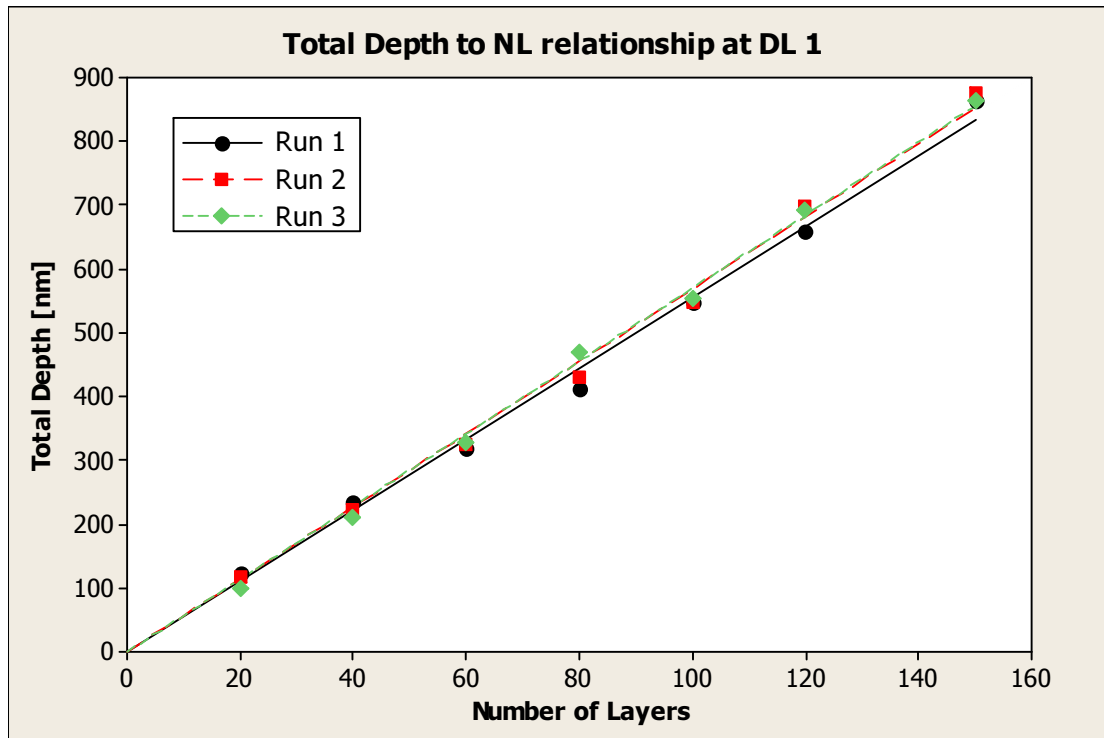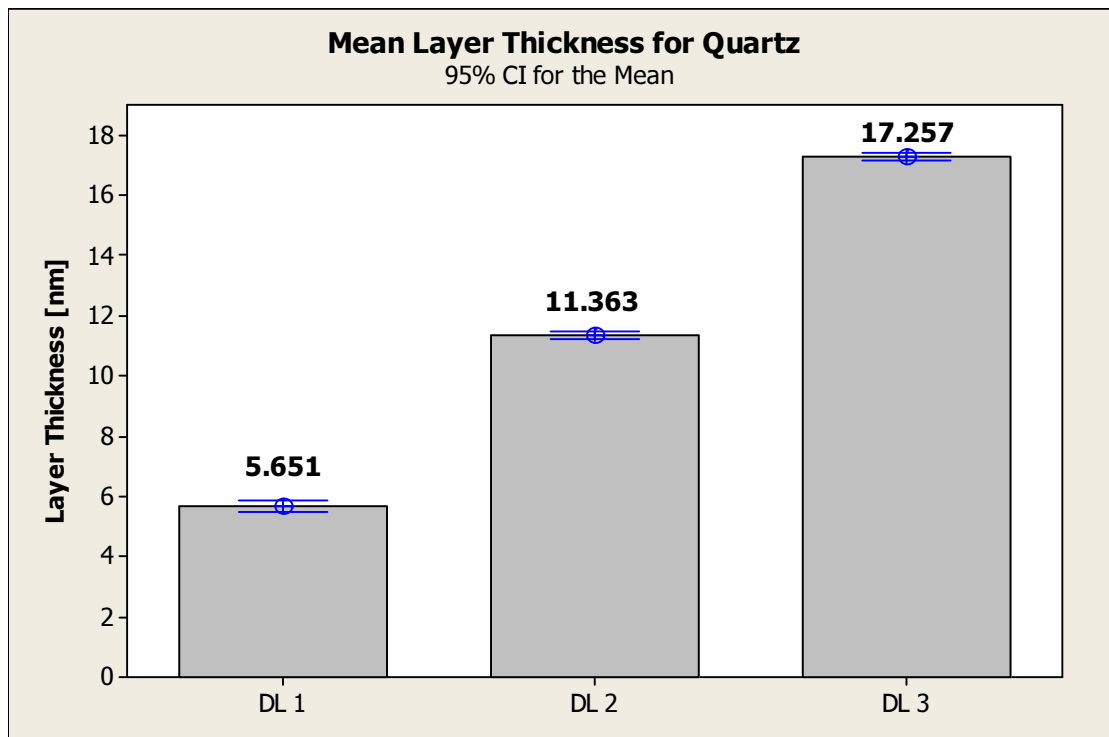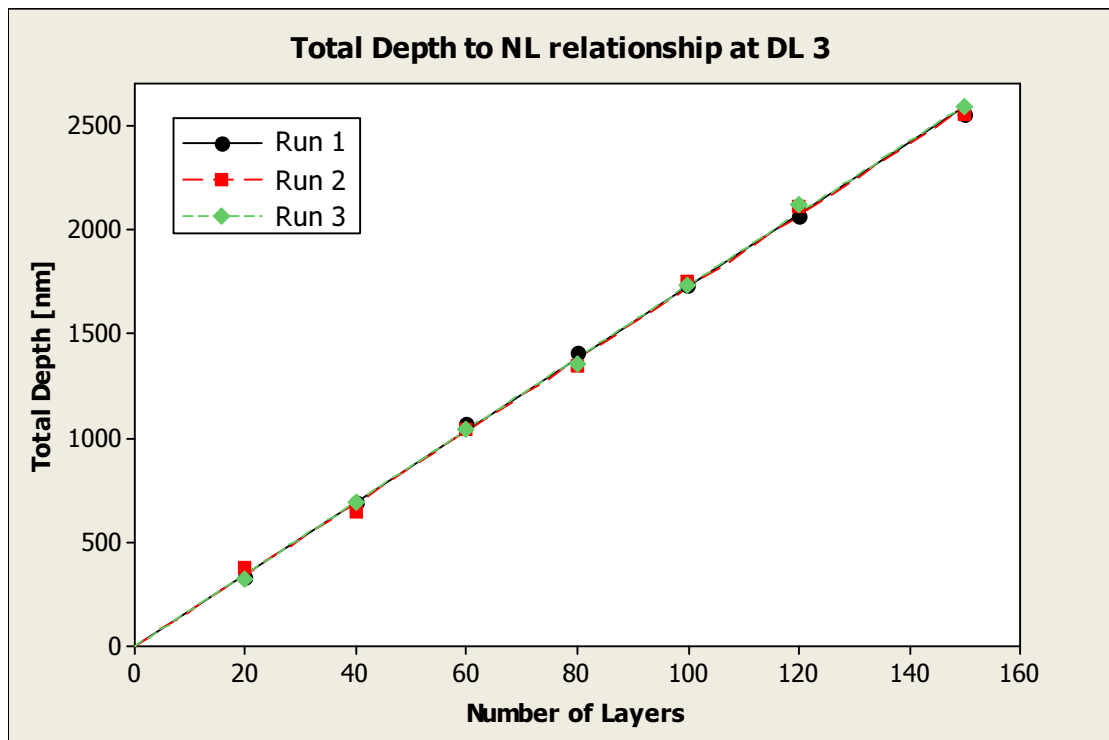
Mean Layer Thickness for Quartz
95% CI for the Mean

Layer thickness, h, obtained for Quartz

$D_L\,[\mu As/cm^2]$	$D_L\,1 = 2x10^3$	$D_L\,2 = 4x10^3$	$D_L\,3 = 6x10^3$
h [nm]	5.7 ±0.3	11.4 ±0.7	17.3 ±1.0

Uncertainty analysis and calculation for the three area doses per layer (D_L)

D_L [$\mu As/cm^2$]	$\bar{h}$, [nm]	$u(\bar{h})$, [nm]	$u(P)$, [nm]	$u_c(h)$, [nm]	ν_{eff}	k	$U = k.u_c(h)$, [nm]
$D_L\,1$	5.651	0.05	0.17	0.18	~100	1.98	0.35
$D_L\,2$	11.363	0.03	0.34	0.34	infinite	1.96	0.67
$D_L\,3$	17.257	0.03	0.52	0.52	infinite	1.96	1.02

FIB milling of 3D features – 61 layers concave pyramid

D_L 1 (Fig. C.6a): calculated H–347.7 ± 18.3nm; actual H–346.1 nm; deviation– 0.5%.

D_L 2 (Fig. C.6b): calculated H– 695.4 ± 42.7nm; actual H–707.1nm; deviation– 1.7%.

D_L 3 (Fig. C.6c): calculated H–1055.3 ± 61 nm; actual H–1001nm; deviation – 5.1%.
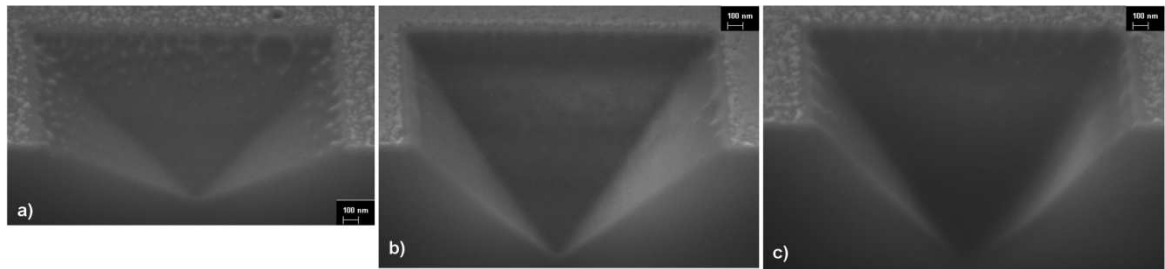
Figure C.6 Concave pyramid with 2x2 µm base, produced by FIB milling of 61 layers with a) D_L 1, b) D_L 2 and c) D_L 3

Data for Silicon (Si)

Establishing of the total depth and individual layer thickness, h, as a function of the selected FIB process parameters

Total Depth to NL relationship at DL 1

Total Depth to NL relationship at DL 2

Total Depth to NL relationship at DL 3
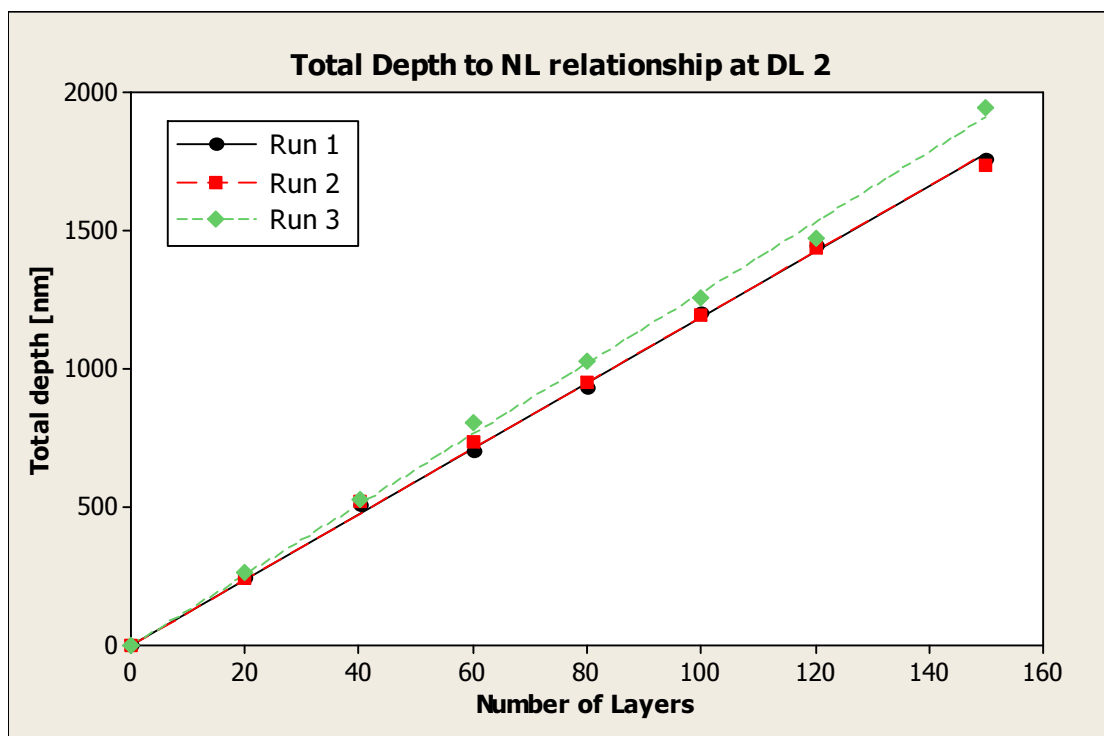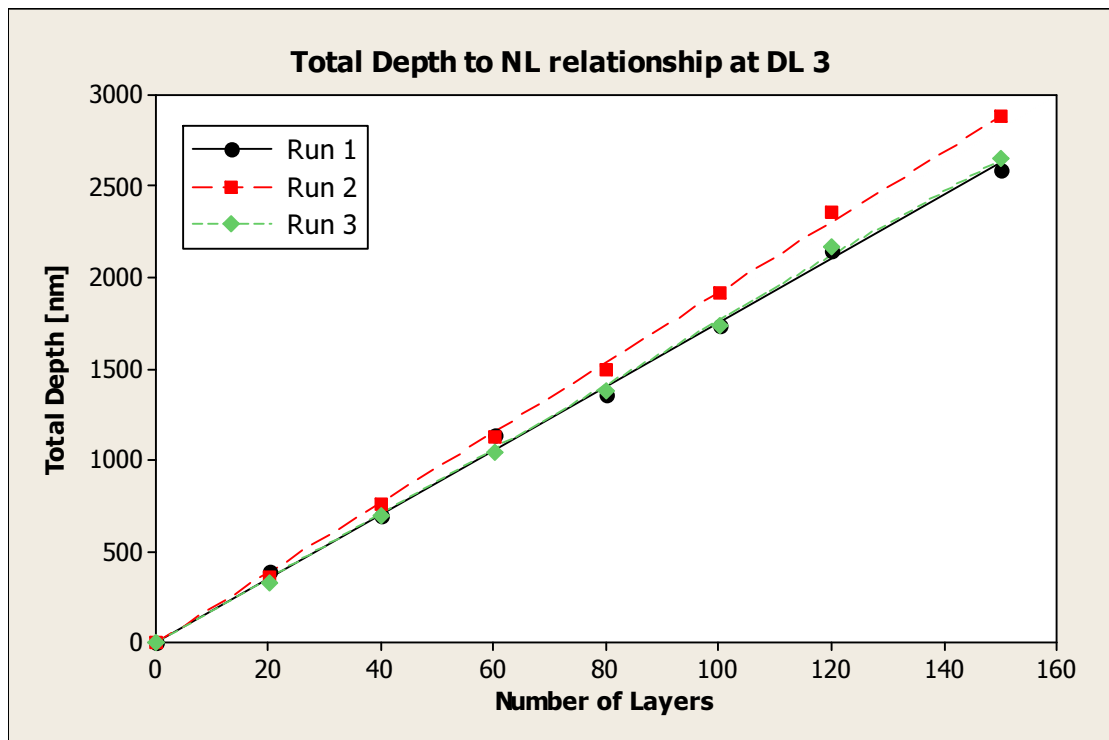
Mean Layer Thickness for Silicon
95% CI for the Mean

Layer thickness, *h*, obtained for Silicon

D_L [μAs/cm^2]	D_L 1 = 2x10^3	D_L 2 = 4x10^3	D_L 3 = 6x10^3
h [nm]	5.9 ±*0.4*	12.2 ±*1.0*	18.1 ±*1.8*

Uncertainty analysis and calculation for the three area doses per layer (D_L)

D_L [μAs/cm^2]	$\bar{h}$, [nm]	$u(\bar{h})$, [nm]	$u(P)$, [nm]	$u_c(h)$, [nm]	v_{eff}	k	$U = k.u_c(h)$, [nm]
D_L 1	5.908	0.03	0.18	0.18	infinite	1.96	0.35
D_L 2	12.153	0.30	0.36	0.47	12	2.18	1.03
D_L 3	18.133	0.54	0.54	0.77	8	2.31	1.77

FIB milling of 3D features – 100 layers convex pyramid

D_L 1 (Fig. C.7a): calculated *H*-359.9±24.4 nm; actual *H* – 364.7nm; deviation – 1.3%.

D_L 2 (Fig. C.7b): calculated *H*- 744.2 ± 61nm; actual *H* – 748.1 nm; deviation – 0.5%.

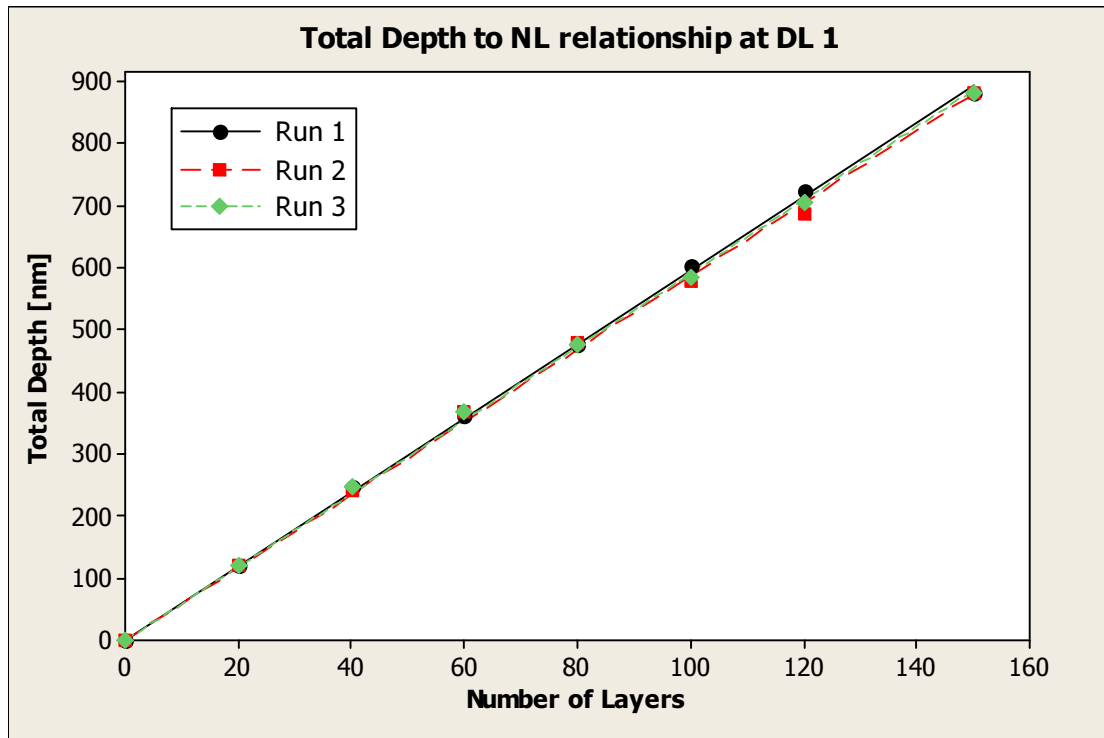**D_L 3** (Fig.C.7c): calculated *H* –1104.1±109.8nm; actual *H* – 1001nm; deviation - 9%.
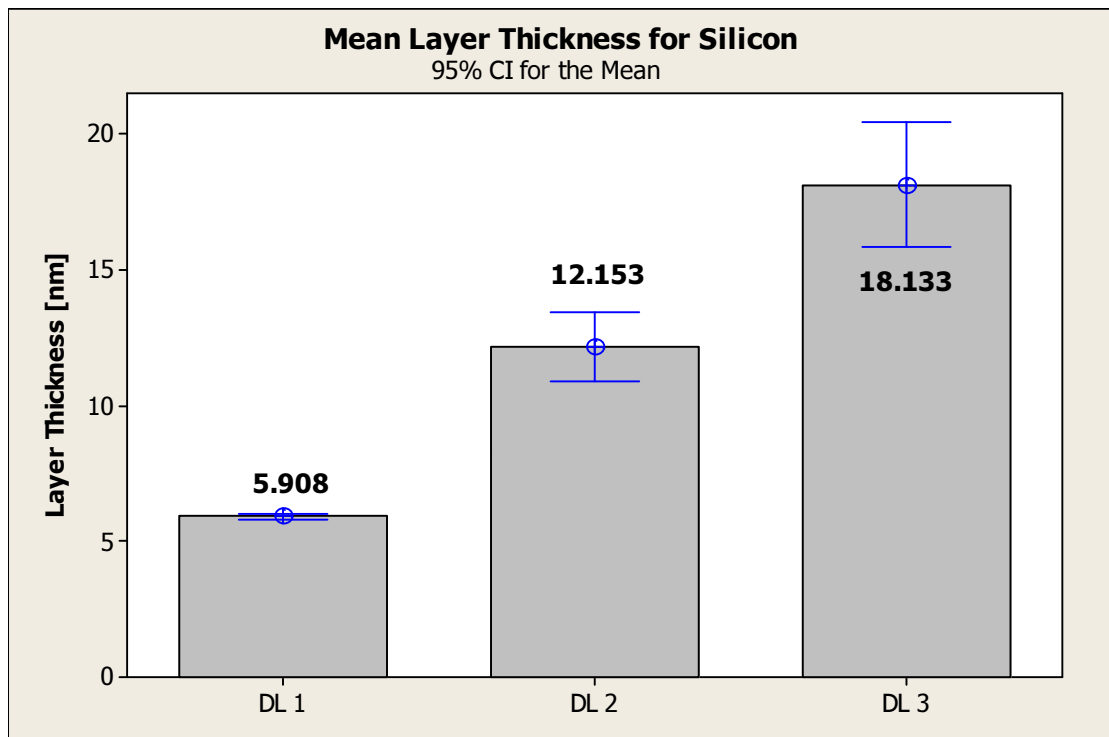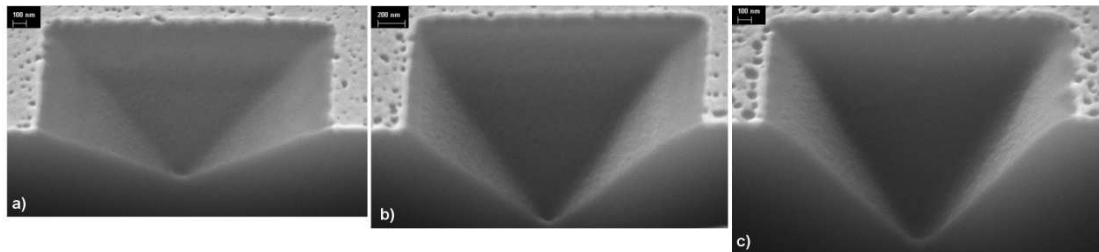

Figure C.7 Concave pyramid with 2x2 μm base, produced by FIB milling of 61 layers with a) D_L 1, b) D_L 2 and c) D_L 3

Data for Ti BMG (Ti$_{42}$Zr$_{24}$Co$_{16}$Ni$_{15}$Be$_{4}$)

Establishing of the total depth and individual layer thickness, h, as a function of

the selected FIB process parameters

Total Depth to NL relationship at DL 3
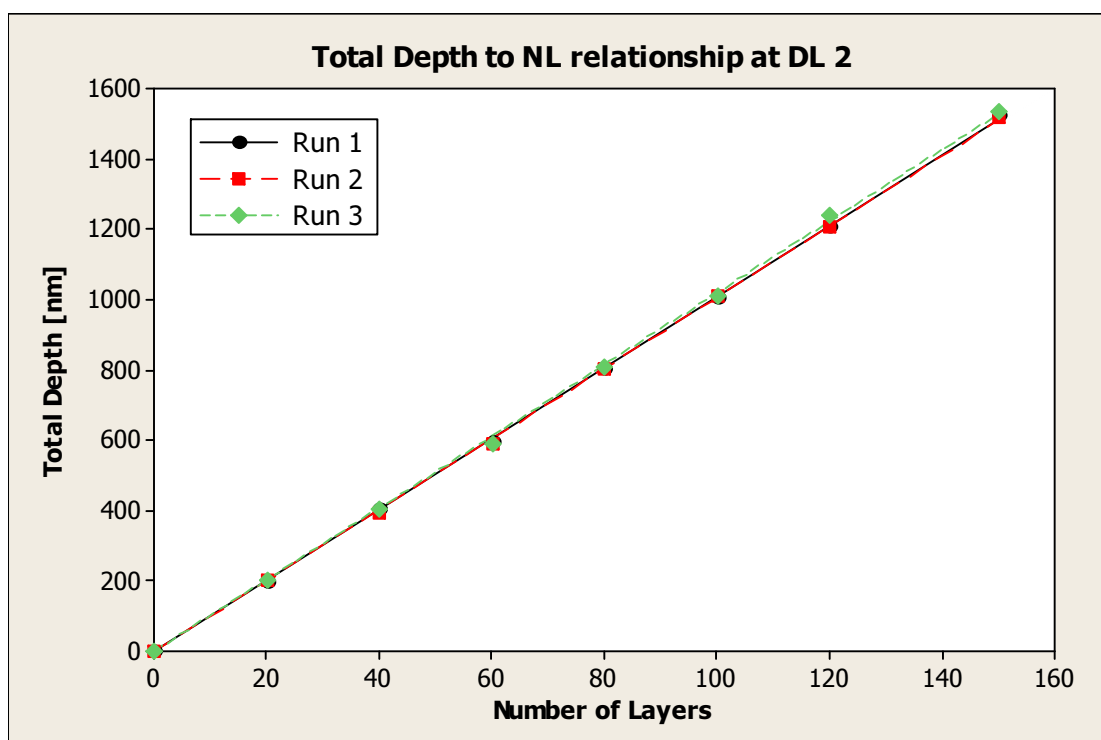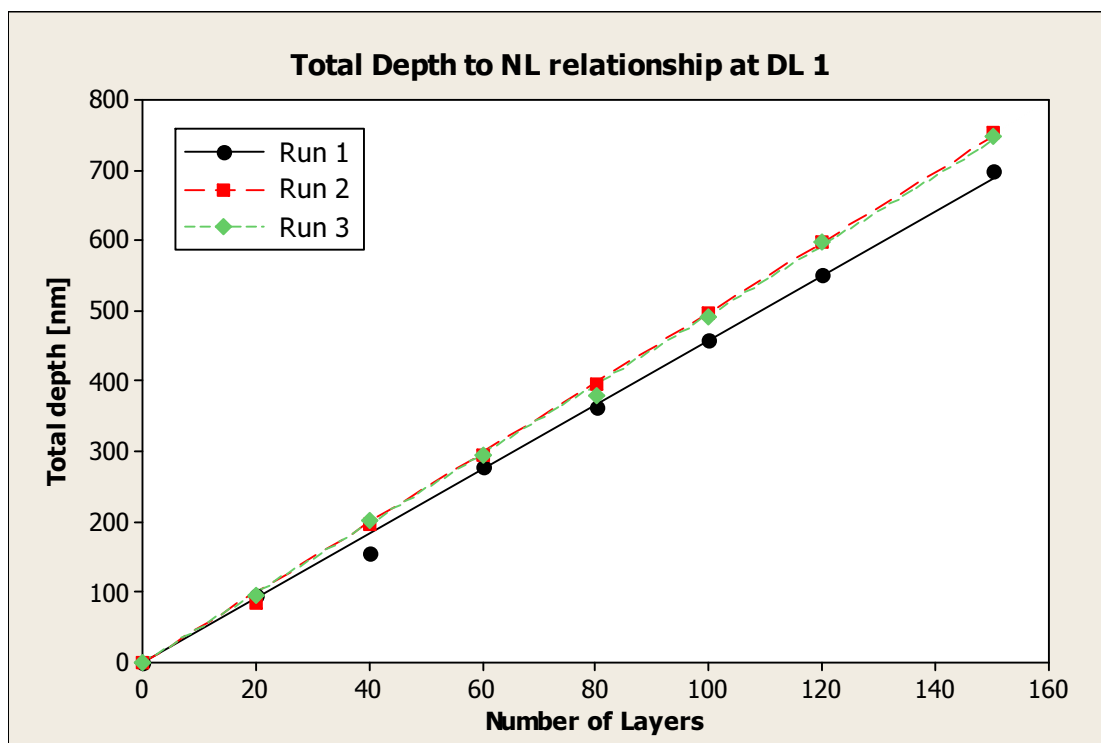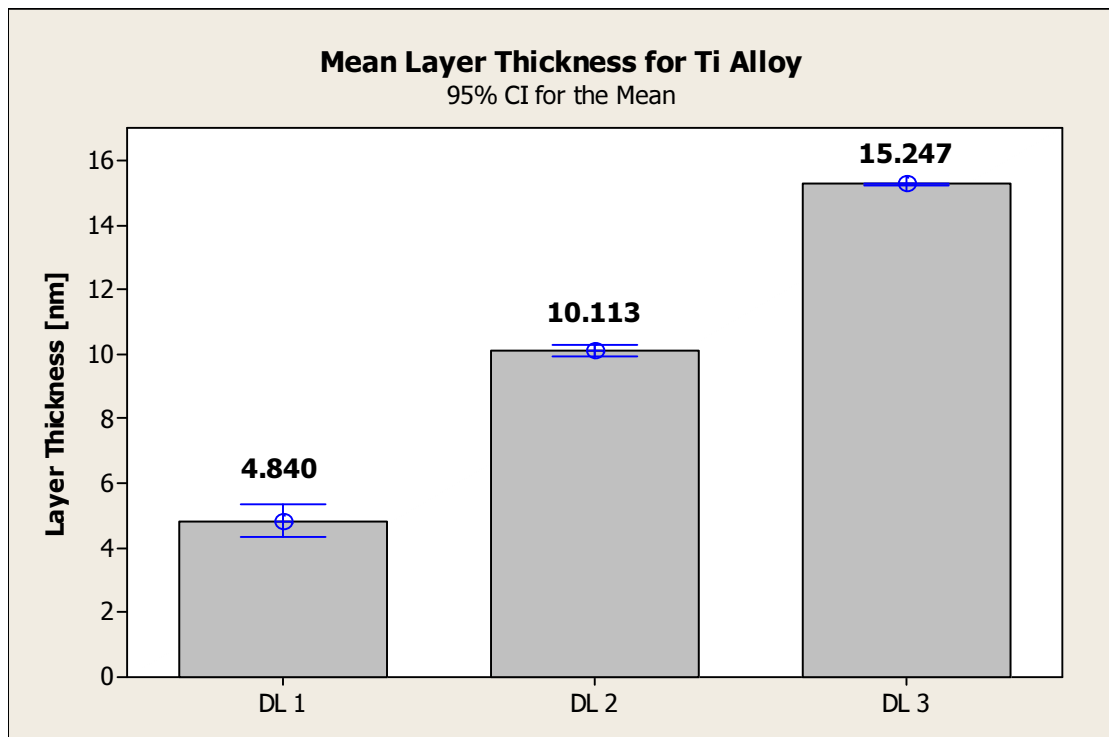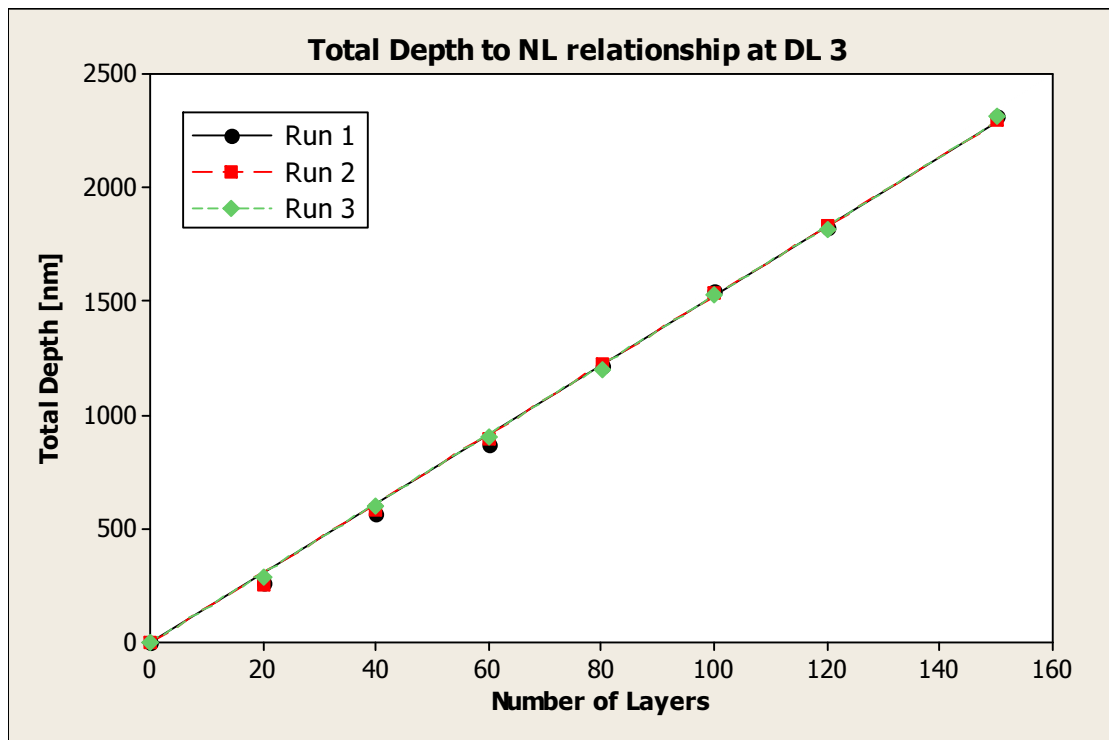
Mean Layer Thickness for Ti Alloy
95% CI for the Mean

Layer thickness, *h*, obtained for Ti alloy

D_L [μAs/cm^2]	D_L 1 = $2x10^3$	D_L 2 = $4x10^3$	D_L 3 = $6x10^3$
h [nm]	4.8 ±0.4	10.1 ±0.6	15.2 ±0.9

Uncertainty analysis and calculation for the three area doses per layer (D_L)

D_L [μAs/cm^2]	$\bar{h}$, [nm]	$u(\bar{h})$, [nm]	$u(P)$, [nm]	$u_c(h)$, [nm]	ν_{eff}	k	$U = k.u_c(h)$, [nm]
D_L 1	4.840	0.12	0.15	0.19	12	2.18	0.41
D_L 2	10.113	0.04	0.30	0.31	infinite	1.96	0.60
D_L 3	15.247	0.003	0.46	0.46	infinite	1.96	0.90

FIB milling of 3D features – 100 layers convex pyramid

D_L 1 (Fig. C.8 a): calculated *H* - 480 ± 40 nm; actual *H* – 512.3 nm; deviation – 6.7%.

D_L 2 (Fig. C.8b): calculated *H* - 1010 ± 60nm; actual *H* – 967.2 nm; deviation – 4.2%.

D_L 3 (Fig. C.8 c): calculated *H* - 1520 ± 90nm; actual *H* – 1486nm; deviation – 2.2%.
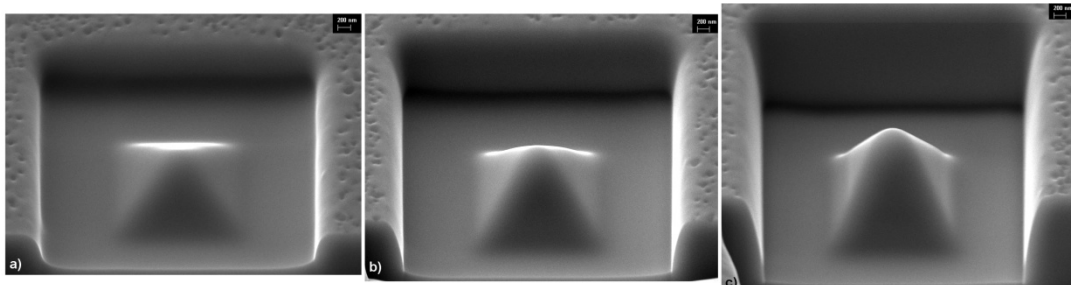
Figure C.8 Convex pyramid with 2x2 μm base in a 4x4 μm trench, produced by FIB milling of 100 layers with a) D_L 1, b) D_L 2 and c) D_L 3
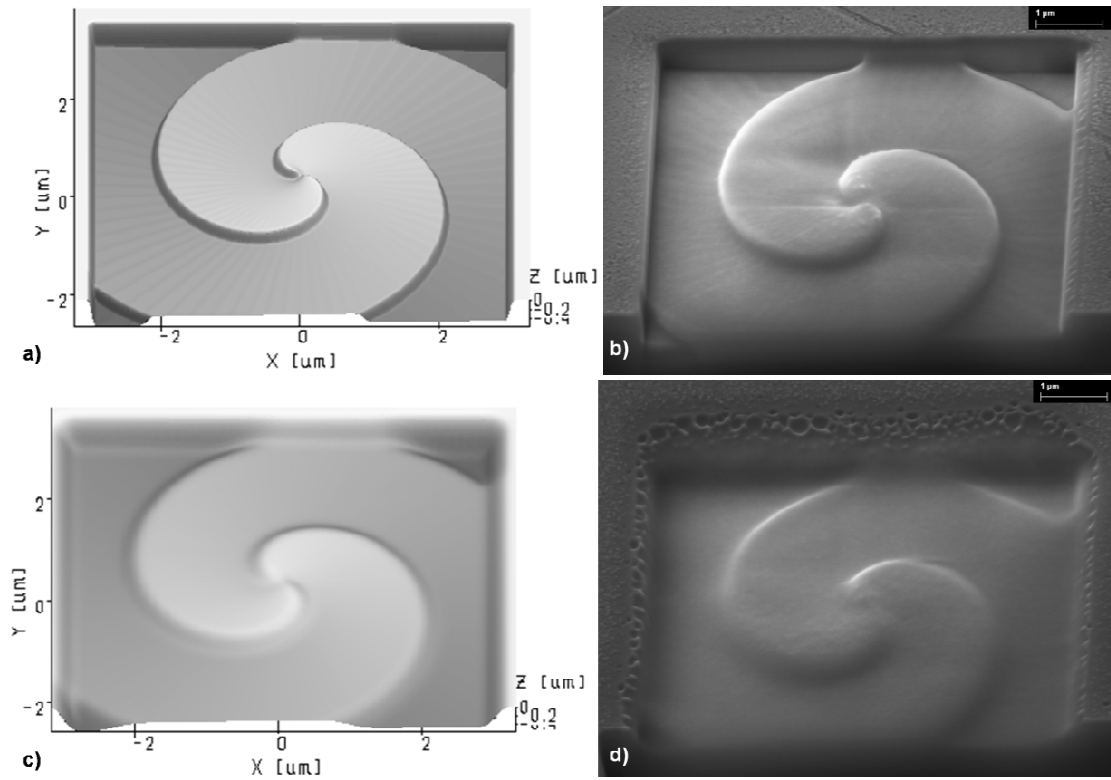
Figure C.9 IonRevSim simulation (left column, a, c) and exposure results (right column, b, d) for a double-wound spiral in quartz for 200 pA and 2 nA, respectively
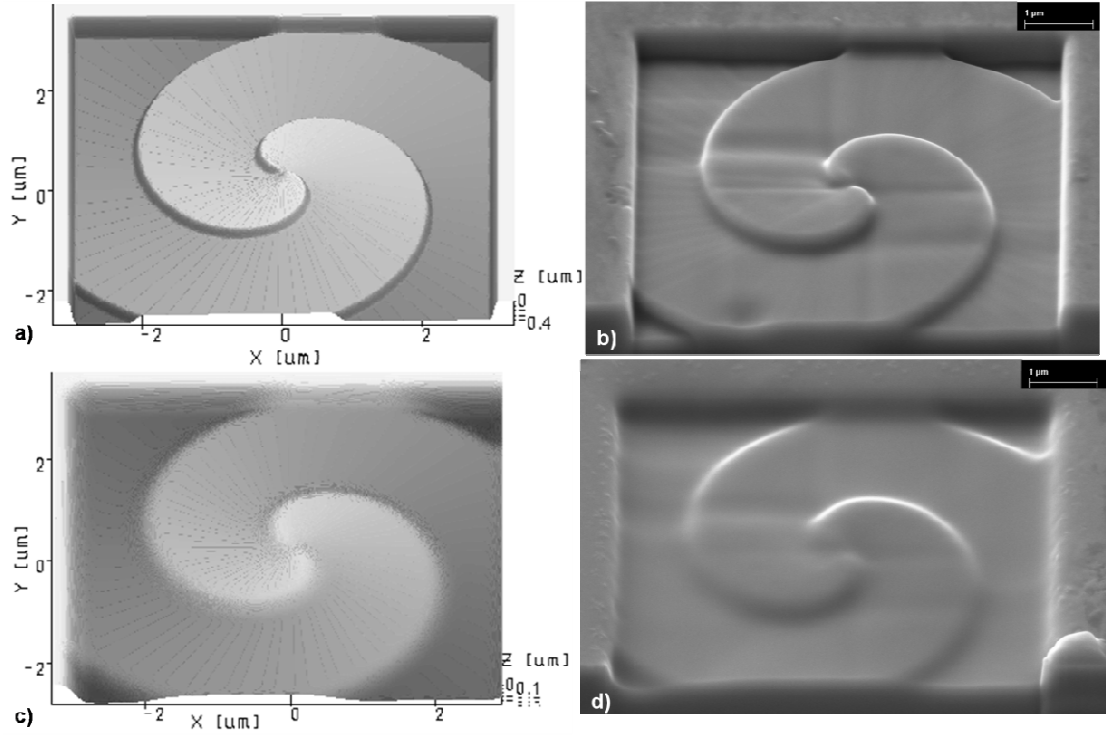
Figure C.10 IonRevSim simulation (left column, a, c) and exposure results (right column, b, d) for a double-wound spiral in nickel for 200 pA and 2 nA, respectively
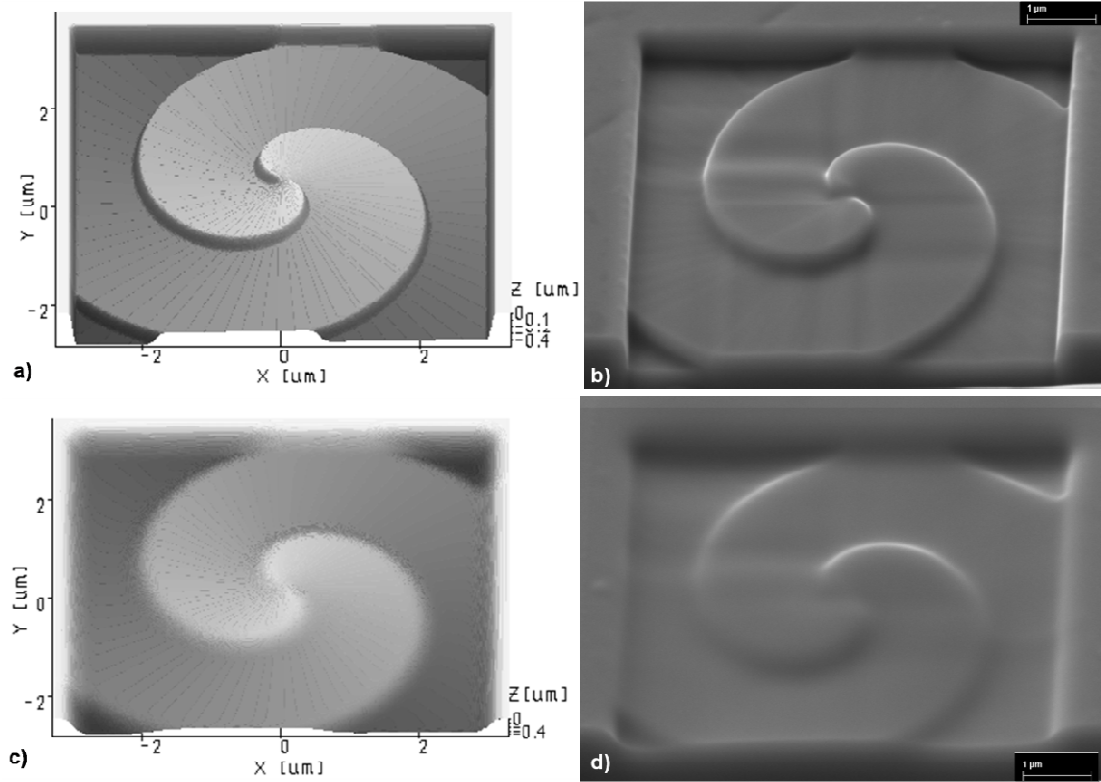
Figure C.11 IonRevSim simulation (left column, a, c) and exposure results (right column, b, d) for a double-wound spiral in Ti BMG for 200 pA and 2 nA, respectively

REFERENCES

Allen Y., Lu W., Farson D. and L. Lee, 2008. *Overview of polymer micro/nanomanufacturing for biomedical applications.* Advances in Polymer Technology **27**, pp. 188-198.

Allen, D., Shore P., Evans R., Fanara C., O'Brien W., Marson S. and W. O'Neill, 2009. *Ion beam, focused ion beam, and plasma discharge machining.* CIRP Annals - Manufacturing Technology **58**(2), pp. 647-662.

Alting L., Kimura F., Hansen H. and G. Bissacco, 2003. *Micro Engineering.* CIRP Annals - Manufacturing Technology **52**(2), pp. 635-657.

Andersen, H. and R. Behrisch, 1981. *Sputtering by particle bombardment / edited by R. Behrisch.* Topics in applied physics **47, 52, 64**, Berlin; New York: Springer-Verlag: 1981.

Arisha A., Young P., and El Baradie, M., 2004. *A simulation model to characterize the photolithography process of a semiconductor wafer fabrication.* Journal of Materials Processing Technology **155-156**, pp. 2071-2079.

Austin M., Zhang W., Ge H., Wasserman D., Lyon S. and S. Chou, 2005. *6 nm half-pitch lines and 0.04 um^2 static random access memory patterns by nanoimprint lithography.* Nanotechnology **16** (8), pp. 1058-1061.

Biersack, J and L. Haggmark, 1980. *A Monte Carlo computer program for the transport of energetic ions in amorphous targets*. Nuclear Instruments and Methods **174** (1-2), pp. 257-269.

Bigot S., Minev R., Dobrev T., Dimov S. and C. Matthews, 2009. *Function and length scale integration in micro/nano manufacturing* in Proceedings of 4M/ICOMM 2009 - The Global Conference on Micro Manufacture, Karlsruhe, Germany, pp. 147-152.

Bischoff L., 2008. *Application of mass-separated focused ion beams in nano-technology*, Nuclear Instruments and Methods B: Beam Interactions with Materials and Atoms **266**(8), pp. 1846-1851

Bissacco G., Hansen H., Tang P. and J. Fugl, 2005. *Precision manufacturing methods of inserts for injection moulding of microfluidic systems*, Proceedings of the ASPE Spring Topical Meeting, Columbus, Ohio, USA, pp. 57-63.

Bissacco G., Valentincic J., Wiwe B. and H. Hansen, 2007. *Characterization of pulses in micro EDM milling based on wear and material removal.* Proceedings of 3rd Intl. Conf. on Multi-Material Micro Manufacture, Borovetz, Bulgaria, 2007, pp. 297-300.

Brecher C., Klar R. and C.Wenzel, 2007. *Development of a dynamic high precision miniature milling machine.* Proceedings of 3rd Intl. Conf. on Multi-Material Micro Manufacture, Borovetz, Bulgaria, pp. 327-330.

Brinksmeier E., Riemer O. and R. Stern, 2001. *Machining of precision parts and microstructures.* Proceedings of the 10th international conference on precision engineering, ICPE, Yokohama, Japan, pp. 3–11.

Brousseau, E., Dimov, S. and D. Pham, 2010. *Some recent advances in multi-material micro- and nano-manufacturing.* International Journal of Advanced Manufacturing Technology **47**, pp. 147-156.

Callister W., 2003. *Material Science and Engineering – an introduction*, J. Wiley Int.:2003.

Carl Zeiss NTS GmbH, Nano Technology Systems, http://www.zeiss.de/nts , last visited: 21-March- 2011.

Catalano M., Taurino A., Lomascolo M., Schertel A. and A. Orchowski, 2006. *Critical issues in the focused ion beam patterning of nanometric hole matrixes on GaAs based semiconducting devices*, Nanotechnology **17**, pp. 1758-1762.

Cecil J., Powell D. and D. Vasquez, 2007. *Assembly and manipulation of micro devices—A state of the art survey*. Robotics and Computer-Integrated Manufacturing **23**(5), pp. 580-588.

Chen Z. and C. Chien, 2006. *Design and Fabrication of a Novel Light Guiding Plate for Backlight System by MEMS Technology* in „Symposium on Design, Test, Integration and Packaging of MEMS/MOEMS - DTIP'06", TIMA Editions,

Grenoble, France, Stresa, Lago Maggiore, Italy, 2006, 5p.

Chia-Jen T., Fuh-Yu C., Chi-Feng C. and C. Chou, 2008. *Fabrication of an antireflective polymer optical film with subwavelength structures using a roll-to-roll micro-replication process*, Journal of Micromechanics and Microengineering **18** (7), pp. 1-9.

Coquillat D., Le Vassor D'Yerville M., Kazan M., Liu C., Watson I., Edwards P., Martin R., Chong H. and R. De La Rue, 2008. *Studies of the photonic and optical-frequency phonon properties of arrays of selectively grown GaN micropyramids.* Journal of Applied Physics **103**, pp. 044910 – 044917.

Dantchev D. and K. Kostadinov, 2006. *On forces and interactions at small distances in micro and nano assembly process*, Proceedings of the 2nd International Conference on Multi Material Micro Manufacture, Grenoble, France, 2006, pp. 241-245.

De Grave, A. and D. Brissaud, 2005. *Collaboration and Integration in the Design of Microelectromechanical Systems (MEMS),* CIRP Design Seminar, Shanghai, China, 2005, 9 p.

Dietzel A., Bruenger W., Loeschner, H. and E. Platzgummer, 2006. *Micro- and nano-structuring using ion beams.* Proceedings of the 2nd International Conference on Multi Material Micro Manufacture, Grenoble, France, 2006, pp. 9-12.

Dimov S., Matthews C., Glanfield A. and P. Dorrington, 2006. *Roadmapping study in*

multi-material micro manufacture. Proceedings of the 2nd International Conference on Multi Material Micro Manufacture, Grenoble, France, 2006, pp. xi–xxv.

Dornfeld D., Min S., and Y. Takeuchi, 2006. *Recent Advances in Mechanical Micromachining.* CIRP Annals - Manufacturing Technology **55**(2), pp. 745-768.

Dubey A. and V. Yadava, 2008. *Laser beam machining-A review.* International Journal of Machine Tools and Manufacture **48**(6), pp. 609-628.

Eriksson T., Hansen H., Gegeckaite A. and M. Arentoft, 2006. *Automated assembly of micro mechanical parts in a microfactory setup.* Proceedings of the 5th International Workshop on Microfactories, Besancon, France, 2006.

FEI Company, http://www.fei.com/products/dualbeams/, last visited: 21-March-2011.

Filiz S., Conley C., Wasserman M. and O. Ozdoganlar, 2007. *An experimental investigation of micro-machinability of copper 101 using tungsten carbide micro-endmills.* International Journal of Machine Tools and Manufacture **47** (7-8), pp. 1088-1100.

Filiz S., Xie L., Weiss L. and O. Ozdoganlar, 2008. *Micromilling of microbarbs for medical implants.* International Journal of Machine Tools and Manufacture **48**(3-4), pp. 459-472.

Frey L., Lehrer C. and H. Ryssel, 2003. *Nanoscale effects in focused ion beam*

processing. Applied Physics A: Materials Science & Processing **76**(7), pp. 1017-1023.

Fu Y., 2001. *Investigation of microlens mold fabricated by focused ion beam technology*, Microelectronic Engineering **56**, pp. 333-338.

Fu X., Li P., Jin A., Chen L., Yang H., Li L., Tang W. and Z. Cui, 2005. *Gas-assisted etching of niobium with focused ion beam.* Microelectronic Engineering **78-79**, pp. 29-33.

Giboz J., Copponnex T. and P. Mele, 2007. *Microinjection molding of thermoplastic polymers: a review.* Journal of Micromechanics and Microengineering **17**, pp. R96-R109.

Gierak J., 2009. *Focused ion beam technology and ultimate applications*, Semiconductor Science and Technology **24**, pp. 043001-043023.

Gower M. and N. Rizvi, 2000. Application *of laser ablation to microengineering*, Proceedings of SPIE, High-power laser ablation III, Vol. 4065, pp. 452-460.

Guo L., 2007. *Nanoimprint Lithography: Methods and Material Requirements,* Advanced Materials **19**, pp. 495–513.

Hansen H, Tosello G, Gegeckaite A, Arentoft M. and L. Marin, 2005. *Classification of assembly techniques for micro products.* Proceedings of the 1st International Conference on Multi Material Micro Manufacture, Karlsruhe, Germany, 2005, pp

283-286.

Hansen H., Carneiro K., Haitjema H. and L. De Chiffre, 2006. *Dimensional micro and nano metrology.* Annals of the CIRP **55**, pp. 721 – 743.

Hansen H., Prichystal J., Møller P. and H. Bladt, 2007. *Complex process chains for manufacturing of invisible displays integrated in bulk metal panels.* Annals of the CIRP **56**, pp. 237 – 240.

Harsono H., Lu H., Liu Y., Lam, Y. and X. Shan, 2006. *Experimental studies on polymer deformation and flow in micro hot embossing*, in Electronics Packaging Technology Conference, 2006. EPTC '06.

Heckele M. and W. Schomburg, 2004. *Review on micro molding of thermoplastic polymers.* Journal of Micromechanics and Microengineering **14**(3), pp. 1-14.

Hon K., Li L. and I. Hutchings, 2008. *Direct writing technology-Advances and developments*, CIRP Annals - Manufacturing Technology **57** (2), pp. 601-620.

Hopman W., Ay F., Hu W., Gadgil V., Kuipers L., Pollnau M. and R. de Ridder, 2007. *Focused ion beam scan routine, dwell time and dose optimizations for submicrometre period planar photonic crystal components and stamps in silicon.* Nanotechnology **18**(19), 195305 (11p).

Hormes J., Göttert J., Lian K., Desta Y. and L. Jian, 2003. *Materials for LiGA and*

LiGA-based microsystems. Nuclear Instruments and Methods in Physics Research Section B: Beam Interactions with Materials and Atoms **199,** pp. 332-341.

Inoue A., 2000. *Stabilization of metallic supercooled liquid and bulk amorphous alloys*, Acta materialia **48**, pp. 279–306.

ISO (International Organization for Standardization) 1995 GUM (Guide to the Expression of Uncertainty in Measurement).

Ivkov J., Babic E. and H. Lieberman, 1989. Journal of Physics: Condensed Matter **1** (1989), p. 551.

Jeon W. and J. Melngailis, 2006. *CMOS and post-CMOS on-chip microwave pulse power detectors*, Solid-State Electronics **50**(6), pp. 951-958.

Jing X., Chen D., Fang D., Huang C., Liu J. and X. Chen, 2007. *Multi-layer microstructure fabrication by combining bulk silicon micromachining and UV-LIGA technology.* Microelectronics Journal **38**(1), pp. 120-124.

Kaesmaier R. and H. Löschner, 2000. *Ion Projection Lithography: Progress of European MEDEA & International Program.* Microelectronic Engineering **53**(1-4), pp. 37-45.

Kapsa J., Robach, Hollinger Y., Gendry G., Gierak M. and D. Mailly, 2004. *STM and FIB nano-structuration of surfaces to localise InAs/InP (0 0 1) quantum dots.* Applied

Surface Science **226** (1-3), pp. 31-35.

Katardjiev I., Carter G., Nobes M., Berg S. and H. Blom, 1994. *Three-dimensional simulation of surface evolution during growth and erosion.* Journal of Vacuum Science & Technology A: Vacuum, Surfaces, and Films **12**(1), pp. 61-68.

Kawasegi N., Morita N., Yamada S., Takano N., Oyama T., Ashida K., Taniguchi J., Miyamoto I., Momota S. and H. Ofune, 2006. *Rapid nanopatterning of a Zr-based metallic glass surface utilizing focused ion beam induced selective etching.* Applied Physics Letters **89**, pp. 143115-3.

Kilner A., Kilner J., Elliott J., Cressey G. and S. Littlewood, 1991. *The effect of orientation on ion beam erosion rates in ionic crystals measured by SIMS depth profiling,* Surface and Interface Analyses **17** (3), pp. 158–164.

Kim H.-B., Hobler G., Steiger A., Lungstein A. and E. Bertagniolli, 2007 a. *Full three-dimensional simulation of focused ion beam micro/nanofabrication.* Nanotechnology **18**(24), 245303 (8p.)

Kim H.-B., Hobler G., Lungstein A. and E. Bertagniolli, 2007 b. *Simulation of ion beam induced micro/nano fabrication.* Journal of Micromechanics and Microengineering **17**(6), pp. 1178-1183.

Kirkup L, 1994. *Experimental Methods: an Introduction to the Analysis and Presentation of Data*, Brisbane: John Wiley & Sons:1994.

Kirkup L. and B. Frenkel, 2006. *An Introduction to Uncertainty in Measurement*, Cambridge: Cambridge University Press: 2006.

Kolew A., Sikora K., Munch D. and M. Worgull, 2010. *Replication of micro and sub-micro structures by means of hot embossed polymer inserts* in Symposium on Design Test Integration and Packaging of MEMS/MOEMS (DTIP), 2010, pp. 339-343.

Kong Y., Peng H. and A. Yee, 2006. *Fabrication of polymeric nanostructures: Techniques and stability issues*, Gyeongju, Republic of Korea, Inst. of Elec. and Elec. Eng. Computer Society, 2006.

Kosugi T., Gamo K., Namba S. and R. Aihara, 1991. *Ion beam assisted etching of GaAs by low energy focused ion beam.* Journal of Vacuum Science & Technology B: Microelectronics and Nanometer Structures **9**(5), pp. 2660-2663.

Kunieda M., Lauwers B., Rajurkar K. and B. Schumacher, 2005. *Advancing EDM through Fundamental Insight into the Process.* CIRP Annals - Manufacturing Technology **54**(2), pp. 64-87.

Krohn V. and G. Ringo, 1975. *Ion source of high brightness using liquid metal.* Applied Physics Letters **27**(9), pp. 479-481.

Lalev G., Dimov S., Kettle J., van Delft F. and R. Minev, 2008. *Data preparation for focused ion beam machining of complex three-dimensional structure,* Proceedings of

the Institution of Mechanical Engineers, Part B: Journal of Engineering Manufacture **222**(1), pp. 67-76.

Lalev G., Petkov P., Sykes N., Hirshy H., Velkova V., Dimov S. and D. Barrow, 2009. *Fabrication and validation of fused silica NIL templates incorporating different length scale features*, Microelectronic Engineering **86** (4-6), pp. 705-708.

Leach R., 2010. *Fundamental Principles of Engineering Nanometrology*. First edition. Elsevier, 2010.

Lee J., Kim Y, Nahm K. and J. Ko, 2006. *Optical simulation of micro-pyramid arrays for the applications in the field of backlight unit of LCD*, IMID/IDMC '06 DIGEST, pp. 1343–1346.

Lee T., Gao K., Chien W. and C. Sun, 2007. *Light extraction analysis of GaN-based light-emitting diodes with surface texture and/or patterned substrate*, Optics Express **15**, pp. 6670-6676.

Lee J., Ho Y., Chen K., Lin H., Fang J., Hsu S., Lin J. and M. Wei, 2008. *Efficiency improvement and image quality of organic light-emitting display by attaching cylindrical microlens arrays*, Optics Express **16**, pp. 21184-21190.

Leech P., Sexton B., Marnock R. and F. Smith, 2004. *Fabrication of hologram coins using electron beam lithography*, Microelectronic Engineering **71** (2), pp. 171-176.

Leech P. and R. Lee, 2006. *Optically variable micro-mirror arrays fabricated by graytone lithography.* Microelectronic Engineering **83**(2), pp. 351-356.

Leech P. and R. Lee, 2007. *Hot embossing of grating-based optically variable images in thermoplastic acrylic lacquer*, Journal of Materials Science **42** (12), pp. 4428-4434.

Lehrer C., Frey L., Petersen S. and H. Ryssel, 2001. *Limitations of focused ion beam nanomachining*. Journal of Vacuum Science & Technology B: Microelectronics and Nanometer Structures **19**, pp. 2533-2538.

Li W., Kang D., Blamire M. and W. Huck, 2003. *Focused ion beam fabrication of silicon print masters.* Nanotechnology **14**(2), pp. 220-223.

Li W., Minev R., Dimov S. and G. Lalev, 2007. *Patterning of Amorphous and Polycrystalline Ni78B14Si8 with a Focused Ion Beam*. Applied Surface Science **253** (12), pp. 5404-5410.

Li W., Dimov S. and G. Lalev, 2007 a. *Focused-ion-beam direct structuring of fused silica for fabrication of nano-imprinting templates*, Microelectronic Engineering **84** (5-8), pp 829-832.

Li Y., Xie H., Guo B., Luo Q., Gu C. and M. Xu, 2010. *Fabrication of high-frequency moire gratings for microscopic deformation measurement using focused ion beam milling.* Journal of Micromechanics and Microengineering **20**(5), 055037 (9p).

Lin L., Cheng Y. and C. Chiu, 1998. *Comparative study of hot embossed micro structures fabricated by laboratory and commercial environments*. Microsystem Technologies **4**, pp. 113-116.

Lin L., Shia T. and C. Chiu, 2000. *Silicon-processed plastic micropyramids for brightness enhancement applications*. Journal of Micromechanics and Microengineering **10**, pp. 395-400.

Liu X., De Vor R., Kapoor S. and K. Ehmann, 2004. *The Mechanics of Machining at the Microscale: Assessment of the Current State of the Science*. Journal of Manufacturing Science and Engineering **126** (4), pp. 666-678.

Lugstein A., Basnar B., Smoliner J. and E. Bertagnolli, 2003. *FIB processing of silicon in the nanoscale regime*. Applied Physics A: Materials Science & Processing **76**(4), pp. 545-548.

Maalouf A., Gadonna M. and D. Bosc, 2009. *An improvement in standard photolithography resolution based on Kirchhoff diffraction studies*. Journal of Physics D: Applied Physics **42**(1), pp. 1-11.

Madou M., 2002. *Fundamentals of microfabrication: the science of miniaturization*, 2nd edition. CRC, New York: 2002.

Mäkelä T., Haatainen T., Majander P. and J. Ahopelto, 2007. *Continuous roll to roll nanoimprinting of inherently conducting polyaniline*. Microelectronic Engineering **84**

(5-8), pp. 877-879.

Malek C. and V. Saile, 2004. *Applications of LIGA technology to precision manufacturing of high-aspect-ratio micro-components and -systems: a review.* Microelectronics Journal **35**(2), pp. 131-143.

Masuzawa T., 2000. *State of the art of micro-machining*. CIRP Annals **49**(2), pp. 473–488.

McGeough J., Leu M., Rajurkar K., De Silva A. and Q. Liu, 2001. *Electroforming process and application to micro/macro manufacturing*, CIRP Annals - Manufacturing Technology **50** (2), pp. 499-514.

Meijer J., Du K., Gillner A., Hoffmann D., Kovalenko V., Masuzawa T., Ostendorf A., Poprawe R. and W. Schulz, 2002. *Laser Machining by short and ultrashort pulses, state of the art and new opportunities in the age of the photons.* CIRP Annals - Manufacturing Technology **51**(2), pp. 531-550.

Melngailis J., 1987. *Focused ion beam technology and applications.* Journal of Vacuum Science & Technology B: Microelectronics and Nanometer Structures **5**(2), pp. 469-495.

Minev R., Dimov S., Koev S., Lalev G. and N. Festchiev, 2008. *Explosive welding of Ni- based amorphous foils for micro-tooling applications*, Proceeding of 4M Conference, Cardiff, pp. 203-206.

Minev R, Ilieva M., Kettle J., Lalev G., Dimov S., Tzaneva D., Dermendjiev I., and R. Shishkov, *Deposition and focused ion beam milling of anticorrosive CrC coatings on tool steel substrates*, International Journal of Advanced Manufacturing Technology **47**(1-4), pp. 29-35.

Orsay Physics, Products FIB, http://www.orsayphysics.com/type-fib.html, last visited: 21 – March – 2011.

Paivanranta B., Baroni P., Scharf T., Nakagawa W., Kuittinen M. and H. Herzig, 2008. *Antireflective nanostructured microlenses*, Microelectronic Engineering **85**, pp. 1089-1091.

Pham D., Dimov S., Petkov P. and S. Petkov, 2002. *Laser milling,* Proceedings of the Institution of Mechanical Engineers, Part B: Journal of Engineering Manufacture **216** (5), pp. 657-667.

Pham D., Dimov S., Bigot S., Ivanov A. and K. Popov, 2004. *Micro- EDM – Recent developments and research issues.* Journal of Material Processing Technology **149**(1–3), pp. 50–57.

Pham D., Elkaseer A., Popov K., Dimov S., Olejnik L. and A. Rosochowski, 2009. *Micromilling of coarse-grained and ultrafine-grained Cu99.9E: Effects of material microstructure on machining conditions and surface quality.* Proceedings of 4M/ICOMM Conference, 2009, pp. 241-244.

Petkov P., Dimov S., Minev R. and D. Pham, 2008. *Laser milling: pulse duration effect on surface integrity.* Proceedings of the Institution of Mechanical Engineers, Part B: Journal of Engineering Manufacture **222**(1), pp. 35–45.

Platzgummer E., Biedermann A., Langfischer H., Eder-Kapl S., Kuemmel M., Cernusca S., Loeschner H., Lehrer C., Frey L., Lugstein A. and E. Bertagnolli, 2006. *Simulation of ion beam direct structuring for 3D nanoimprint template fabrication.* Microelectronic Engineering. **83**(4-9), pp. 936-939.

Pietarinen J., Siitonen S., Tossavainen N., Laukkanen J. and M. Kuittinen, 2006. *Fabrication of Ni-shims using UV-moulding as an intermediate step.* Microelectronic Engineering **83**(3), pp. 492-498.

Piotter V., Bauer W., Hanemann T., Heckele M. and C. Muller, 2008. *Replication technologies for HARM devices: status and perspectives.* Microsystem Technologies **14** (9), pp. 1599-1605.

Platzgummer E, Loeschner H. and G. Gross, 2008. *Projection maskless patterning for nanotechnology applications*, 52nd International Conference on Electron, Ion, and Photon Beam Technology and Nanofabrication, AVS, 2008, pp. 2059-2063.

Prenitzer B., Urbanik-Shannon C., Giannuzzi L., Brown S., Irwin R., Shofner T., and F. Stevie, 2003. *The correlation between ion beam/material interactions and practical FIB specimen preparation,* Microscopy and Microanalysis **9**, pp. 216–236.

Quintana I., Dobrev T., Aranzabe A., Lalev G. and S. Dimov, 2009. *Investigation of amorphous and crystalline Ni alloys response to machining with micro-second and pico-second lasers*, Applied Surface Science **255** (13-14), pp. 6641-6646.

Rajurkar K., Levy G., Malshe A., Sundaram M., McGeough J., Hu X., Resnick R. and A. DeSilva, 2006. *Micro and Nano Machining by Electro-Physical and Chemical Processes.* CIRP Annals - Manufacturing Technology **55**(2), pp. 643-666.

Rees A., Dimov S., Ivanov A., Herrero A. and L. Uriarte, 2007. *Micro-EDM: factors affecting the quality of electrodes dressed on the machine*. Proceedings of the Institution of Mechanical Engineers, Part B: Journal of Engineering Manufacture **221** (3), pp. 409–418.

Rees A., Brousseau E., Dimov S., Gruber H. and I. Paganetti, 2008. *Wire electro discharge grinding: surface finish optimisation*. Proceedings of the 4th Internatinal Conference on multimaterial micro-manufacture, 4M2008, Cardiff, pp. 233–236.

Resnick D., Sreenivasan S. and C. Willson, 2005. *Step & flash imprint lithography*, Materials Today **8** (2), pp. 34-42.

Reyntjens S. and R. Puers, 2001. *A review of focused ion beam applications in microsystem technology,* Journal of Micromechanics and Microengineering **11**, pp. 287 – 300.

Rommel M., Jambreck J., Ebm C., Platzgummer E., Bauer A. and L. Frey, 2010. *Influence of FIB patterning strategies on the shape of 3D structures: Comparison of experiments with simulations.* Microelectronic Engineering **87**(5-8), pp. 1566-1568.

Santschi C., Jenke M., Hoffmann P. and J. Brugger, 2006. *Interdigitated 50Â nm Ti electrode arrays fabricated using XeF 2 enhanced focused ion beam etching.* Nanotechnology **17**(11), pp. 2722-2729.

Scholz S., Griffits C., Dimov S., Brousseau E., Lalev G. and P. Petkov, 2009. *New process chains for replicating micro and nano structured surfaces with bio-mimetic applications*, ANTEC 2009, Chicago, 2009.

Seliger L., Kubena L., Olney D., Ward W. and V. Wang, 1979. *High-resolution, ion-beam processes for microstructure fabrication.* Journal of Vacuum Science and Technology **16** (6), pp. 1610-1612.

Seo J. and L. Lee, 2004. *Disposable integrated microfluidics with self-aligned planar microlenses*, Sensors and Actuators B: Chemical **99**, pp. 615-622.

Shinji M. and O. Yukinori, 1996. *Focused ion beam applications to solid state devices,* Nanotechnology **7**, pp. 247-258.

Smentkowski V., 2000. *Trends in sputtering,* Progress in Surface Science **64**, pp. 1-58.

Srinivasan U., Helmbrecht M., Rembe C., Muller R. and R. Howe, 2002. *Fluidic self-assembly of micromirrors onto microactuators using capillary forces.* IEEE Journal of Selected Topics in Quantum Electronics **8**(1), pp. 4-11.

Stanishevsky A., 1999. *Focused ion beam patterning of diamondlike carbon films.* Diamond and Related Materials **8**(7), pp. 1246-1250.

Stanishevsky A., 2001. *Patterning of diamond and amorphous carbon films using focused ion beams*, Thin Solid Films **398-399**, pp. 560-565.

Sudraud P., Ben Assayag G. and M. Bon, 1988. *Focussed-ion-beam milling, scanning-electron microscopy, and focussed-droplet deposition in a single microcircuit surgery tool,* Journal of Vacuum Science Technology B: Microelectronics and Nanometer Structures **6**, pp. 234-238.

Svintsov A., Zaitsev S., Lalev G., Dimov S., Velkova V. and H. Hirshy, 2009. *FIB sputtering optimization using Ion Reverse Software.* Microelectronic Engineering **86**(4-6), pp. 544-547.

Tang P., 2008. *Utilising electrochemical deposition for micro manufacturing.* Proceedings of the International Conference on Multi-Material Micro Manufacture, Whittles Publishing Ltd., Cardiff, 2008.

Theilade, U. and H. Hansen, 2007. *Surface microstructure replication in injection molding.* The International Journal of Advanced Manufacturing Technology **33**(1),

pp. 157-166.

Toepke, M. and J. Kenis, 2005. *Multilevel Microfluidics via Single-Exposure Photolithography*, Journal of American Chemical Society **127**, pp. 7674-7675.

Trupke M., Ramirez-Martinez F., Curtis E., Ashmore J., Eriksson S., Hinds E., Moktadir Z., Gollasch C., Kraft M., Vijaya Prakash G. and J. Baumberg, 2006. *Pyramidal micromirrors for microsystems and atom chips*. Applied Physics Letters **88** (7), p. 071116-3.

Tseng A., 2004. *Recent developments in micromilling using focused ion beam technology*, Journal of Micromechanics and Microengineering **14**, pp. R15 – R 34.

Tseng A., Insua I., Park J. and C. Chen, 2005. *Milling yield estimation in focused ion beam milling of two-layer substrates.* Journal of Micromechanics and Microengineering **15**(1), pp. 20-28.

Tsuchiya K., Murakami A., Fortmann G., Nakao M. and Y. Hatamura, 1999. *Micro assembly and micro bonding in nano manufacturing world.* SPIE Proceedings Vol. 3834 (Microrobotics and Microassembly), pp. 132-140.

Urbanek M., Uhlir V., Babor P., Kolibalova E., Hrncir T., Spousta J. and T. Šikola, 2010. *Focused ion beam fabrication of spintronic nanostructures: an optimization of the milling process*. Nanotechnology **21**(14), p. 145304-7.

Van Brussel H., Peirs J., Reynaerts D., Delchambre A., Reinhart G., Roth N., Weck M. and E. Zussman, 2000. *Assembly of Microsystems.* CIRP Annals - Manufacturing Technology **49**(2), pp. 451-472.

Vasile M., Xie J. and R. Nassar, 1999. *Depth control of focused ion-beam milling from a numerical model of the sputter process.* Journal of Vacuum Science & Technology B: Microelectronics and Nanometer Structures **17**(6), pp. 3085-3090.

Velkova V., Lalev G., Hirshy H., Scholz S., Hiitola-Keinänen J., Gold H., Haase A., Hast J., Stadlober B. and S. Dimov, 2010. *Design and validation of a novel master-making process chain for organic and large area electronics on flexible substrates.* Microelectronic Engineering **87**(11), pp. 2139-2145.

Velkova V., Lalev G., Hirshy H., Omar F., Scholz S. and S. Dimov, 2011 a. *Process chain for serial manufacture of 3D micro- and nano-scale structures.* CIRP Journal of Manufacturing Science and Technology, *In press*

Velkova V., Lalev G., Leach R. and S. Dimov, 2011 b. *Methodology for depth prediction in layer-based FIB milling of complex 3D features.* Microelectronic Engineering (submitted).

Velten T., Bauerfeld F., Schuck H., Scherbaum S., Landesberger C. and K. Bock, 2010. *Roll-to-roll hot embossing of microstructures*, in Symposium on Design Test Integration and Packaging of MEMS/MOEMS (DTIP), 2010, pp. 326-331.

Vick D., Sauer V., Fraser A., Freeman M. and W. Hiebert, 2010. *Bulk focused ion beam fabrication with three-dimensional shape control of nanoelectromechanical systems*. Journal of Micromechanics and Microengineering **20**(10), pp. 105005 (9p).

Wang L., 1997. *Design optimization for two lens focused ion beam columns.* Journal of Vacuum Science & Technology B: Microelectronics and Nanometer Structures **15**(4), pp. 833-839.

Wang Q., Luo Q. and C. Gu, 2007. *Nickel silicide nanowires formed in pre-patterned SiO 2 trenches and their electrical transport properties.* Nanotechnology **18**(19), p. 195304.

Wang X., Lu P., Dai N., Li Y., Liao C., Zheng Q. and L. Liu**,** 2007. *Noncrystalline micromachining of amorphous alloys using femtosecond laser pulses.* Materials Letters **61**, pp 4290–4293.

Ward J., 1985. *A Monte Carlo calculation of the virtual source size for a liquid metal ion source.* Journal of Vacuum Science & Technology B: Microelectronics and Nanometer Structures **3**(1), pp. 207-213.

Wilson R. et al., 1997. *Relative Sputtering Rates and Ion Yields of Semiconductors, Metals, and Insulators Under Oxygen and Cesium Ion Bombardment*, SIMS VI, Versailles, France, 1997.

Yan J, Oowada T., Zhou T. and T. Kuriyagawa, 2009. *Precision machining of*

microstructures on electroless-plated NiP surface for molding glass components. Journal of Materials Processing Technology **209**, pp. 4802-4808.

Youn S., Takahashi M., Goto H. and R. Maeda, 2006. *Microstructuring of glassy carbon mold for glass embossing - comparison of focused ion beam, nano/femtosecond-pulsed laser and mechanical machining*, Microelectronic Engineering **83** (11-12), pp. 2482-2492.

Zaitsev S., Svintsov A., Ebm C., Eder-Kapl S., Loeschner H., Platzgummer E., Lalev G., Dimov S., Velkova V. and B. Basnar, 2009. *3D ion multibeam processing with the CHARPAN PMLP tool and with the single ion-beam FIB tool optimized with the IonRevSim software*, Alternative Lithographic Technologies, Proceedings of the SPIE, Vol. 7271, pp. 72712P-1 - P-8.

Zhang G., Liu Y. and B. Zhang, 2006. *Effect of annealing close to Tg on notch fracture toughness of Pd-based thin-film metallic glass for MEMS applications*, Scripta Materialia **54**, pp. 897–901.

Zheng H., Liu H., Lim G., Nikumb S. and Q. Chen, 2006. *Ultrashort pulse laser micromachined microchannels and their application in an optical switch.* The International Journal of Advanced Manufacturing Technology **27**(9), pp. 925-929.

LIST OF PUBLICATIONS

Velkova V., Lalev G., Hirshy H., Scholz S., Hiitola-Keinänen J., Gold H., Haase A., Hast J., Stadlober B. and S. Dimov, 2010. *Design and validation of a novel master-making process chain for organic and large area electronics on flexible substrates.* Microelectronic Engineering **87**(11), pp. 2139-2145.

Velkova V., Lalev G., Hirshy H., Omar F., Scholz S. and S. Dimov, 2011. *Process chain for serial manufacture of 3D micro- and nano-scale structures.* CIRP Journal of Manufacturing Science and Technology, *In press*, doi:10.1016/j.cirpj.2011.03.005

Velkova V., Lalev G., Leach R. and S. Dimov, 2011. *Methodology for accuracy management and depth prediction in layer-based FIB milling of complex 3D features.* Microelectronic Engineering (submitted).

Velkova V., Lalev G., Minev R., Svintsov A., Zaitsev S. and S. Dimov, 2011. *Depth investigation in FIB milling of different amorphous and single crystal tooling materials.* Applied Surface Science (submitted).

Svintsov A., Zaitsev S., Lalev G., Dimov S., Velkova V. and H. Hirshy, 2009. *FIB sputtering optimization using Ion Reverse Software.* Microelectronic Engineering **86** (4-6), pp 544-547.

Lalev G., Petkov P., Sykes N., Hirshy H., Velkova V., Dimov S. and D. Barrow, 2009. *Fabrication and validation of fused silica NIL templates incorporating different*

length scale features. Microelectronic Engineering **86** (4-6), pp 705-708.

Zaitsev S., Svintsov A., Ebm C., Eder-Kapl S., Loeschner H., Platzgummer E., Lalev G., Dimov S., Velkova V. and B. Basnar, 2009. *3D ion multibeam processing with the CHARPAN PMLP tool and with the single ion-beam FIB tool optimized with the IonRevSim software*, Alternative Lithographic Technologies, Proceedings of the SPIE, Vol. 7271, pp. 72712P-1 - P-8.

Velkova V., Lalev G., Hirshy H., Scholz S. and S. Dimov, 2009. *Novel process chain for fabrication of Ni shims*, 4M/ICOMM 2009 - THE GLOBAL CONFERENCE ON MICRO MANUFACTURE: 2009, pp.411-414

Lalev G., Petkov P., Sykes N., Velkova V., Dimov S. and D. Barrow, 2008. *Template fabrication incorporating different length scale features*, Proceedings of International Conference 4M2008: Multi-Material Micro Manufacture, pp. 261-264.